Springer Theses
Recognizing Outstanding Ph.D. Research

Kerry J. Knox

Light-Induced Processes in Optically-Tweezed Aerosol Droplets

Springer

Springer Theses

Recognizing Outstanding Ph.D. Research

For further volumes:
http://www.springer.com/series/8790

Aims and Scope

The series "Springer Theses" brings together a selection of the very best Ph.D. theses from around the world and across the physical sciences. Nominated and endorsed by two recognized specialists, each published volume has been selected for its scientific excellence and the high impact of its contents for the pertinent field of research. For greater accessibility to non-specialists, the published versions include an extended introduction, as well as a foreword by the student's supervisor explaining the special relevance of the work for the field. As a whole, the series will provide a valuable resource both for newcomers to the research fields described, and for other scientists seeking detailed background information on special questions. Finally, it provides an accredited documentation of the valuable contributions made by today's younger generation of scientists.

Theses are accepted into the series by invited nomination only and must fulfill all of the following criteria

- They must be written in good English.
- The topic of should fall within the confines of Chemistry, Physics and related interdisciplinary fields such as Materials, Nanoscience, Chemical Engineering, Complex Systems and Biophysics.
- The work reported in the thesis must represent a significant scientific advance.
- If the thesis includes previously published material, permission to reproduce this must be gained from the respective copyright holder.
- They must have been examined and passed during the 12 months prior to nomination.
- Each thesis should include a foreword by the supervisor outlining the significance of its content.
- The theses should have a clearly defined structure including an introduction accessible to scientists not expert in that particular field.

Kerry J. Knox

Light-Induced Processes in Optically-Tweezed Aerosol Droplets

Doctoral Thesis accepted by
University of Bristol, United Kingdom

Springer

Author
Dr. Kerry J. Knox
Department of Chemistry
University of British Columbia
2036 Main Mall
Vancouver V6T 1Z1
BC, Canada
e-mail: kerry.knox@cantab.net

Supervisor
Prof. Jonathan P. Reid
School of Chemistry
University of Bristol
Bristol BS8 1TS
UK
e-mail: j.p.reid@bristol.ac.uk

ISSN 2190-5053 e-ISSN 2190-5061

ISBN 978-3-642-16347-0 e-ISBN 978-3-642-16348-7

DOI 10.1007/978-3-642-16348-7

Springer Heidelberg Dordrecht London New York

Cover design: eStudio Calamor, Berlin/Figueres

Printed on acid-free paper

Springer is part of Springer Science+Business Media (www.springer.com)

Supervisor's Foreword

Aerosols play an important role in a diverse range of technological and scientific domains. Not only do atmospheric particles have significant consequence for human health, increasing rates of morbidity and mortality, but they are responsible for the formation of clouds. As well as providing facile reaction pathways for the oxidation of sulphur dioxide to produce acid rain, aerosols and clouds have a significant impact on the radiative budget of the atmosphere, representing one of the largest uncertainties in understanding past climatic change and in quantifying future trends. Polar stratospheric clouds also play an important role in the recycling of stable halogen sink compounds to reactive halogens that are responsible for the formation of the Ozone Hole. Technological domains include the use of aerosols in the delivery of drugs to the lungs and in the delivery of fuels for combustion. Despite their widespread significance, they remain challenging to study; new techniques are required to explore further their properties and the dynamics of their transformation.

This thesis reports on the development and applications of a single-beam gradient force optical trap (optical tweezers) for studying aerosol properties and processes. After a general introduction to the topic of aerosols and a review of the conventional techniques available for studying heterogeneous aerosol processes, the fundamental concepts underpinning the equilibrium state of aerosol and the kinetics of mass transfer are introduced. This review focuses, in particular, on the quantity often referred to as the mass accommodation coefficient, α, which is used to quantify the proportion of gas-phase molecular collisions with a liquid surface that lead to adsorption. This is a critical quantity for predicting the activation and growth of aerosols and cloud droplets in the atmosphere and for assessing whether the aerosol can be treated as being always in true thermodynamic equilibrium. Measuring this quantity is fraught with problems, and existing published values span a wide range covering almost two orders of magnitude. It is the ultimate aim of the work presented here to develop a completely new empirical approach to the investigation of the kinetics of condensation and particle growth.

The description of this new experimental strategy begins with an introduction to the 'nuts and bolts' of using aerosol optical tweezers in Chap. 3. This is followed

in Chap. 4 by the first detailed studies of the influences of optical forces on tweezed aerosol particles, including observations of the phenomena of optical binding. Characterising trapped particles is crucial for performing measurements of chemical and physical change, and Chap. 5 presents the first studies using fluorescence spectroscopy to characterise aerosol particle size. The exciting observation of the non-linear process of four-wave mixing, which yields light over a wide wavelength range through the mixing of photons of two wavelengths to give two further wavelengths, is also described. Spherical aerosol droplets form ideal low-loss optical cavities at discrete wavelengths commensurate with whispering gallery modes, allowing droplets to act in a similar way as high finesse laser cavities, lowering the threshold for non-linear processes such as stimulated Raman scattering and four-wave mixing. Chapter 6 goes on to investigate the very low level of light absorption that occurs in optically trapped water droplets when trapped with green light. Perturbations in particle size of a few nanometres are shown to accompany small changes in trapping laser power, providing an ultra-sensitive method for making measurements of optical absorption in very small, sub-picolitre, samples.

All of the earlier chapters reach a culmination in Chap. 7, where the methods of optical trapping and optical spectroscopy are brought together in a preliminary investigation of the kinetics of particle size change, either by condensation or evaporation. Subsequent work is showing the importance of understanding in detail the optical properties of a droplet during growth or evaporation, and the detailed accounting that must be done for the small amounts of latent heat that must be transferred. However, this chapter illustrates clearly the value in studying the dynamics of single aerosol particles if the properties of an ensemble of particles are to be fully understood.

Bristol, November 2010 Prof. Jonathan P. Reid

Acknowledgements

I would first like to thank my supervisor Professor Jonathan Reid for his invaluable guidance and advice throughout my PhD, for the high standards he maintains in all aspects of his research and for all of the hard work he does. I feel very lucky to have been involved with Jonathan's research during what has been an exciting and productive time.

I would like to thank many past and present members of the Reid group for their help in the laboratory and with computing and for useful discussions. In particular Drs. Nana Kwamena, Laura Mitchem, Svemir Rudić and Jon Wills and Jason Butler and Rachael Miles have been very helpful. I would like to thank Caroline Berry for helping with some of this work as part of her final-year research project.

Beyond the Reid group I would like to thank Drs. Daniel Burnham, Christian Heinisch and Andrew Hudson for helpful discussions and the provision of useful computer programmes.

Vancouver, November 2010 Kerry J. Knox

Contents

Chapter 1
Introduction

This thesis describes studies of the properties of aerosol droplets and the development of new techniques for probing processes on a single-particle basis. Optical tweezers are used to isolate and manipulate single aerosol droplets, while imaging methods and spectroscopic techniques are used to characterise them. This introductory chapter outlines the motivation for studying aerosols followed by a summary of existing techniques for the characterisation of aerosol properties. The strategy relevant to the experiments presented in this thesis, using optical tweezers, is reviewed in detail. Finally, the specific aims of this work are described and a summary of the studies is provided.

1.1 Aerosols

An aerosol is a dispersion of fine solid or liquid particles in a gas medium. They play a significant role in numerous scientific disciplines, including combustion science, drug delivery to the lungs, air quality monitoring and atmospheric chemistry and physics [1, 2]. In this work the properties of aerosols relevant to atmospheric science are of most interest and the discussion here is limited to atmospheric aerosols.

1.1.1 Atmospheric Aerosols

Atmospheric aerosols have many natural and anthropogenic sources. Primary particles are emitted directly into the atmosphere; naturally-occurring examples include emissions from volcanic eruptions, sea spray, mineral dust and plant material such as pollen, while anthropogenic sources include the burning of fossil

K. J. Knox, *Light-Induced Processes in Optically-Tweezed Aerosol Droplets*,
Springer Theses, DOI: 10.1007/978-3-642-16348-7_1,

fuels in factories and power stations and in combustion engines [3, 4]. Aerosol particles produced by aircraft engines provide a surface for condensation of water, giving rise to the familiar contrails which can be seen in the sky in the wake of aeroplanes. Secondary aerosol particles are formed by the conversion of gas-phase species into the particulate phase via nucleation, chemical reaction and condensational growth [3, 4].

Natural sources are estimated to release $3{,}100 \times 10^{12}$ g of aerosol particles every year, while anthropogenic sources produce 450×10^{12} g per year [2]. There are large temporal and spatial variations in the number concentrations of aerosol particles resulting from the distribution of aerosol sources, the complexity of transport and deposition mechanisms and their short atmospheric lifetime, which is typically less than a week. Developing a global picture of the distribution of aerosols is challenging and as a result the current understanding of the atmospheric distribution of aerosols is limited [5, 6].

Atmospheric aerosol particles are typically composed of a complex mixture of species. The major chemical components are sea salt, sulphates, nitrates, ammonium, mineral dust, carbon and organic compounds. The composition of aerosol particles varies dramatically depending on where the particles were formed, and may even be highly heterogeneous within a sample of particles analysed from a particular location. Hundreds of organic compounds alone have been found in atmospheric aerosol, and hence characterising the composition of aerosol particles is not straightforward [4, 6].

The diameter of atmospheric aerosol particles varies from tens of Ångströms to hundreds of mircrometres. Particles with diameters of less than 1 μm are referred to as fine particles, while those with diameters greater than 1 μm are referred to as coarse. Fine particles can be separated further into nucleation and accumulation modes. The nucleation mode includes particles smaller than 0.1 μm in diameter, while the accumulation mode includes those ranging from 0.1 to 1 μm. Removal processes are relatively inefficient for the accumulation mode and hence particles in this regime have the longest atmospheric lifetimes. The accumulation mode accounts for most of the surface area of atmospheric aerosol, while the coarse mode accounts for most of the aerosol mass. The experiments detailed in this thesis were carried out on particles representative of the coarse mode.

1.1.2 Effects of Aerosols on the Atmosphere

Atmospheric aerosols play a key role in atmospheric chemistry and in determining the radiative balance of the atmosphere. They also have a marked effect on human health; the inhalation of particulate matter has been found to cause or aggravate respiratory and cardiovascular diseases and to lead to increased mortality rates [7, 8].

By providing a site for heterogeneous chemical reactions aerosols have an impact on the concentration and distribution of trace gases in the atmosphere.

The chemical processing of aerosol particles also affects their physical characteristics and composition, which can influence their impact on the radiative balance and on health. A pertinent example of the role of aerosol in the chemistry of the atmosphere is in the rapid springtime depletion of stratospheric ozone in the polar regions. Here stratospheric cloud particles, formed during the winter months, provide a catalytic surface upon which $ClONO_2$ is hydrolysed, releasing HOCl to the gas phase. The cloud particles also act as a surface for reaction of HOCl with HCl, releasing Cl_2. The HOCl and Cl_2 produced are photolysed to produce reactive chlorine radicals which catalyse the rapid destruction of ozone once the sun returns in early spring each year, giving a sudden and marked depletion of ozone referred to as the ozone hole [9, 10].

In perturbing the radiative balance of the atmosphere, aerosols give rise to a net cooling effect. Radiative forcing describes the effect of an atmospheric component on global temperature. Relative to pre-industrial times the increased atmospheric concentration of aerosols has led to radiative forcing estimated to be between -0.4 and -2.7 W m^{-2}, compared with the positive radiative forcing caused by long-lived greenhouse gases of 2.6 ± 0.3 W m^{-2} [11]. While aerosols have therefore counteracted some of the global warming arising from increased greenhouse gas emissions, this is not likely to remain the case and the magnitude of the cooling remains a subject of considerable debate [12]. Efforts to improve air quality have resulted in a reduction in anthropogenic aerosol emissions and, because aerosol particles have short atmospheric lifetimes compared with greenhouse gases, the relative importance of the aerosol cooling and greenhouse gas warming components will shift towards greenhouse gases in the future. It has been argued that the stabilising of atmospheric aerosol number concentrations will result in future climate change following or exceeding the most extreme predictions which have been made by the Intergovernmental Panel on Climate Change (IPCC) [12].

The effects of aerosols on the radiative balance can be separated into three categories: the direct effect, the indirect effect and the semi-direct effect. The direct effect describes the scattering and absorption of incoming solar and outgoing terrestrial radiation. Scattering of solar flux back into space by aerosol particles cools the atmosphere, while absorption and subsequent re-radiation of flux in the infrared in all directions warms the atmosphere. Reflective aerosols, such as those containing sulphate, scatter strongly and cool the atmosphere, while particles containing carbon are highly absorbing and cause a net warming effect [5]. The radiative forcing of aerosols relative to pre-industrial times as a result of the aerosol direct effect is estimated to be -0.5 ± 0.4 W m^{-2}.

The indirect effect describes the effect of aerosol on cloud cover and cloud properties. The radiative forcing relative to pre-industrial times as a result of the aerosol indirect effect is estimated to be between -0.3 and -1.8 W m^{-2}. Clouds scatter solar flux away from the surface of the Earth, giving rise to a cooling effect. Clouds also have a greenhouse effect, reflecting outgoing terrestrial flux back towards the surface. As a result, depending on where they form, their altitude and their optical properties, clouds can have a net warming or cooling effect on climate [5].

Aerosol particles can act as cloud condensation nuclei (CCN), a role which has an impact on the extent of cloud cover and hence cloud radiative forcing and which is indeed always necessary for clouds to form. While relative humidities of up to several hundred percent are required for homogeneous nucleation of water droplets, in the presence of aerosol particles cloud droplets can form at much lower relative humidities, typically from just over 100–110% [4]. Aerosol particle composition, structure, size and any chemical processing they have undergone affect CCN activity and the formation of clouds, indirectly influencing the radiative balance of the atmosphere.

As well as governing the formation of clouds, the optical properties and lifetime of clouds are influenced by the aerosol number concentration and the distributions in size and composition. The Twomey effect describes the observation that higher numbers of CCN will tend to produce clouds consisting of larger numbers of smaller cloud droplets [13]; these clouds tend to have a higher reflectivity, or albedo, than those composed of fewer, larger droplets, which has an influence on the radiative forcing of clouds [3, 4, 14]. Additionally, the properties of cloud droplets affect precipitation rates and cloud lifetime [14, 15]. The presence of smaller cloud droplets leads to a decrease in the precipitation efficiency, and as precipitation represents the major removal mechanism for atmospheric aerosol, the properties of aerosols play a role in determining their lifetime in the atmosphere. Given the complexity and interdependence of the variables associated with cloud formation, optical properties and lifetime, it is perhaps not surprising that the indirect effect represents the largest uncertainty in the current knowledge of anthropogenic climate radiative forcing [11, 16, 17].

The semi-direct effect is concerned with absorbing aerosol particles in clouds, for example soot, which are thought to cause warming and enhanced evaporation of the cloud, reducing cloud lifetime [18]. There is currently no consensus on the importance of this effect.

1.1.3 Current Challenges in Atmospheric Aerosol Science

While the role of greenhouse gases in climate change is well understood, there are large errors associated with measurements of the radiative forcing caused by aerosol [11, 16]. This can be attributed to the inherent difficulties associated with studying aerosol particles [5]. While atmospheric gases will be molecularly dispersed and are thus relatively easy to characterise, a sample of aerosol particles will contain distributions of particle size, morphology, composition and mixing state. Typical atmospheric aerosol particles will be composed of a complex mixture of chemical components, which may include organic or inorganic species, surfactants and pollutants such as black carbon, depending on their formation mechanism and processing in the atmosphere. All of these particle properties interact with the optical and cloud nucleating properties of the aerosols and, as a result, understanding and predicting the effects of aerosols is challenging. Further,

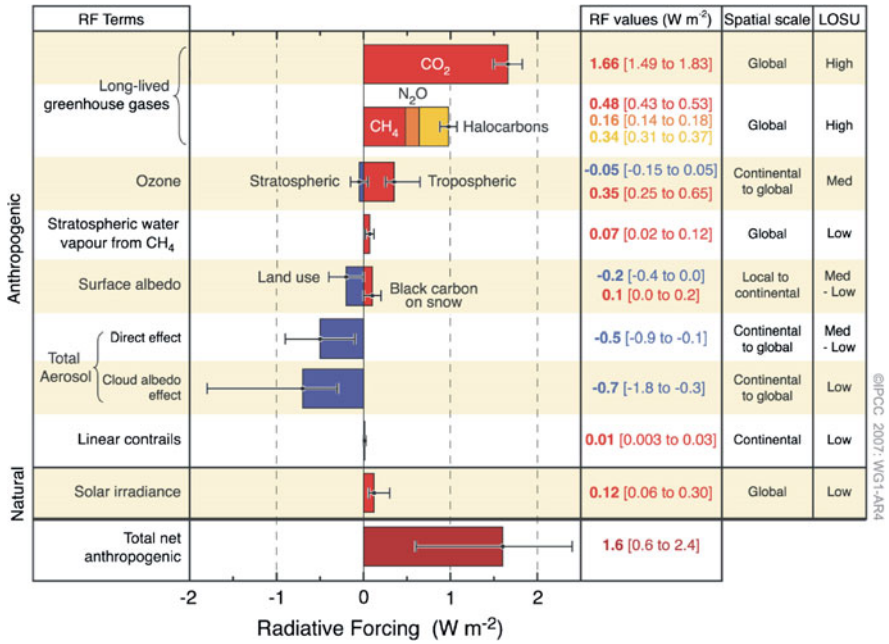

Fig. 1.1 Global average radiative forcing estimates for a variety of atmospheric constituents for 2005, relative to 1750. The right-hand column, 'LOSU', refers to the level of scientific understanding of the radiative forcing of an atmospheric constituent. Figure is a reproduction of Figure SPM.2 from Ref. [11]

the distributions of aerosol sizes and compositions in the atmosphere display considerable regional and temporal variation, and the development of an accurate global picture of the effect of aerosols on climate is therefore a highly complex task.

Figure 1.1 shows the global average radiative forcing estimates for a variety of atmospheric constituents, including greenhouse gases and aerosols, as presented in the Fourth Assessment Report of the IPCC, released in 2007 [11]. The right-hand column, labelled 'LOSU', refers to the level of scientific understanding of the radiative forcing of an atmospheric constituent. Quantifying the impact of aerosols on the radiative balance of the atmosphere remains one of the largest uncertainties in predicting future climate.

It is alarming to note that the error associated with the aerosol indirect effect, referred to in Fig. 1.1 as the cloud albedo effect, is of a similar size to that given in the Third Assessment Report of the IPCC which was released in 2001 [16]. In 2001 the indirect effect was estimated to range from 0 to -2 W m^{-2}, while in 2007 the uncertainty was only slightly smaller, with the predicted radiative forcing ranging from -0.3 to -1.8 W m^{-2}.

There are many areas of aerosol research which must be developed if the uncertainty associated with the effect of aerosols on radiative forcing, as well as

atmospheric chemistry and health impacts, is to be reduced. Some key examples are discussed below.

1.1.3.1 Optical Properties of Aerosol Particles

The magnitude of the aerosol direct effect represents a key deficiency in the current understanding of the effect of aerosols on radiative forcing. Understanding the optical properties of aerosols, and resolving the effects of particle size, morphology and composition on these optical properties, is central to reducing the uncertainty associated with the magnitude of the aerosol direct effect. Studying the optical properties of aerosol particles is made challenging by the difficulty associated with resolving the relative contributions of light scattering and absorption to light extinction [4].

In particular the optical properties of particles of mixed composition are poorly defined; for example, mixed inorganic/organic aerosols can display a range of complex particle structures, ranging from core–shell structures, where organic components are observed to coat the surface of aqueous droplets, through to the inclusion of black or elemental carbon within aqueous droplets [19]. Carbon accounts for most of the light absorption by aerosols in the atmosphere, but there are large and complicated data sets currently associated with the optical properties of carbonaceous aerosol because of the wide range of structures which these particles can adopt [4]. The dependence of the optical properties of carbonaceous aerosol on particle morphology, mixing state and chemical aging has yet to be resolved [20].

The wavelength dependence of the optical properties of aerosol particles is another area which has not been studied in great detail [19]. The wavelength dependencies for absorption by carbonaceous aerosol and dust aerosols measured during field studies carried out in recent years have been found to be highly variable [21]. In addition, there is now considerable recognition that brown carbon, often mixtures of humic-like substances (HULIS) of high molecular weight, can play a significant role in ultraviolet light absorption. Recent simulations of the absorption of solar flux in the ultraviolet have overestimated the observed terrestrial ultraviolet irradiance by 8 and 25%, for an urban and a rural site, respectively [22]. It has been suggested that organic compounds may yet be determined to be the ‘dark matter’ of the atmosphere which accounts for the missing contribution to the absorption of ultraviolet radiation [23, 24]. The influence of this on the aerosol direct effect has yet to be quantified.

1.1.3.2 Thermodynamic Equilibrium Particle Size

The optical properties of aerosol particles are highly dependent on particle size, and understanding the factors governing the thermodynamic equilibrium size of particles is crucially important in achieving rigorous quantification of the aerosol

direct effect. Determining the thermodynamic size of aerosol particles composed of a complex combination of species is, however, not straightforward and the quantitative understanding of this for multi-component atmospheric aerosol particles remains limited [4]. This is particularly true for understanding the properties of aerosols at the intermediate relative humidities typical of atmospheric conditions, ranging between 20 and 80%. Under such conditions, the aerosol may exist in a metastable state, a supersaturated aqueous-solute droplet, rather than in the thermodynamically most stable state, usually a solid particle. This is a consequence of the slow kinetics of nucleation to form solid phases. Studying such supersaturated states is impossible using most conventional bulk phase techniques where crystallisation is fast and, thus, is largely only accessible directly through aerosol measurements. Direct measurements are essential as solute concentrations in such supersaturated states may be extremely high, often greater than ten molar, leading to real solution behaviour and the formation of non-ideal interactions between organic and inorganic solutes that are not observed for more dilute solutions under conditions accessible to bulk phase studies. Reid and co-workers have recently demonstrated a technique for investigating the thermodynamic size of complex mixed composition aqueous aerosol droplets which promises to improve understanding in this area [25].

Not only is the determination of equilibrium size for complex mixtures of inorganic and organic solutes of crucial importance for the direct effect, but understanding the activation of CCN is dependent on a rigorous treatment of the solution thermodynamics and surface composition of complex mixtures of solutes. Thus, models that address the equilibrium size at the high relative humidities above saturation which are relevant for cloud formation are crucial for quantifying the magnitude of the indirect effect.

1.1.3.3 Kinetics of Aerosol Mass Transfer

Even if the thermodynamic particle size is well defined, whether an aerosol size distribution can legitimately be predicted using thermodynamic principles must be evaluated by considering the kinetic factors limiting mass transfer rates. These factors are, however, poorly understood [4, 26]. A key example of a deficiency in the current understanding of aerosol mass transfer lies in the controversy surrounding the magnitude of the mass accommodation coefficient, α, of water at the aerosol surface, which determines the rate at which an aerosol particle can take up water.

The rigorous determination of α is vitally important for atmospheric science for a number of reasons. It is a key parameter in determining the number concentrations of aerosol particles which can act as CCN and hence the magnitude of the aerosol indirect effect [27]. Indeed, it represents probably the largest single uncertainty in our ability to quantify the indirect effect. Further, it is also necessary to consider kinetic limitations on the rate of droplet growth when establishing suitable residence times in experimental chambers which are employed in the

study of the properties of aerosol particles. In such measurements, it is generally assumed that the particles are at thermodynamic equilibrium with the partial pressure of water in the surrounding gas phase, although confirmation of this assumption is essential.

Despite being the subject of over 40 experimental and theoretical studies spanning nine decades, α remains the subject of much debate, with little consensus even now over its magnitude. The reported values of α span three orders of magnitude, from ~ 0.001 to 1 [28]. Further, the effect of organic species on the uptake properties of aqueous aerosol has not been characterised definitively [4, 29]. While some laboratory studies have found no effect on the uptake kinetics of water surfaces by an insoluble organic film [30], others have revealed a clear effect [31–36]. Further, the majority of the laboratory studies have involved single organic compounds and are hence not fully representative of the behaviour of complex atmospheric aerosols [19].

Currently, many cloud modelling studies assume that aerosol sizes are thermodynamically determined [37]. It has been argued that neglecting the kinetic factors limiting aerosol mass transfer may result in an overestimate of the radiative forcing by aerosols, by as much as several W m^{-2} [27, 38]. On the contrary, it has also been argued that neglecting the kinetics of droplet growth leads to an underestimation of the radiative forcing by the aerosol indirect effect [28]. This illustrates the level of debate in this area and the importance of improving the understanding of aerosol uptake processes. The significance of α will be discussed in more detail in Chap. 2.

1.1.3.4 Chemical Processing of Aerosol Particles

The chemical processing and aging of mixed composition aerosols is another area of considerable uncertainty [4, 26]. This is important both because it affects the chemistry of the atmosphere, and because the optical properties and CCN activity of aerosols are affected by changes to their properties as a result of chemical processing in the atmosphere [19]. For example, Bertram et al. have demonstrated that the heterogeneous oxidation of organic monolayers characteristic of tropospheric aerosol surfaces by gas-phase OH radicals is highly efficient [39]. This reaction is expected to affect the hydrophilicity and hence CCN activity of organic atmospheric aerosol. Thus, chemical processing can provide a further feedback mechanism linking the chemical, physical and optical properties of aerosol and their influence on global and regional climate, the chemistry of the atmosphere, and the impact of aerosols on health.

1.2 Previous Aerosol Measurements

There are many techniques for studying the properties of aerosols in order to address the key questions in atmospheric aerosol science. These range from field

measurements to modelling studies. Laboratory studies can act as a bridge between field and modelling studies, providing a basis for understanding the physical and chemical properties of aerosol particles, and allowing proper interpretation of results from field studies and appropriate representation of these properties in modelling studies. Laboratory-based strategies for characterising the properties of aerosol particles can be separated into bulk and particle-phase techniques.

1.2.1 Bulk Techniques

Flat liquid surfaces have been widely used to provide a model for interfacial properties of aerosols. An example of a bulk technique employs a vertical or horizontal wetted-wall flow reactor. These have been used to study the uptake or reaction of trace gases at a rotating or stationary liquid surface which coats the inner surface of a flow tube. Loss of the trace gas is measured using mass spectrometry or an optical technique and is used to derive the rate of uptake. The uptakes of OH and HO_2 radicals at water and sulphuric acid surfaces and of HOCl and HCl vapour at sulphuric acid surfaces have been studied using this method by Ravishankara and co-workers [40, 41]. This group has also used flow reactors to study heterogeneous reactions occurring at liquid surfaces, for example of HOCl and HCl in sulphuric acid [42]. Thornberry and Abbatt combined a coated-wall flow tube with chemical ionization mass spectrometry to investigate the heterogeneous reaction between gas-phase ozone and three liquid unsaturated fatty acids [43].

Cox and co-workers have used flow tubes to measure the behaviour of trace species at ice surfaces, which represent aerosol particles present in the upper atmosphere. Studies have included the interaction of HOBr and HCl with ice surfaces, the uptake of HI and HBr and the kinetics of the reactive uptake of $ClONO_2$ at temperatures relevant for the upper troposphere [44–46]. This work illustrates the usefulness of bulk-phase techniques to carry out studies at a wide range of atmospherically-relevant temperatures.

Donaldson and co-workers made use of a stationary liquid surface and laser-induced fluorescence to study the effect of organic films on the uptake kinetics of gas-phase anthracene and pyrene at a flat air-aqueous interface [34, 47]. For both of these compounds the uptake coefficients were increased by the presence of an octanol film. The reaction of surface-adsorbed anthracene with gas-phase ozone was also studied using this technique [48, 49].

In a liquid jet reactor a liquid is forced through a capillary, forming a jet with a diameter of $\sim$100 μm. The jet is exposed to a trace gas and uptake rates are determined via analysis of the collected liquid. Cappa et al. have used this method to study evaporation from liquid water microjets at reduced pressures [50]. They observed that the H_2O/D_2O isotope fractionation of evaporating molecules differs from that for vapour at equilibrium and that the fractionation depends on the D_2O mole fraction and temperature, from which they reasoned that there is an energetic barrier to evaporation.

Detailed insights into the interactions of molecules at liquid surfaces can be gained by directing a beam of gas-phase molecules towards an interface [51]. Typically the liquid surface is constantly refreshed by means of a rotating wheel and the energy distributions of the inelastically-scattered products are probed by time-of-flight mass spectrometry or laser-induced fluorescence. These studies require high vacuum conditions, and as a result only low vapour pressure liquids, for example sulphuric acid and long-chain hydrocarbons, can be studied using this method. Nathanson and co-workers have studied the gas–liquid collisions and proton exchange of HCl, DCl and HBr with supercooled sulphuric acid and liquid glycerol surfaces [52–55]. They have also investigated the effect of a butanol or hexanol film on the entry of HCl and HBr to a sulphuric acid surface and the effect of a hexanol film on the evaporation of water from the same surface [56, 57]. McKendrick and co-workers have investigated the inelastic scattering of reactive species at organic liquid interfaces. Studies have included the heterogeneous reaction of a range of long-chain liquid hydrocarbons with $O(^3P)$ to produce OH [58–62] and the inelastic scattering of OH radicals at surfaces of squalane and the inert perfluorinated polyether Krytox 1506 [63]. $O(^3P)$ and the OH radical are important atmospheric oxidants and consequently gas–liquid interactions such as these are important both for the chemistry of the atmosphere and because resulting chemical processing can modify the CCN activity of organic aerosol particles.

Techniques which use a bulk surface are extremely valuable; a particular advantage is that a wide range of interfacial properties can be studied, often with very precise control of experimental conditions such as gas-phase composition, humidity and temperature. These techniques are not, however, capable of simulating certain particle-specific characteristics, for example curvature and particle structure.

1.2.2 Particle-Phase Techniques

Particle-phase techniques intrinsically take into account particle-specific characteristics. Particle-phase strategies can be further separated into two broad categories: ensemble and single-particle techniques.

1.2.2.1 Ensemble Studies

Ensemble techniques are used to study collections of droplets. An example is the droplet train apparatus, in which a flow of droplets is created using a vibrating orifice. The droplet 'train' falls through a chamber under gravity and uptake or reaction at the particle surfaces can be studied by monitoring changes in the gas-phase composition of the chamber by mass spectrometry or optical techniques [64]. Davidovits and co-workers have made extensive use of this technique to study the kinetics of trace gas uptake onto aerosol droplets [65–71]. The droplet

train apparatus can also be used to make single particle measurements, which will be discussed later.

Expansion chambers have been used to measure rates of particle growth. A collaboration between the Universities of Vienna and Helsinki has developed an experiment which involves using light scattering to monitor the rate of growth of water droplets in an expansion chamber in order to determine mass accommodation coefficients [72, 73]. The droplets are formed by condensation onto silver particles and then introduced into an expansion chamber, where they experience relative humidities of 130–150% and hence grow rapidly. These relative humidities are much higher than those which exist in the atmosphere, and it has been questioned whether expansion chambers can accurately represent water uptake and cloud droplet growth in the natural environment [28].

A differential mobility analyser (DMA) can be used to measure the size distribution of an ensemble of aerosol particles. It is used to separate particles from an aerosol flow into a narrow distribution based on their mass to charge ratio, after which they are passed to a condensation particle counter. DMAs are routinely applied to the study of the hygroscopic growth of aerosol particles. To achieve this, two DMAs are typically connected in series, with an intermediate relative humidity conditioner, and the effect of relative humidity on particle size can therefore be determined. This is often referred to as the hygroscopicity by tandem differential mobility analysis (HTDMA) approach. Badger et al. have used this approach to study the phase transitions and hygroscopic growth of aerosol particles containing humic acid and mixtures of humic acid and ammonium sulphate [74]. Kramer et al. have used this approach to study the microstructural rearrangement of NaCl aerosol particles when exposed to water vapour [75]. A limitation of this technique was highlighted by Chan et al. They considered whether the typical residence times of a few seconds in the humidity conditioner are sufficient to allow particles to attain their equilibrium size [29]. They found that typical residence times are not always sufficient and that measurements of hygroscopic growth should in the future be carried out and reported as a function of residence time.

Flow tube reactors, introduced above, can also be used to study uptake or reactions at the surface of aerosol particles. A flow of aerosol particles is generated and introduced to the reactor, where the particles are exposed to trace gases and uptake and reactions studied by monitoring the change of the gas-phase composition. A DMA is often used to determine the size distribution of aerosols present in the reactor. Hanson et al. used a flow tube reactor and mass spectrometry to study the reaction of $BrONO_2$ with H_2O on sulphuric acid aerosol particles [76], while Cox and co-workers have studied the reactive uptake of N_2O_5 by mixed humic acid and ammonium sulphate aerosol particles. The atmospheric relevance of findings from flow tube reactors must be carefully considered; typical residence times are only on the order of seconds and high concentrations of trace gases, unrepresentative of the atmosphere, are typically used in order to overcome detection sensitivity limits.

Rudich and co-workers have used cavity ring-down spectroscopy to study the optical properties of aerosol particles [77, 78]. This has included studies of

sampled atmospheric aerosol as well as laboratory-generated absorbing and non-absorbing particles and absorbing particles coated with non-absorbing shells [79, 80]. The various mixing rules which can be used to predict the optical properties of mixed composition particles have been tested by this method [79].

Ensemble techniques are valuable in that they can be devised to closely mimic atmospheric conditions, under which aerosol particles exist as part of size and compositional distributions. Ensemble techniques do involve, however, an inherent averaging of the particle properties and this can mask the nature of the underlying processes involved.

1.2.2.2 Single-Particle Studies

Single-particle techniques are free from the averaging present in ensemble measurements and are hence able to resolve the influence of particle size, composition, phase and mixing state on aerosol behaviour and properties. Numerous laboratory-based strategies have been applied to the characterisation of single aerosol particles. Traditional single-particle studies involve using a droplet train arrangement devised such that droplets which pass through a spectroscopic detection region are sampled one at a time. Reid and co-workers have used this technique to study the evaporation dynamics of mixed composition alcohol/aqueous aerosol droplets [81–84].

By isolating a single particle, studies can be carried out over longer timescales, enabling evolving particle properties to be studied. Further, the study of certain properties, for example the kinetics of aerosol mass transfer, is simplified by using stationary particles as modelling heat and mass transfer is more straightforward than in the case of a moving particle. Three modes of single-particle isolation are commonly used: electrostatic, acoustic and optical.

An electrostatic trap, or electrodynamic balance (EDB), can be used to isolate a single charged aerosol particle between electrodes to which an electric field is applied [85, 86]. Typically a vertical DC field is used to counter gravity, developed from the initial technique established by Millikan for measuring the charge on an electron, while an AC field is used to confine the particle in the horizontal plane. Various electrode designs exist, with a common example consisting of two parallel ring-shaped electrodes. In order to maintain stable trapping the fields applied are adjusted by a feedback system as the particle mass changes; this also serves as a sensitive measure of evolving particle mass [87–91]. Depending on the optical access provided by the electrode design, electrostatically-trapped particles may also be characterised using light scattering techniques. A great number of aerosol studies have been carried out using the EDB, including studies of the phase transitions of aerosol particles with varying relative humidity of the gas phase [87–91], studies of chemical ageing achieved by exposing the particles to ozone [92, 93] and studies of ice nucleation and freezing achieved by controlling the EDB chamber temperature [94, 95]. The optical absorption of a single strongly-absorbing aerosol droplet isolated using an EDB was studied by repeatedly

exposing it to an infrared laser and monitoring the resulting droplet size changes with high time resolution using light scattering measurements [96]. The rate of heat and mass transfer during droplet size changes was modelled and used to determine the droplet temperature with and without laser heating, although the absorption coefficient of the droplet was not determined in this work.

Acoustic levitation employs the radiation pressure of intense ultrasonic waves to isolate single particles. In this way Tuckermann et al. have characterised the resistance to mass transfer of water provided by surface layers of various organic species through monitoring the evaporation of acoustically-levitated aerosol droplets [36]. The droplets studied are usually considerably larger than those studied with electrostatic or optical trapping, and may be as large as millimetres. In addition, the gas-phase composition and temperature is difficult to quantify and interpret owing to the very nature of the pressure gradients required to form the acoustic wave and trap a droplet. This can significantly complicate the analysis of aerosol properties and dynamics.

Optical levitation uses the radiation pressure of a light beam to suspend particles against gravity. This technique was first demonstrated by Ashkin and Dziedzic in 1971 for glass spheres illuminated with a weakly-focussed Gaussian beam in air [97]. The beads were held against gravity and, further, experienced a weak lateral force which directed them towards the centre of the Gaussian beam. Ashkin was the first to levitate liquid droplets in air in 1975 and demonstrated that the levitating power must be adjusted to trap a droplet of changing mass in a stable fashion [98]. Particle characterisation is commonly achieved using light scattering techniques. Studies which have been performed on aerosol particles isolated using optical levitation include the photopolymerisation of droplets containing a monomer by Esen et al. and Musick et al. and the freezing of sulphuric acid/water droplets by Mund and Zellner [99–103].

Optical tweezers represent a recent extension of the technique of optical levitation, in which three-dimensional confinement of single particles is achieved by tightly focussing the illuminating Gaussian beam [104]. They are the tool used to isolate single particles for the experimental studies detailed in this thesis. A detailed description of the technique follows.

1.3 Optical Tweezers

A trap formed by optical tweezers is more correctly referred to as a single-beam gradient-force optical trap, created by tightly focussing a Gaussian laser beam using a conventional microscope objective. The feature which distinguishes this technique from optical levitation is the tight focussing of the trapping laser beam. This imparts strong trapping forces which result in three-dimensional confinement of a trapped particle. Condensed phase optical tweezing is a mature technique, pioneered by Ashkin in 1986 [104]. Since then there have been numerous studies that make use of condensed phase optical tweezers, the majority of which have

been in the biological sciences. Interesting examples include studies involving trapping living cells [105] and a demonstration of tying a 'molecular knot' in an actin filament by optically-tweezing and manipulating the ends of the filament [106]. The optical forces experienced by particles in condensed phase tweezers are well understood. As a result, by tethering biological material to plastic beads which can be manipulated using optical tweezers, measurements of mechanical properties of individual biological proteins have been possible. The force exerted by a single molecular motor has been measured to be ~ 5 pN [107]. The force required to separate a DNA double helix into separate single strands has been measured to be ~ 65 pN [108].

Optical tweezers have also been used in the field of rheology. Padgett and co-workers have, for example, used tweezed microspheres to measure and create fluid flow. By trapping a particle in a fluid flow and then switching the optical trap on and off, the resulting displacement of a trapped particle can be used to determine the fluid flow rate [109]. Alternatively, flow can be generated by two counter-propagating spinning particles. These 'micropumps' can generate flow rates of ~ 200 fL s^{-1} [110]. By studying the Brownian motion of trapped particles, precise viscosity measurements can be made in very small sample volumes [110].

Optical tweezers have also been used to initiate chemical reactions. Kitamura and co-workers have used optical tweezers to produce and simultaneously trap polymer microparticles via laser-induced polymerization of a bulk phase monomer solution [111].

A major development in the field of optical tweezing has been the use of holograms to generate the optical traps [112, 113]. In this approach the trapping beam is reflected by a spatial light modulator to form a hologram, the form of which can be precisely controlled and which determines the geometry of the optical field produced. This allows for the trapping of arrays of many particles arranged in almost any geometry and also offers three-dimensional control of the position of the trapped particles. The holographic patterns can be digitally controlled and as a result concerted movements of trapped particles can be pre-programmed. Padgett and co-workers have used holographic optical tweezers to build three-dimensional crystal structures [114]. They have also developed a method of controlling the hologram which takes information from a video image of the hand of a user; the movements of the finger tips are mirrored in the movement of the optical traps, creating a 'microhand' with which to manipulate optically-tweezed microparticles [115].

1.3.1 Aerosol Optical Tweezing

Airborne, or aerosol, optical tweezers are a much newer tool. Although Ashkin demonstrated the first optical levitation of liquid droplets in air in 1975 [98], it was not until over two decades later that optical tweezers were applied to the trapping of airborne solid [116] and liquid [117] particles. Single aerosol droplets 2–20 μm

in diameter can be held indefinitely and manipulated using this approach. The first detailed characterisations of trapped aerosol droplets were reported in 2004; Reid and co-workers described the optically-controlled coagulation of aerosol droplets [118], while Ward and co-workers detailed the chemical aging of oleic acid droplets by reaction with ozone [119].

During the five years since, Reid and co-workers have demonstrated the scope of the technique for studying a wide range of aerosol droplet properties on a single-particle basis, particularly when combined with cavity-enhanced Raman spectroscopy (CERS), enabling the characterisation of evolving droplet size [120], coagulation processes [121], the mixing state of aqueous/decane droplets and aqueous droplets containing a surfactant [122–124] and the hygroscopic properties of mixed component droplets [25, 125, 126]. These studies indicate the power of applying optical tweezers to the study of aerosol properties on a single-particle basis; however, the potential for studying aerosol properties of relevance for atmospheric science is yet to be fully exploited. Optical tweezers have not been applied so far to the study of aerosol optical properties, such as absorption, or the kinetics of aerosol mass transfer, both of which are central to improving the current understanding of the effects of aerosols on radiative forcing. These areas are the focus of the studies presented in this thesis.

For aerosol-phase studies, optical tweezing offers several distinct advantages over other commonly applied methods of particle isolation for single-particle studies. Active feedback control of the power of the trapping beam is not required, even if the particle mass changes significantly by condensation, evaporation or coagulation. Optical tweezers offer a significant lateral restoring force, and hence droplets can be held indefinitely, even if the droplet environment is perturbed by the introduction of a gas flow or evacuation of the trapping chamber. Lateral stability also means that the trapped particles may be translated using movement of the trapping beam. By splitting the trapping beam using simple optical components multiple traps can be established separated by only tens of μm, enabling comparative studies of droplet properties and investigations of particle interactions and controlled coagulation processes [122]. This is not possible with electrostatic or acoustic trapping methods. Recent work has demonstrated that arrays of tens of aerosol droplets can be isolated using holographic optical trapping techniques [127, 128]. As the trapped droplets are held with high positional stability close to the tight laser focus created by the microscope objective, this objective can also be used to collect the light scattered by the trapped droplets with high efficiency, providing spectra with high signal to noise ratios, even for small droplets and short spectral acquisition times.

Recently, it has been demonstrated that solid aerosol particles can also be trapped from a nebulised flow of aerosol droplets using optical tweezers [129]. Droplets were isolated from a nebulised stream generated from a suspension of silica particles in ethanol and after evaporation of the solvent silica particles were trapped in a stable state. This demonstration illustrates the applicability of optical tweezing to the isolation of a wide range of microparticles.

1.3.2 Optical Forces

An optically-tweezed particle experiences two optical forces: a scattering and a gradient force [130]. The trapping beam used in the studies described in this thesis has a wavelength, λ, of 532 nm, and the droplets are of diameter, d, of $\sim$6–16 μm. For situations where $d >> \lambda$, as is the case here, a ray optics approach may be used to explain the optical forces arising from the interaction of a Gaussian beam with a particle [131].

The scattering force arises from the transfer of momentum of photons from the trapping laser beam scattered by the particle and acts in the direction of the propagation of the trapping beam. The effect is illustrated in Fig. 1.2a. The gradient force results from momentum transfer associated with refraction of the trapping light at the particle boundaries; it has a component in the lateral plane and another in the axis of propagation of the trapping light. The origin of the axial gradient force is illustrated in Fig. 1.2b for trapping downbeam of the laser focus. As light passes through the particle, refraction of light occurs at the particle interfaces, resulting in the transfer of momentum to the particle and giving rise to an axial gradient force which acts towards the region of maximum light intensity.

The lateral component of the gradient force acts to pull a particle into the region of maximum light intensity if the particle has a higher refractive index than the surrounding medium. Figure 1.3 illustrates the origin of the lateral gradient force. If the particle is displaced to the side of the trapping beam, the intensities of the light rays entering the particle are not symmetric about the centre of the particle. Refraction of light rays of differing intensity on either side of the particle results in a force which acts to restore the particle to the centre of the illuminating Gaussian beam.

For stable trapping the gradient force must dominate the scattering force [130]. A high gradient force is achieved by using a high numerical aperture objective to

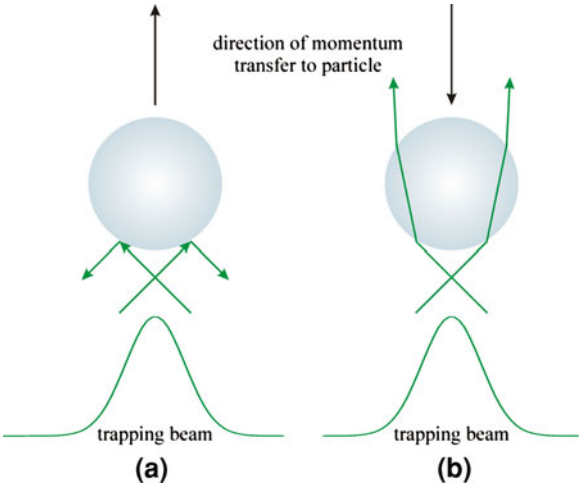

Fig. 1.2 Origin of optical forces acting in the axis of the trapping beam propagation: **a** scattering force **b** axial gradient force

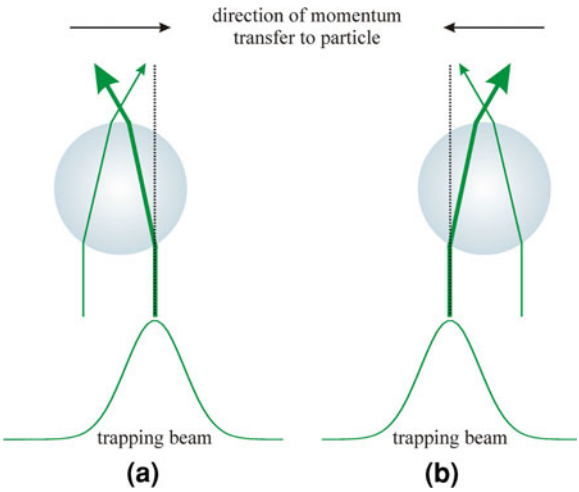

Fig. 1.3 Origin of optical gradient forces acting to restore the particle to the position of highest light intensity in the lateral plane. Particle displacements to left and right are shown in (**a**) and (**b**), respectively

strongly focus the trapping beam. It is also important to overfill the back aperture of the objective, as this ensures that the droplet is illuminated with the central portion of the Gaussian beam, the intensity of which changes markedly with distance from the central axis of the beam in this region. Typical trapping forces are on the order of tens of picoNewtons [131]. In the experimental arrangement employed in these studies the microscope objective is inverted and hence the gravitational force on the droplet counteracts the scattering force. The gravitational force is, however, typically a factor of 10^6 smaller than the optical gradient forces experienced by a trapped particle [104]. Consequently, the trapping forces in optical tweezers are as much as a factor of 10^6 larger than the forces used in particle levitation, where the levitation force must only balance the gravitational force exerted on an object.

1.4 Project Aims

It is clear that reducing the uncertainties associated with the direct and indirect effects should be a priority for aerosol science. Central to improving the understanding of the direct effect is the quantification of aerosol optical properties and the development of an improved understanding of the effect of aerosol composition on these properties and their wavelength dependence. Improving the understanding of the indirect effect will involve studies of the cloud nucleating properties of aerosol particles. A particular problem which needs addressing is the conjecture surrounding the magnitude of the mass accommodation coefficient of water at aerosol surfaces. This is a key example of an aerosol property for which the effect of the aerosol composition has not been definitively established.

The previously employed methods for measuring the mass accommodation coefficient of water suffer from a number of limitations; these will be discussed in detail in Chap. 2.

The work presented in this thesis seeks to address two central deficiencies in the current understanding of aerosol effects on radiative forcing. The work aims to:

- Develop a sensitive, quantitative technique for measuring aerosol optical absorption that may be used to study the absorption by both water soluble and insoluble organic components.
- Develop a technique for measuring the mass accommodation coefficient of water at the surface of an aqueous aerosol droplet which avoids the limitations of previous techniques.

As the optical and kinetic properties of mixed composition particles in particular are poorly understood, it is desirable that the techniques developed should be flexible enough to be applicable to the study of aerosol particles with a range of compositions and structures. In the case of the absorption technique it is desirable that a range of illumination wavelengths can be investigated.

In order to resolve robustly the effect of particle composition these techniques should be based on a single-particle approach. Moreover, discriminating between the effect of variations in particle composition from that of changes in the particle environment will necessitate comparative studies on simultaneously-isolated particles. Based on these conditions, and the ease with which optical tweezers can be coupled to spectroscopic techniques, optical tweezers have been chosen as the particle isolation method for these studies. The abundance and importance of water in the atmosphere, arising partly from the role it plays in clouds, has led to this work being focussed on characterising the properties of aqueous aerosol droplets.

In order to achieve these two central aims two secondary research goals were also addressed. Firstly, a study of the optical forces experienced by optically-tweezed aerosol droplets was undertaken. The current understanding of the trapping behaviour of optically-trapped particles in the aerosol phase is limited yet a detailed understanding is essential if the findings from studies carried out using aerosol optical tweezers are to be rigorously interpreted. Secondly, in order to provide a basis for studying the absorption of atmospherically-relevant aerosol droplets, a spectroscopic study of optically-tweezed aerosol droplets containing absorbing fluorescent chromophores was carried out.

1.5 Thesis Summary

Throughout these studies optical tweezers are used to isolate aerosol particles. The evolving aerosol droplet size is monitored using cavity-enhanced Raman spectroscopy (CERS) and in many cases the response of the droplet size to perturbations in its environment is used to gain information about other fundamental aerosol properties.

Chapter 2 will outline the theory describing the thermodynamic and kinetic factors which determine aerosol droplet size. This will include a discussion of the significance of the mass accommodation coefficient of water at an aerosol interface and the previous methods which have been used to measure it.

Chapter 3 describes the experimental equipment used in the studies presented in this thesis and also the theoretical basis of the spectroscopic techniques and droplet size determination.

Chapter 4 describes the findings of the optical manipulation studies which were undertaken to better understand the optical forces experienced by optically-tweezed aerosol droplets. Imaging of the trapped droplets in two orthogonal planes has enabled measurements of the displacement of the droplet in the axis of the trapping beam and the observation of several trapping phenomena. This is the first study of this kind carried out for aerosol optical tweezers.

Chapter 5 describes spectroscopic studies of optically-tweezed aerosol droplets containing absorbing chromophores. This represents not only a step towards characterising the optical absorption of weakly absorbing aerosol droplets, but also a new approach to characterising the composition of optically-tweezed aerosol droplets; additionally, it has relevance for identifying biological species in aerosol particles. This has not been investigated in detail, yet is clearly of great interest in terms of human health [6]. This represents the first detailed study of fluorescence from optically-tweezed aerosol droplets, as well as the first observation of a parametric mixing process in a single aqueous microdroplet under conditions of continuous-wave illumination.

Chapter 6 describes a new method for measuring the optical absorption of aerosol particles. This work represents not only a novel technique for studying aerosol absorption, but also a new approach to ultra-sensitive absorption spectroscopy. This technique makes use of the ability to establish multiple optical tweezers to perform comparative studies. It is applicable to a wide range of aerosol compositions and is capable of resolving the wavelength dependence of the optical absorption.

Chapter 7 describes a new technique for measuring the kinetics of aerosol mass transfer, which is an extension of the absorption technique described in Chap. 6. This represents a new technique for measuring the mass accommodation of water at an aerosol surface and offers many advantages over existing techniques. It is flexible enough to be applicable to a range of aerosol compositions and makes use of the ability to establish multiple optical tweezers to perform comparative studies.

References

1. P.C.L. Kwok, H.K. Chan, Pharm. Res. **25**, 277 (2008)
2. J.P. Reid, in *Colloid Science: Theory, Methods and Applications*, ed. by T. Cosgrove (Blackwells Publishing, Oxford, 2005), p. 180
3. J.H. Seinfeld, S.N. Pandis, *Atmospheric Chemistry and Physics: From Air Pollution to Climate Change* (Wiley, New York, 1998)

4. U. Pöschl, Angew. Chem. Int. Ed. **44**, 7520 (2005)
5. T.R. Karl, K.E. Trenberth, Science **302**, 1719 (2003)
6. U. Pöschl, Anal. Bioanal. Chem. **375**, 30 (2003)
7. D.W. Dockery, C.A. Pope, Annu. Rev. Public Health **15**, 107 (1994)
8. R.M. Harrison, J.X. Yin, Sci. Total Environ. **249**, 85 (2000)
9. O.B. Toon, R.P. Turco, Sci. Am. **264**, 68 (1991)
10. B.S. Berland, M.A. Tolbert, S.M. George, J. Phys. Chem. A **101**, 9954 (1997)
11. IPCC, Climate Change 2007, The Physical Science Basis, Contribution of Working Group I to the Fourth Assessment Report of the Intergovernmental Panel on Climate Change, ed. by S. Solomon, D. Qin, M. Manning, Z. Chen, M. Marquis, K.B. Averyt, M. Tignor, H.L. Miller (Cambridge University Press, Cambridge and New York, 2007)
12. M.O. Andreae, C.D. Jones, P.M. Cox, Nature **435**, 1187 (2005)
13. S.A. Twomey, M. Piepgrass, T.L. Wolfe, Tellus Ser. B Chem. Phys. Meteorol. **36**, 356 (1984)
14. W.W. Kellogg, Science **256**, 598 (1992)
15. D. Rosenfeld, Science **287**, 1793 (2000)
16. IPCC, Climate Change 2001, The Physical Science Basis, Contribution of Working Group I to the Third Assessment Report of the Intergovernmental Panel on Climate Change, ed. by F. Joos, A. Ramirez-Rojas, J.M.R. Stone, J. Zillman (Cambridge University Press, Cambridge and New York, 2001)
17. D. Rosenfeld, Science **312**, 1323 (2006)
18. J. Hansen, M. Sato, R. Ruedy, J. Geophys. Res. Atmos. **102**, 6831 (1997)
19. S. Fuzzi et al., Atmos. Chem. Phys. **6**, 2017 (2006)
20. T.C. Bond, R.W. Bergstrom, Aerosol Sci. Technol. **40**, 1 (2006)
21. R.W. Bergstrom, P. Pilewskie, P.B. Russell, J. Redemann, T.C. Bond, P.K. Quinn, B. Sierau, Atmos. Chem. Phys. **7**, 5937 (2007)
22. M.Z. Jacobson, J. Geophys. Res. Atmos. **104**, 3527 (1999)
23. M.O. Andreae, A. Gelencser, Atmos. Chem. Phys. **6**, 3131 (2006)
24. E. Dinar, A.A. Riziq, C. Spindler, C. Erlick, G. Kiss, Y. Rudich, Faraday Discuss. **137**, 279 (2008)
25. K.L. Hanford, L. Mitchem, J.P. Reid, S.L. Clegg, D.O. Topping, G.B. McFiggans, J. Phys. Chem. A **112**, 9413 (2008)
26. U. Pöschl, Y. Rudich, M. Ammann, Atmos. Chem. Phys. **7**, 5989 (2007)
27. P.Y. Chuang, R.J. Charlson, J.H. Seinfeld, Nature **390**, 594 (1997)
28. P. Davidovits et al., Geophys. Res. Lett. **31**, L22111 (2004)
29. M.N. Chan, C.K. Chan, Atmos. Chem. Phys. **5**, 2703 (2005)
30. C.N. Cruz, S.N. Pandis, J. Geophys. Res. Atmos. **103**, 13111 (1998)
31. E.K. Rideal, J. Phys. Chem. **29**, 1585 (1925)
32. M.N. Chan, C.K. Chan, Atmos. Environ. **41**, 4423 (2007)
33. J.A. Thornton, J.P.D. Abbatt, J. Phys. Chem. A **109**, 10004 (2005)
34. B.T. Mmereki, S.R. Chaudhuri, D.J. Donaldson, J. Phys. Chem. A **107**, 2264 (2003)
35. E.K. Bigg, Atmos Res. **20**, 82 (1986)
36. R. Tuckermann, S. Bauerecker, H.K. Cammenga, J. Colloid Interf. Sci. **310**, 559 (2007)
37. R.J. Charlson, S.E. Schwartz, J.M. Hales, R.D. Cess, J.A. Coakley, J.E. Hansen, D.J. Hofmann, Science **255**, 423 (1992)
38. A. Nenes, S. Ghan, H. Abdul-Razzak, P.Y. Chuang, J.H. Seinfeld, Tellus Ser. B Chem. Phys. Meteorol. **53**, 133 (2001)
39. A.K. Bertram, A.V. Ivanov, M. Hunter, L.T. Molina, M.J. Molina, J. Phys. Chem. A **105**, 9415 (2001)
40. D.R. Hanson, J.B. Burkholder, C.J. Howard, A.R. Ravishankara, J. Phys. Chem. **96**, 4979 (1992)
41. D.R. Hanson, A.R. Ravishankara, J. Phys. Chem. **97**, 12309 (1993)
42. D.J. Donaldson, A.R. Ravishankara, D.R. Hanson, J. Phys. Chem. A **101**, 4717 (1997)
43. T. Thornberry, J.P.D. Abbatt, Phys. Chem. Chem. Phys. **6**, 84 (2004)

44. J.C. Mossinger, R.G. Hynes, R.A. Cox, J. Geophys. Res. Atmos. **107**, 4740 (2002)
45. C.J. Percival, J.C. Mossinger, R.A. Cox, Phys. Chem. Chem. Phys. **1**, 4565 (1999)
46. M.A. Fernandez, R.G. Hynes, R.A. Cox, J. Phys. Chem. A **109**, 9986 (2005)
47. B.T. Mmereki, D.J. Donaldson, Phys. Chem. Chem. Phys. **4**, 4186 (2002)
48. B.T. Mmereki, D.J. Donaldson, J. Phys. Chem. A **107**, 11038 (2003)
49. B.T. Mmereki, D.J. Donaldson, J.B. Gilman, T.L. Eliason, V. Vaida, Atmos. Environ. **38**, 6091 (2004)
50. C.D. Cappa, W.S. Drisdell, J.D. Smith, R.J. Saykally, R.C. Cohen, J. Phys. Chem. B **109**, 24391 (2005)
51. G.M. Nathanson, Annu. Rev. Phys. Chem. **55**, 231 (2004)
52. P. Behr, J.R. Morris, M.D. Antman, B.R. Ringeisen, J.R. Splan, G.M. Nathanson, Geophys. Res. Lett. **28**, 1961 (2001)
53. J.R. Morris, P. Behr, M.D. Antman, B.R. Ringeisen, J. Splan, G.M. Nathanson, J. Phys. Chem. A **104**, 6738 (2000)
54. B.R. Ringeisen, A.H. Muenter, G.M. Nathanson, J. Phys. Chem. B **106**, 4988 (2002)
55. B.R. Ringeisen, A.H. Muenter, G.M. Nathanson, J. Phys. Chem. B **106**, 4999 (2002)
56. J.R. Lawrence, S.V. Glass, S.C. Park, G.M. Nathanson, J. Phys. Chem. A **109**, 7458 (2005)
57. S.V. Glass, S.C. Park, G.M. Nathanson, J. Phys. Chem. A **110**, 7593 (2006)
58. H. Kelso, S.P.K. Köhler, D.A. Henderson, K.G. McKendrick, J. Chem. Phys. **119**, 9985 (2003)
59. S.P.K. Köhler, M. Allan, H. Kelso, D.A. Henderson, K.G. McKendrick, J. Chem. Phys. **122**, 024712 (2005)
60. S.P.K. Köhler, M. Allan, M.L. Costen, K.G. McKendrick, J. Phys. Chem. B **110**, 2771 (2006)
61. M. Allan, P.A.J. Bagot, M.L. Costen, K.G. McKendrick, J. Phys. Chem. C **111**, 14833 (2007)
62. M. Allan, P.A.J. Bagot, R.E. Westacott, M.L. Costen, K.G. McKendrick, J. Phys. Chem. C **112**, 1524 (2008)
63. P.A.J. Bagot, C. Waring, M.L. Costen, K.G. McKendrick, J. Phys. Chem. C **112**, 10868 (2008)
64. D.R. Worsnop, M.S. Zahniser, C.E. Kolb, J.A. Gardner, L.R. Watson, J.M. Vandoren, J.T. Jayne, P. Davidovits, J. Phys. Chem. **93**, 1159 (1989)
65. J. Boniface, Q. Shi, Y.Q. Li, J.L. Cheung, O.V. Rattigan, P. Davidovits, D.R. Worsnop, J.T. Jayne, C.E. Kolb, J. Phys. Chem. A **104**, 7502 (2000)
66. J.L. Cheung, Y.Q. Li, J. Boniface, Q. Shi, P. Davidovits, D.R. Worsnop, J.T. Jayne, C.E. Kolb, J. Phys. Chem. A **104**, 2655 (2000)
67. J.T. Jayne, S.X. Duan, P. Davidovits, D.R. Worsnop, M.S. Zahniser, C.E. Kolb, J. Phys. Chem. **95**, 6329 (1991)
68. J.T. Jayne, S.X. Duan, P. Davidovits, D.R. Worsnop, M.S. Zahniser, C.E. Kolb, J. Phys. Chem. **96**, 5452 (1992)
69. J.T. Jayne, D.R. Worsnop, C.E. Kolb, E. Swartz, P. Davidovits, J. Phys. Chem. **100**, 8015 (1996)
70. C.E. Kolb, P. Davidovits, J.T. Jayne, Q. Shi, D.R. Worsnop, Prog. React. Kinet. Mechanism **27**, 1 (2002)
71. E. Swartz, Q. Shi, P. Davidovits, J.T. Jayne, D.R. Worsnop, C.E. Kolb, J. Phys. Chem. A **103**, 8824 (1999)
72. P.M. Winkler, A. Vrtala, P.E. Wagner, M. Kulmala, K.E.J. Lehtinen, T. Vesala, Phys. Rev. Lett. **93**, 075701 (2004)
73. P.M. Winkler, A. Vrtala, R. Rudolf, P.E. Wagner, I. Riipinen, T. Vesala, K.E.J. Lehtinen, Y. Viisanen, M. Kulmala, J. Geophys. Res. Atmos. **111**, D19202 (2006)
74. C.L. Badger, I. George, P.T. Griffiths, C.F. Braban, R.A. Cox, J.P.D. Abbatt, Atmos. Chem. Phys. **6**, 755 (2006)
75. L. Kramer, U. Pöschl, R. Niessner, J. Aerosol Sci. **31**, 673 (2000)
76. D.R. Hanson, A.R. Ravishankara, E.R. Lovejoy, J. Geophys. Res. Atmos. **101**, 9063 (1996)

77. M. Lang-Yona, Y. Rudich, E. Segre, E. Dinar, A. Abo-Riziq, Anal. Chem. **81**, 1762 (2009)
78. C. Spindler, A.A. Riziq, Y. Rudich, Aerosol Sci. Technol. **41**, 1011 (2007)
79. A.A. Riziq, C. Erlick, E. Dinar, Y. Rudich, Atmos. Chem. Phys. **7**, 1523 (2007)
80. A.A. Riziq, M. Trainic, C. Erlick, E. Segre, Y. Rudich, Atmos. Chem. Phys. **8**, 1823 (2008)
81. R.J. Hopkins, J.P. Reid, J. Phys. Chem. A **109**, 7923 (2005)
82. R.J. Hopkins, J.P. Reid, J. Phys. Chem. B **110**, 3239 (2006)
83. R.J. Hopkins, C.R. Howle, J.P. Reid, Phys. Chem. Chem. Phys. **8**, 2879 (2006)
84. C.R. Howle, C.J. Homer, R.J. Hopkins, J.P. Reid, Phys. Chem. Chem. Phys. **9**, 5344 (2007)
85. R.F. Wuerker, H. Shelton, R.V. Langmuir, J. Appl. Phys. **30**, 342 (1959)
86. E.J. Davis, Aerosol Sci. Technol. **26**, 212 (1997)
87. L. Treuel, S. Schulze, T. Leisner, R. Zellner, Faraday Discuss. **137**, 265 (2008)
88. C. Marcolli, U.K. Krieger, J. Phys. Chem. A **110**, 1881 (2006)
89. C.G. Peng, A.H.L. Chow, C.K. Chan, Aerosol Sci. Technol. **35**, 753 (2001)
90. C.G. Peng, C.K. Chan, Atmos. Environ. **35**, 1183 (2001)
91. C. Peng, M.N. Chan, C.K. Chan, Environ. Sci. Technol. **35**, 4495 (2001)
92. A.K.Y. Lee, C.K. Chan, Atmos. Environ. **41**, 4611 (2007)
93. A.K.Y. Lee, C.K. Chan, J. Phys. Chem. A **111**, 6285 (2007)
94. P. Stockel, H. Vortisch, T. Leisner, H. Baumgartel, J. Molecular Liquids **96**(7), 153 (2002)
95. P. Stockel, I.M. Weidinger, H. Baumgartel, T. Leisner, J. Phys. Chem. A **109**, 2540 (2005)
96. C.B. Richardson, H.B. Lin, R. Mcgraw, I.N. Tang, Aerosol Sci. Technol. **5**, 103 (1986)
97. A. Ashkin, J.M. Dziedzic, Appl. Phys. Lett. **19**, 283 (1971)
98. A. Ashkin, J.M. Dziedzic, Science **187**, 1073 (1975)
99. C. Esen, T. Kaiser, G. Schweiger, Appl. Spectroscopy **50**, 823 (1996)
100. J. Musick, J. Popp, M. Trunk, W. Kiefer, Appl. Spectroscopy **52**, 692 (1998)
101. C. Mund, R. Zellner, J. Mol. Struct. **661**, 491 (2003)
102. C. Mund, R. Zellner, ChemPhysChem **4**, 630 (2003)
103. C. Mund, R. Zellner, ChemPhysChem **4**, 638 (2003)
104. A. Ashkin, J.M. Dziedzic, J.E. Bjorkholm, S. Chu, Opt. Lett. **11**, 288 (1986)
105. M.T. Wei, A. Zaorski, H.C. Yalcin, J. Wang, M. Hallow, S.N. Ghadiali, A. Chiou, H.D. Ou-Yang, Opt. Express **16**, 8594 (2008)
106. Y. Arai, R. Yasuda, K. Akashi, Y. Harada, H. Miyata, K. Kinosita, H. Itoh, Nature **399**, 446 (1999)
107. J.T. Finer, R.M. Simmons, J.A. Spudich, Nature **368**, 113 (1994)
108. S.B. Smith, Y.J. Cui, C. Bustamante, Science **271**, 795 (1996)
109. H. Mushfique, J. Leach, R. Di Leonardo, M.J. Padgett, J.M. Cooper, Proc. Inst. Mech. Eng. Part C J. Mech. Eng. Sci. **222**, 829 (2008)
110. R. Lugowski, B. Kolodziejczyk, Y. Kawata, Opt. Commun. **202**, 1 (2002)
111. Y. Tsuboi, M. Nishino, T. Sasaki, N. Kitamura, J. Phys. Chem. B **109**, 7033 (2005)
112. M. Reicherter, T. Haist, E.U. Wagemann, H.J. Tiziani, Opt. Lett. **24**, 608 (1999)
113. J.E. Curtis, B.A. Koss, D.G. Grier, Opt. Commun. **207**, 169 (2002)
114. M. Padgett, J. Leach, G. Sinclair, J. Courtial, E. Yao, G. Gibson, P. Jordan, J. Cooper, J. Laczik, Proc. Soc. Photo-Optical Instrum. Eng. **5514**, 371 (2004)
115. G. Whyte, G. Gibson, J. Leach, M. Padgett, D. Robert, M. Miles, Opt. Express **14**, 12497 (2006)
116. R. Omori, T. Kobayashi, A. Suzuki, Opt. Letters **22**, 816 (1997)
117. N. Magome, M.I. Kohira, E. Hayata, S. Mukai, K. Yoshikawa, J. Phys. Chem. B **107**, 3988 (2003)
118. R.J. Hopkins, L. Mitchem, A.D. Ward, J.P. Reid, Phys. Chem. Chem. Phys. **6**, 4924 (2004)
119. M.D. King, K.C. Thompson, A.D. Ward, J. Am. Chem. Soc. **126**, 16710 (2004)
120. L. Mitchem, J. Buajarern, R.J. Hopkins, A.D. Ward, R.J.J. Gilham, R.L. Johnston, J.P. Reid, J. Phys. Chem. A **110**, 8116 (2006)
121. J. Buajarern, L. Mitchem, A.D. Ward, N.H. Nahler, D. McGloin, J.P. Reid, J. Chem. Phys. **125**, 114506 (2006)
122. L. Mitchem, J. Buajarern, A.D. Ward, J.P. Reid, J. Phys. Chem. B **110**, 13700 (2006)

123. J. Buajarern, L. Mitchem, J.P. Reid, J. Phys. Chem. A **111**, 9054 (2007)
124. J. Buajarern, L. Mitchem, J.P. Reid, J. Phys. Chem. A **111**, 11852 (2007)
125. L. Mitchem, R.J. Hopkins, J. Buajarern, A.D. Ward, J.P. Reid, Chem. Phys. Lett. **432**, 362 (2006)
126. J.R. Butler, L. Mitchem, K.L. Hanford, L. Treuel, J.P. Reid, Faraday Discuss. **137**, 351 (2008)
127. D.R. Burnham, D. McGloin, Opt. Express **14**, 4175 (2006)
128. J.R. Butler, J.B. Wills, L. Mitchem, D.R. Burnham, D. McGloin, J.P. Reid, Lab Chip **9**, 521 (2009)
129. M.D. Summers, D.R. Burnham, D. McGloin, Opt. Express **16**, 7739 (2008)
130. K. Svoboda, S.M. Block, Annu. Rev. Biophys. Biomol. Struct. **23**, 247 (1994)
131. J.E. Molloy, M.J. Padgett, Contemporary Phys. **43**, 241 (2002)

Chapter 2
Aerosol Mass Transfer

The size distribution of aerosol particles has a significant impact on their chemical and physical properties, including their optical properties and ability to act as cloud condensation nuclei in the atmosphere [1]. Understanding the factors which determine the particle size underpins all of aerosol science and is essential for the construction of accurate atmospheric models of past, present and future climate [2].

This chapter will outline the thermodynamic and kinetic factors which control the size of aerosol particles, in particular aqueous aerosol droplets containing inorganic and organic solutes. Theory predicting thermodynamic equilibrium droplet size will first be discussed, followed by a description of the kinetic aspects of aerosol mass transfer which can limit the rate at which the equilibrium size is established.

2.1 Thermodynamic Equilibrium Droplet Size

Water plays a highly significant role in the atmosphere as a result of its abundance and is the major constituent of clouds. Atmospheric water exists in the gas-phase and in the condensed phase as aerosol droplets and ice particles. Aqueous aerosol droplets will rarely consist of pure water; instead they will contain a range of soluble and insoluble species depending on where and how they formed. The discussion here will therefore focus on the equilibrium size of aqueous droplets containing common atmospheric constituents such as inorganic salts.

2.1.1 Deliquescence and Efflorescence

The size of aqueous aerosol droplets is determined by the equilibrium partitioning of water into the condensed phase and, thus the relative humidity of the droplet

K. J. Knox, *Light-Induced Processes in Optically-Tweezed Aerosol Droplets*,
Springer Theses, DOI: 10.1007/978-3-642-16348-7_2,

environment. This relative humidity, RH, is defined as the ratio of the partial pressure of water, p_w, to the temperature-dependent saturation vapour pressure of water, p^0, and is often expressed as a percentage, hence [1]:

$$\mathrm{RH} = \frac{p_w}{p^0} \times 100 \tag{2.1}$$

Inorganic salt particles are solid and crystalline at low RH, while at higher RH they take up water and become solution droplets. The variation of particle water content does not vary smoothly with RH over the entire range from 0 to 100%. A solid particle of an inorganic salt does not take up water significantly until a critical RH is reached, known as the deliquescence RH (DRH), which is characteristic of the salt in question. At this RH a phase transition occurs and the particle abruptly takes up water, producing a saturated salt solution. As the RH increases further the particle grows by absorbing more water. If the RH decreases the particle will lose water by evaporation until the particle crystallises at a characteristic RH. This crystallisation RH (CRH) is not found to be equal to the DRH. In fact the CRH is generally considerably lower than the DRH. As a result there is a range of RH, between the CRH and DRH, over which an aerosol droplet can exist in a supersaturated metastable state. This metastable state exists because nucleation sites are required for crystallisation of the salt content of the droplets. In free aerosol particles these are not available and a droplet must first reach a state of critical supersaturation before nucleation and crystallisation can take place. This hysteresis is illustrated in Fig. 2.1 for NaCl, calculated using the Aerosol Inorganics Model (AIM), which was developed by Clegg et al. in 1998 [3]. The variation of the total particle mass with RH is expressed relative to the dry particle mass. It should be noted that some compounds, for example H_2SO_4 and some organic compounds, take up or lose water smoothly as the RH is increased or decreased, respectively. This is a result of their highly hygroscopic nature. The behaviour of H_2SO_4 is also shown in Fig. 2.1.

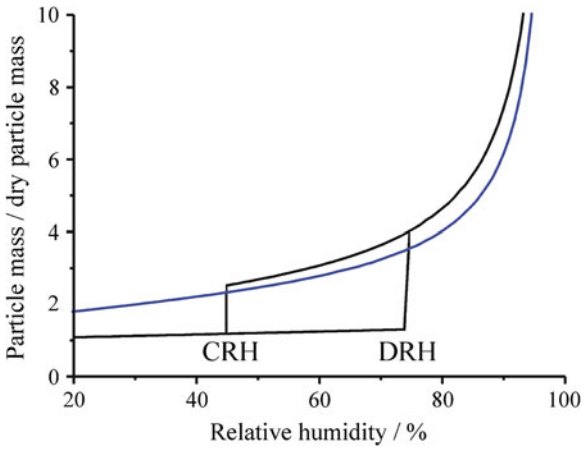

Fig. 2.1 Variation in particle mass, relative to the dry particle mass, with RH at 25 °C for NaCl and H_2SO_4, shown in *black* and *blue*, respectively. Calculated using AIM [3]

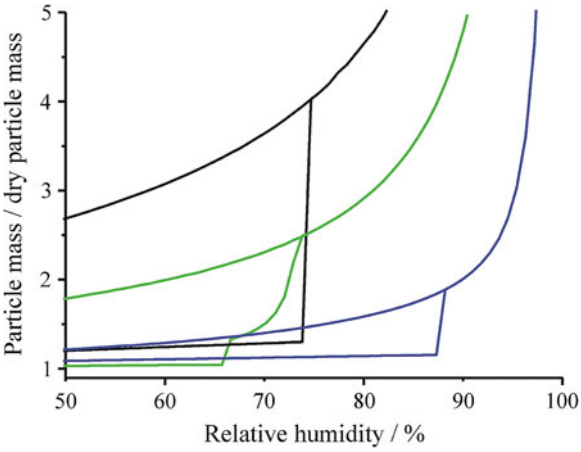

Fig. 2.2 Deliquescence behaviour of an NaCl, glutaric acid and mixed composition particle consisting of NaCl and glutaric acid (57 and 43% by mass, respectively) at 25°C, shown in *black*, *blue* and *green* respectively. Calculated using AIM [3]

Most aerosol mass is in fact of mixed composition. In this situation similar behaviour is observed, however, 'stepped' deliquescence occurs over an RH range determined by the mixture of the species in the droplet [4]. An example is provided in Fig. 2.2 for a mixture of NaCl (57% by mass) and glutaric acid (43% by mass), again calculated using AIM. The variation of particle mass with RH for NaCl and glutaric acid particles is included for comparison; it can be seen that deliquescence for the mixed composition particle occurs at a lower RH than the DRH of both pure NaCl and glutaric acid particles and is not abrupt.

The inorganic salt used in most of the experiments discussed in this thesis is NaCl, which has a DRH of 75.3 ± 0.1 [4]. The experiments are performed under conditions of high RH of ~85–98%; they are therefore not complicated by crystallisation and the droplet size can be considered to vary smoothly with RH.

2.1.2 Variation of Droplet Size with Relative Humidity above the DRH

The factors determining the equilibrium size of an aqueous droplet can be understood by considering the partial pressure of water at the droplet surface with variation in solute concentration or, equivalently, droplet size. A droplet will be at equilibrium if the partial pressure of water at its surface, $p_{w,d}$, is equal to that in the surrounding gas-phase, p_w. The p_w is determined by the RH. The factors determining $p_{w,d}$ are the curvature of the droplet surface and the droplet solute concentration.

The curvature or Kelvin effect describes the observation that the vapour pressure of a substance above a curved surface is greater than that above a flat surface. For a pure water droplet, the smaller the radius the higher the degree of curvature

and hence the higher the vapour pressure above the droplet surface. This effect arises because a molecule at a curved interface has fewer neighbouring molecules than one at a flat interface, and hence the sum of the intermolecular forces experienced by the molecule is lower. As a result less energy is required to liberate such a molecule into the gas phase. The effect is described by Kelvin equation [1]:

$$\frac{p_c}{p^0} = \exp\left(\frac{2M_w\sigma_w}{RT\rho_w r}\right) \tag{2.2}$$

where p_c is the vapour pressure above a curved water droplet surface, M_w is the molar weight of water, σ_w is the surface tension of a water/air interface, R is the molar gas constant, T is the temperature, ρ_w is the density of water and r is the droplet radius. A consequence of this effect is that a pure water droplet would require an RH of $> 100\%$ in its surroundings to maintain a stable equilibrium size. The effect of curvature on the p_c is only significant for droplet radii of less than ~ 0.05 μm, as illustrated by Fig. 2.3.

The solute effect describes the observation that the addition of a solute to a solution reduces the vapour pressure of the solvent at the surface. In an ideal solution the added solute molecules take the place of some of the solvent molecules in the solution and this reduces the mole fraction and thus the vapour pressure of the solvent at the interface. Hence the solute effect is given by Raoult's law [1]:

$$p_{w,s} = x_w p^0 \tag{2.3}$$

where $p_{w,s}$ is the vapour pressure of water above a solution and x_w is the mole fraction of water in the droplet. For a droplet containing a fixed amount of solute, as the droplet radius increases the solute will become more dilute, diminishing the solute effect.

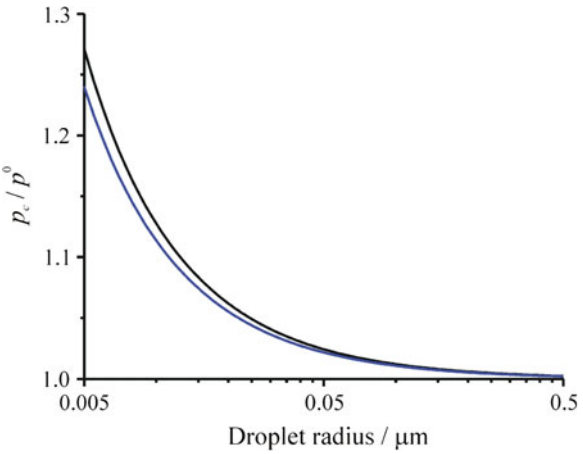

Fig. 2.3 The variation of the ratio of the vapour pressure of water over a droplet to that over a flat surface with droplet diameter at 273 and 293 K, shown in *black* and *blue*, respectively

For non-ideal solutions solute–solvent interactions must be considered. These are accounted for by replacing x_w with the activity of water, a_w, which is defined by

$$a_w = \gamma_w x_w \tag{2.4}$$

where γ_w is the concentration-dependent activity coefficient of water. The solute effect is therefore described by [1]

$$p_{w,s} = a_w p^0 \tag{2.5}$$

Determining γ_w for combinations of solutes at varying concentrations is a key challenge in gaining an understanding of the thermodynamic behaviour of aqueous atmospheric aerosols [5]. For dilute solutions $\gamma_w \rightarrow 1$ and the solution behaviour can be considered ideal.

The combination of these two factors determines the vapour pressure at the surface of a droplet containing a solute and thus the droplet size which is in equilibrium with a given surrounding gas-phase partial pressure of water [1]:

$$\frac{p_{w,d}}{p^0} = a_w \exp\left(\frac{2M_w\sigma_w}{RT\rho_w r}\right) \tag{2.6}$$

In the limit of dilute solutions this expression can be expressed in a simplified form [1]:

$$\ln\left(\frac{p_{w,d}}{p^0}\right) = \frac{2M_w\sigma_w}{RT\rho_w r} - \frac{3n_s M_w}{4\pi\rho_w r^3} \tag{2.7}$$

where n_s is the number of moles of solute in the droplet; the solute is assumed to be non-volatile and hence n_s will remain constant as the droplet size changes.

This approach to understanding equilibrium droplet size was first proposed by Köhler in 1921 [6]. Figure 2.4 shows the equilibrium behaviour of aqueous NaCl

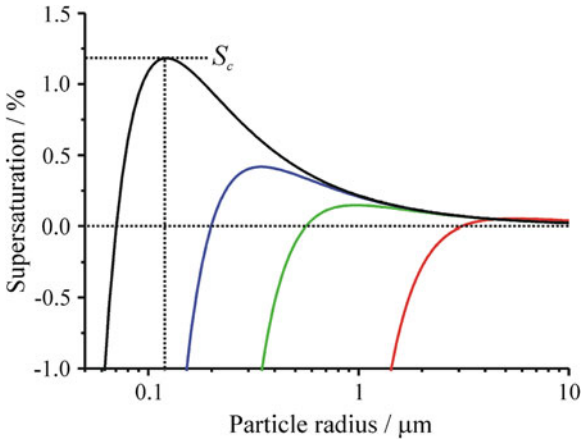

Fig. 2.4 Köhler curves for NaCl particles with $r_d = 0.01$, 0.02, 0.04 and 0.08 μm shown in *black*, *blue*, *green* and *red* respectively. S_c labels the critical supersaturation for the droplet with the smallest dry particle radius

aerosol droplets of various dry particle radii, r_d, with varying supersaturation, S, which is the RH expressed relative to 100%, calculated using Eq. 2.7 introduced above. The dry particle radius is calculated from the droplet solute mass loading and the density of the solute, assuming a spherical geometry. It can be seen from Fig. 2.4 that particles with a larger solute loading, and hence r_d, attain a larger equilibrium size at a given RH.

These 'Köhler curves' are determined by both the solute and curvature effects. At subsaturations or for large r_d the solute effect determines the form of the curve and in order to maintain $p_{w,d}$ equal to p_w the droplet size increases with increasing RH. As the droplet size increases and the solute becomes more dilute the Kelvin effect becomes relatively more important. As a result there is a critical size above which a droplet will spontaneously take up water, limited only by the kinetics of mass transfer. The supersaturation corresponding to the critical size is termed the critical supersaturation, S_c, and is labelled for the droplet with the smallest dry particle radius in Fig. 2.4. Aerosol particles can act as cloud condensation nuclei in the atmosphere and are considered 'activated' once they have surpassed the transition to this regime of spontaneous growth, within which they will go on to become cloud droplets. The activation of aerosol particles is a process of critical importance as a result of the significance of clouds in determining the radiative balance of the atmosphere [1].[1]

The droplets relevant to the experiments presented in this thesis are of diameters of $\sim$6–16 μm, and as a result it is not necessary to include the Kelvin effect when considering equilibrium droplet behaviour under these conditions [1]. The droplet size can therefore be predicted from:

$$\frac{p_{w,d}}{p^0} = a_w \tag{2.8}$$

As mentioned earlier, determining the variation of a_w with solute concentration is not trivial. In these studies the following empirical relationship is used to relate the particle size to r_d and the RH [5, 7]:

$$\mathrm{GF} = \left[1 + \left(a + bRH + cRH^2\right)\frac{RH}{1 - RH}\right]^{\frac{1}{3}} \tag{2.9}$$

where GF is the droplet growth factor, which is defined as the ratio of the particle radius, also termed the wet particle radius, r_w, to r_d:

$$\mathrm{GF} = \frac{r_w}{r_d} \tag{2.10}$$

and a, b and c are experimentally-determined constants which are specific to the solute present in the aqueous droplet.

[1] See Sect. 1.1.2 for a detailed discussion.

In several experiments mixed composition droplets are investigated. In order to predict the equilibrium behaviour of such droplets the Zdanovskii, Stokes and Robinson (ZSR) approximation is used, which assumes that each component takes up water independently [5]. For example, for a droplet composed of two or more solutes the mass loading of each solute would be determined, and from these the volume of water which would be associated with each component would be calculated by using Eq. 2.9 and the appropriate values of a, b and c. A volume sum would then be used to determine the overall r_w of the mixed composition droplet.

2.2 Kinetics of Aerosol Mass Transfer

Understanding the kinetics of mass transfer between the gaseous and condensed phases of aerosols is of crucial importance for rationalising many atmospheric processes, for example heterogeneous chemistry at the surface of aerosol particles and the formation and stability of clouds [1, 8–11]. Although the equilibrium state can be readily predicted, it is often important to consider if the aerosol size distribution can legitimately be considered to be determined solely by thermodynamic principles. Two key quantities central to aerosol mass transfer are the mass accommodation coefficient, α, and the evaporation coefficient, γ_e. These quantities play a role in determining the rate of uptake of gaseous species by, and evaporation from, aerosol particles, respectively, governing the timescale for a droplet to attain a thermodynamic equilibrium size.

In the work presented in Chap. 7 a new technique for the determination of α and γ_e for the uptake or evaporation of water at an aqueous surface is demonstrated. These quantities have been the subject of many experimental studies, yet remain the subject of much debate [9, 12]. As well as studying the mass transfer of water to and from aqueous droplets containing only inorganic solutes, the effect of dissolved organic compounds on mass transfer is also investigated. The process of uptake of water at an aqueous surface and its atmospheric importance will now be discussed in detail, followed by a description of the differences and similarities in the case of evaporation.

2.2.1 Uptake by a Liquid Aerosol Droplet

The incorporation of a gaseous species into a liquid aerosol droplet can involve the combination of a number processes, as illustrated in Fig. 2.5 [12]. First, the molecule must diffuse in the gas phase to the region close to the droplet surface. It must then be accommodated at the particle surface and transferred to the bulk. Surface-adsorbed molecules may desorb back into the gas phase. Surface and liquid-phase reactions may occur, and surface and liquid-phase diffusion may play a role in determining the uptake rate.

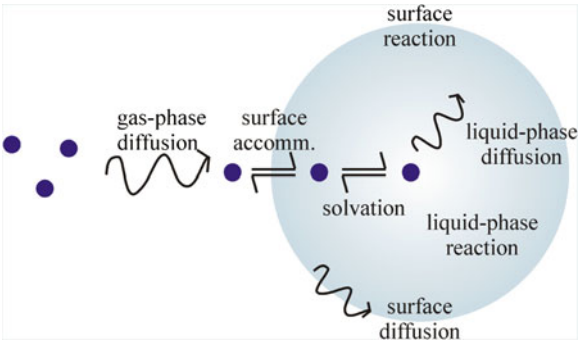

Fig. 2.5 Range of processes involved in uptake of a gas-phase species by a liquid aerosol particle

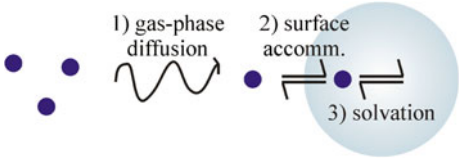

Fig. 2.6 Illustration of uptake as a three-step process

For non-reactive uptake of water into an aqueous droplet, which is considered in this work, the picture is simplified, as shown in Fig. 2.6.

The maximum possible rate of uptake, $J_{u,max}$ (molecules m^{-2} s^{-1}), is given by the collision rate of gas-phase molecules with a surface, which is defined by the Hertz–Knudsen equation [12, 13]:

$$J_{u,\max} = \frac{\Delta p_v}{\sqrt{2\pi M_a k_B T}} \tag{2.11}$$

where Δp_v is the water vapour pressure difference between the surrounding environment and the particle surface (Pa), M_a is the relative molecular mass of the adsorbing species (kg), k_B is the Boltzmann constant (J K^{-1}) and T is the temperature (K). This expression for J_u can be simplified using the mean speed of molecules in a gas, $\bar{c}$ (m s^{-1}) [14]:

$$\bar{c} = \sqrt{\frac{8k_B T}{\pi M_a}} \tag{2.12}$$

and the ideal gas law to express Δp_v as the corresponding difference in molecular density of gas molecules, Δn_g (molecules m^{-3}) The resulting simplified expression for $J_{u,max}$ is [12]:

$$J_{u,\max} = \frac{\Delta n_g \bar{c}}{4} \tag{2.13}$$

While this represents the maximum possible rate, there are several kinetic factors which will limit the actual rate of uptake observed. For non-reactive uptake these factors can be related to the three-steps shown in Fig. 2.6.

(1) Diffusion: As the gas-phase molecules of interest enter the surface their concentration is depleted near to the surface and more must travel to the region close to the surface by gas-phase diffusion. Unless diffusion is fast enough the collision rate, and thus flux, is diminished.
(2) Surface accommodation: The proportion of colliding molecules which become incorporated into the particle must be considered. If less than 100% of the molecular collisions lead to incorporation then the mass flux will be diminished.
(3) Solvation: The relative rates of solvation and re-evaporation of the gaseous molecules must be considered.

The combined effect of these factors on the rate of uptake can be expressed by a measured uptake coefficient, γ_{meas}. The measured rate of uptake, J_{meas}, will thus be given by the maximum rate of uptake multiplied by γ_{meas}, where $0 \leq \gamma_{meas} \leq 1$ [12]:

$$J_{meas} = \gamma_{meas} J_{u,\max} \tag{2.14}$$

2.2.1.1 The Resistance Model for Uptake

The individual contributions of the factors affecting γ_{meas} represent coupled differential equations which cannot be solved analytically [15]. The factors can, however, be conveniently considered using the resistance model of gas uptake, an approach first proposed by Schwartz [16, 17]. It assumes that the factors can be decoupled and so allows the effects to be examined separately. The approach is widely used [12, 15, 18, 19] and has been shown to introduce an error of $< 10\%$ compared with numerical solutions of the coupled problem [20, 21]. Using the resistance model gives the following expression describing the effect of the combined resistances in the case of non-reactive uptake [12, 15, 18, 19]:

$$\frac{1}{\gamma_{meas}} = \frac{1}{\Gamma_{diff}} + \frac{1}{\alpha} + \frac{1}{\Gamma_{sol}} \tag{2.15}$$

where $1/\Gamma_{diff}$ is used to describe the resistance to uptake as a result of the rate of gas-phase diffusion, α is the mass accommodation coefficient and $1/\Gamma_{sol}$ describes the resistance to uptake as a result of gas/liquid partitioning. The resistance model for gas uptake is analogous to that of electrical resistance in an electrical circuit. Figure 2.7 shows an electrical circuit analogy for non-reactive uptake. Continuing the electrical circuit analogy, Γ_{diff}, α and Γ_{sol} can be considered to be conductances for mass transfer.

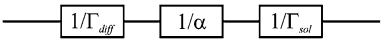

Fig. 2.7 Electrical resistance analogy for non-reactive uptake

An alternative, equivalent kinetic framework for aerosol uptake has been proposed by Pöschl et al. [22]. In this model aerosol particles are considered to have a surface double-layer, consisting of a sorption layer and a quasi-static layer, where the uptake or loss of volatile and non-volatile molecules occurs, respectively. This framework is particularly useful for describing reactive uptake.

Each of the three resistances to uptake will now be examined in more detail.

2.2.1.2 Gas-phase Diffusion

The rate of gas-phase diffusion is straightforward to calculate in the case of uptake by a bulk liquid surface. Diffusion is governed by a continuous concentration gradient of the species being taken up, which is assumed to extend to the interface, as represented the Maxwell equation (1890) [1, 23]:

$$\frac{\partial c_R}{\partial t} = -\frac{1}{R^2}\frac{\partial}{\partial R}(R^2 J_R) \tag{2.16}$$

where c_R is the concentration of the species at a radial position R, t is time and J_R is the molar flux of the species at R. This assumption works well for aerosol droplets which are large compared with the mean free path of the gas-phase molecules, for example in the case of droplets >100 μm in radius at atmospheric pressure [23]. However, for smaller droplets, which are more abundant in the atmosphere, gas diffusion has no straightforward analytical solution [15]. This is because the concentration gradients of gas-phase species within about one mean free path of the surface are considerably altered compared to those far from the droplet [23].

Commonly the empirically-determined Fuchs–Sutugin relation is used to describe the resistance to uptake caused by gas-phase diffusion for a stationary droplet [1, 15, 19]:

$$\frac{1}{\Gamma_{diff}} = \frac{0.75 + 0.283Kn}{Kn(1 + Kn)} \tag{2.17}$$

where Kn is the dimensionless Knudsen number, given by [1, 12]:

$$Kn = \frac{\lambda_{mfp}}{r} \tag{2.18}$$

where λ_{mfp} is the gas-phase molecular mean free path and the r is the droplet radius. The mean free path of a gas-phase molecule in an ideal gas is given by [14]:

$$\lambda_{mfp} = \frac{k_B T}{\sqrt{2}\pi d_g^2 p} \tag{2.19}$$

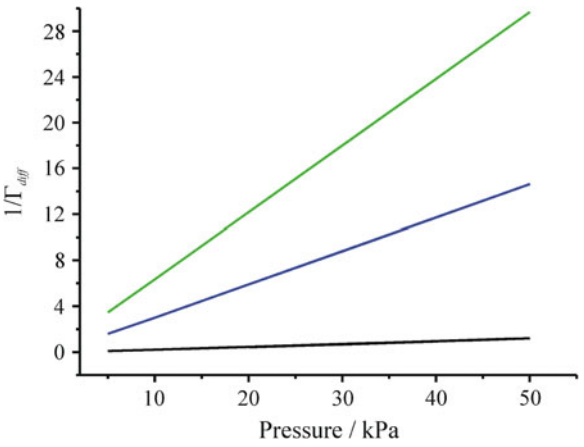

Fig. 2.8 The dependence of $1/\Gamma_{diff}$ on pressure for droplet radii of 0.5, 5 and 10 μm, shown in *black*, *blue* and *green*, respectively

where d_g is the diameter of the gas molecules (m) and p is the pressure (Pa). Hence for uptake of a given molecular species $1/\Gamma_{diff}$ varies with temperature, pressure and the particle size. As the temperature increases or the pressure or particle size decreases, $1/\Gamma_{diff}$ decreases. The dependence of $1/\Gamma_{diff}$ on pressure for the diffusion of water in air of 100% RH for droplet radii of 0.5, 5 and 10 μm is shown in Fig. 2.8.

The mean free path is often expressed in the following equivalent form [15]:

$$\lambda_{mfp} = \frac{3D_g}{\bar{c}} \tag{2.20}$$

where D_g is the diffusion constant of the gas-phase species in the surrounding gas medium ($m^2\ s^{-1}$). D_g depends on the properties of both the diffusing molecules (such as their size and shape) and the medium (such as its viscosity), and the interaction between the two.

The Fuchs–Sutugin relation is valid over a wide range of *Kn* [19]. It assumes a static spherical boundary condition around the droplet [19, 24].

2.2.1.3 Mass Accommodation

The proportion of colliding molecules which will be incorporated into the surface is described by the mass accommodation coefficient, α [9, 12]:

$$\alpha = \frac{\text{number of molecules adsorbed into the bulk}}{\text{number of molecular collisions with the surface}} \tag{2.21}$$

This is effectively a sticking probability and hence takes values from 0 to 1. The value of α depends on the intermolecular interactions between the adsorbing molecule and the surface and can be considered as a surface resistance to uptake.

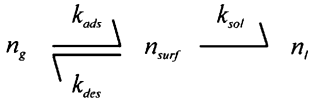

Fig. 2.9 Two-stage mass accommodation process

Mass accommodation is commonly represented as a two-stage process; molecules are first adsorbed at the surface and then transferred to the bulk [25, 26]. Adsorbed species may also desorb from the surface back into the gas phase. This process is illustrated in Fig. 2.9, where k_{ads}, k_{des} and k_{sol} are the rate constants for surface adsorption, surface desorption and solvation, respectively. The rate of re-evaporation is excluded from this description as this effect is dealt with by Γ_{sol}. The number concentrations of the species in the gas-phase, at the surface and in the liquid-phase are represented by n_g, n_{surf} and n_l, respectively.

Molecules can only be considered to be adsorbed if they become thermally equilibrated with the surface; the quantity describing the probability of a molecule equilibrating with the surface is the thermal accommodation coefficient, s. Studies of the uptake of deuterated water on water droplets have shown that D-H isotope exchange on the surface proceeds with unit probability and it can therefore be assumed that $s = 1$ at typical experimental temperatures [18]. Several other studies have also concluded that s is likely to be equal to one under atmospheric conditions [22, 27].

The temperature dependence of α can provide information about the mechanism of uptake at a surface. Using the two-stage model of mass accommodation outlined above and considering α as the proportion of molecules which become thermally accommodated at the surface less the proportion which desorb, a flux balance can be written [12]:

$$\frac{\alpha n_g \bar{c}}{4} = \frac{s n_g \bar{c}}{4} - n_s k_{des} \tag{2.22}$$

This net incoming flux at the surface must be equal to the flux into the liquid [12, 18]:

$$\frac{\alpha n_g \bar{c}}{4} = n_s k_{sol} \tag{2.23}$$

Combining these two equations to eliminate n_g and n_s gives:

$$\frac{\alpha}{s - \alpha} = \frac{k_{sol}}{k_{des}} \tag{2.24}$$

As discussed above s can be taken to be unity and so:

$$\frac{\alpha}{1 - \alpha} = \frac{k_{sol}}{k_{des}} \tag{2.25}$$

Replacing the rate constants, k, using the appropriate expressions for Gibbs free energy of activation, ΔG^* (J mol^{-1}), determined from transition state theory [14]:

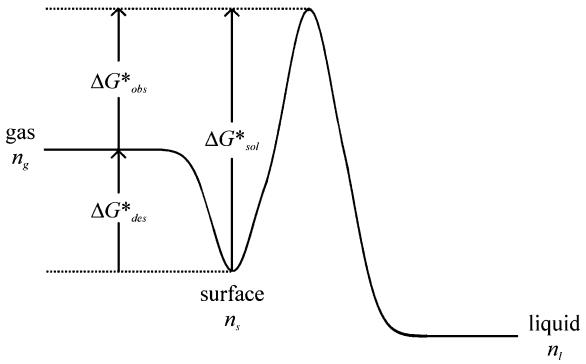

Fig. 2.10 A postulated free energy diagram for the two-stage model of mass accommodation [28]

$$\Delta G^* = -RT \ln \frac{k_B T}{hk} \tag{2.26}$$

where h is Planck's constant (J s), yields [25, 26]:

$$\frac{\alpha}{1-\alpha} = \frac{\exp\left(\frac{-\Delta G^*_{sol}}{RT}\right)}{\exp\left(\frac{-\Delta G^*_{des}}{RT}\right)} = \exp\left(\frac{-\Delta G^*_{obs}}{RT}\right) \tag{2.27}$$

where ΔG^*_{sol} is the free energy of activation for solvation of an absorbed molecule into the bulk, ΔG^*_{des} is the free energy of activation for desorption of a molecule from the surface to the gas phase and hence ΔG^*_{obs} is the free energy of transition for the uptake of a molecule from the gas into the bulk. A free energy diagram postulated by Nathanson et al. to illustrate the two-stage model of mass accommodation is provided in Fig. 2.10 [28].

The temperature dependence of α allows the sign of ΔG^*_{obs} and hence the relative sizes of ΔG^*_{sol} and ΔG^*_{des} to be determined. If ΔG^*_{obs} is negative then a negative temperature dependence of α would be observed.

ΔG^*_{obs} is related to the observed enthalpy and entropy changes of activation by [14]:

$$\Delta G^*_{obs} = \Delta H^*_{obs} - T\Delta S^*_{obs} \tag{2.28}$$

ΔH^*_{obs} and ΔS^*_{obs} were found to be negative for water uptake on a water surface by Li et al. by fitting of Eq. 2.27 to experimental data collected at temperatures varying between 250 and 290 K [18]. They reason that the patterns in the values of ΔH^*_{obs} and ΔS^*_{obs} measured for the uptake of a range of small molecules are consistent with a mechanism of uptake which involves the formation of a loosely-bound trace-gas/water cluster at the gas/liquid interface [18, 28].

There remains debate over the temperature dependence of α, however, [9]. While the study by Li et al. observed a clear dependence on temperature, a study by Winkler et al. observed no temperature dependence over the same temperature range [29]. The experiments from these two studies were, however, conducted under dramatically different conditions, sufficiently so that it has been speculated

that the mechanism for mass accommodation may be different in the two cases [9]. The experimental differences will be discussed later in this chapter.

2.2.1.4 Solubility

$1/\Gamma_{sol}$ describes the resistance to uptake resulting from equilibrium liquid/gas partitioning of the species of interest. This will determine the proportion of molecules entering the bulk which remain and do not re-evaporate. Henry's law relates the partial pressure of a species, p (Pa), to its solution phase concentration, C (mol m^{-3}) [14]:

$$p = HC \tag{2.29}$$

where H is Henry's Law constant (Pa m^3 mol^{-1}). In the case of uptake of a trace species into water droplets during droplet train experiments, Γ_{sol} has been shown to be described by [18]:

$$\frac{1}{\Gamma_{sol}} = \frac{\bar{c}}{8RTH}\sqrt{\frac{\pi t}{D_l}} \tag{2.30}$$

where t is the gas–liquid interaction time (s) and D_l is the liquid-phase diffusion constant of the molecules in water (m^2 s^{-1}). The resistance as a result of liquid/gas-phase partitioning increases with interaction time as a result of the solubility limit of the trace species being approached.

In these studies, however, we are dealing with the uptake of water into an aqueous droplet and in this case it is not clear what value of H would be appropriate. Previous experimental studies have proved inconclusive as to whether resistance due to solubility should be considered in the case of water uptake on water [18]. $1/\Gamma_{sol}$ is therefore neglected in the following analysis.

2.2.2 Consideration of the Rate Determining Step

In the absence of reactions and solubility considerations, the rate of uptake will be limited by gas-phase diffusion and mass accommodation. It is important to understand the relative size of the resistances to uptake arising from these processes in order to determine which, if either, is the rate-controlling process. This is important both in terms of understanding atmospheric processes and for designing experiments to measure mass transfer coefficients.

Three flow regimes exist, characterised by the value of the dimensionless Kn. Which process controls the rate of uptake depends on which flow regime applies. As previously introduced, Kn is the mean free path of gas-phase molecules, λ_{mfp}, divided by a representative physical length scale. Here the droplet radius is the appropriate representative physical length scale. For uptake of a given molecular species, Kn varies with temperature, pressure and the particle size.

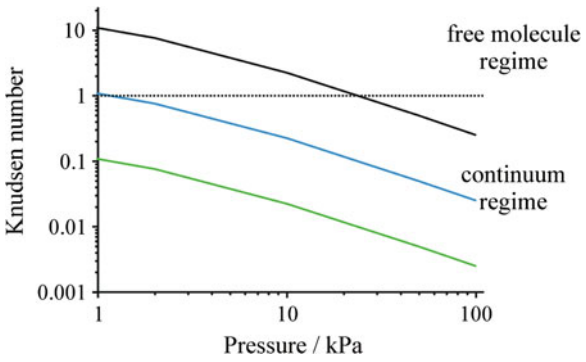

Fig. 2.11 The variation of *Kn* with pressure at a temperature of 291 K for three particle sizes; 0.5 μm (*black line*), 5 μm (*blue line*) and 50 μm (*green line*)

The regimes and the associated *Kn* are [1, 22]

1. The continuum regime: $Kn \ll 1$
2. The transition or Knudsen regime: $Kn \sim 1$
3. The free molecule regime: $Kn \gg 1$

In the continuum regime molecules do not travel far between collisions compared with the size of the particle undergoing uptake. The rate of gas-phase diffusion is slow compared to mass accommodation and uptake can be analysed using gas-phase diffusion equations as this process is limiting. This regime is characteristic of high pressure or low temperature and large particle sizes. In the free molecule regime gas-phase molecules travel a long way between collisions compared with the length scale of the particle, and hence the rate of gas-phase diffusion is not limiting. Mass accommodation at the surface becomes the rate determining process. In the transition regime mass transport can be influenced by both processes. The variation of *Kn* with pressure is shown in Fig. 2.11 at a temperature of 291 K for three particle sizes.

It can be seen from Fig. 2.11 that as the pressure is reduced the regime in which mass accommodation dominates is approached. For small droplets the transition between regimes occurs at higher pressures. For very large droplets gas diffusion can be seen to dominate at all pressures. Mass accommodation is important for uptake by 0.5 μm radius particles at most atmospheric pressures. This size is typical of the atmospheric aerosol accumulation mode, which accounts for most of the aerosol surface area and much of the mass in the atmosphere [1]. This emphasizes the importance of understanding mass accommodation as it is likely to be the rate determining step for a large proportion of atmospheric aerosols.

2.2.3 Atmospheric Importance of α

The rigorous determination of α for water on aqueous surfaces is vitally important for atmospheric science for a number of reasons, including:

- For inclusion in cloud physics models. It is important to consider if the growth of aerosol particles, which may result in them becoming cloud condensation nuclei, is thermodynamically or kinetically determined [30]; α is a key parameter in this process.
- For establishing suitable residence times in experimental chambers, for example cloud condensation chambers [30] and differential mobility analysers [31], kinetic limitations on the rate of droplet growth must be considered.
- For understanding the effect of aerosol composition, and in particular surface composition, on α. Taking into account the presence of surface-active organic compounds in aerosol droplets may result in the growth of particles moving from the equilibrium to the kinetically-controlled regime under certain conditions [30].

Each of these situations will now be discussed in more detail.

2.2.3.1 Cloud Physics Models

The mass accommodation coefficient of water on aqueous surfaces is fundamental to understanding the activation of aerosol particles to act as cloud condensation nuclei (CCN). As discussed in Sect. 2.1.2, the variation of the equilibrium size with RH of a particle consisting of soluble inorganic species can be described by a Köhler plot [1]. Once a particle reaches a certain supersaturated RH, known as the droplet critical supersaturation, S_c, it is termed 'activated' and will grow spontaneously, limited only by the kinetic resistances detailed above [1, 30]. These kinetic limitations, including mass accommodation, must be quantified in order to determine whether the growth of aqueous aerosol droplets as they approach and surpass S_c is thermodynamically or kinetically controlled. If the growth of aerosol particles in the atmosphere is purely thermodynamically controlled then the droplets will always be in equilibrium with the surrounding RH and the size distributions of CCN can be determined from knowledge of the local RH and temperature conditions and equilibrium Köhler theory. If, however, the kinetics of droplet growth play a role then this must be taken into consideration in order to accurately predict the distributions of activated particles. The distribution of activated droplets in turn controls the size and number distributions of cloud droplets, which determine the light scattering properties and stability of clouds and hence have an effect on their radiative forcing, termed the aerosol indirect effect [8, 10, 30, 32–36].

Currently many cloud modelling studies assume aerosol sizes are thermodynamically determined, with the number of activated CCN, n_{CCN}, predicted from the local supersaturation, S [10]:

$$n_{CCN} = AS^B \tag{2.31}$$

where A and B are empirically determined parameters. This assumption may, however, result in an overestimate of the radiative forcing by aerosols, by several

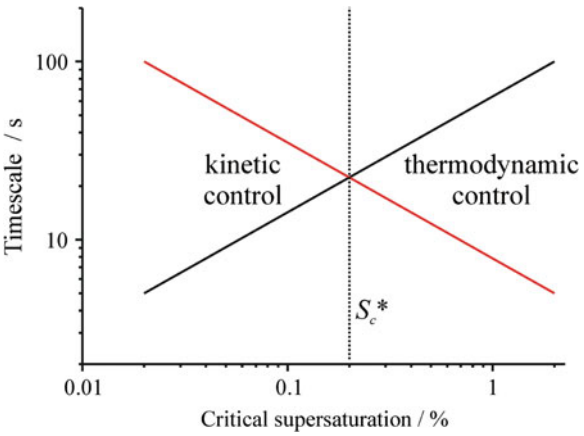

Fig. 2.12 Plot to illustrate the crossover between the regimes of kinetically- and thermodynamically-controlled particle size. τ_{growth} and τ_{eqm} are shown in *red* and *black*, respectively. The quantities on this plot, although typical of atmospheric conditions, are for illustrative purposes only

W m^{-2}, as more particles will be assumed to become activated than if kinetic limitations are taken into account [30, 34].

An alternative view is that neglecting kinetics of droplet growth leads to underestimating the number of activated particles and hence the radiative forcing by the aerosol indirect effect. It is argued that it if growth is delayed by kinetic factors then conditions of higher supersaturation will exist because less water vapour condenses onto droplets, ultimately leading to a greater number of activated particles, resulting in more, but smaller, cloud droplets [9]. This illustrates the level of debate in this area and the importance of furthering the understanding of aerosol uptake processes.

Whether or not kinetics play a role in determining the size of droplets depends on how the timescale of droplet growth, τ_{growth}, compares with the timescale on which the local RH changes, τ_{eqm}. As warm air parcels rise in the atmosphere their temperature decreases, causing the local RH to increase, with the result that the droplets must grow in order to stay in equilibrium. It is useful to define the S_c at which $\tau_{growth} = \tau_{eqm}$, namely S_c^*. Above this value kinetics are unimportant, while below this they must be considered, as illustrated in Fig. 2.12.

S_c^* has been modelled by comparing the timescales for the rate of change of RH in a typical air parcel, using a cloud parcel model, with the timescale for the rate of droplet growth derived from the growth equations of Fukata and Walter [23, 30]. It was found that S_c^* is sensitive to the value of α only for $\alpha < 0.1$ [30]. Hence, if $\alpha > 0.1$ precise knowledge of α is not necessary for determining whether equilibrium or kinetics determine droplet activation. Further to this, cloud modelling studies have found that under typical atmospheric conditions, because of the competing effects of the resistances of mass accommodation and gas-phase diffusion, the proportion of activated droplets is relatively insensitive to changes in α for $\alpha > 0.1$ [18, 23]; hence for these purposes precise knowledge of α is not necessary for evaluating the kinetic factors unless $\alpha < 0.1$. Cloud modelling studies suggest that α cannot be < 0.036 [36, 37].

2.2.3.2 Experimental Equilibration Timescales

It is important to consider the appropriate residence time to use for experimental chambers in the study of CCN size and number distributions. For example, previous studies using cloud condensation chambers [30] and differential mobility analysers [31] have allowed times of seconds to tens of seconds for droplet equilibration. However, calculations including kinetic limitations on the rate of droplet growth and relying on knowledge of α have found that timescales of droplet growth can in fact vary from less than a second up to hundreds of seconds [30], indicating that much longer equilibration times should be used.

If the thermodynamically-determined growth of aerosol particles is examined without accounting for kinetic limitations then underestimated values of droplet growth factors will be reported.

2.2.3.3 Effect of Composition

As well as establishing the value of α for pure water surfaces, it is also important to understand the dependence of α on droplet composition. A technique which is sufficiently sensitive to resolve the variation of α with droplet composition is highly desirable.

It is well established that the presence of organic species can affect the thermodynamic behaviour of inorganic aqueous droplets [38, 39], hence affecting the distribution of particles between the kinetic and equilibrium regimes for a given local supersaturation. The effect of organics on equilibrium droplet behaviour has been studied using optical tweezers by Reid and co-workers [40].

Organic species may also have a dramatic effect on aerosol kinetics via α, although this has not yet been definitively proven [31]. As organic species tend to be hydrophobic in nature there is a tendency for them to partition to the droplet surface, so even small quantities may be effective in retarding mass accommodation at the surface [41]. While some studies have found no effect on the uptake kinetics of water surfaces by an insoluble organic film [28], others have found a clear effect [42, 43]. A study of the rate of water evaporation from liquid microjets revealed an extreme sensitivity of the evaporation coefficient to the composition of the liquid phase [13], which suggests that α may too be highly sensitive to composition. In a study by Tuckermann et al. the relative permittivities of a range of surfactants to water evaporation were measured. This work indicated that the nature of the organic compound is important in determining the mass transport properties of aerosol [36]. This supports suggestions that the kinetics of droplet activation vary with geographical area, depending on the composition of aerosol particles present [13].

An indication that surface-active compounds may have an effect on the mass transfer processes of aerosol droplets has previously been gained using optical tweezers. A step-change in the evaporation rate of a surfactant-containing aqueous droplet was observed, proposed to be associated with formation of a complete

surface coverage of surfactant molecules retarding evaporation of water from the droplet [44]. The same behaviour has been observed for droplets containing atmospheric organics isolated using an electrodynamic balance [45] and the technique of acoustic levitation [36].

2.2.4 Importance in Other Fields

The relevance of the work described in this thesis is not limited to atmospheric science. Many industrial processes depend on mass transfer to and from aerosol particles, for example the burning of fuel in combustion engines. In addition, in the practice of drug delivery to the lungs using medical nebulisers it is important to understand the relative timescale of the passage of the drugs through the airways during inhalation compared with that of water uptake as a result of increasing RH inside the body. This is necessary in order to determine the size of the drug-containing particles when they reach the surfaces of the lungs in order to evaluate their penetration efficiency to the bloodstream.

2.2.5 Evaporation from an Aerosol Droplet

The equivalent model for evaporation of water molecules from an aqueous droplet involves reversible transport of liquid-phase molecules to and from the surface, followed by desorption from the surface to the gas phase and gas-phase diffusion away from the droplet. The maximum rate of evaporation is hence limited by gas-phase diffusion and a resistance associated with the surface.

The maximum evaporative flux, $J_{e,max}$, is again given by the Hertz–Knudsen equation [13]:

$$J_{e,\max} = \frac{\Delta p_{w,d}}{\sqrt{2\pi M_e k_B T}} \tag{2.32}$$

where M_e is the relative molecular mass of the evaporating species (kg).

The overall resistance to evaporation is described by a constant, $\gamma_{e,meas}$, which includes the effects of gas-phase diffusion and the surface resistance. The measured evaporative flux, $J_{e,meas}$, is given by [13]:

$$J_{e,meas} = \gamma_{e,meas} J_{e,\max} \tag{2.33}$$

The surface resistance is associated with both the reversible transport of liquid-phase molecules to and from the surface and desorption from the surface to the gas phase. The appropriate surface conductance for this process is the evaporation coefficient, γ_e. Analogous to the resistance model for uptake, the overall resistance to evaporation can be described by

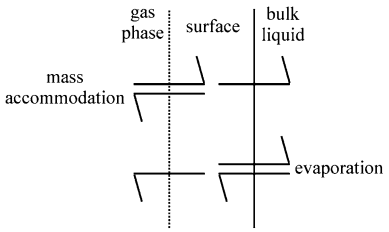

Fig. 2.13 Surface processes associated with mass accommodation and evaporation

$$\frac{1}{\gamma_{e,meas}} = \frac{1}{\Gamma_{diff}} + \frac{1}{\gamma_e} \tag{2.34}$$

Knudsen defined γ_e as [46]:

$$\gamma_e = \frac{\text{number of molecules transferred to the vapour phase}}{\text{number of molecules emitted from the liquid phase}} \tag{2.35}$$

This describes the proportion of molecules which arrive at the interface from the bulk and which eventually desorb from the surface. As for α, γ_e can take values between 0 and 1.

There is disagreement in the published literature over whether α and γ_e are physically equivalent quantities and should therefore have the same value. It has been argued that by microscopic reversibility they are equivalent quantities [12]. Several studies claim equivalence of the two values and quantify α via purely evaporative measurements [30, 47]. Other authors reason that although the processes are closely related they are not physically equivalent and hence there is no reason why the values should be the same [13, 46].

Whether the quantities are equivalent depends on the formulations for uptake and evaporation used. Figure 2.13 illustrates that in the formulation used in this work the processes associated with the resistances described by $1/\alpha$ and $1/\gamma_e$ are not physically equivalent.

The experimental approach used in this work represents a valuable opportunity to study both evaporation and uptake under identical experimental conditions. Both quantities will be determined without the need for any prior assumption about their equivalence.

Knowledge of γ_e is important for atmospheric studies. While γ_e it is not involved in determining particle number concentrations, it is involved in determining droplet size distributions, which are important for quantifying the aerosol direct effect.

2.2.6 Previous Experimental Studies

Despite the significance of aerosol mass transport, α and γ_e remain highly contentious quantities. Over forty experimental studies of α have been published since

the first measurement by Rideal in 1925 [9, 31]. The reported values of α span three orders of magnitude, from $\sim$0.001 to 1 [9]. Reported values of γ_e also span three orders of magnitude [13].

Measurement of aerosol mass transport is challenging; it was even claimed in 1975 by Sherwood et al. that "not only is there no useful theory to employ in predicting α, there is no easy way to experimentally measure it." [17, 48]. Determination of α or γ_e generally relies on measuring a rate of mass transfer and comparing this with the theoretical rate. As a result, determination is not straightforward because the magnitude of the other resistances to mass transport must be well-known. In particular the resistance from gas-phase diffusion is problematic. Under standard experimental conditions this factor will tend to dominate the determination of the rate of mass transfer and as a consequence α and γ_e can be difficult to elucidate. Conditions of low pressure will often be needed to address this and increase the sensitivity of experiments. There are problems associated with how to deal with gas-phase diffusion, because, as outlined above, no analytical solution exists in the case of small particles. Knowledge of surface temperature and the maintenance of a surface free from contaminants are other experimental challenges.

Previous experimental studies of α and γ_e for water at an aqueous surface can be separated into three broad categories, based on the form of the surface being investigated:

- Bulk, planar sample of liquid phase
- Ensemble of droplets
- Single droplet

For a given technique the rate of mass transfer may be measured in a variety of ways:

- Change in volume of the liquid phase
- Change in liquid-phase composition
- Change in gas-phase composition

The latter two measurement techniques rely on isotopic labelling, for example using $H_2^{17}O$ or D_2O as the gas-phase species undergoing uptake [18].

2.2.6.1 Bulk Techniques

Bulk sample techniques are used to investigate the rate of uptake by a macroscopically flat surface. One example of a bulk technique employs a vertical or horizontal wetted wall flow reactor, for which uptake into a liquid flowing on the inner surface of a tube is measured. Rideal's early measurement was a bulk technique which measured the transfer of water between two chambers held at different temperatures and connected by a tube [31]. Uptake in this type of system takes place in the continuum regime and hence the effect of gas-phase diffusion is easier to interpret than in the case of studies on particles in the free particle or

transition regime, although dominance of gas-phase diffusion limits the sensitivity of such techniques to surface accommodation. These techniques offer little insight into the uptake of atmospheric aerosol particles for which surface accommodation is often more important than gas-phase diffusion.

2.2.6.2 Ensembles of Droplets

Measurements on ensembles of droplets have recently been carried out by two groups; a collaboration between the Universities of Vienna and Helsinki (UV/UH) [29, 49] and another between Boston College and Aerodyne Research Inc. (BC/ARI) [18]. The former study reports that $\alpha = 1$ while the later reports values of 0.17 ± 0.03 at 280 K and 0.32 ± 0.04 at 258 K.

The BC/ARI studies were performed using a droplet train flow reactor [15, 50–53]. The droplets are created by a vibrating orifice aerosol generator (VOAG) with a backing pressure and then fall through a gas in a sealed flow tube. Successive droplets are generally separated by several droplet diameters. The change in the gas-phase composition is monitored using infrared absorption spectroscopy and used to derive the amount of uptake taking place. The change in gas-phase concentration of $H_2^{17}O$ as a function of available droplet surface area for uptake is used to determine α for water self-accommodation. Experiments were also carried out for uptake of D_2O. This case represents reactive uptake, because of rapid isotopic substitution of H and D atoms, and a higher rate of uptake is observed, as expected.

Measurements were carried out at a range of pressures and hence *Kn*; measurements were performed for $0.04 \leq Kn \leq 0.6$. This technique offers a continually-renewed liquid-phase surface which prevents the build-up of contaminants. The VOAG produces droplets of a well defined size so the surface area for uptake is well known; this is a crucial quantity for analysis of the experimental data.

In the analytical procedure for this work, gas-phase diffusion is treated using a modified version of the Fuchs–Sutugin relation. Instead of using *Kn*, a modified value of *Kn* is used in which the droplet radius is replaced by an effective radius of twice the orifice radius. This modification of the Fuchs–Sutugin relation has been found to be necessary for fitting the variation of the measured rates of uptake with pressure in this and previous studies from the collaboration [15, 50–52, 54]

This empirical scaling affects the value of $1/\Gamma_{diff}$ and hence the value of α determined by this technique. Although it can be reasoned that no dependence on droplet diameter is expected, this reasoning does not correctly predict the magnitude of the scaling found to be necessary [54]. The reasoning involves considering that the effective droplet surface area for gas-phase diffusion is reduced by a factor of the droplet diameter divided by the distance between droplets, as this is the fraction of the total time that a given region is occupied by a droplet from the train, and that the distance between droplets is a function of droplet diameter and the orifice diameter.

It is not expected that an unmodified Fuchs–Sutugin approach should be appropriate for the analysis of data collected in this way. The Fuchs–Sutugin

relation is based on static boundary conditions not valid for a droplet train experiment [24]. The key consideration is whether diffusive transport to a moving droplet is similar enough to that to a static droplet for a simple modification such as the one used to be valid.

Fluid-dynamical numerical modelling of the flow patterns of falling droplet trains shows that perturbations of diffusive flow to the droplets will exist near droplets, with depletion in the region near to droplet, resulting from microconvection between the droplets caused by their relative flow [19, 24]. This would result in an increase in the gas-phase resistance to uptake. This modelling work found that an effective radius of 1.2 times the droplet radius should be required to account for this additional gas-phase resistance in the case of falling droplets, which is considerably larger than twice the orifice radius [19]. A further fluid dynamical simulation showed that even with modification, the Fuchs–Sutugin relation cannot exactly represent diffusion to a train of moving droplets [55]. Because of the uncertainty surrounding treating diffusion to moving droplets, this fluid dynamical study suggests that the results of the BC/ARI study are consistent with a value of α of between 0.2 and 1.

The UV/UH experiment involves monitoring the rate of growth of water droplets using Mie scattering as they grow in an expansion chamber. The droplets are formed by condensation onto silver particles and then introduced into an expansion chamber, where they experience saturation ratios of 1.3–1.5. Gas-phase diffusion is accounted for and the observed growth curves are compared to theoretical curves in order to determine α. The study excluded values of $\alpha < 0.80$ for temperatures of 250–270 K and values of $\alpha < 0.4$ for temperatures up to 290 K. They conclude that all of their data are consistent with a value of $\alpha = 1$.

It has been reasoned that the discrepancies in the magnitude and temperature dependence of α between the two studies could be a result of the operation of different mechanisms of mass accommodation [9]. The experimental conditions are certainly considerably different; in the BC/ARI study saturation ratios of 1.01 are typical, while the UV/UH study features ratios of 1.3–1.5. Conditions of saturation as high as 1.3–1.5 are not representative of typical atmospheric cloud formation conditions.

Work by Cappa et al. on evaporation from liquid water microjets under condition of free molecular evaporation showed that the H_2O/D_2O isotope fractionation of evaporating molecules differs from that for vapour at equilibrium and that the fractionation depended on the D_2O mole fraction and temperature [13]. They reasoned that this indicates that there is an energetic barrier to evaporation and hence γ_e and α must be less than one.

2.2.6.3 Single Droplet Studies

A recent study by Zientara et al. used single droplets isolated using an electrodynamic balance [30]. The evolution of the size of evaporating droplets was investigated using elastic light scattering and compared with theory in order to

determine γ_e. γ_e is considered equivalent to α and results were obtained in good agreement with the magnitude and dependence of those of the BC/ARI collaboration; $\alpha \sim 0.18$ at 273.1 K and ~ 0.13 at 293.1 K.

Shaw and Lamb used an electrodynamic balance to simultaneously measure the rate of homogeneous nucleation of ice and the evaporation rate of liquid water droplets as a function of pressure [47]. The homogeneous nucleation rate is used as a highly sensitive measure of droplet temperature, and as the temperature of an evaporating droplet is a function of γ_e and the thermal accommodation coefficient, these quantities are determined. They assumed that γ_e and α are equal and reported $0.04 < \alpha < 0.1$ at a temperature of 238.1 K.

2.2.7 Field Studies

The mass accommodation coefficient has been investigated in field studies. The studies, termed CCN closure experiments, compare observations of CCN concentration with concentrations predicted for given particle size and composition distributions [56]. When closure is not achieved it is usually the case that the CCN concentration has been over predicted. Assuming that the discrepancy can be attributed to kinetic limitations on droplet activation a value of α can be determined. One such study found that closure was achieved by using a value of α of 0.06, although it was found that the value can vary from 0.03 to 1.0 [57]. Similar studies have shown that the value of α necessary to correctly predict the CCN concentration varies considerably from day to day and even during the same day, attributed to chemical aging of the aerosol particles [56]. These studies highlight the importance of resolving the effects of aerosol composition on mass transfer.

2.2.8 Theoretical Work

Several molecular dynamics (MD) studies have reported a water self-accommodation coefficient of close to or equal to unity for temperatures between 300 and 350 K [55, 58, 59]. A study has also suggested that α is the same regardless of the molecule being taken up [58]. The MD studies do not agree with experiments which find that α is < 1, that it is temperature dependent and that interactions between the gas-phase species and the surface are important.

Davidovits et al. have questioned whether MD simulations can adequately simulate uptake on a water surface [60]. It has been suggested that the restricted spatial and temporal scales of MD simulations mean that these studies sample a different accommodation process to that studied in laboratory experiments [9].

It is also thought that the potential energy surfaces used in the simulations do not adequately describe the real situation.

2.2.9 Summary

This chapter has outlined the factors which determine the equilibrium droplet size. These factors form the basis of the technique for measuring droplet absorption described in Chap. 6. The theoretical framework for understanding the kinetics of aerosol mass transfer has also been described, as well as the atmospheric significance of the mass accommodation coefficient of water at an aerosol surface. Studies of the kinetics of aerosol mass transfer are the subject of Chap. 7.

References

1. J.H. Seinfeld, S.N. Pandis, *Atmospheric Chemistry and Physics: From Air Pollution to Climate Change* (Wiley, New York, 1998)
2. C. Pilinis, S.N. Pandis, J.H. Seinfeld, J. Geophys. Res. Atmos. **100**, 18739 (1995)
3. S.L. Clegg, P. Brimblecombe, A.S. Wexler, J. Phys. Chem. A **102**, 2155 (1998)
4. I.N. Tang, H.R. Munkelwitz, Atmos. Environ. Part A–General Topics **27**, 467 (1993)
5. A.J. Prenni, P.J. De Mott, S.M. Kreidenweis, Atmos. Environ. **37**, 4243 (2003)
6. H. Köhler, Geofysiske Publikasjoner **2**, 3 (1921)
7. G.B. Ellison, A.F. Tuck, V. Vaida, J. Geophys. Res. Atmos. **104**, 11633 (1999)
8. D. Rosenfeld, Science **287**, 1793 (2000)
9. P. Davidovits et al., Geophys. Res. Lett. **31**, L22111 (2004)
10. R.J. Charlson, S.E. Schwartz, J.M. Hales, R.D. Cess, J.A. Coakley, J.E. Hansen, D.J. Hofmann, Science **255**, 423 (1992)
11. R.J. Charlson, S.E. Schwartz, J.M. Hales, R.D. Cess, J.A. Coakley, J.E. Hansen, D.J. Hofmann, Science **256**, 598 (1992)
12. P. Davidovits, C.E. Kolb, L.R. Williams, J.T. Jayne, D.R. Worsnop, Chem. Rev. **106**, 1323 (2006)
13. C.D. Cappa, W.S. Drisdell, J.D. Smith, R.J. Saykally, R.C. Cohen, J. Phys. Chem. B **109**, 24391 (2005)
14. P. Atkins, J. de Paula, *Physical Chemistry* (Oxford University Press, Oxford, 2002)
15. Q. Shi, Y.Q. Li, P. Davidovits, J.T. Jayne, D.R. Worsnop, M. Mozurkewich, C.E. Kolb, J. Phys. Chem. B **103**, 2417 (1999)
16. S.E. Schwartz, J.E. Freiberg, Atmos. Environ. **15**, 1129 (1981)
17. S.E. Schwartz, in *Chemistry of Multiphase Atmospheric Systems* ed. by W. Jaeschke (Springer, Heidelberg, 1986), p. 415
18. Y.Q. Li, P. Davidovits, Q. Shi, J.T. Jayne, C.E. Kolb, D.R. Worsnop, J. Phys. Chem. A **105**, 10627 (2001)
19. M. Sugiyama, S. Koda, A. Morita, Chem. Phys. Lett. **362**, 56 (2002)
20. D.R. Hanson, A.R. Ravishankara, J. Phys. Chem. **97**, 12309 (1993)
21. D.R. Hanson, A.R. Ravishankara, E.R. Lovejoy, J. Geophys. Res. Atmos. **101**, 9063 (1996)
22. U. Pöschl, Y. Rudich, M. Ammann, Atmos. Chem. Phys. **7**, 5989 (2007)
23. N. Fukuta, L.A. Walter, J. Atmos. Sci. **27**, 1160 (1970)

24. J.F. Widmann, E.J. Davis, J. Aerosol Sci. **28**, 1233 (1997)
25. J.T. Jayne, S.X. Duan, P. Davidovits, D.R. Worsnop, M.S. Zahniser, C.E. Kolb, J. Phys. Chem. **95**, 6329 (1991)
26. P. Davidovits, J.T. Jayne, S.X. Duan, D.R. Worsnop, M.S. Zahniser, C.E. Kolb, J. Phys. Chem. **95**, 6337 (1991)
27. M. Zientara, D. Jakubczyk, K. Kolwas, M. Kolwas, J. Phys. Chem. A, **112**, 5152 (2008)
28. G.M. Nathanson, P. Davidovits, D.R. Worsnop, C.E. Kolb, J. Phys. Chem. **100**, 13007 (1996)
29. P.M. Winkler, A. Vrtala, P.E. Wagner, M. Kulmala, K.E.J. Lehtinen, T. Vesala, Phys. Rev. Lett. **93**, 075701 (2004)
30. P.Y. Chuang, R.J. Charlson, J.H. Seinfeld, Nature **390**, 594 (1997)
31. M.N. Chan, C.K. Chan, Atmos. Chem. Phys. **5**, 2703 (2005)
32. IPCC, Climate Change 2007: The Physical Science Basis. Contribution of Working Group I to the Fourth Assessment Report of the Intergovernmental Panel on Climate Change, ed. by S. Solomon, D. Qin, M. Manning, Z. Chen, M. Marquis, K.B. Averyt, M. Tignor, H.L. Miller (Cambridge University Press, Cambridge, New York, USA, 2007)
33. IPCC, Climate Change 2001: The Physical Science Basis. Contribution of Working Group I to the Third Assessment Report of the Intergovernmental Panel on Climate Change, ed. by F. Joos, A. Ramirez-Rojas, J.M.R. Stone, J. Zillman (Cambridge University Press, Cambridge, New York, USA, 2001)
34. A. Nenes, S. Ghan, H. Abdul-Razzak, P.Y. Chuang, J.H. Seinfeld, Tellus Series B-Chem. Phys. Meteorol. **53**, 133 (2001)
35. J.G. Hudson, S.S. Yum, J. Atmos. Sci. **54**, 2642 (1997)
36. S.S. Yum, J.G. Hudson, Y.H. Xie, J. Geophys. Res. Atmos. **103**, 16625 (1998)
37. J.G. Hudson, T.J. Garrett, P.V. Hobbs, S.R. Strader, Y.H. Xie, S.S. Yum, J. Atmos. Sci. **57**, 2696 (2000)
38. C.N. Cruz, S.N. Pandis, J. Geophys. Res. Atmos. **103**, 13111 (1998)
39. M.L. Shulman, M.C. Jacobson, R.J. Charlson, R.E. Synovec, T.E. Young, Geophys. Res. Lett. **23**, 603 (1996)
40. K.L. Hanford, L. Mitchem, J.P. Reid, S.L. Clegg, D.O. Topping, G.B. McFiggans, J. Phys. Chem. A **112**, 9413 (2008)
41. G.T. Barnes, Nature **220**, 1025 (1968)
42. E.K. Rideal, J. Phys. Chem. **29**, 1585 (1925)
43. R. Tuckermann, S. Bauerecker, H.K. Cammenga, J. Colloid Interf. Sci. **310**, 559 (2007)
44. J. Buajarern, Ph.D. thesis: Fundamental studies of inorganic and organic aqueous aerosols using optical tweezers, University of Bristol, Bristol, UK, 2007
45. M.L. Shulman, R.J. Charlson, E.J. Davis, J. Aerosol Sci. **28**, 737 (1997)
46. R. Marek, J. Straub, Int. J. Heat Mass Transf. **44**, 39 (2001)
47. R.A. Shaw, D. Lamb, J. Chem. Phys. **111**, 10659 (1999)
48. T.K. Sherwoood, R.L. Pigford, C.R. Wilke, *Mass Transfer* (McGraw-Hill, New York, 1975)
49. P.M. Winkler, A. Vrtala, R. Rudolf, P.E. Wagner, I. Riipinen, T. Vesala, K.E.J. Lehtinen, Y. Viisanen, M. Kulmala, J. Geophys. Res. Atmos.**111**, D19202 (2006)
50. D.R. Worsnop, M.S. Zahniser, C.E. Kolb, J.A. Gardner, L.R. Watson, J.M. Vandoren, J.T. Jayne, P. Davidovits, J. Phys. Chem. **93**, 1159 (1989)
51. E. Swartz, Q. Shi, P. Davidovits, J.T. Jayne, D.R. Worsnop, C.E. Kolb, J. Phys. Chem. A **103**, 8824 (1999)
52. Q. Shi, P. Davidovits, J.T. Jayne, D.R. Worsnop, C.E. Kolb, J. Phys. Chem. A **103**, 8812 (1999)
53. G.N. Robinson, D.R. Worsnop, J.T. Jayne, C.E. Kolb, P. Davidovits, J. Geophys. Res. Atmos.**102**, 3583 (1997)
54. D.R. Worsnop, Q. Shi, J.T. Jayne, C.E. Kolb, E. Swartz, P. Davidovits, J. Aerosol Sci. **32**, 877 (2001)
55. A. Morita, M. Sugiyama, H. Kameda, S. Koda, D.R. Hanson, J. Phys. Chem. B **108**, 9111 (2004)
56. C.R. Ruehl, P.Y. Chuang, A. Nenes, Atmos. Chem. Phys. **8**, 1043 (2008)

57. C. Fountoukis et al., J. Geophys. Res. Atmos.**112**, D10S30 (2007)
58. J. Vieceli, M. Roeselova, D.J. Tobias, Chem. Phys. Lett. **393**, 249 (2004)
59. T. Tsuruta, G. Nagayama, J. Phys. Chem. B **108**, 1736 (2004)
60. P. Davidovits, D.R. Worsnop, L.R. Williams, C.E. Kolb, M. Gershenzon, J. Phys. Chem. B **109**, 14742 (2005)

Chapter 3
Experimental Techniques

In these studies optical tweezers were used to isolate and manipulate individual aqueous aerosol droplets containing a range of inorganic and organic solutes. Raman and fluorescence spectroscopy were used to characterise the trapped particles as a means of studying aerosol optical and kinetic properties.

In the technique of aerosol optical tweezing a laser is focussed using a microscope objective to form an optical trap within a sealed chamber. Two traps can be created in order to simultaneously manipulate a pair of droplets. Aerosol droplets are delivered to the trap from a flow generated by a medical nebuliser. Droplets from 2 to 20 μm in diameter can be trapped for a period of up to a few days [1]. Once isolated, the droplets are imaged in one or two planes using brightfield microscopy and studied spectroscopically by collecting the inelastically-scattered light. An additional laser source may be used to provide secondary illumination of the trapped droplets. The experimental set-up is shown schematically in Fig. 3.1.

The separate elements of the experimental set-up will be described in Sects. 3.1–3.5 of this chapter, while Sects. 3.6 and 3.7 will respectively discuss the theoretical and practical aspects of determining the size of aerosol droplets using cavity-enhanced Raman spectroscopy.

3.1 Trapping Light Source and Optical Components

The optical traps are formed by a continuous-wave (CW) Nd:YVO_4 laser (Coherent, Verdi V-5) operating at 532 nm and with a maximum light power output of 5 W. The vertically polarised laser output is coupled into a polarisation-maintaining single-mode fibre (Elliot Scientific) in order to deliver the beam to the experimental set-up. A fibre-coupler is used to collimate the beam delivered to the set-up. A wavelength of 532 nm is selected as it is the closest

K. J. Knox, *Light-Induced Processes in Optically-Tweezed Aerosol Droplets*,
Springer Theses, DOI: 10.1007/978-3-642-16348-7_3,

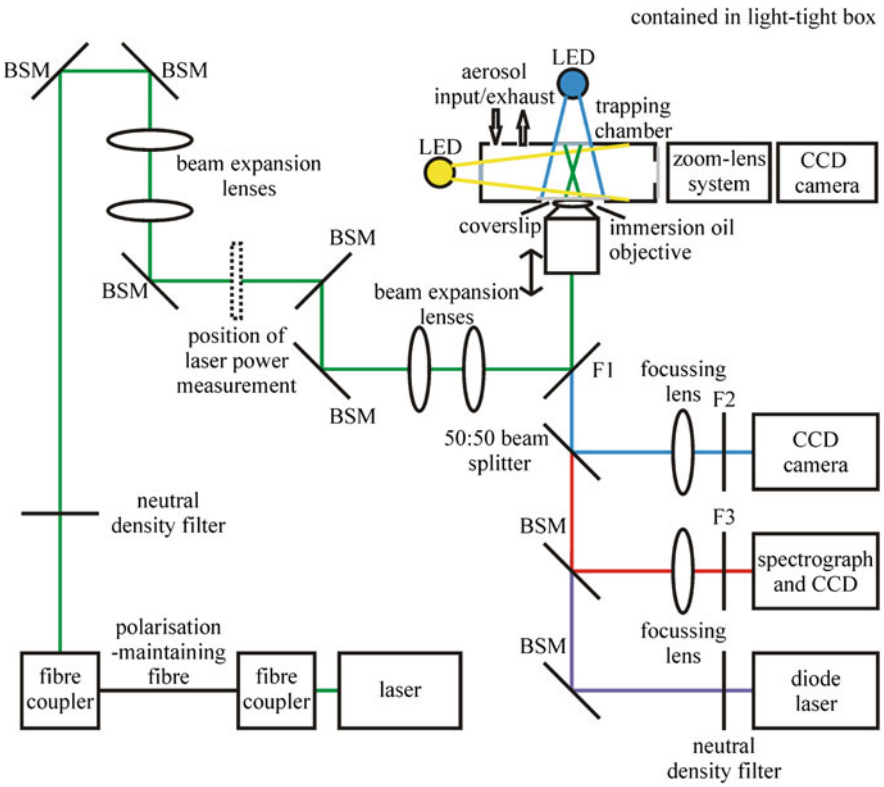

Fig. 3.1 Schematic experimental set-up. BSM represents a beam steering mirror. F1, F2 and F3 represent a high-reflectivity 45° 532 nm, a high-reflectivity 0° 532 nm filter and a 550 nm long pass filter, respectively

conveniently-available laser wavelength to the minimum in the imaginary part of the complex refractive index, k, of water. k is a measure of the absorbance of a medium [2, 3]. The absorption coefficient, α_a, is related to k by the following expression [2]:

$$\alpha_a = \frac{4\pi k}{\lambda} \tag{3.1}$$

where λ is the wavelength of illuminating radiation, and hence a smaller value of k corresponds to lower absorbance and therefore less heating. The variation of k for water with wavelength is shown in Fig. 3.2.

The trapping wavelength of 532 nm ensures that heating of aqueous droplets as a result of illumination by the trapping beam is minimised and is typically less than 1 K [1].

A circular graduated neutral density filter is used to control the laser power and several steering mirrors allow alignment of the beam. Two pairs of lenses of mismatched focal length are used to expand the laser beam diameter to ensure

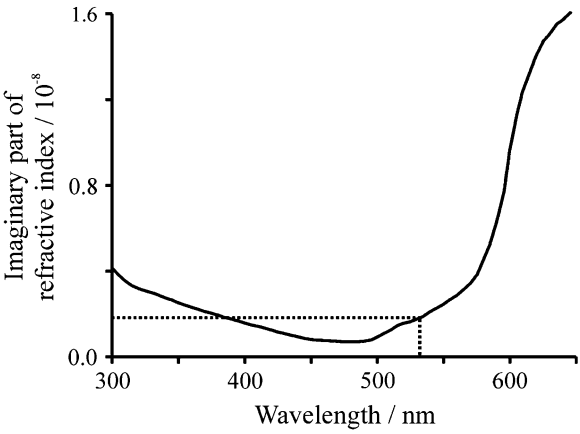

Fig. 3.2 Variation of the imaginary part of the complex refractive index of water with wavelength

overfilling of the back-aperture of the microscope objective used to focus the beam, which is required to maximise the gradient force and ensure stable trapping [4]. The expanded beam is reflected onto the back-aperture of the objective using a high reflectivity 532 nm mirror at 45°.

A high-numerical aperture oil immersion microscope objective (Olympus, 100 × magnification, infinity-corrected, numerical aperture (NA) of 1.25, working distance 0.13 mm) is selected to focus the laser beam in order to create the steep light gradients necessary for stable trapping, as discussed in Sect. 1.3.2 [4]. The objective is inverted, creating an optical trap for which the scattering force acts in the opposite direction to gravity.

Above the immersion oil layer the trapping beam passes into the trapping chamber through a borosilicate coverslip (R. A. Lamb, thickness number 1: 130–170 μm, diameter 35 mm) as shown in Fig. 3.1. The coverslips are pre-soaked in a solution of 50:50 water:Decon 90 (Fisher Scientific) for at least an hour. A coating of this surfactant solution increases the wetting properties of the coverslips so that aqueous solution deposited from the aerosol flow spreads out on the coverslip, rather than forming islands which would create a path of uneven refractive index between the microscope objective and the trapped particle, adversely affecting trapping efficiency.

The aqueous layer present on the coverslip gives rise to relative humidity (RH) gradients in the trapping chamber which will vary considerably between and during experiments [5]. The variability in the chamber environment highlights the need for an in situ control, i.e. a second trapped droplet.

Ideally the laser beam waist, d_w, at the focus would be diffraction-limited and given by [6]:

$$d_w = \frac{1.27 f \lambda}{D} \tag{3.2}$$

where f is the focal length of the objective, in this case 1.8 mm, and D is the effective beam diameter at the objective lens, which here is equal to the diameter

of the back aperture of the objective, which is 0.45 cm. This gives a value for d_w of 0.27 μm. However, owing to spherical aberration which results from refractive index mismatches in the path between the objective and the focal point this figure is likely to be an underestimate.

The laser power is measured at a fixed position in the beam path, as shown in Fig. 3.1. Laser powers used for trapping are typically 30–100 mW measured at this position. In order to determine the power at the trapping position the transmittance of the microscope objective has been measured to be 55 ± 2% using the dual objective technique [7]. This technique employs a second objective of the same model as the trapping objective to re-collimate the trapping beam, enabling its power to be measured using a power meter. The second objective is assumed to be of the same transmittance as the trapping objective and hence by comparing the power measured prior to the first objective with that measured after the second objective, the transmission of the trapping objective, O_t, may be determined from:

$$O_t = (\text{Fraction of power transmitted through 2 objectives})^{1/2} \quad (3.3)$$

The arrangement of the two objectives used in this technique is shown in Fig. 3.3. A layer of immersion oil is used between each objective and a coverslip, ensuring that the technique takes into account losses in the immersion oil layer and coverslip and at the oil/coverslip interface. However, losses as a result of total internal reflection at the coverslip/aqueous layer and aqueous layer/air interfaces are not considered. Figure 3.4 shows the arrangement for the dual objective technique which would be required to take account of these losses, but it is not possible to implement this in practice.

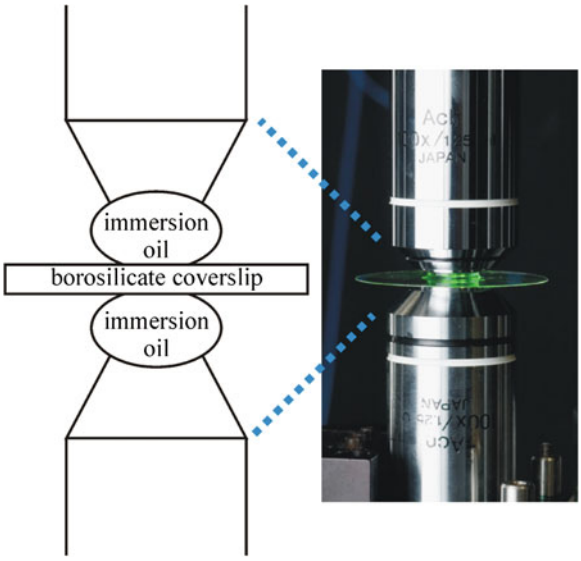

Fig. 3.3 Dual objective technique [8]

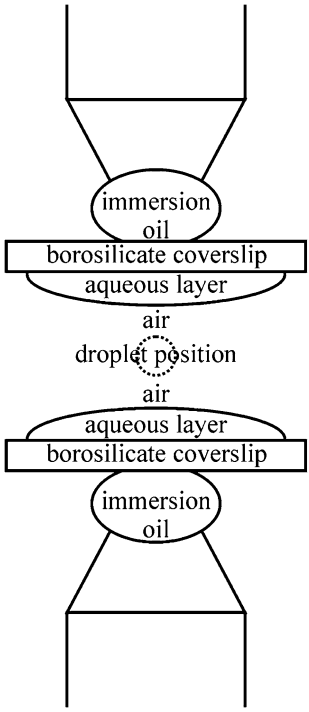

Fig. 3.4 Diagram showing ideal dual objective set-up

The transmission through the optics between the point at which the power is routinely measured and the trapping objective was also determined. Combining this transmittance with that of the microscope objective, the transmission of the system from the point at which the laser power is measured to the trap is 35 ± 2%. Thus the trapping power is 35 ± 2% of the laser power measured.

In order to simultaneously confine and independently manipulate two droplets the configuration described above can be modified by inserting a beam splitter into the beam path, producing two traps from a single laser beam, based on the method outlined by Fällman and Axner [9]. The power and position of these two traps may then be controlled independently. The set-up is shown schematically in Fig. 3.5, which also illustrates how the light scattered by each droplet may be collected simultaneously and separately; this will be discussed later in this chapter.

The requirement that the back-aperture of the trapping microscope objective must be overfilled means that in order to translate an optical trap without affecting its trapping efficiency the trapping beam must only pivot about the back-aperture (rather than translate) so as not to change the degree of overfilling [9]. To achieve this, two gimbal-mounted mirrors, a beam splitter and an extra pair of focussing lenses are inserted into the trapping beam. The optical components are arranged such that the gimbal-mounted mirrors are positioned at the image plane of the back-aperture of the objective. Consequently, a tilting of a mirror results in a

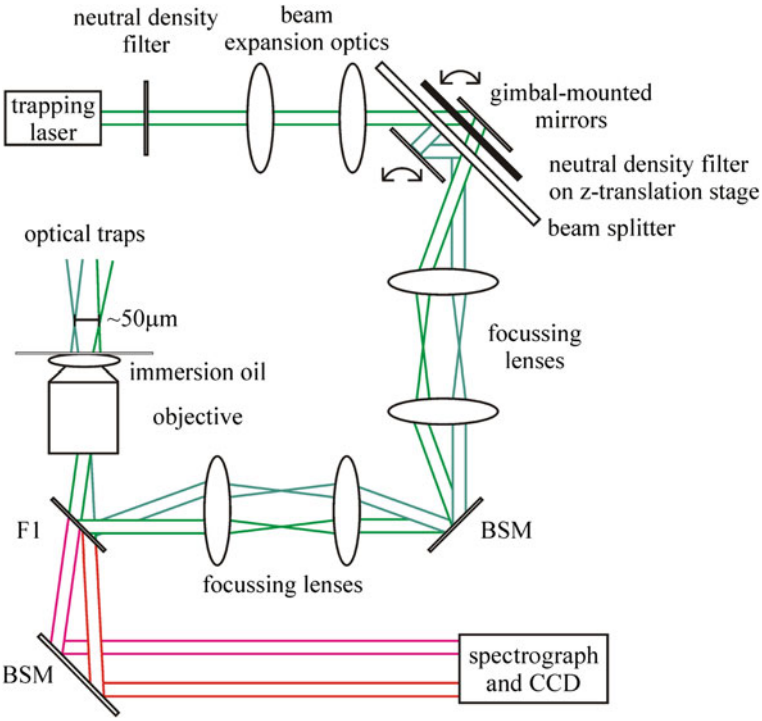

Fig. 3.5 Schematic illustration of the dual trapping configuration. BSM represents a beam steering mirror and F1 a high-reflectivity 45° 532 nm filter

change of the beam angle at the back-aperture but not a change in position. The degree of overfilling and hence trapping efficiency are therefore unchanged.

Each of the gimbal-mounted mirrors controls the angle of one of the trapping beams and thus the in-plane movement of one of the optical traps, achieving independent movement control.

Independent power control is achieved by inserting a graduated neutral density filter in the path of one of the beams, in the region of one of the gimbal-mounted mirrors. The filter is mounted on a z-translation stage and the power of the trap may therefore be adjusted by varying the vertical position of the neutral density filter. The ability to trap two droplets simultaneously facilitates comparative studies of aerosol properties and provides an in situ control droplet.

3.2 Additional Illumination

The use of an additional laser light source enables the droplets to be illuminated by a different wavelength and intensity of light, independent of the light field necessary for trapping.

A 408 nm diode laser (APMT18/5407, Power Technology Inc.) with a maximum power of 30 mW was used as the illumination source for experiments featuring a second laser beam. The beam was introduced to the droplet through the trapping objective. A range of powers was used, controlled by a neutral density filter.

3.3 Trapping Chambers

Custom-fabricated stainless steel trapping chambers are used to maintain a controllable droplet environment. A standard chamber is shown in Fig. 3.6. Ports allow for delivery of the aerosol flow from a nebuliser and aerosol exhaust out of the chamber. Rubber o-rings are used to create an airtight seal between the lid and the chamber. The coverslips are mounted above a window cut in the base of the chamber, sealed using rubber o-rings.

The trapping chamber is mounted above the inverted microscope objective. The vertical position of the chamber and objective are adjustable by means of z-translation stages. The focus of the beam within the aerosol chamber, and hence the trap position, is controlled by adjusting the relative height of the chamber and objective. For stable trapping the chamber must be positioned so that the laser focus is positioned above the coverslip and any aqueous layer present on the coverslip surface.

A quartz window in the top of the chamber allows for bright-field illumination of the droplets from above for imaging in the horizontal plane, referred to as in-plane imaging. A blue light-emitting diode (LED, Luxeon, 455 nm) is used to provide illumination. As the wavelengths of spectroscopic interest are greater than

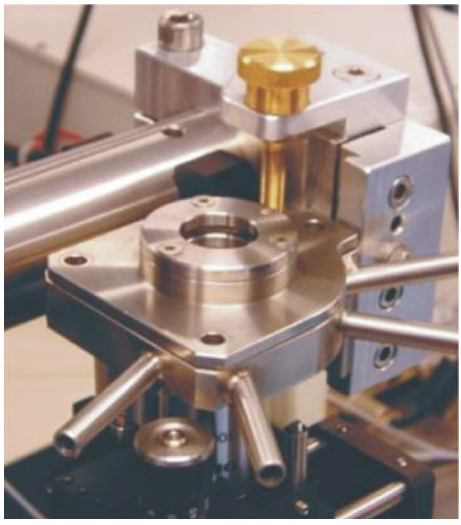

Fig. 3.6 Standard trapping chamber

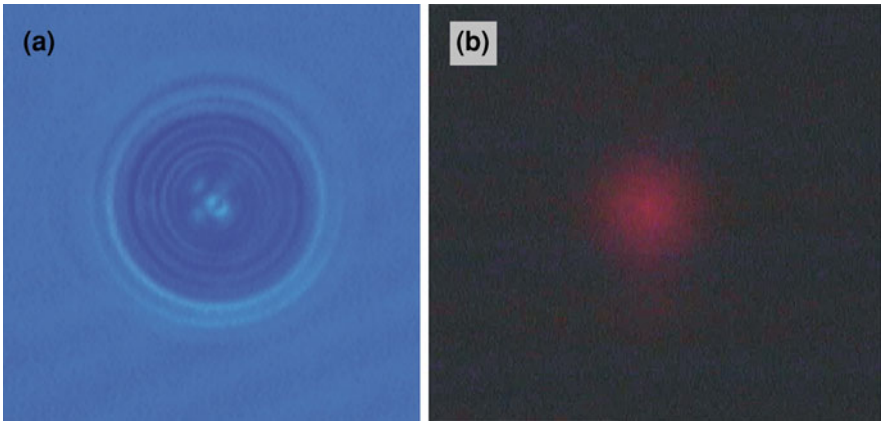

Fig. 3.7 Examples of in-plane images of **a** an illuminated aqueous droplet and **b** a fluorescing droplet containing quantum dots

600 nm, the choice of blue illumination allows for straightforward removal of this light before it reaches the spectrograph by using a 550 nm long pass filter. The trapping objective is used to collect the images. The imaging light reaches a charge-couple device (CCD) camera (Watec, LCL-211H) following reflection by a 50:50 beam splitter. A high reflectivity 532 nm 0° mirror in front of the camera reduces the amount of the remaining elastically-scattered light which reaches the camera. A 10 cm focussing lens is used to focus the image. Both still images and videos with a maximum frame rate of 30 Hz can be recorded. The image obtained will depend on the position of the droplet relative to the focal plane of the objective and is also vulnerable to spherical aberration due to the refractive index steps arising from the aqueous layer and coverslip.

Imaging experiments carried out using quantum dots relied on collecting fluorescently-scattered light from the dots, rather than external brightfield illumination. Hence it was necessary to increase the collection efficiency and so a high-sensitivity, electron-multiplied, cooled CCD camera was used (PhotonMax 512B, Princeton Instruments) in place of the standard CCD camera.

Examples of in-plane images of an illuminated aqueous droplet and a fluorescing droplet containing quantum dots are shown in Fig. 3.7a, b respectively.

Two specialist chambers were used for specific experimental functions. Details of these are given below.

3.3.1 Side-Imaging Chamber

The side-imaging chamber is shown in Fig. 3.8. Additional windows in opposite sides of the chamber allow the droplets to be illuminated and imaged at 90° to the trapping beam, referred to as side-imaging, as well as in the horizontal plane.

Fig. 3.8 Side-imaging chamber [8]

The illumination enters the chamber through a quartz window, while the images are collected through a borosilicate coverslip (R. A. Lamb, thickness number 1: 130–170 μm, diameter 35 mm).

A zoom lens system is used to collect and magnify the side-images rather than another individual objective as it is not possible to approach the droplet from the side closer than a few centimetres because of engineering restraints on the chamber size. This is further than the short working distances of affordable high magnification and NA microscope objectives. The zoom lens system incorporates an objective (Mitoyu, 20× magnification, infinity-corrected, NA of 0.42) with a long working distance coupled to a zoom lens (6.5:1.0 ratio) and a 1× adapter. The overall magnification of the system is up to 45.72× and the working distance is 25–35 mm. The zoom lens (Navitar, Zoom 6000) is mounted at 90° to the trapping objective on a translational stage allowing control over the x, y and z position of the imaging system.

A CCD camera is again used to collect the side images. Illumination is provided by either a white fibre light source or a white LED (Luxeon). A typical side image is shown in Fig. 3.9.

3.3.2 Low Pressure Chamber

In order to perform measurements below atmospheric pressure, a custom chamber has been designed which allows the chamber pressure to be reduced using a mechanical rotary vacuum pump (Edwards). The main features of the low pressure chamber are illustrated in Fig. 3.10. As usual the chamber is machined from stainless steel and has a removable lid. The base of the chamber has three evenly-spaced ports which are connected simultaneously to the pump. The even spacing of the ports means that the chamber can be evacuated without a trapped droplet being disturbed from a stable trapping position by an asymmetric flow of air out of

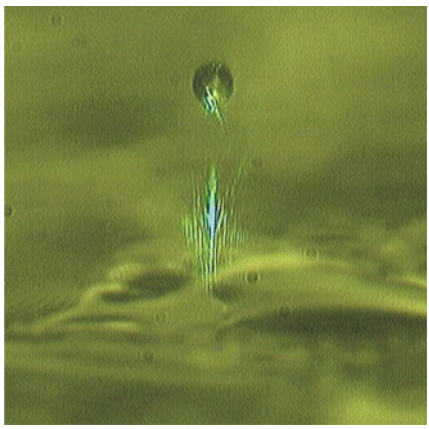

Fig. 3.9 A trapped droplet imaged from the side

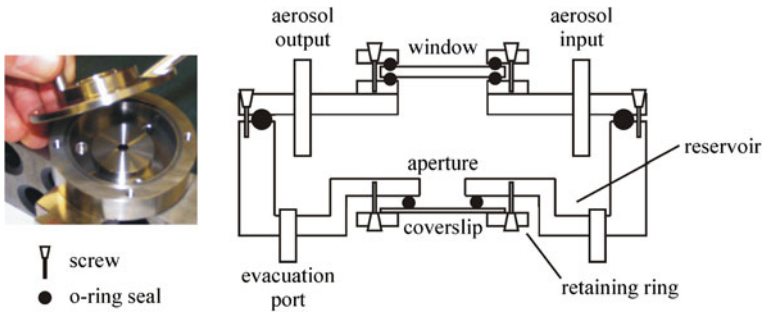

Fig. 3.10 Image and schematic cross-sectional diagram showing the construction of the low pressure chamber

the chamber. A needle valve allows the rate of air evacuation to be controlled so that the droplet is not destabilised by a high flow-rate. A 0–1,000 Torr baratron (MKS Instruments) measures the pressure in the chamber. Rubber o-rings are used to seal all positions of contact between individual parts of the chamber construction.

The chamber features a raised coverslip platform in the centre of the chamber. This allows a reservoir of aqueous solution to be present in the chamber which means that a high RH can be maintained through replenishment of the gas-phase water which will be lost as the chamber is evacuated. The aperture in the base of the chamber is smaller than that in the trapping chambers used to carry out experiments at atmospheric pressure. This minimises the curvature of the coverslip which results from the pressure difference across the coverslip as the chamber pressure is reduced. Despite the thickness of the coverslip being only around 150 μm, chamber pressures of as low as 5 kPa are achievable.

3.4 Aerosol Delivery and Solution Preparation

An ultrasonic medical nebuliser (NE U07, Omron) is used to create the flow of aerosol droplets in air from which individual droplets are trapped. The nebuliser has a flow-rate of approximately 1 mL min^{-1} and generates a distribution of particle sizes between $\sim$1 and 5 μm, with a mean mass diameter of 3.5 μm. Solutions of inorganic or organic solutes are loaded into the reservoir of the nebuliser and the flow from the nebuliser directed into the trapping chamber. For the majority of experiments the solutions are aqueous, with the solvent being deionised water (Purite deionising system, water conductivity of 10 μS cm^{-1}). For a few experiments organic solvents were used instead of water.

All droplets studied contain involatile solutes. This is required to reduce the vapour pressure of the droplets in accordance with the solute effect [2], in order to maintain a stable droplet size in conditions of less than 100% RH. As the vapour pressure above a curved surface is always greater than that above a flat surface, in accordance with the Kelvin effect, a droplet would always evaporate in conditions of less than supersaturation without the presence of a dissolved solute [2, 10].[1] All chemicals were used as received without further purification. The sources and purities of the chemicals used are summarised in Appendix II.

The composition of the aerosol droplets when first loaded into the optical trap has been shown to be the same as that loaded into the nebuliser reservoir [5]. This was demonstrated by nebulising directly onto a refractometer (Misco, PA203) and comparing the refractive index with that of the solution in the nebuliser reservoir. The refractometer measures the refractive index with a precision of $\pm$0.0001 and is routinely used as a means of verifying the composition of the salt solutions nebulised, by comparing the values obtained with standard calibration curves [11]. By determining the droplet size when first trapped from the aerosol flow and the composition of the nebulised solution the solute loading of the droplet can be determined, and hence the solute concentration may be determined at all times by considering the evolving droplet size [5].

In the case of dual trapping the two traps may be simultaneously loaded with droplets of the same composition from a single aerosol flow, or sequentially loaded with droplets of differing compositions. Because of the small distance between the two trapping positions it is not possible to load the traps with droplets of completely independent compositions. Typically a sample droplet containing a species of interest, for example an organic compound, will first be loaded into one of the traps. A second 'control' droplet consisting of an aqueous solution of an inorganic solute such as NaCl will then be loaded into the second trap.

Loading of the second trap results in a change in the size of the sample droplet, both because inorganic aerosol becomes incorporated into this droplet from the flow following coagulation, and because introducing the second aerosol flow causes the chamber RH to change. In order to determine the solute loading of the

[1] See Sect. 2.2.1.2 for a fuller explanation.

sample droplet following trapping of the second droplet it is necessary to account for both of these effects. The RH of the chamber upon the introduction of the second aerosol flow is determined by the composition of this flow and can be predicted using thermodynamic models for water partitioning between the solution and gas phases for salt solutions [5, 12]. The equilibrium size of the sample droplet size which would occur at this RH can be predicted using Köhler theory and assuming that the droplet solute loading is still that of the droplet when first loaded. As a first approximation the difference between the observed droplet size and this predicted droplet size can be attributed to the inclusion of inorganic solute mass into the sample droplet, and the magnitude of the difference can be used to determine the amount of solute which has been added. As the RH change and inclusion events occur simultaneously, and because the sizing process depends on knowing the composition and hence refractive index of the droplet, iterating the above process improves the accuracy with which the sample droplet composition is determined. Typically only two iterations are necessary to return a consistent mixed organic/inorganic sample droplet composition. This process has been discussed further by Hanford et al. [12].

A limitation of aerosol optical tweezers is associated with trap loading. Because of the narrow trapping region, trap loading is somewhat uncontrolled; it is necessary to flood the trapping chamber with a large number of aerosol droplets from a nebulised stream in order that one passes close enough to the trapping region with a low enough speed to become trapped. This makes control of the chamber environment challenging. Further, the compositions of aerosol droplets which can be trapped are limited to those which can be nebulised.

3.5 Spectroscopy

Inelastically-scattered light is used to spectroscopically probe the size of trapped droplets. Raman and fluorescently-scattered light are of particular interest. More than 99.9% of the elastically-scattered light from the droplet is reflected back along its original path by the high-reflectivity 45° 532 nm filter below the objective. Inelastically-scattered light passes through this notch filter and the 50:50 beam splitter used to direct imaging light to the CCD camera, and is then directed towards a spectrograph and CCD.

3.5.1 Spectrograph

A spectrograph with a focal length of 0.5 m is used to disperse the collected wavelengths of light onto the CCD. Two spectrographs were used in the course of the work (Acton, SpectraPro 500i and Jobin–Yvon, Triax 550). A 10 cm lens is used to focus the scattered light into the entrance slit of the spectrograph, the width

of which can be adjusted using a micrometer dial. A 550 nm long pass filter is placed in front of the spectrograph to remove the blue imaging light and the small amount of remaining 532 nm elastically-scattered light.

Depending on the wavelength range of interest, experiments were carried out using a 300, 600, 1,200 or 1,800 groove mm^{-1} spectrograph grating. The higher the number of grooves mm^{-1} of the grating used, the wider the angle over which the collected wavelengths of light are dispersed. This increases the spectral resolution but also reduces the wavelength range recorded on a CCD a given number of pixels wide.

3.5.2 CCD

The light dispersed by the spectrograph is imaged onto a non-intensified CCD. In the case of the Acton spectrograph this was a Princeton Instruments, PIXIS CCD which is thermoelectrically cooled to −50 °C by means of a Peltier cooling system and circulating air. In the case of the Jobin–Yvon spectrograph a liquid nitrogen cooled CCD was used. Both CCD cameras feature chips which measure 256 pixels high by 1,064 pixels wide. Because the spectrograph disperses the wavelengths of light in the horizontal axis the width of the chip, in conjunction with the spectrograph grating used, determines the spectral resolution and wavelength range of the spectra recorded. The effect of the grating on the spectral range and resolution of a CCD 1,064 pixels wide is summarised in Table 3.1.

The light scattered by a trapped droplet generally spans a height of ∼10 rows of CCD pixels. A subset of the full 256 pixel CCD height is therefore selected to contribute to a recorded spectrum in order to maximise the spectral signal-to-noise ratio. A background level of electrons is thermally-generated throughout the CCD array independently of the photon-generated signal, termed dark noise. It is a reduction of this dark noise which gives rise to the improvement in signal-to-noise ratio when the number of rows sampled is reduced.

The ability to specify subsets of CCD pixels to contribute to recorded spectra also allows the spectra from more than one droplet to be collected simultaneously. By directing the light from each droplet to different vertical positions on the CCD chip signals can be recorded separately and simultaneously. This procedure is shown schematically in Fig. 3.5. Figure 3.11b shows an image of the scattered light from two simultaneously-trapped droplets falling on the CCD. The resulting

Table 3.1 Spectral resolution of CCD for a range of spectrograph gratings

Grating	Wavelength range recorded/nm	Spectral resolution/nm $pixel^{-1}$
300	∼151	∼0.12
600	∼75	∼0.08
1,200	∼38	∼0.04
1,800	∼25	∼0.03

droplet spectra are shown in part (a), each integrated over seven rows of CCD pixels. Figure 3.11c shows a brightfield image of the two trapped droplets.

3.5.3 Acquisition and Processing of Spectra

The spectral fingerprints are recorded and processed using WinSpec32 (Roper Scientific) or SpectraMax32 (Galactic Industries Corporation) software in the case of the Acton or Jobin–Yvon spectrograph, respectively. Successive spectra may be recorded at a specified rate; an integration time of one second is typically used for the collection of a cavity-enhanced Raman spectrum such as those shown in Fig. 3.11a, but an integration time of as low as 0.2 s is achievable.

3.6 Particle Sizing I: Theoretical Aspects

Cavity-enhanced Raman spectroscopy (CERS) has been used throughout the studies presented in this thesis for the determination of the size of the trapped droplets. This section will outline the theoretical basis for CERS. This includes Raman scattering and Mie scattering theory which describes light scattering by a sphere.

3.6.1 Raman Scattering

In these experiments Raman light scattered by the intermolecular O–H stretching vibrations of water is collected from the trapped aqueous droplets. The trapping laser beam with a wavelength of 532 nm is used as the excitation source.

In Raman scattering an incident photon of frequency ν_0 excites a molecule to a short-lived virtual state. The subsequent relaxation from this virtual energy state back to a vibrational energy level of the electronic ground state is essentially instantaneous. The molecule can return to its original vibrational state in an elastic scattering process, in which case there is no energy change. If, however, the molecule returns to a different vibrational state there is a difference in the wavelength of the scattered light compared with the incident, termed the Raman shift [13]. The Raman shift is characteristic of the scattering medium and Raman spectroscopy has therefore been used extensively for compositional analysis. If the molecule relaxes to a higher vibrational state energy is transferred from the incident light to the molecule and the scattered light occurs at a longer wavelength. This is termed Stokes scattering. In anti-Stokes scattering the resulting vibrational energy level is lower than the original one; the molecule has lost energy and the light is scattered at a shorter wavelength than the incident radiation.

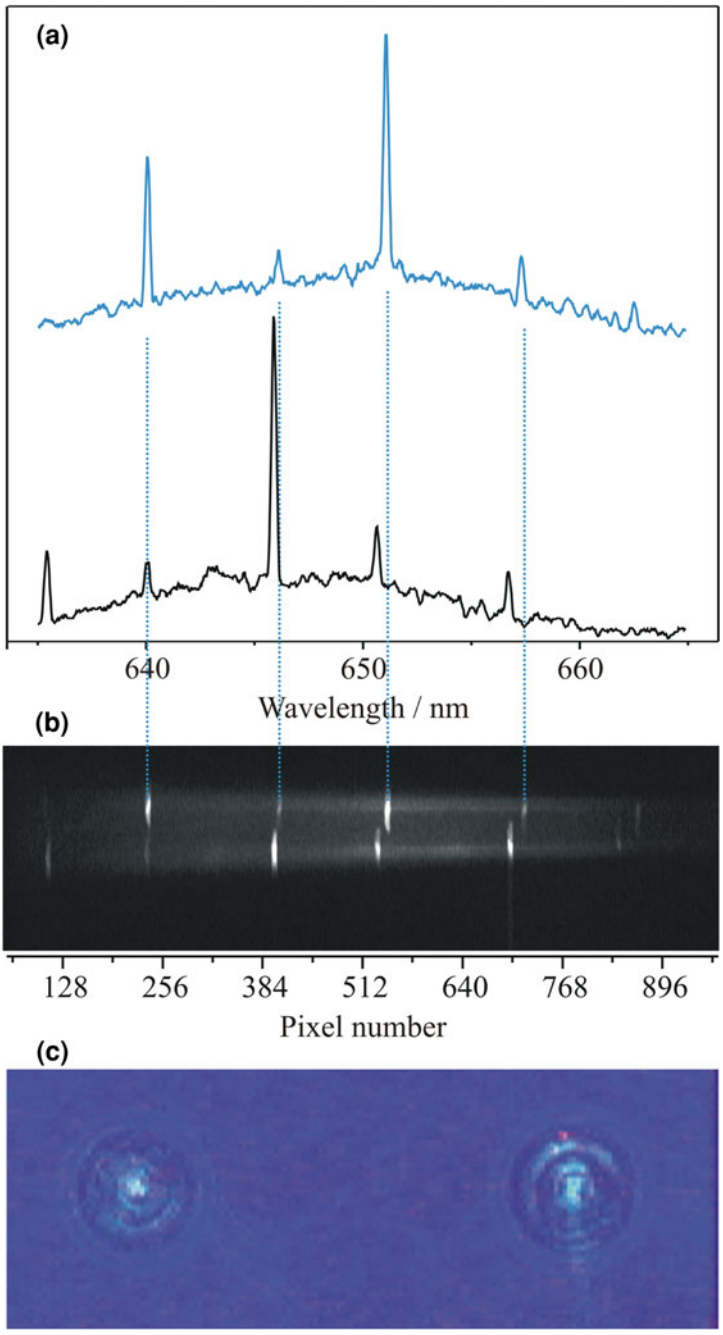

Fig. 3.11 **a** Spectra from two simultaneously-trapped droplets. The blue spectrum is from the smaller of the two droplets, evident as the spacing of the resonant modes is greater. **b** Image of the scattered light from the two droplets falling on the CCD. Dotted lines relate the bright patches on the upper strip of light on the CCD to the associated high-intensity features in the spectrum of the smaller droplet. **c** A brightfield image of the two droplets. The left-hand droplet gives rise to the upper strip of light on the CCD detector

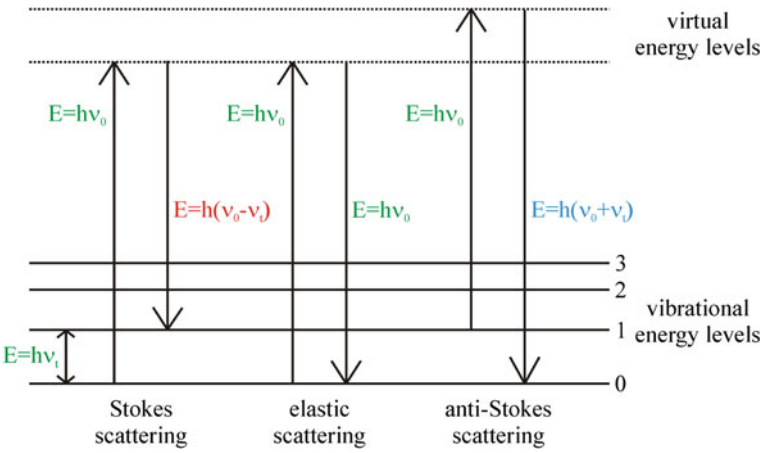

Fig. 3.12 Energy level diagram to illustrate the Raman scattering process. ν_0 is the frequency of the incident radiation and ν_t is the Raman shift in the frequency domain

Figure 3.12 illustrates Stokes and anti-Stokes Raman scattering, with elastic scattering shown for the purposes of comparison.

Raman scattering is a weak process; typically only one photon in 10^7 will produce a Raman transition. As anti-Stokes scattering depends on the population of excited vibrational states the intensity of this process is low and Raman spectra are dominated by Stokes scattering. For a molecular vibration to be Raman-active the vibrational motion must involve a change in molecular polarisability [13]. This condition is met by all three normal modes of water: the symmetric and anti-symmetric O–H stretching modes and the bending mode.

While Raman spectroscopy has previously been used for studying the composition of aerosol particles [14–19], in the work presented in this thesis it is only used in combination with Mie theory for the purposes of droplet sizing. A typical Raman spectrum collected from an aqueous optically-tweezed droplet with a radius of $\sim$5 μm is shown in Fig. 3.13. The broad envelope corresponds to the Stokes Raman band of the O–H stretching vibrations of water. The broad band shape arises from the distribution of the H bonding environments in the droplet, while the sharp peaks superimposed upon this are the result of stimulated Raman scattering, which will be discussed next.

3.6.2 Stimulated Raman Scattering

A photon emitted by spontaneous Raman scattering at a given frequency can stimulate the emission of further photons at this frequency. This phenomenon, known as stimulated Raman scattering (SRS), was first reported by Woodbury and Ng in 1962 [20]. The presence of a Raman scattered photon at frequency, ν,

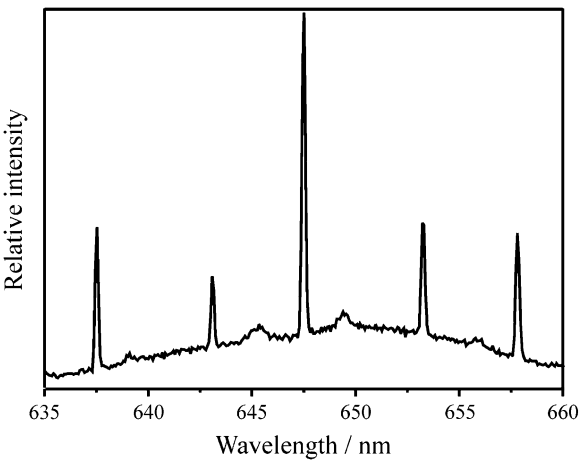

Fig. 3.13 A typical Raman spectrum (532 nm illumination) collected from an aqueous optically-tweezed droplet showing the broad spontaneous band arising from the OH stretching vibrational modes of water, superimposed on which are sharp, cavity-enhanced peaks which correspond to stimulated Raman scattering

enhances the Raman scattering cross-section at v and hence stimulates the emission of further photons at that frequency [21].

The intensity of the stimulated Raman scattering at a given wavelength, $I_{SRS}(\lambda)$, is given by [22]:

$$I_{SRS}(\lambda) = I_0(\lambda)\exp[(IG - L)z] \tag{3.4}$$

where $I_0(\lambda)$ is the spontaneous Raman scattering intensity at λ, I is the laser intensity, G is the gain factor, L describes the losses and z is the propagation distance. The gain factor is proportional to the concentration of the molecular Raman scatterer and the Raman scattering cross-section. It can be seen that for SRS to occur a threshold condition must be met; the gain per unit of propagation length must be greater than the losses, i.e. $IG > L$.

3.6.3 Mie Scattering Theory

Mie scattering theory was developed by Gustav Mie in 1908 [23, 24]. It describes the internal and scattered electromagnetic fields arising from illumination of a sphere with an incident light field and hence the intensities of scattered light. The intensity of the scattered light, which varies with scattering angle, is determined by the ratio of the droplet size to the wavelength of the illuminating light and the refractive index of the sphere. The droplet size parameter, x, is a convenient quantity describing the ratio of the droplet size to the wavelength of the illuminating light [25]:

$$x = \frac{2\pi rN}{\lambda} \tag{3.5}$$

where r is the particle radius and N is the refractive index of the surrounding medium.

Refractive index, N, is a complex quantity, given by:

$$N = m + ik \tag{3.6}$$

where m is the real part of the refractive index, i is $\sqrt{-1}$ and k is the imaginary part of the refractive index. m describes the speed of light in a medium compared with that in a vacuum, while k governs absorption. Mie theory assumes that the particle is of homogeneous refractive index and is in conditions of plane wave illumination.

Mie theory can be used to predict the scattering efficiency of a sphere as a function of size parameter. The scattering efficiency, Q_{sca}, is defined as the ratio of the cross-section for light scattering, C_{sca}, to the geometrical cross-section of the particle, G_{xs}:

$$Q_{sca} = \frac{C_{sca}}{G_{xs}} \tag{3.7}$$

$G_{xs} = 4\pi r^2$ for a spherical particle of radius r.

The variation of Q_{sca} with size parameter for a droplet with a composition of 20 g L^{-1} NaCl is shown in Fig. 3.14. For illumination with 532 nm wavelength light the ranges of size parameters shown in parts (a) and (b) correspond to the droplet radius varying between 3 and 8 μm and 5 and 5.2 μm, respectively. The broad oscillations in the magnitude of Q_{sca} arise from interference of the scattered light with that which is not deviated by the particle.

Fine ripple structure in Q_{sca} is evident in Fig. 3.14a, and the expanded region provided in Fig. 3.14b. This resonant structure is observed to depend on the particle size parameter and refractive index, and hence measurements of wavelength-resolved light scattering can be used to determine the size of microspheres, provided that the droplet refractive index is accounted for [26]. The fine structure

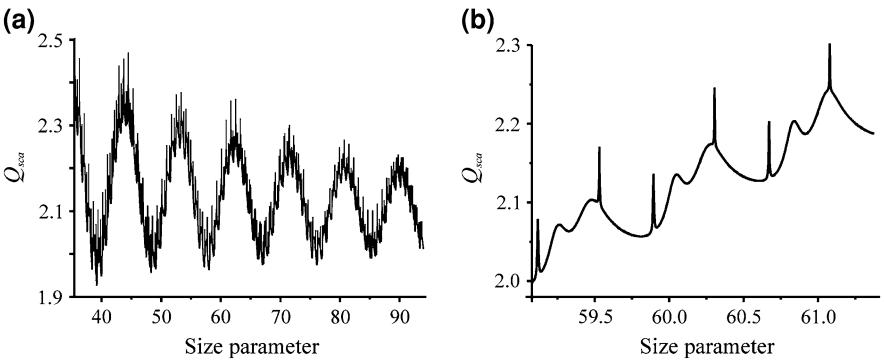

Fig. 3.14 **a** Q_{sca} as a function of size parameter for a droplet with a composition of 20 g L^{-1} NaCl illuminated with 532 nm wavelength light. **b** Expanded region of plot

arises as a result of the ability of a microsphere act as an optical cavity, supporting standing waves of circulating light. Such standing waves are commonly termed whispering gallery modes and are the subject of the next section.

3.6.4 Whispering Gallery Modes

Microdroplets can act as optical cavities for the light with which they are illuminated or which they scatter. Discrete wavelengths of light can undergo total internal reflection at the droplet interface, setting up a circulating standing wave inside the droplet with a pathlength of an integer number of wavelengths, known as a whispering gallery mode (WGM) or morphology dependent resonance (MDR) [27, 28]. As a result of the efficiency of the reflection at the droplet interface, significant light intensities can build in the droplet cavity modes, determined by the cavity build up factor, which describes the rate at which the light intensity in a mode increases [22]. Two standing waves are illustrated in Fig. 3.15 for coupling of the trapping illumination into the droplet (green) and for a standing wave of inelastically-scattered light (red) of a longer wavelength.

WGMs can be assigned a mode number, n_{mode}, polarisation, P, and mode order, l, [22]. The mode number defines the number of wavelengths forming the standing wave in the electromagnetic field circulating the droplet circumference. The standing waves shown in green and red in Fig. 3.15 have mode numbers of six and four, respectively. The larger the droplet the higher n_{mode} for standing waves formed from light of a given wavelength. Modes with no radial dependence in the electric component of the field are defined as modes of transverse electric (TE) polarisation and modes with no radial dependence in the magnetic component as transverse magnetic (TM). These two possible polarisations of WGMs are illustrated in Fig. 3.16.

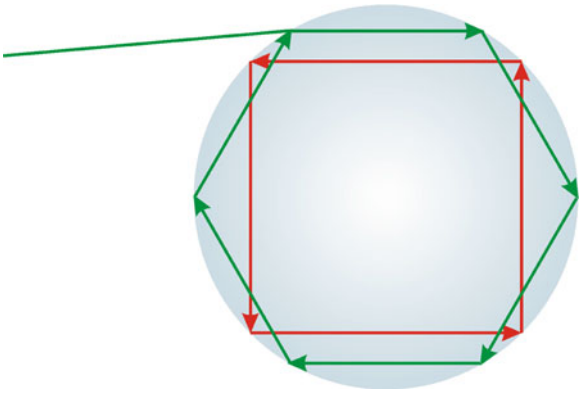

Fig. 3.15 Total internal reflection of light from the trapping beam which has coupled into the droplet and of inelastically-scattered light of a longer wavelength, shown in *green* and *red*, respectively

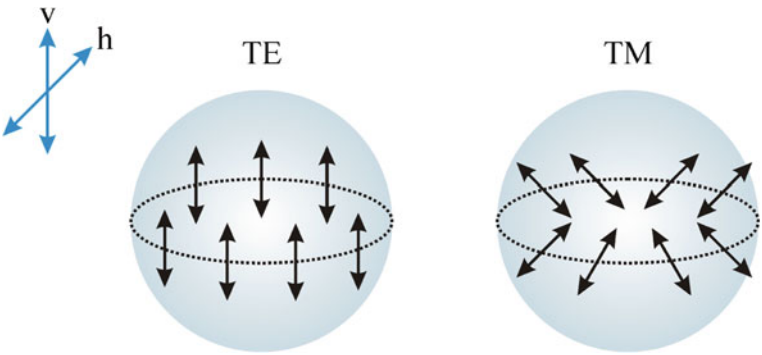

Fig. 3.16 Transverse electric and transverse magnetic polarisation WGMs. Arrows indicate the plane in which the electric component of the field of the light in the mode oscillates. Arrows marked v and h define the vertical and horizontal directions, respectively

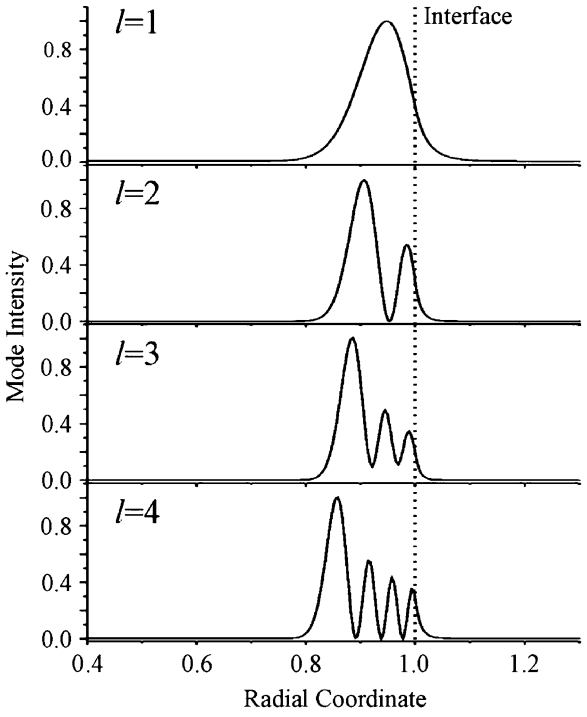

Fig. 3.17 Radial distribution of WGM intensities of varying mode order. Figure reproduced by permission of the PCCP Owner Societies from [22], http://dx.doi.org/10.1039/b313370b

The mode order specifies the number of maxima existing in the radial dependence of the mode intensity. The radial dependence of the mode intensity is shown for the lowest four mode orders in Fig. 3.17.

Figure 3.18 shows the calculated internal intensity distribution for a mode with $n_{mode} = 60$ and $l = 2$ supported by a droplet of size parameter 53.3130188 [22].

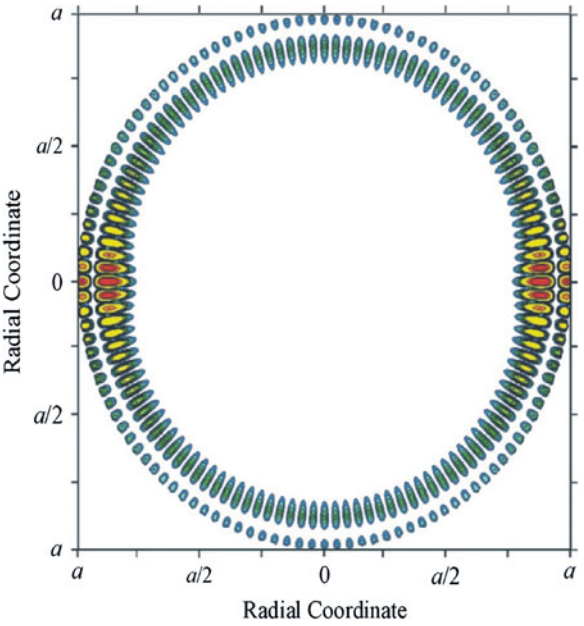

Fig. 3.18 Calculated internal intensity distribution for a mode with $n_{mode} = 60$ and $l = 2$ supported by a droplet of size parameter 53.3130188. Here a is the droplet radius. Figure reproduced by permission of the PCCP Owner Societies from [22], http://dx.doi.org/10.1039/b313370b

The lifetime of a WGM is defined by the mode quality factor, Q [29]:

$$Q = \frac{energy\ stored\ per\ cycle}{energy\ lost\ per\ cycle} \tag{3.8}$$

The higher the Q of a mode the longer the mode lifetime and hence the higher the intensity of light which can build up in the mode. The higher n_{mode} and the lower l, the higher the cavity Q [30]. As a result of the variation of Q, modes of high n_{mode} or low l are sharper and more intense than those of low n_{mode} or high l. Modes of TE polarisation are of higher Q than TM modes [29, 31].[2]

WGMs provide a mechanism for optical feedback in microparticles, amplifying spontaneous scattering processes. An example of an optical process which undergoes such 'cavity-enhancement' is stimulated Raman scattering. This effect was first observed for a levitated water/glycerol droplet by Thurn and Kiefer in 1984 [32]. Spontaneously-scattered Raman photons emitted with an appropriate trajectory can couple into a WGM. If a sufficient density of photons builds up in the cavity mode then the threshold for SRS will be surpassed. As a result of the spatial confinement of the Raman-scattered photons in cavity modes the threshold is reached in microdroplets for much lower incident light intensities than for bulk samples and SRS is observed at wavelengths commensurate with WGMs [33]. As a result microdroplet Raman spectra feature sharp resonances at WGM wavelengths, as shown in Fig. 3.13.

[2] The Q of cavity modes will be discussed in more detail in Sect. 5.3.4.2.

The wavelengths of WGMs are dependent on the size of the optical cavity and can be predicted using Mie scattering theory. As a result, comparing the wavelengths of resonances in droplet Raman spectra with theoretical predictions from Mie theory allows the determination of droplet size. Provided that the droplet refractive index is accounted for, the size of micrometre radius droplets can be determined with nanometre accuracy in this way [26, 34].

3.7 Particle Sizing II: Practical Aspects

Having set out the theoretical basis for CERS, this section will describe the procedure used to determine droplet sizes from experimental spectra in practice.

An estimate of the droplet size can be determined from the spacing between the resonances in a droplet Raman spectrum which arise from modes in a progression of a given polarisation and mode order, *Sp(r)*, which can be approximated by the expression [35]:

$$Sp(r) = \frac{\lambda^2 \tan^{-1}(m^2 - 1)^{1/2}}{2\pi r(m^2 - 1)^{1/2}} \tag{3.9}$$

Precise size determination can be achieved by comparing experimental CERS spectra with those predicted from Mie scattering theory. This is carried out using a custom programme, Size and Compositional Analysis of Tweezed Aerosols (SCATA), written by Dr. J. P. Reid for the sizing and compositional analysis of droplet spectra (2007). Figure 3.19 shows the CERS fingerprints for three droplets of different sizes in the range 3.7–8.0 μm. The spectra have been compared with Mie scattering theory and the WGMs assigned using the SCATA programme. Resonances arising from first order modes are observed in the spectrum shown in Fig. 3.19a, while first and second order modes are observed in spectra (b) and (c).

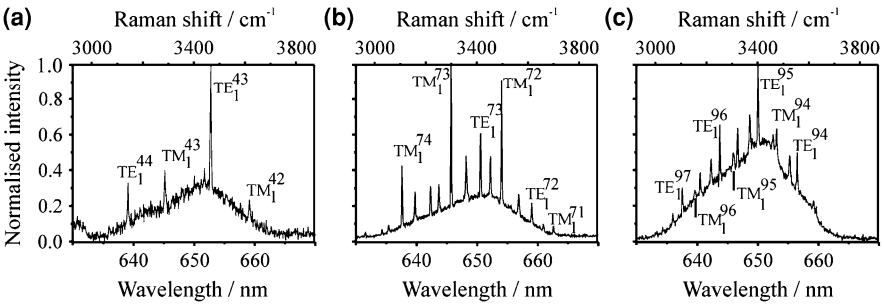

Fig. 3.19 CERS spectra for three droplets of radii: **a** 3.78 μm, **b** 6.20 μm, **c** 7.95 μm. The resonances arising from first order modes are labelled with the notation $P_l^{n_{mode}}$, where *P* is the polarization of the mode, which is either TE or TM, n_{mode} is the mode number and *l* is the mode order

The resonances arising from first order modes are labelled with the notation $P_1^{n_{mode}}$. It can be seen that the mode spacing decreases with increasing droplet size and the mode number increases, reflecting the increasing number of wavelengths required to form the standing wave. For the smallest droplet, only first order modes are of a sufficiently high quality factor to support stimulated Raman scattering, although second order modes are supported for the larger two droplet sizes [36].

The SCATA programme can be used to assign the resonant modes in spectra from homogeneous droplets and from those with a core/shell structure. The description here is limited to the treatment of droplets of homogeneous refractive index, relevant to the studies presented in this thesis. Central to the determination of droplet size is the treatment of the droplet refractive index. The treatment of refractive index will be outlined first, followed by the sizing procedure.

3.7.1 Treatment of Refractive Index

In order to determine the evolving size of a droplet from a series of collected spectra, it is essential to consider the variation of droplet refractive index with size and hence concentration. For each solution used to generate aerosol a calibration is performed to determine the variation of the refractive index of the solution with concentration. This is carried out by preparing stock solutions of varying concentration and the use of a commercially-available refractometer which returns the refractive index of the solutions at 589 nm. An example of calibration data obtained for aqueous NaCl is provided in Fig. 3.20.

Determining the gradient of a plot of refractive index variation with concentration, and fixing the refractive index for a solute free solution as the refractive index of water, which is 1.3331 at 589 nm, allows the refractive index of the

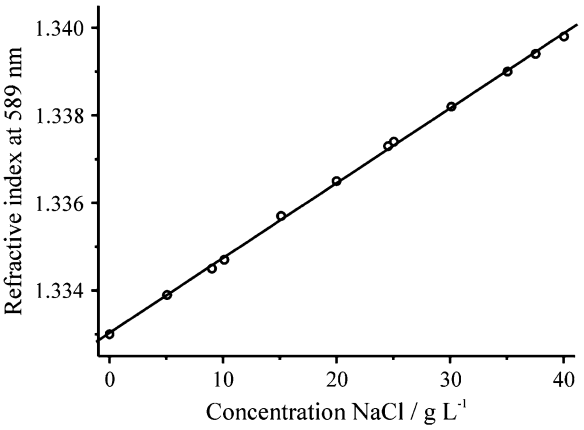

Fig. 3.20 The variation of solution refractive index with concentration for aqueous NaCl

droplet at 589 nm to be determined for any solute concentration. This is important for sizing droplets of evolving size and hence solute concentration.

The variation of the droplet refractive index with wavelength, referred to as the dispersion, must also be considered. The refractive index of a droplet varies with wavelength across the range collected in an experimental spectrum. The variation of refractive index with wavelength can be described by a Cauchy relationship [11]:

$$m(\lambda) = A + \left(\frac{B}{\lambda^2}\right) \tag{3.10}$$

where A and B are empirical constants. Over the typical spectral wavelength range of around 30 nm either side of $\sim$650 nm relevant to the CERS spectra the variation can be well approximated by a linear dependence, as shown in Fig. 3.21 for two concentrations of NaCl, each at three temperatures.

The refractometer returns a value of the refractive index which has been corrected for a temperature of 20 °C. The temperature in the laboratory is in fact maintained at 18 °C. It can however be seen from Fig. 3.21 that the dependence of the refractive index on temperature is weak. The error in the refractive index introduced by a 5 °C temperature difference, for example between 20 and 25 °C is $\sim 5 \times 10^{-4}$ or 0.04%, which has a negligible effect on the sizing calculation [36].

The gradient of a linear fit to the variation of the refractive index with wavelength dispersion, $dm/d\lambda$, has been found to be linearly related to the value of m at 589 nm for NaCl solutions, as shown in Fig. 3.22. The value of m at 589 nm can therefore be used to determine the refractive index dispersion for a droplet of a given solute concentration. The accuracy of this approach remains to be tested for other solutes and will be the subject of future investigations.

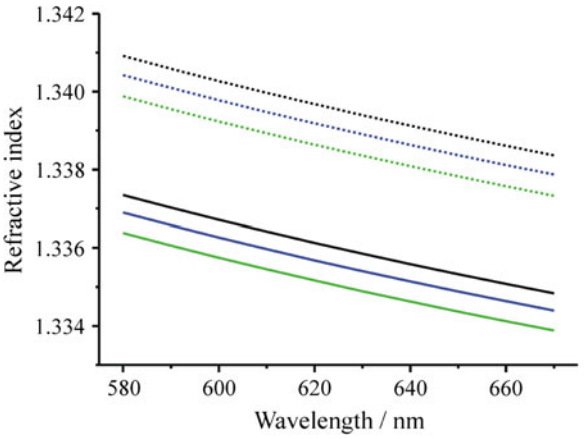

Fig. 3.21 Refractive index variation of aqueous NaCl solutions with wavelength [11]. *Solid lines* represent a solution of 20 g L^{-1} NaCl at temperatures of 15, 20 and 25 °C shown in *black*, *blue* and *green*, respectively. *Broken lines* show 40 g L^{-1} NaCl at temperatures of 15, 20 and 25 °C shown in *black*, *blue* and *green*, respectively

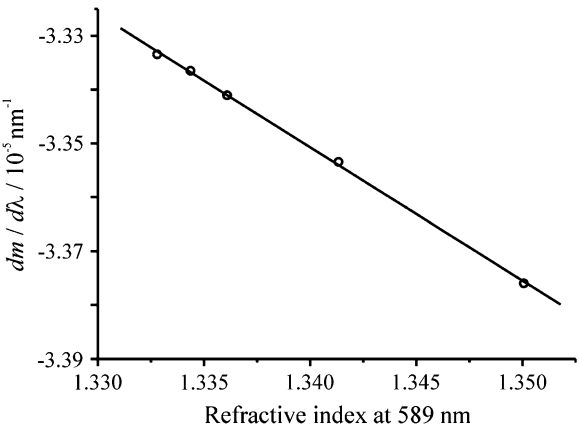

Fig. 3.22 The variation of the gradient of the refractive index dispersion with the value of *m* at 589 nm for aqueous NaCl solutions

3.7.2 Sizing Procedure

Having established the treatment of droplet refractive index, the process by which the evolving size of a droplet is determined from a series of cavity-enhanced spectra will be described.

Firstly a peak search is performed to identify the wavelengths of the resonant modes in a sequence of up to 5,000 experimental spectra. A gradient searching algorithm is used. Secondly the user identifies at least two resonances in the first droplet spectrum as being from the same mode progression. This identifies the spacing between modes of a given polarisation and mode order. The user also specifies the concentration of the solution from which the aerosol was generated, which is taken to be the concentration of the droplet when first trapped, and the gradient of the concentration dependence of the refractive index of the solution. That the composition of the droplet when first trapped is the same as that of the nebulised solution has been verified by comparing the refractive index of samples of a solution before and after the nebulisation step and through detailed analysis of the comparative RH response of two simultaneously-trapped droplets of varying compositions [5, 12]. SCATA determines the refractive index of the droplet at the spectral wavelengths by the procedure outlined above and hence Eq. 3.9 can be used to gain an approximate droplet size, r_{approx}, for each spectral frame in the experimental run.

Next a spectral fitting algorithm is used to determine the precise droplet sizes as follows. A set of spectra are simulated between user-specified maximum and minimum radius limits, which are fixed for the entire experimental run and are chosen based on the values of r_{approx} for the experimental run. Spectra are simulated at 0.1 nm increments in radius. Every 15 nm in size Mie scattering theory is used to simulate a spectrum, while at intermediate increments the resonant wavelengths are predicted by means of a linear interpolation between the resonant wavelengths predicted from Mie theory for the nearest droplet sizes above and below the range considered, significantly improving the computational efficiency. The wavelength

dependent refractive index of the droplet is determined according to the fitting process outlined above and included in the Mie scattering calculations.

The first experimental spectrum is then compared to this set of simulated spectra. For each simulated spectrum the average difference between the wavelengths of the resonant modes and those of the experimental spectrum is determined. The simulated spectrum with the smallest average difference is taken to correspond to the true droplet size and the resonant modes are assigned accordingly. This process establishes the size of the droplet soon after trapping and hence the solute loading of the droplet. As the solute loading will remain constant throughout the experimental run, the refractive index is known precisely for the entirety of the run by considering the evolving droplet size.

The next spectrum is sized in the same way, considering the droplet refractive index to be equal to that of the previous droplet. The size determined for this droplet is then used to determine a better estimate of the droplet concentration and hence refractive index based on knowledge of the solute loading of the droplet. This concentration is used to refine the refractive index of the droplet and the spectral fitting process is repeated for the refined droplet refractive index.

The sizing process is repeated for the entire experimental run, which typically consists of several thousand spectral frames. Example input and sizing output files are provided in Appendix I.

References

1. R.J. Hopkins, L. Mitchem, A.D. Ward, J.P. Reid, Phys. Chem. Chem. Phys. **6**, 4924 (2004)
2. J.H. Seinfeld, S.N. Pandis, *Atmospheric Chemistry and Physics: From Air Pollution to Climate Change* (John Wiley and Sons, New York, 1998)
3. D. Segelstein, M.S. Thesis: The Complex Refractive Index of Water, University of Missouri, Kansas City, USA, 1981
4. K. Svoboda, S.M. Block, Annu. Rev. Biophys. Biomol. Struct. **23**, 247 (1994)
5. J.R. Butler, L. Mitchem, K.L. Hanford, L. Treuel, J.P. Reid, Faraday Discuss. **137**, 351 (2008)
6. K.J. Baldwin, D.N. Batchelder, S. Webster, in *Handbook of Raman Spectroscopy: From the Research Laboratory to the Process Line*, ed. by I.R. Lewis, H.G.M. Edwards (CRC Press, Boca Raton, 2001), p. 145
7. N.B. Viana, M.S. Rocha, O.N. Mesquita, A. Mazolli, P.A.M. Neto, H.M. Nussenzveig, Phys. Rev. E **75**, 021914 (2007)
8. Photography by D. Jones, University of Bristol, Bristol (2008)
9. E. Fällman, O. Axner, Appl. Opt. **36**, 2107 (1997)
10. G. McFiggans et al., Atmos. Chem. Phys. Discuss. **5**, 8507 (2005)
11. R.C. Millard, G. Seaver, Deep Sea Res. A **37**, 1909 (1990)
12. K.L. Hanford, L. Mitchem, J.P. Reid, S.L. Clegg, D.O. Topping, G.B. McFiggans, J. Phys. Chem. A **112**, 9413 (2008)
13. P. Atkins, J. de Paula, *Physical Chemistry* (Oxford University Press, Oxford, 2002)
14. J. Musick, J. Popp, M. Trunk, W. Kiefer, Appl. Spectrosc. **52**, 692 (1998)
15. L. Mitchem, J. Buajarern, R.J. Hopkins, A.D. Ward, R.J.J. Gilham, R.L. Johnston, J.P. Reid, J. Phys. Chem. A **110**, 8116 (2006)
16. K.H. Fung, I.N. Tang, Appl. Spectrosc. **46**, 159 (1992)
17. K.H. Fung, I.N. Tang, J. Colloid Interf. Sci. **130**, 219 (1989)

18. K.H. Fung, D.G. Imre, I.N. Tang, J. Aerosol Sci. **25**, 479 (1994)
19. J.P. Reid, H. Meresman, L. Mitchem, R. Symes, Int. Rev. Phys. Chem. **26**, 139 (2007)
20. E.J. Woodbury, W.K. Ng, in *Proceedings of the Institute of Radio Engineers*, 1962, vol. 50, p. 2367
21. J.B. Snow, S.X. Qian, R.K. Chang, Opt. Lett. **10**, 37 (1985)
22. R. Symes, R.M. Sayer, J.P. Reid, Phys. Chem. Chem. Phys. **6**, 474 (2004)
23. G. Mie, Ann. Phys. **25**, 377 (1908)
24. G. Mie, Royal Aircraft Establishment, Library translation of Annalen der Physik article (1976). http://diogenes.iwt.uni-bremen.de/vt/laser/papers/RAE-LT1873-1976-Mie-1908-translation.pdf
25. P.W. Barber, S.C. Hill, *Light Scattering by Particles: Computational Methods* (World Scientific Publishing Co. Inc., Singapore, 1990)
26. H.B. Lin, J.D. Eversole, A.J. Campillo, Rev. Sci. Instrum. **61**, 1018 (1990)
27. A. Ashkin, J.M. Dziedzic, Appl. Opt. **20**, 1803 (1981)
28. R.E. Benner, P.W. Barber, J.F. Owen, R.K. Chang, Phys. Rev. Lett. **44**, 475 (1980)
29. J.D. Eversole, H.B. Lin, C.D. Merritt, A.J. Campillo, Appl. Spectrosc. **48**, 373 (1994)
30. H.B. Lin, A.L. Huston, J.D. Eversole, A.J. Campillo, P. Chylek, Opt. Lett. **17**, 970 (1992)
31. J.D. Eversole, H.B. Lin, A.L. Huston, A.J. Campillo, P.T. Leung, S.Y. Liu, K. Young, J. Opt. Soc. Am. B **10**, 1955 (1993)
32. R. Thurn, W. Kiefer, J. Raman Spectrosc. **15**, 411 (1984)
33. A.B. Matsko, A.A. Savchenkov, R.J. Letargat, V.S. Ilchenko, L. Maleki, J. Opt. B Quantum Semiclassical Opt. **5**, 272 (2003)
34. L. Mitchem, J.P. Reid, Chem. Soc. Rev. **37**, 756 (2008)
35. S.C. Hill, R.E. Benner, in *Optical Effects Associated with Small Particles*, vol. 3, ed. by P.W. Barber, R.K. Chang (World Scientific Publishing Co, Singapore, 1988)
36. R.M. Sayer, R.D.B. Gatherer, R.J.J. Gilham, J.P. Reid, Phys. Chem. Chem. Phys. **5**, 3732 (2003)

Chapter 4
Optical Manipulation in Aerosol Optical Tweezers

Condensed phase optical manipulation techniques were pioneered by Ashkin, who demonstrated the first use of radiation pressure to guide particles in 1970 [1] and later the first single-beam gradient force trap (optical tweezers) in 1986 [2]. Since then there have been numerous studies that make use of condensed phase optical tweezers, and that have sought to characterise the gradient forces operating in the trapping region. A notable example is the use of optical tweezers to measure the mechanical properties of biological organelles such as motor proteins and bacterial pili [3–5]. These studies rely on precise knowledge of the restoring force of the optical traps used to manipulate the biological material.

Airborne, or aerosol, optical tweezers are a much newer tool. Although Ashkin demonstrated the first optical levitation of liquid droplets in air in 1975 [6], it was not until over two decades later that optical tweezers were applied to the trapping of airborne solid [7] and liquid [8] particles. The first detailed characterisations of trapped aerosol droplets were carried out by Ward and co-workers [9] and Reid and co-workers [10] in 2004. There have been very few studies of optical forces experienced by trapped aerosol droplets and, as a consequence, the behaviour of liquid particles trapped in air is poorly understood compared to trapping in the condensed phase [11–15]. A thorough understanding of the forces operating in aerosol optical tweezers is essential if the results from studies of aerosol properties are to be correctly interpreted.

4.1 Theory of Optical Forces

Tweezed particles experience two optical forces: a gradient force which acts in three dimensions to confine the particle laterally and axially to the position of

Electronic supplementary material The online version of this chapter (doi:10.1007/978-3-642-16348-7_4) contains supplementary material, which is available to authorized users.

K. J. Knox, *Light-Induced Processes in Optically-Tweezed Aerosol Droplets*, Springer Theses, DOI: 10.1007/978-3-642-16348-7_4,

highest light intensity, and a scattering force which acts to accelerate the particle in the axial direction of beam propagation.[1] For stable three-dimensional confinement the trapping configuration must be devised such that the gradient force dominates the scattering force [16]. The other force acting on the droplets is gravity which, because an inverted microscope objective arrangement is used, opposes the scattering force in these studies.

4.1.1 Refractive Index Steps in Optical Tweezers

In an optical trap the trapping beam must first be focussed through several media of varying refractive indices before reaching the trapping plane, affecting the forces experienced by a trapped particle. In aerosol tweezers there is generally an additional step in refractive index for the light to pass through compared with condensed phase tweezers, arising from an aqueous layer deposited on the coverslip above which the droplet is trapped. The media through which the trapping beam must travel in typical experimental arrangements for aerosol and condensed phase optical tweezers are compared in Fig. 4.1. As a result of this extra refractive index step, gaining an understanding of the trapping forces is more complicated for aerosol optical tweezers than for those in the condensed phase. The matter is further complicated by the fact that the thickness of the aqueous layer will not remain constant between and during experiments.

While the refractive index of the objective lens, oil and coverslip are deliberately matched, refractive index mismatches exist between the coverslip and the aqueous layer and between the aqueous layer and air. These mismatches in refractive index introduce spherical aberration to the trapping beam [11, 17]. For some droplet sizes this spherical aberration is necessary to allow stable trapping [18].

4.1.2 Theoretical Models of Forces in Optical Tweezers

Several theoretical approaches have been proposed for modelling the forces in condensed phase optical traps. Studies of the optical gradient forces acting on trapped particles have found that an electromagnetic theory treatment is applicable to small particles, while large particles are well accounted for by a ray optics approach [19]. However, for particle diameters of 1–10 μm, the range addressed in our studies, neither approach produces predictions of trapping forces which agree with experimental observations [20–22]. More recently a Mie–Debye modelling method has been reported which produces results which are reasonably consistent with experimental data [23]. The method uses the Debye wave representation to

[1] See Sect. 1.3.2 for a detailed discussion.

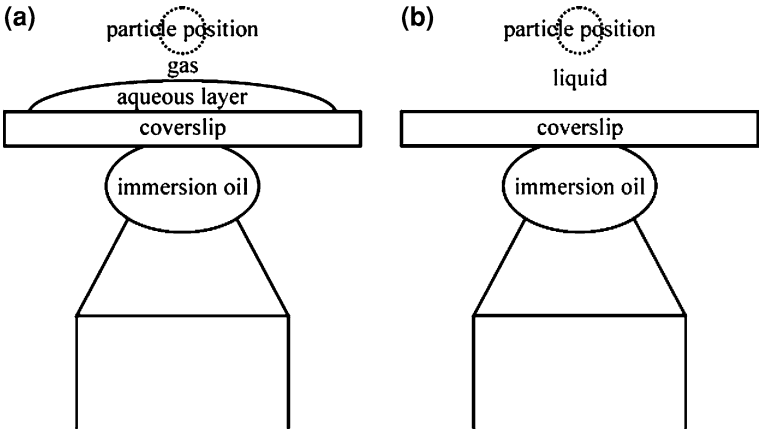

Fig. 4.1 A comparison of the media which the trapping beam must travel through for **a** aerosol and **b** condensed phase optical tweezers

produce a wave description of the trapping beam at the focus when modelling the gradient force, and Mie theory to describe the scattering force. This approach was extended to include transverse trapping forces by Mazolli et al. [24]. The Mie–Debye theory does not take into account the effects of spherical aberration on the trapping beam focus that results from a mismatch in refractive index between the coverslip and the dispersing medium, leading Viana et al. to develop the Mie–Debye-spherical aberration (MDSA) theory. This approach incorporates the effect of spherical aberration into the Mie–Debye theory by combining it with work by Török et al. which describes the effect on the beam focus of travelling across an interface between surfaces of mismatched refractive index [25].

The MDSA theory is the most complete description of the forces in optical tweezers in the condensed phase to date. It predicts that there is no dependence of the trapping position on laser power. Further, it predicts that spherical aberration gives rise to a minimum size particle which can be stably trapped, a decrease in the trapping force with the height of the laser focus above the coverslip, and the existence of several equilibrium trapping positions for a trapped particle [17, 21]. While all of these predictions have been shown to be consistent with experimental observations in the condensed phase, the extent to which they apply to aerosol tweezers has not been tested. The experiments presented in this chapter seek to test several of the predictions of MDSA theory for aerosol tweezers, in particular the dependence of the trapping position on laser power and the existence of several equilibrium trapping positions.

In order to extend the MDSA theoretical approach to aerosol optical tweezers it is necessary to include a further refractive index step in the MDSA theory. This development of the theory is underway by collaborators, D. R. Burnham and Dr. D. McGloin at the University of Dundee, and promises to provide a robust theory with which to compare our experimental findings [26].

4.2 Summary of Studies

Through the addition of a zoom lens and camera at 90° to the trapping laser beam the position of optically-tweezed droplets in the direction of the laser propagation, referred to as the axial displacement, has been studied directly [27]. In conjunction with imaging in the plane of the optical trap and cavity-enhanced Raman spectroscopy (CERS), this approach has been used to investigate the optical forces experienced by a trapped aerosol droplet. By varying the power of the trapping laser and observing changes in the axial position of a trapped particle through the acquisition of side images it has been possible to examine the fine balance between the gradient and scattering forces, a key parameter in optical manipulation [20].

As a result of these studies the discrepancy between sizing trapped particles from imaging techniques and CERS has been reconciled. By examining the axial positions of different droplets within two parallel optical traps it has been possible to rationalise the observation that aerosol coagulation appears to occur at separations of less than the sum of the particle radii [28]. Further, the plausibility of using measurements of the axial position of a particle within an optical trap as a new tool for probing the evolving size of the particle has been assessed. The side-imaging capability has also enabled several examples of interesting and important droplet-trapping phenomena to be observed, for example the existence of more than one stable trapping position [29] and optical binding of pairs of aerosol droplets.

These studies represent both the first to examine the axial displacement of optically-trapped liquid aerosol droplets and the first to study axial displacements in optical tweezers by direct observation through such a 'side-imaging' technique.

4.3 Experimental Considerations

4.3.1 Optical Trapping

The vertical position of the focus of the beam within the aerosol chamber, and hence the trap position, is controlled by adjusting the relative height of the chamber and the objective. The focus is maintained at the same height throughout the experiments described here. The laser power is controlled using a graduated neutral density filter; laser powers of between 10 and 100 mW, measured prior to the beam expansion optics, are typical in these measurements. The trapping power at the beam focus is $35 \pm 2\%$ of the laser power, determined using the dual objective approach [21]. All subsequent powers quoted are laser powers, rather than trapping powers.

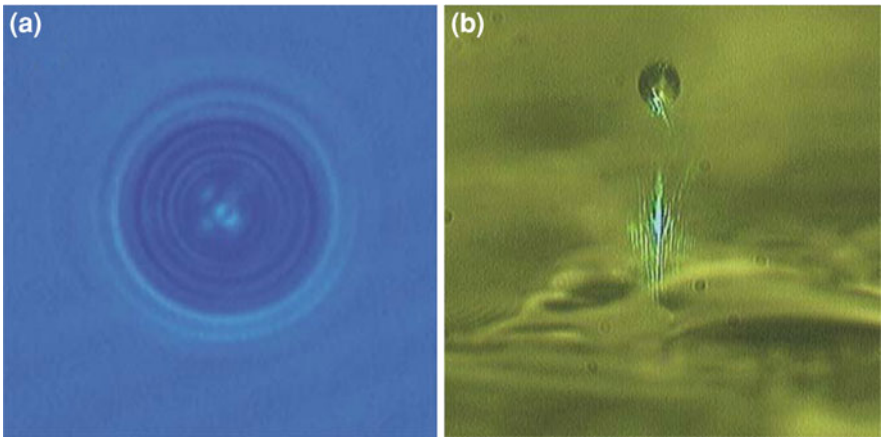

Fig. 4.2 **a** A typical in-plane image of an optically-trapped droplet. **b** A typical side image of an optically-trapped droplet

4.3.2 Imaging

By using the side-imaging trapping chamber, the trapped aerosol particle can be simultaneously imaged from below (referred to as an in-plane image) and from the side (referred to as a side image), allowing the lateral and axial positions of the particle to be investigated simultaneously.[2] The zoom lens system is mounted at 90° to the trapping objective on a translational stage allowing control over the x, y and z position of the imaging system. Typical in-plane and side images are shown in Fig. 4.2a and b, respectively, for droplets with radii of $\sim$5 μm. In the image shown in Fig. 4.2b the camera is angled away from the horizontal plane, providing a three-dimensional perspective of the trapped particle above the coverslip. The droplet is trapped at a height of a few tens of microns above the coverslip and the aqueous layer produced during the nebulisation step can be observed resting on the coverslip.

Figure 4.3 shows a side image captured with the zoom lens system positioned in the horizontal plane. The reflection of the droplet in the coverslip can be seen in the lower half of the image. A smaller droplet resting on the coverslip surface, along with its reflection, can be seen at the right-hand side of the image, defining the horizontal position of the coverslip, shown here with a dotted line. Analysis of side images such as that shown in Fig. 4.3 allows the height of the droplet above the coverslip to be determined by measuring the distance between the centre of the droplet and its reflection and halving this value. The pixels of highest intensity are taken to be at the centre of the droplet and droplet reflection. The width of this bright spot is typically ten pixels, resulting in an error in the measured height of

[2] See Sect. 3.3.1 for more details.

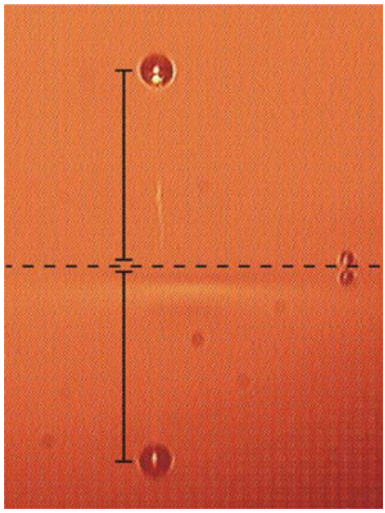

Fig. 4.3 Side image of an optically-tweezed aqueous droplet (radius approximately 5 μm) above a borosilicate coverslip. The reflection of the droplet in the coverslip can be seen in the lower half of the image. A smaller droplet resting on the coverslip surface, along with its reflection, can be seen at the right-hand side of the image, defining the horizontal position of the coverslip, shown here with a *dotted line*

the droplet of approximately 2%. The height determined in pixels is converted to μm by using the spectroscopically-determined droplet radius as a calibration tool.

4.3.3 Spectroscopy

In conjunction with the brightfield images, Raman spectra of the trapped particle are acquired at 1-s time intervals. In this work a relatively coarse 600 groove mm^{-1} spectrograph grating was used. This degrades the accuracy of resolving the resonant wavelengths, which incurs an increase in the droplet size error, but in all cases this error is less than ± 30 nm.

4.4 Studies of Axial Displacement

Several methods are currently used to study the displacement of optically-trapped solid particles immersed in a liquid along the direction of laser propagation. The methods that have been developed are indirect, relying on a calibration step in which a test particle is tethered to a piezo-electrically-translatable stage. The stage is then moved to known axial positions and a calibration curve for an appropriate observable quantity is derived. Observable quantities include power fluctuations in the back-scattered light from the trapped particle measured by back-focal-plane interfermometry [30–34], the intensity of the two-photon excitation fluorescence signal from a labelled bead, which provides a measure of the irradiance sampled by the trapped bead and thus the axial position [35], the image size [36, 37] and the degree of focus of the image [38]. The degree of focus has been rigorously applied through the calculation of the Shannon's information entropy of the image, which

is at a minimum when the particle is positioned at the focal plane of the collection optics [39]. The relationship between the change in the axial position of the focus of the optical trap and the movement of an externally mounted lens [40] has been used to move optically-trapped single cells with respect to the image plane of a scanning laser microscope, facilitating three-dimensional imaging [41].

Examining the axial displacement of a trapped aerosol droplet presents challenges that are not relevant to measurements in the solution phase. Most significantly, any integral calibration step would be destructive for the liquid droplets. Additionally, as liquid aerosol particles have an inherent distribution of sizes and compositions when generated, which will have a bearing on all of the above observable quantities, calibrated measurements of the axial displacement for a single control particle are not appropriate.

First, the dependence of the axial position of a trapped droplet on droplet size, laser power and droplet refractive index is examined. Next, the effect of the axial displacement on the in-plane image is addressed. Finally, the possibility of probing the evolving size of a droplet by characterising the axial displacement of the particle within the optical trap is considered.

4.4.1 Variation of Droplet Position with Droplet Size and Laser Power

The optical forces which act laterally to restore an aerosol droplet to its equilibrium trapping position have been previously studied through the use of in-plane imaging [28]. The restoring capability of the forces acting axially will now be examined through the use of side imaging.

4.4.1.1 Dependence on Droplet Size

Figure 4.4 shows the variation in the equilibrium trapping height of two droplets of different size, 5.10 μm (left) and 7.52 μm in radius, recorded under the same

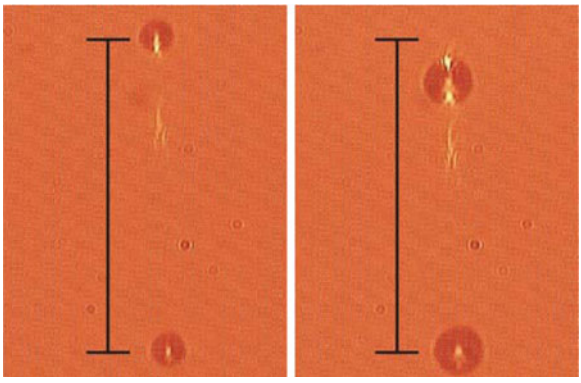

Fig. 4.4 Side images taken for two droplets of different size (5.10 μm (*left*) and 7.52 μm) trapped using the same laser power and imaged using the same zoom lens magnification

magnification and trapped at the same laser power. It is apparent from these two images that the smaller particle sits at a higher equilibrium height for a given laser power. This is behaviour which is not observed in condensed phase optical tweezers, suggesting that the optical trapping forces may exhibit considerable variation with particle size, laser power and trapping conditions in the case of aerosol tweezers. This will be discussed further in Sect. 4.5.2.

4.4.1.2 Dependence on Trapping Power

The axial position of the trapped particle has been found to exhibit a pronounced dependence on the laser power. Figure 4.5 shows the in-plane and side images for a droplet of radius 7.11 μm. In the side images shown in Fig. 4.5a–e, a guide of fixed length is placed level with the centre of the droplet reflection. As the laser power increases the droplet moves higher with respect to the coverslip and, as a consequence, the distance between the droplet and its reflection increases. This behaviour is not observed in condensed phase optical tweezers, where trapped particles are confined to the position of highest light intensity by the gradient force. The observation that the particle position depends on the laser power suggests that the increased scattering force arising with increased laser power is able to counteract the gravitational and gradient forces acting downwards on the particle, displacing the trapped droplet higher above the equilibrium trapping position. This assumes that the equilibrium trapping position of the particle is down-beam of the focus of the laser beam and thus vertically above it for this experimental arrangement [32]. The variation in the in-plane images shown in Fig. 4.5 is consistent with this change in trapping height, as detailed later.

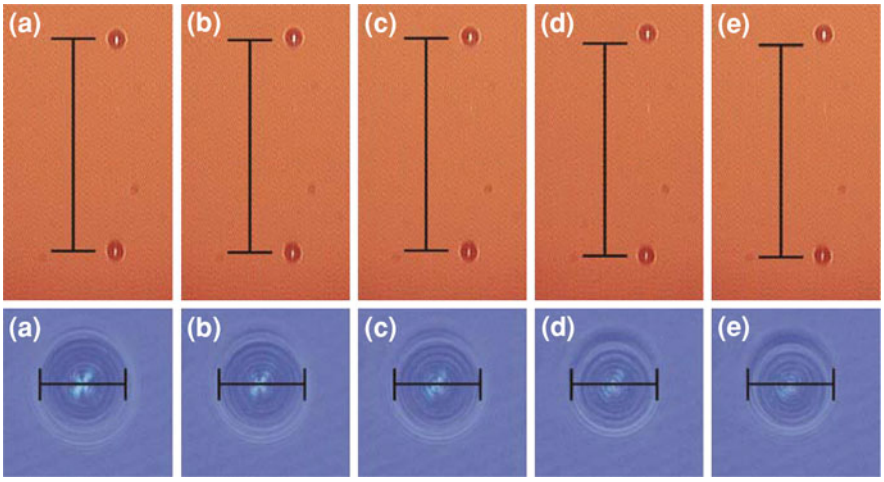

Fig. 4.5 Variation of side and in-plane images with laser power for a droplet of radius 7.11 μm. The images were recorded at the following laser powers: **a** 47 mW, **b** 58 mW, **c** 69 mW, **d** 83 mW, **e** 90 mW

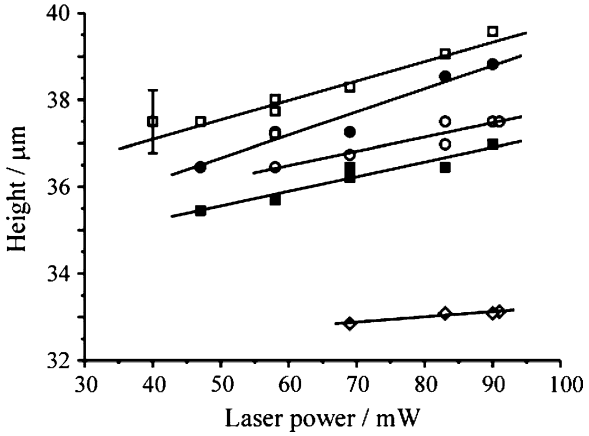

Fig. 4.6 Variation of droplet height with laser power for five droplets trapped consecutively. The droplet radii and power gradients, respectively, are: 6.61 μm and 0.045 μm mW^{-1} (*open squares*), 7.00 μm and 0.053 μm mW^{-1} (*filled circles*), 7.70 μm and 0.033 μm mW^{-1} (*open circles*), 7.08 μm and 0.034 μm mW^{-1} (*filled squares*), 8.39 μm and 0.012 μm mW^{-1} (*open diamonds*). The error in the height measurement is illustrated by an error bar for one data point. This is representative of the error for all points; further error bars have been omitted for clarity

The dependence of the equilibrium height of a trapped particle on laser power is shown in Fig. 4.6 for a selection of particles with radii in the range 6.6–8.4 μm. The error associated with determining the droplet height from the pixels of highest intensity at the centre of the droplet and droplet reflection is illustrated by an error bar for one data point. The general trend of these data supports the previous observation that the trapping height is inversely related to droplet size, but it should be noted that the order of two data sets (the 7.08 and 7.70 μm radius droplets) is reversed in sequence, reflecting the challenging nature of these measurements. Similar trends in the dependence of the axial displacement on laser power are observed for each of the droplets, with increased laser power leading to an increase in the height at which the droplet sits above the coverslip. This suggests that the scattering force plays a significant role in governing the axial position of the particle in aerosol optical tweezers.

All of the above observations are consistent with an axial trap which is dominated by the gradient force, but which is susceptible to the effects of the scattering and gravitational forces acting on the particle.

Figure 4.7 illustrates the trend observed in the power dependence for a single droplet evaporating from a larger to a smaller radius over a period of several hours. The droplet size is responding to a falling relative humidity in the trapping chamber in accordance with Köhler theory [42, 43]. By performing several power analyses of droplet position spread over several hours, a study of the effect of particle size can be carried out for a single trapped droplet. It can be seen that as the droplet evaporates to a smaller equilibrium size it sits higher for a given laser

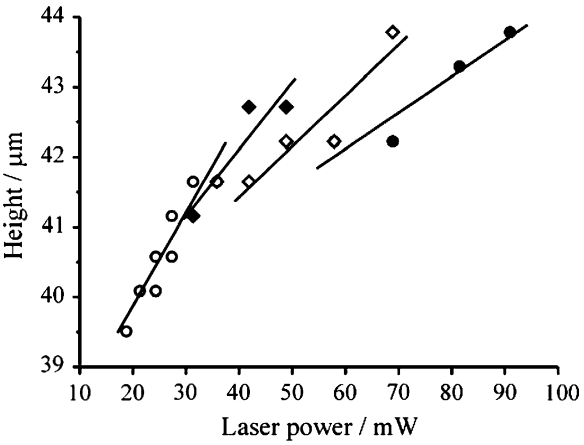

Fig. 4.7 Variation of droplet height with laser power for a single droplet of evolving size. The droplet radii are: 6.16 μm (*filled circles*), 5.81 μm (*open diamonds*), 5.38 μm (*filled diamonds*), 5.35 μm (*open circles*)

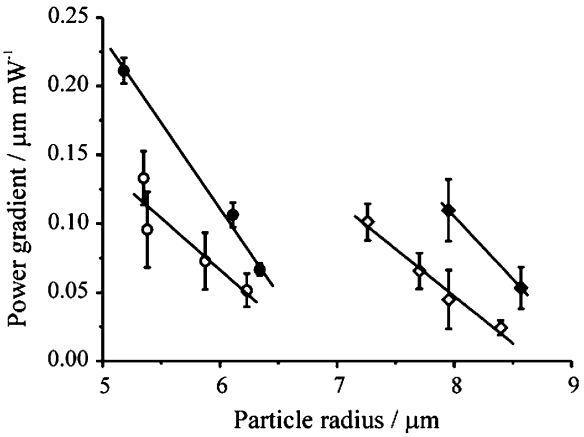

Fig. 4.8 Tracking the power gradient for four droplets as they evaporate with time. The data set represented by *open circles* is that illustrated in Fig. 4.7

power. Further, the gradient of the height as a function of laser power increases, referred to as the power gradient.

Variations in the power gradient recorded during several similar evaporative experiments for four different droplets are summarised in Fig. 4.8. Although there is considerable variation between individual droplets, the trend of increasing power gradient with decreasing droplet size is clear. This suggests that the power gradient may prove to be a promising method for monitoring evolving particle size.

The power gradients recorded for many particles ranging from 3 to 9 μm in radius are summarised in Fig. 4.9a. The error bars represent the error in the slope of the height as a function of laser power. From these data it is evident that the axial position of smaller particles responds more strongly to variations in laser power than the position of larger particles. It should be noted that the scattering force, which is a function of cross-sectional area, would be expected to vary by

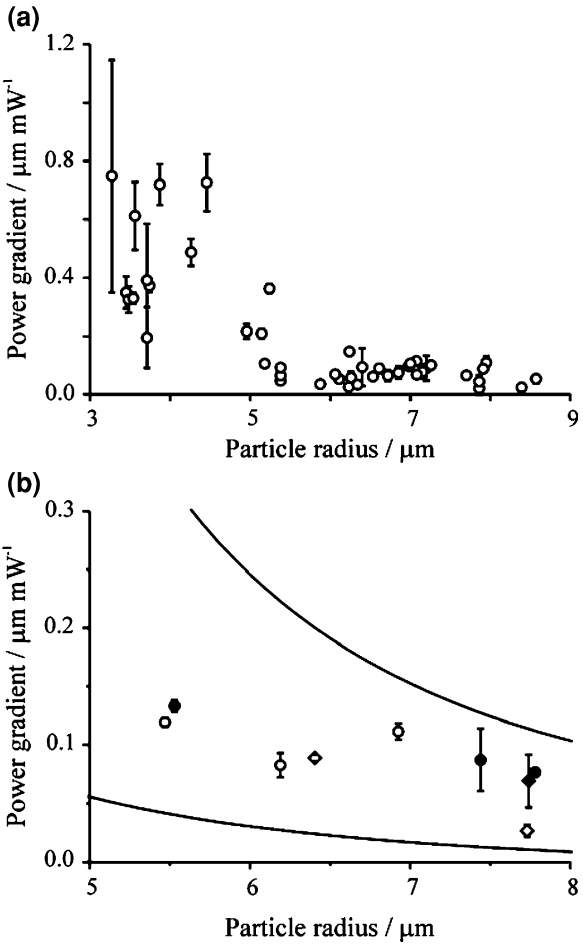

Fig. 4.9 **a** Variation in power gradient with droplet size. **b** Variation in power gradient with droplet size for droplets with enhanced NaCl concentrations: 40 g L^{-1} (*filled circles*), 60 g L^{-1} (*open circles*), 80 g L^{-1} (*filled diamonds*), 100 g L^{-1} (*open diamonds*). An envelope defined by *solid lines* represents the minimum and maximum power gradients for a given radius, derived from part **a**

approximately one order of magnitude, while the gravitational force, which is a function of droplet mass, will vary by a factor of $\sim$30 across this size range.

Although the variation in power gradient for any one droplet during evaporation is pronounced, as seen in Fig. 4.7, the scatter shown in Fig. 4.9a reflects the observation that there is considerable variation from droplet to droplet. One plausible reason for this may be variations in particle composition (salt concentration) and hence refractive index and mass. Such variations would lead to subtle variations in the interplay of the gradient, scattering and gravitational forces acting on a trapped particle.

To examine the effect of droplet composition on the power gradient, droplets were trapped from nebulised aqueous solutions with NaCl concentrations spanning the range 40–100 g L^{-1}. The results are illustrated in Fig. 4.9b. The data sets for elevated salt concentrations fall within the envelope for all particles reported in Fig. 4.9a and so it is apparent that there is no systematic relationship between

power gradient and the salt concentration of the solution initially nebulised. Even the maximum variation in refractive index and mass examined (0.96 and 5.4% respectively for 100 g L^{-1} NaCl droplets compared with 20 g L^{-1}) were not observed to cause a detectable change in the dependency of the power gradient on size within the accuracy of these experiments. However, as the relative humidity of the trapping chamber was not controlled during these experiments, a higher salt concentration corresponds to a larger equilibrium droplet size in accordance with Köhler theory. It is likely that this coarse change in mass due to a change in equilibrium size is likely to obscure these minor changes in refractive index and initial mass. The general shift in the aerosol size distribution to larger sizes with increased salt concentration at a given relative humidity makes it difficult to directly compare power gradient trends for different salt concentrations.

As well as affecting the trapping position, varying the laser power changes the amount of energy absorbed by a droplet and hence its temperature.[3] This means that the change in laser power does not occur in isolation and is fact accompanied by a change in droplet size and hence mass and refractive index. The droplet size change accompanying a trapping power change is on the order of one nm in radius per mW; an increase in laser power is accompanied by a decrease in the droplet size and vice versa. For a typical measurement this change in droplet size typically corresponds to a change in droplet mass of $<2\%$ and is not therefore expected to introduce significant error to the measurement.

4.4.2 Dependence of In-Plane Images on Droplet Height

It has been demonstrated that the height of a tweezed droplet is dependent on laser power and as a result there is also a power dependence associated with the in-plane droplet image. The focus and size of images collected using the achromatic microscope objective will be affected by the position of the droplet relative to the laser focus, as this is also the focus for collection of the image. This demonstrates that image-based methods for determining the size of tweezed aerosol particles are not robust and that a spectroscopic method, or at least a method which takes into account the power dependence of the image, should be employed. The error incurred through using the image can be as much as 30% within the power range that has been investigated. This is illustrated by Fig. 4.10, which shows two droplets simultaneously isolated using the dual trapping approach.[4] In the in-plane image the left-hand droplet appears to be 1.7 times larger than the right-hand droplet, but is actually only 1.4 times larger, determined by CERS. As has been shown, larger droplets sit lower, and hence closer to the focal plane of the collection optics, than smaller ones at the same laser power. There is therefore a

[3] This will be discussed in detail in Chap. 6.

[4] See Sect. 3.1 for a detailed description.

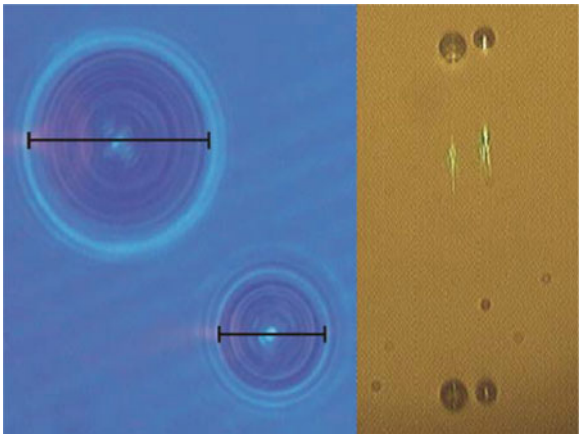

Fig. 4.10 Influence of droplet position on apparent size from in-plane image. The larger droplet (6.85 μm radius, the left-hand droplet in both images), is sitting lower than the smaller droplet (5.04 μm radius) hence its size is exaggerated in the in-plane image. Guides showing the dark part of the image taken to represent the droplet diameter are shown on the in-plane droplet images

systematic discrepancy between the true and apparent size from in-plane imaging which increases with decreasing particle size. This is also evident in Fig. 4.5a–e: as the laser power increases the droplet moves higher with respect to the coverslip and, as a consequence, the droplet appears to shrink when imaged in-plane, even though its true size does not change significantly. A guide of fixed length, indicating the dark part of the image taken to represent the diameter of the droplet in Fig. 4.5a, is centred on the droplet images in (b) to (e) to emphasise the change in apparent droplet size.

The observation in Fig. 4.10 of such a mismatch in the trapping height of two droplets of different size also explains the previous observation that two water droplets coagulate at a separation of less than the sum of the two droplet radii, as determined from the in-plane image [28]. Although such an observation could be consistent with a distortion in the shape of liquid droplets prior to coagulation, due to interparticle interactions as they approach, it is also possible that the droplets may reside at different axial positions in the two optical traps, a factor that is not readily addressed by examining a simple in-plane image. As suggested in this previous work, the observations here would support the conclusion that this arises from the coagulation of two droplets located at different axial trapping positions, a concern which must be accounted for when considering measurements of separation at coagulation inferred from the in-plane images.

4.4.3 A New Method for Sizing Optically-Tweezed Aerosol Droplets

The accurate characterisation of size is a challenge when working with microscopic particles [44]. The development of novel methods of particle sizing is thus an attractive experimental goal and the variation of the power gradient of

liquid aerosol particles described above represents a plausible method for achieving this. This is a welcome solution to the problem of sizing small or inhomogeneous droplets for which CERS cannot be applied [45]. As the spacing between cavity modes increases with decreasing particle size, CERS is difficult to apply to particles with a radius of less than 3 μm owing to the reduced number of cavity modes observable within a given spectral range. Further, CERS cannot be applied to inhomogeneous droplets, for example in phase segregated droplets.

A demonstration of the use of this method for sizing particles is now presented, using the data represented by open diamonds in Fig. 4.8. This data set represents a single trapped droplet, the power gradient of which was measured on four occasions during a 90-min period. The evolving particle size was monitored by CERS using spectra collected during the power gradient analyses and was found to decrease during this time, governed by the declining chamber relative humidity. The power gradient and size variations with time are given in Fig. 4.11a. As the particle radius decreases the associated power gradient increases, consistent with the previous observations. The relationship between power gradient and particle radius is shown in Fig. 4.11b.

The accuracy of using the power gradient to determine the particle radius is now considered. A line of best fit was applied to the region from 7 to 8.7 μm on Fig. 4.9a and the associated relationship used to predict the droplet radii from the measured power gradients. Figure 4.11c shows the correlation between the radii determined from the power gradient and the spectroscopically-determined radii. A solid line represents an exact match between true and predicted radius. Deviation from an exact match is in part caused by the scatter present on Fig. 4.9a, attributed to differences in particle composition and hence refractive index and mass.

A detailed understanding of the effect of particle composition will be required before this approach will represent a robust method for sizing optically-trapped particles. However, subject to the resolution of the effect of particle composition, this example clearly demonstrates that the approach has the potential to provide a useful method of particle sizing, particularly for smaller particles for which the power gradient is more sensitive to particle size.

4.5 Studies of Trapping Phenomena

The addition of the side-imaging capability to the experimental set-up has facilitated the observation of several interesting trapping phenomena. Aerosol coagulation has been observed in two orthogonal planes, and multiple stable trapping positions and optical binding have been observed for the first time in aerosol optical tweezers. These phenomena offer insights into the forces experienced by a trapped aerosol droplet.

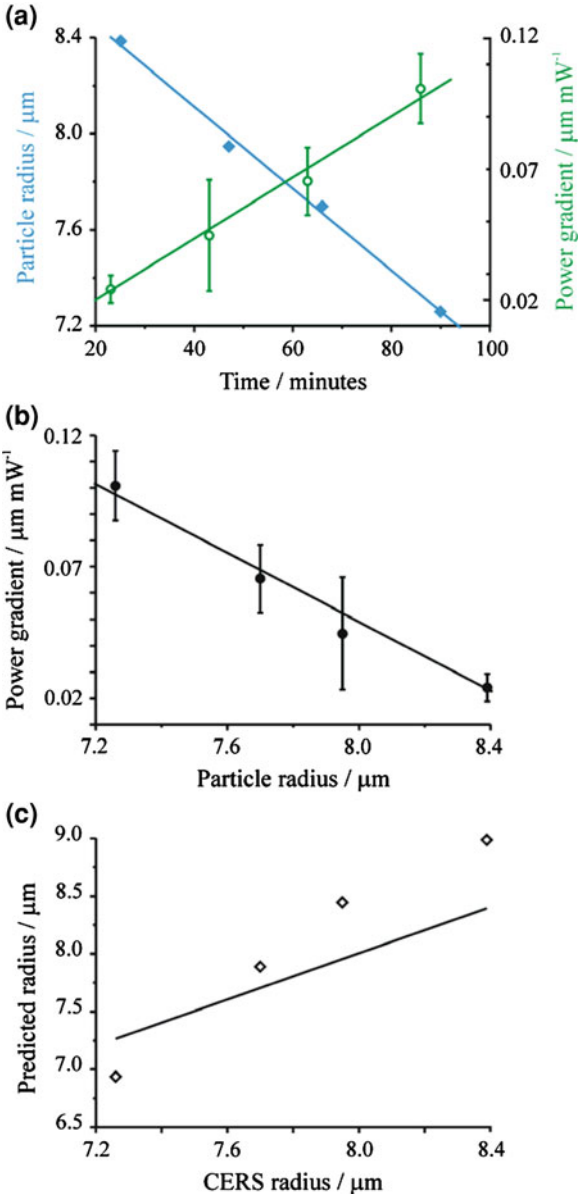

Fig. 4.11 **a** The time evolution of particle radius and power gradient. Particle radii are represented by *closed diamonds* and power gradients by *open circles*. **b** The variation of power gradient with particle radius. **c** The power gradient-predicted radii plotted as a function of the spectroscopically-determined radii. A *solid line* represents an exact match between the CERS and predicted radius. The differences between the CERS and predicted radius from smallest to largest particle are: −0.33, 0.18, 0.49, 0.61 μm

4.5.1 Aerosol Coagulation

Aerosol coagulation has been observed for a pair of aqueous droplets in two orthogonal planes, as shown in video Clip 1 (see supplementary material) and illustrated in Fig. 4.12. Coagulation is achieved by translating the droplets in the

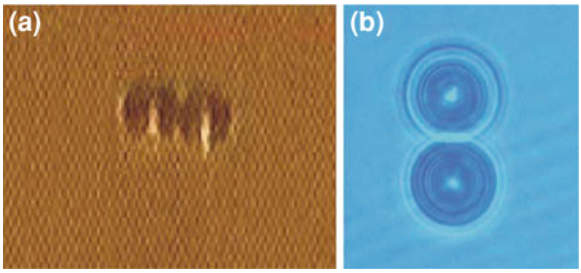

Fig. 4.12 Coagulation imaged in two orthogonal planes; **a** from the side and **b** in-plane. The images were taken one frame before coagulation

plane of the optical trap using the gimbal-mounted mirrors. This has proved useful in rationalising the earlier observation that coagulation can take place at separations (measured using the in-plane image) which are smaller than the sum of the two spectroscopically-determined radii [28]. Viewing coagulation from the side confirms that in the case of aqueous droplets this observation is not the result of particle deformations resulting from interparticle interactions, but is in fact consistent with the particles not being aligned in the same z-plane. This introduces significant error in the determination of the droplet separation from the in-plane image. This highlights the importance of being able to observe droplets in two orthogonal planes as it allows the height of the droplets concerned to be equalised, or at least known, before proceeding with studies of coagulation or particle interactions. This will be important for future studies of droplet coagulation or interparticle interactions.

The droplet coagulation event is observed to occur during a single video frame, and hence the process has been shown to occur on a timescale of <0.03 s.

4.5.2 Multiple Stable Trapping Positions

It has been observed that two stable trapping positions exist along the axis of the laser beam for a droplet trapped at a given laser power, typically separated by several microns. Images of the same droplet of radius 3.86 μm residing in two stable trapping positions, separated by 3.8 ± 0.2 μm, are shown in Fig. 4.13.

This is the first time bistability of trapping position has been observed for optically-tweezed aerosol droplets. This behaviour has previously only been predicted and observed in the case of condensed phase optical tweezers [21]. The existence of more than one stable trapping position is an effect of spherical aberration on the laser focus. A different form of bistability has previously been observed in a fibre trap for polystyrene beads immersed in water [46]. In a fibre trap two weakly-focussed laser beams are arranged horizontally such that they counter-propagate; the separation between the focal positions is typically chosen to be several hundred μm. Particles become trapped in the region between the two laser beam foci. Gradient forces operate to confine the particles to the axis of the laser beams but, compared with optical tweezers, scattering forces play a more

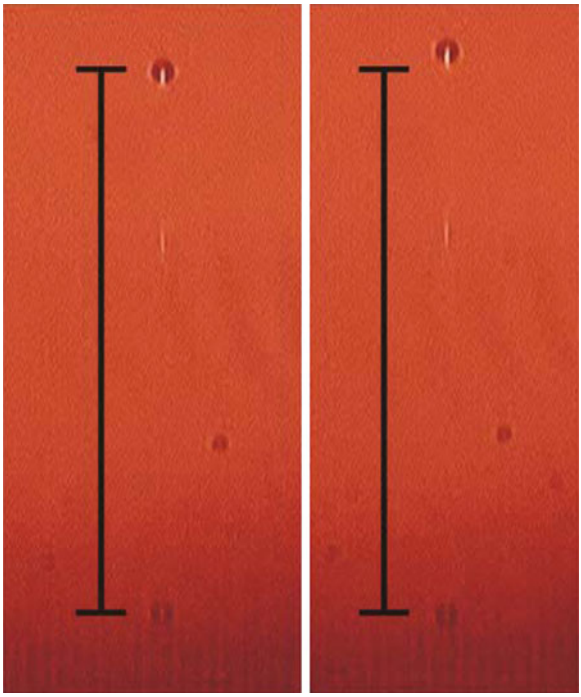

Fig. 4.13 Two stable positions for a droplet of radius 3.86 μm, separated by 3.8 ± 0.2 μm. The laser power is ~35 mW. The centres of the reflections have been set to the same vertical level. A guide of fixed length has been added to the images

significant role and the counter-propagating arrangement of the beams is necessary to maintain the particles at a fixed horizontal position. In this example of bistability the two stable trapping positions are associated with the focal regions of each of the two beams. In the work presented here the existence of more than one stable trapping position associated with a single laser focus is observed.

While most trapped droplets remain trapped in the same axial position for a given trapping power, droplets have at times been observed to spontaneously move between these stable trapping positions. It has been observed that for a given droplet there will be a particular trapping power at which the droplet will move between the two positions; for droplets which do not spontaneously move, by adjusting the trapping power a power at which this will occur can be found. On some occasions a single hop is observed, while on other occasions droplets have been observed to oscillate continuously between the two trapping positions. Examples of a single hop and oscillating droplet motion may be viewed in Clips 2 and 3, respectively. In Clip 3 there is a second trapped droplet which does not change trapping position. The corresponding in-plane video associated with Clip 3 can be viewed as Clip 4, which shows the apparent size of one of the droplets changing as its distance from the collection optics varies.

Typical examples of axial separations between the stable hopping positions include separations of 3.8 ± 0.2 and 3.6 ± 0.2 μm for droplets of radii 3.86 and 5.47 μm respectively. These correspond to separations of ~ 1 and 0.7 droplet radii

respectively. No systematic dependence of the interparticle separation on droplet size or trapping power has been observed. The separation of the two positions will depend on the degree of spherical aberration; a more detailed study is required to quantify the effect of this variable.

Continuous oscillation of droplets between the stable trapping positions occurs at a range of frequencies. The frequency of such oscillation, or droplet 'hopping', ranges from $\sim$0.5 to several Hz. The frequency of oscillation has been observed to vary for a given droplet, as shown in Clip 5 and the associated in-plane video available as Clip 6. In this case the frequency of oscillation increased with time and eventually the droplet became destabilised and was lost from the trap. This can be attributed to the lateral stability in the trap being insufficient to maintain the moving droplet in the beam axis.

In some cases a hopping droplet settles into one of the available trapping positions, for example the droplets in Clips 7 and 8 for which the droplets, of radii 3.54 and 5.47 μm respectively, settle in the upper of the two available trapping positions. Clip 9 is the in-plane video for the droplet in Clip 8. In Clip 2, which shows a single 'hop', the droplet settles in the lower trapping position. This suggests that the positions are of unequal stability, an observation supported by the modelling studies of condensed phase trapping by Viana et al. [21].

The equilibrium positions can be considered as two longitudinal potential wells, with the movement of the droplet between them being associated with the Brownian motion of the droplets within the wells [21]. The droplet will remain in a given potential well until its thermal motion enables it to escape. This explains why the trapping power is important for observing this phenomenon; it will determine the depth of the potential wells, which need to be deep enough to stably trap the droplet, but shallow enough that thermally-activated escape from a potential well is statistically likely at the temperatures at which the droplets are trapped. A theoretical framework for thermally-activated escape from potential wells was first developed by Kramers in 1940, resulting in his theory for transition rates [48]. The theory relates the frequency of oscillation between two bound states to the form of the potential wells of the states. Recently McCann et al. used condensed phase dual optical tweezers, separated by $\sim$0.5 μm, as a quantitative test for Kramers' theory of transition rates [49]. The frequency of the motion of silica microspheres between the two traps was analysed and found to be in excellent agreement with the theory. The experiment allowed the form of the three-dimensional potential mapped out by the two traps to be determined.

The motion of droplets between potential wells within the same gradient force trap, as observed here, can in principle be used in the same way to map out the potential surface of aerosol optical tweezers. The average residence time in a trap, t, is given by [50]:

$$t = t_0 \exp\left(\frac{U}{k_B T}\right) \tag{4.1}$$

where U is the potential well depth, k_B is the Boltzmann constant, T is the temperature and t_0 is given by:

$$t_0 = \frac{6\pi\rho_a r}{m_d \omega^2} \tag{4.2}$$

where ρ_a is the dynamic viscosity of air, r and m_d are the droplet radius and mass, respectively and ω is the natural frequency of the trap. The axial hopping frequencies observed can hence be used to estimate U in the axial direction for the trapping positions. While ω for these traps has not been measured, a typical value for micron-sized droplets trapped in air is $\sim$2 kHz [26]. For a typical droplet of radius 4 μm, the observed hopping frequency range of 3–0.5 Hz corresponds to a well depth of $U/k_BT = 5$–7. This is of the same order of magnitude as values for U/k_BT of 4.1–5.8 and 2.8–3.5 which have previously been reported for silica spheres trapped in water using a fibre trap and a dual optical trapping arrangement, respectively [48, 49]. Direct comparison with these values is not possible, however, as they refer to U in the lateral direction and because the refractive index contrast between the particles and the surrounding medium is different in the various experiments, affecting the trapping forces. To my knowledge a value of U relevant for the axial direction has not previously been reported for optical tweezers.

Using a model provided by collaborators at the University of Dundee it has been possible to predict the existence of multiple stable trapping positions in aerosol tweezers [26]. This model is an MDSA approach which includes the effect of the aqueous layer as a further refractive index step. The commented MathCad code of the model is provided in Appendix III. Taking as an example the droplet of radius 3.86 μm which is shown in Fig. 4.13, the force acting on the droplet as a function of axial displacement from the laser focus has been modelled and is shown in Fig. 4.14. The calculations were performed for droplet refractive indices of 1.34, 1.36 and 1.38, shown in black, blue and green, respectively. The trapping

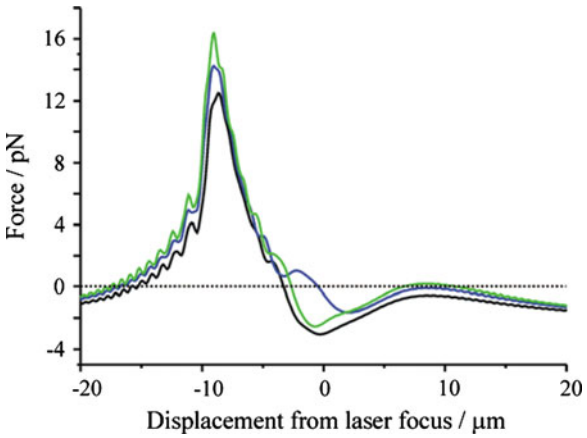

Fig. 4.14 The force acting on a trapped droplet of radius 3.86 μm as a function of displacement from the laser focus, modelled for droplet refractive indices of 1.34, 1.36 and 1.38, shown in *black, blue* and *green*, respectively

power was measured to be 12.5 mW, while the aqueous layer is assumed to have a composition equal to that of the nebulised solution, 20 g L^{-1} NaCl, and a thickness of 10 μm. Stable trapping positions occur at displacements for which the force curve crosses the Force = 0 axis, shown with a dotted line, with a negative gradient.

It can be seen that the location of the stable trapping positions, and the occurrence of multiple stable positions, is sensitive to the droplet composition. For the droplet compositions included in Fig. 4.14, only for a droplet refractive index of 1.38 are two stable trapping positions predicted, separated by 13.4 μm, although the second is very weak, evident from the shallow gradient of the force curve as it crosses the Force = 0 axis. The two positions are situated either side of the laser focal plane. If, however, a finer variation in refractive index is examined, quite different results are obtained. Figure 4.15 shows the modelled force acting on a droplet of the same radius but with refractive indices of 1.3640, 1.3645 and 1.3650, shown in black, blue and green, respectively. It can be seen that two stable trapping positions exist for a refractive index of 1.3645, separated by 2.0 μm.

While a separation of 2.0 μm is close to the experimentally-observed separation of 3.8 ± 0.2 μm, the droplet refractive index required to model this represents a droplet concentration of 190 g L^{-1} NaCl. This droplet is expected to have a concentration of ~80 g L^{-1} NaCl. This discrepancy can be attributed to uncertainty in other quantities necessary to model the forces. The calculation is highly sensitive to the trapping power, the size of the trapped droplet and the thickness and composition of the aqueous layer. The sensitivity of the stable trapping positions to the thickness of the aqueous layer is illustrated by Fig. 4.16, which shows modelled trapping forces for the droplet with a refractive index of 1.3645 from Fig. 4.15 for layer thicknesses ranging from 2 to 20 μm. The separation between the trapping positions varies from 1.9 to 2.1 μm for layer thicknesses of 5 to 15 μm, and it can be seen that for layer thicknesses of 2 and 20 μm only a single stable trapping position is predicted in this region. The thickness and composition of the aqueous layer are not constant and are difficult to determine experimentally,

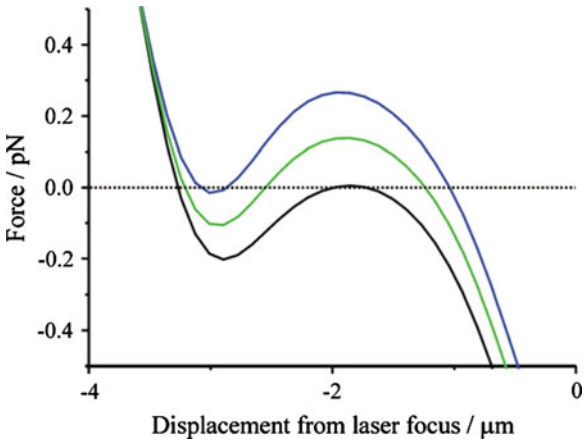

Fig. 4.15 The force acting on a trapped droplet of radius 3.86 μm as a function of displacement from the laser focus, modelled for droplet refractive indices of 1.3640, 1.3645 and 1.3650, shown in *black, blue* and *green*, respectively

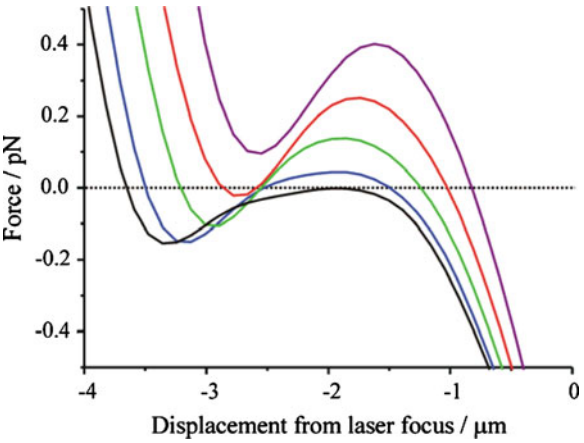

Fig. 4.16 The force acting on a trapped droplet of radius 3.86 μm as a function of displacement from the laser focus, modelled for a droplet refractive index of 1.3645 and for an aqueous layer with a composition of 20 g L^{-1} NaCl and with a thicknesses of 2, 5, 10, 15 and 20 μm shown in *black, blue, green, red* and *purple*, respectively

and as a result, while it is interesting to note that multiple stable positions can be predicted for certain experimental conditions, the determination of absolute trapping positions from theory is difficult.

The existence of more than one stable trapping position, and the potential for a trapped droplet to move rapidly between them, will have an impact on studies for which the droplet height is important, for example those relying on the position of a trapped droplet relative to collection optics and other trapped droplets.

4.5.3 Optical Binding

Interparticle forces have been observed to exist between polarisable particles exposed to a light field, a phenomenon termed optical binding. Optical binding and the creation of associated 'optical matter' is interesting from a number of perspectives. The use of optical matter as a theoretical and experimental model for the organisation of atoms, molecules and colloids into extended structures is an emerging field and is likely to prove useful in understanding processes such as phase transitions [50]. Optical binding forces also have the potential to be used for the nanoscale manipulation of matter, for example the construction of microscopic structures from nanoscopic building blocks. The ease and precision of controlling the light field used to build the structures is expected to allow complex structures to be built [50]. Crystals of microscopic species could also be constructed as a model for molecular crystals. In the condensed phase it would be possible to fix the microstructures by freezing or curing the medium in which the particles are suspended. The future possibility of building 'optical molecules' from atoms has also been suggested [49].

The work presented here represents the first observation of optical binding in aerosol optical tweezers. The binding observed is longitudinal, acting along the

axis of the trapping beam. Optical binding of this type is of significant interest in that, for example, aerosol droplets can provide a model for the self-assembly of deformable particles. In contrast to condensed phase studies, aerosol optical binding offers the possibility to study interparticle forces in the under-damped environment. Further, the increased refractive index contrast between the particles and the surrounding medium in the aerosol phase gives rise to stronger interparticle interactions. In the future closely associated pairs of droplets could be used to study the effect of neighbouring droplets on rates of gas-phase diffusion to droplets, a subject of ongoing debate.[5] Chains of bound droplets could also provide a model for droplet train experiments.

4.5.3.1 Previous Studies

Optical binding was first observed by Golovchenko and co-workers for pairs of plastic microspheres immersed in water in the presence of a single laser beam [51]. A simple diffraction grating was used to split a loosely-focussed beam into several parallel beams and as a result the plastic microspheres were observed to arrange themselves at discreet separations transversely across the axis of the laser beam. The optical traps did not result in three-dimensional confinement of the particles; instead the trapped particles were accelerated by radiation pressure until they reached the wall of the trapping chamber where they were held in position. That the particles were optically-bound was shown from the diffusive motion of the beads, which was found to be concerted. Further, the particles were separated by discrete distances, often integer multiples of the wavelength of the trapping light.

Related work, also led by Golovchenko, used more complicated diffraction gratings to split and re-form the light beam into multiple beams, creating, for example, cubic close-packed arrangements of trapping beams [50]. As expected this created two-dimensional cubic close-packed arrangements of the microspheres. The optical binding interaction became apparent from the observation that after around ten spheres had become trapped, crystal-faceting and motion of the spheres occurred. Microspheres trapped near the periphery of the 'optical crystal' were seen to move towards the centre of the close-packed arrangement. This demonstrated that the spheres were not only interacting with incident light field but also with the light scattered by the particles already bound.

While Golovchenko observed binding perpendicular to the incident light beam, longitudinal optical binding along the axis of the trapping beam has been reported by Dholakia and co-workers for fibre trapping using two counter-propagating laser beams in the condensed phase in the case of silica spheres in water [49]. The effect has also been successfully modelled [52]. The experimental work observed the trapping of multiple particles in the trapping region, separated by 48 μm, a much greater distance than those over which electrostatic forces act, implying that the

[5] As discussed in Sect. 2.2.6.

binding is optical in origin. The trapping of multiple particles results from the refocusing of the laser beam by a trapped particle. This creates a further trapping region in the path of the laser beam and a series of equidistantly separated particles can therefore be trapped, resulting in an optically-coupled chain of particles. Similar behaviour was observed by Singer et al.; chains of equidistantly-separated particles were observed for beads smaller than the laser wavelength, while it was found that beads which were considerably larger than the laser wavelength formed axial 'stacks' with the particles in contact with each other [53]. The interparticle distance in the separated chains was found to increase with increasing bead diameter.

Optical binding was first observed in the aerosol phase for pairs of oil droplets trapped in air, again using a fibre trap consisting of two counter-propagating weakly-focussed Gaussian laser beams [54]. The inter-particle separation was found to take discrete values which are multiples of half the laser wavelength. In later work a chain of three separated oil droplets was successfully created using this method [56]. In the earlier work it was reasoned that the multiple trapping positions were associated with the interference pattern arising from the interaction of the two counter-propagating laser beams. Theoretical multiple scattering calculations supporting this reasoning were presented [54, 56]. This rationale has, however, been disputed and it has been suggested that the droplet binding is in fact due to refocusing of a laser beam by trapped particles, resulting in a further gradient force trap [57], as observed by Dholakia and co-workers.

In the case of single-beam optical traps, studies of the assembly of optical structures have been limited to the related phenomenon of optical stacking in the condensed phase. In this approach a laser beam is focussed just above the top surface of a sample chamber, creating a cone of light extending to the lower surface of the chamber [58]. Particles which enter the cone of light will be directed to the top of the chamber by radiation pressure, where they will be held against the chamber roof. This approach does not constitute three-dimensional optical confinement of the particles as is the case for optical tweezers. A further particle entering the cone of light will be guided towards the first trapped particle and once it has made contact with this particle it will come to rest. This process

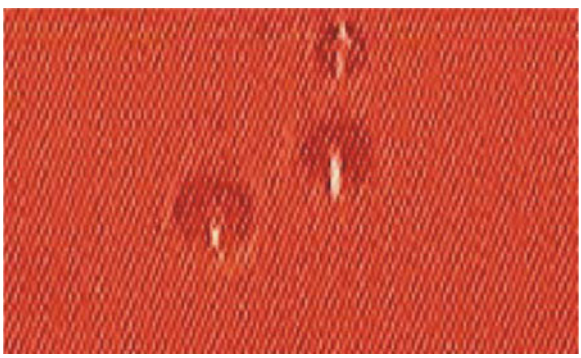

Fig. 4.17 Optical binding of two aqueous aerosol droplets in optical tweezers

will continue, building up an optical 'stack' of particles. This method has been used to collect Raman spectra from stacks of red blood cells [59]. Creating a well-defined collection of particles boosts signal-to-noise ratios and it has been reasoned that this may prove useful for characterising groups of cells, for example tumour cells.

4.5.3.2 Results and Discussion

Pairs of water droplets have been observed to become optically bound using a single-beam gradient force trap. This behaviour can be viewed in Clip 10. Figure 4.17 shows a single frame taken from this clip. The image shows two droplets trapped in the normal manner, referred to as primary droplets, with a secondary, optically-bound droplet down-beam of the right-hand droplet and separated from the primary droplet by ~ 17 μm. Trapping a secondary droplet is not a controlled procedure; it relies on a droplet entering the appropriate region with a low enough speed to become trapped.

This behaviour can be explained by refocusing of the trapping beam by a primary droplet, which will act as a lens for the trapping beam, creating a second gradient force trap, as introduced above.

In the small-angle approximation the focussing length, f, of a spherical droplet of radius r is given by [60]:

$$f = \frac{r}{2\Delta m} \tag{4.3}$$

where Δm is the difference between the refractive indices of the droplet and the surrounding medium. For a 20 g L^{-1} NaCl droplet of radius 5 μm trapped in air this gives a focussing length of 7 μm, which is in reasonable agreement with the droplet separations observed in this work.

The observation described here of multiple trapping in the presence of a single beam suggests that refocusing could indeed be the cause for the multiple trapping observed by Stout and co-workers, rather than an interference effect as they suggest [54].

Trapping of a secondary droplet does not occur very often, and the droplets are less-stably trapped, remaining in the trap for only a few minutes. Moreover, the secondary droplets observed are smaller in size than the primary droplets. These observations are consistent with the trapping efficiency of the secondary trap being lower than that of the primary trap. This is expected, as refocusing of the trapping beam by the primary droplet will result in a looser focus than that created by the microscope objective.

It is expected that the secondary droplet will also act to refocus the light with which it is trapped, creating a further gradient force trap. The trapping efficiency of a tertiary trap such as this would, however, be reduced even further than that of the secondary trap, which explains why third-bound droplets are not observed.

4.5.3.3 Bistability in Optical Binding

Bistability in the axial separation of the two bound droplets has been observed and can be viewed in Clip 10. The secondary droplet can be seen to 'hop' between two stable positions, the difference in the two separations being ~ 3 μm. The two positions are illustrated in Fig. 4.18, which consists of snapshots taken from Clip 10. This observation is consistent with the spherical aberration in the primary trap, which gives rise to the bistability in this trap, resulting in spherical aberration in the secondary trap.

The bistability confirms that the secondary trap is a gradient force trap formed by the refocusing of light and not simply the result of radiation pressure. Bistability has previously been observed in the separation between two bound particles in a counter-propagating fibre trap [60]. In that work it was attributed to feedback between the bound spheres, in that changing the separation of the spheres alters the electromagnetic field distribution and hence the forces between them.

Towards the end of Clip 10 the secondary droplet can be seen to be pulled off-axis, presumably as a result of air currents in the trapping chamber. The primary droplets are not displaced, indicating that the secondary trap is of lower lateral stiffness than the first.

The effect of laser refocusing by trapped particles has been beautifully visualised by Dholakia and co-workers [60]. Microspheres were immersed in an aqueous solution in which fluorescein dye had been dissolved and by using a femtosecond pulsed laser as the trapping beam the refocusing of light by the microspheres was observed via the patterns of fluorescence of the dye. The effect was visualised for the cases of one to four bound microspheres in a fibre trap with two counter-propagating beams. The results are summarised in Fig. 4.19, which has been adapted from Figs. 3 and 4 of Ref. [60]. Images labelled (a) are theoretically-predicted light distributions, while those labelled (b) are false-colour images of the observed fluorescence patterns. In images 1 and 2 one of the counter-propagating beams is blocked; in image 1 the particle is held stationary by optical tweezers in a perpendicular axis to the fibre beam, while in image 2 the particles were free to move and hence are accelerating in the direction of beam propagation at the time this image was recorded.

Fig. 4.18 Observation of axial bistability in the optical binding of two aqueous aerosol droplets in optical tweezers

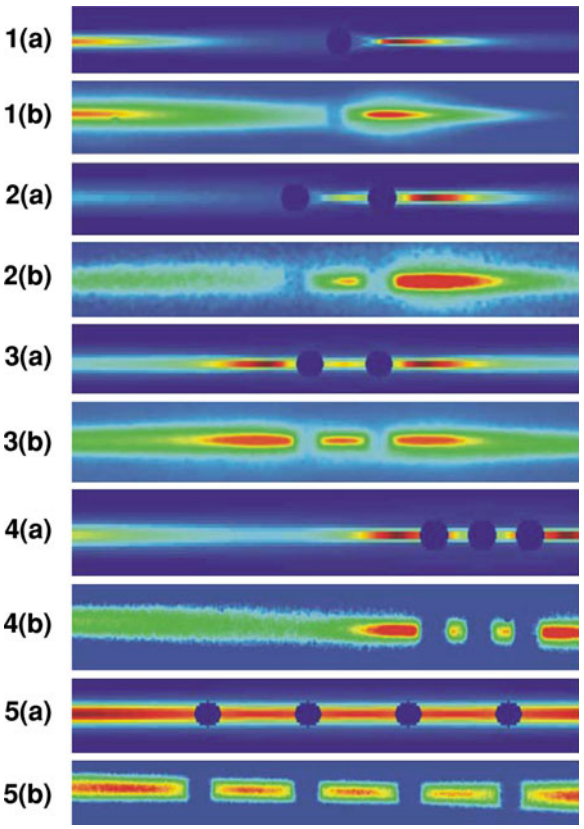

Fig. 4.19 Images taken with permission from Figs. 3 and 4 of Ref. [60]. Images labelled (**a**) are theoretically-predicted light distributions, while those labelled (**b**) are false-colour representations of the observed fluorescence patterns. In images 1 and 2 one of the counter-propagating beams is blocked. Images 3–5 involve the binding of two, three and four microspheres, respectively, for counter-propagating beams

In these studies stronger refocusing was observed for larger Δm, which may explain why optical binding has not previously been observed in condensed phase optical tweezers. Aerosol tweezers benefit from a larger Δm than those in the condensed phase, for example Δm for water droplets in air is 0.33, compared with 0.22 for a typical polymer bead trapped in water.

Equivalent visualisation in the aerosol phase is possible by tracing the movement of particles in the region of the trapping beam in order to infer the optical forces that are operating and hence trace out the light distributions. Two preliminary examples of droplet movement close to the trapping region may be viewed in Clips 11 and 12. Clip 11 shows a droplet approaching an optical trap from the side, where it is accelerated upwards. It then falls under gravity and the process is repeated. Clip 12 shows the optical binding of two droplets trapped in scattered light close to the coverslip, to the side of the main trapping beam. Tracking the movement of particles in and close to the trapping region offers the possibility to trace out the light distributions present in aerosol optical tweezers.

Currently no method exists to model such optical binding in optical tweezers and this represents a future direction of theoretical work being carried out at by

collaborators at the University of Dundee. Calculations have, however, been performed for optically-bound particles within the same [61] and different [62] rings of Laguerre–Gaussian beams.

4.6 Summary

Optical tweezing provides a valuable new tool for characterising the properties of aerosols. These studies have examined in detail the dependence of the axial position of the trapped particle on laser power and particle size through the addition of a side-imaging capability. With an increase in laser power, the trapped particle resides in an equilibrium position further displaced above the laser focus. Similarly, smaller droplets reside further above the laser focus than large droplets. The systematic dependence of the axial position on particle size and laser power provides a new method for determining the size of a trapped particle through the measurement of the power gradient. Bistability in the trapping position and optical binding have been observed for the first time in aerosol optical tweezers. These studies have significance both for the rigorous interpretation of data obtained using aerosol studies optical tweezers and for the modelling of optical traps.

References

1. A. Ashkin, Phys. Rev. Lett. **24**, 156 (1970)
2. A. Ashkin, J.M. Dziedzic, J.E. Bjorkholm, S. Chu, Opt. Lett. **11**, 288 (1986)
3. D.G. Grier, Nature **424**, 810 (2003)
4. M. Andersson, O. Axner, B.E. Uhlin, E. Fällman, Proc. Soc. Photo Opt. Instrum. Eng. **6326**, 489 (2006)
5. M. Andersson, O. Axner, F. Almqvist, B.E. Uhlin, E. Fällman, ChemPhysChem **9**, 221 (2008)
6. A. Ashkin, J.M. Dziedzic, Science **187**, 1073 (1975)
7. R. Omori, T. Kobayashi, A. Suzuki, Opt. Lett. **22**, 816 (1997)
8. N. Magome, M.I. Kohira, E. Hayata, S. Mukai, K. Yoshikawa, J. Phys. Chem. B **107**, 3988 (2003)
9. M.D. King, K.C. Thompson, A.D. Ward, J. Am. Chem. Soc. **126**, 16710 (2004)
10. R.J. Hopkins, L. Mitchem, A.D. Ward, J.P. Reid, Phys. Chem. Chem. Phys. **6**, 4924 (2004)
11. D.R. Burnham, D. McGloin, Opt. Exp. **14**, 4175 (2006)
12. K. Svoboda, S.M. Block, Annu. Rev. Biophys. Biomol. Struct. **23**, 247 (1994)
13. J.E. Molloy, M.J. Padgett, Contemp. Phys. **43**, 241 (2002)
14. A. Rohrbach, Opt. Exp. **13**, 9695 (2005)
15. G. Knoner, S. Parkin, T.A. Nieminen, N.R. Heckenberg, H. Rubinsztein-Dunlop, Phys. Rev. Lett. **97**, 157402 (2006)
16. A. Ashkin, Biophys. J. **61**, 569 (1992)
17. N.B. Viana, A. Mazolli, P.A.M. Neto, H.M. Nussenzveig, M.S. Rocha, O.N. Mesquita, Appl. Phys. Lett. **88**, 131110 (2006)
18. D.R. Burnham, *School of Physics and Astronomy* (University of St. Andrews, St. Andrews, 2007). (Personal communication)

19. T. Tlusty, A. Meller, R. Bar-Ziv, Phys. Rev. Lett. **81**, 1738 (1998)
20. K. Svoboda, S.M. Block, Annu. Rev. Biophys. Biomol. Struct. **23**, 247 (1994)
21. N.B. Viana, M.S. Rocha, O.N. Mesquita, A. Mazolli, P.A.M. Neto, H.M. Nussenzveig, Phys. Rev. E **75**, 021914 (2007)
22. W.H. Wright, G.J. Sonek, M.W. Berns, Appl. Opt. **33**, 1735 (1994)
23. P.A.M. Neto, H.M. Nussenzveig, Europhys. Lett. **50**, 702 (2000)
24. A. Mazolli, P.A.M. Neto, H.M. Nussenzveig, Proc. R. Soc. Lond. Ser. A Math. Phys. Eng. Sci. **459**, 3021 (2003)
25. P. Török, P. Varga, Z. Laczik, G.R. Booker, J. Opt. Soc. Am. A Opt. Image Sci. Vis. **12**, 1605 (1995)
26. D. R. Burnham, Ph.D. thesis: Microscopic Applications of Holographic Beam Shaping and Studies of Optically Trapped Aerosols, University of St. Andrews, St. Andrews, 2009
27. K.J. Knox, J.P. Reid, K.L. Hanford, A.J. Hudson, L. Mitchem, J. Opt. A Pure Appl. Opt. (Special Issue: Opt. Manipulation) **9**, 180 (2007)
28. J. Buajarern, L. Mitchem, A.D. Ward, N.H. Nahler, D. McGloin, J.P. Reid, J. Chem. Phys. **125**, 114506 (2006)
29. K.J. Knox, D.R. Burnham, L.I. McCann, S.L. Murphy, D. McGloin, J.P. Reid, J. Opt. Soc. Am. B Opt. Phys. **27**, 582 (2010)
30. A. Pralle, M. Prummer, E.L. Florin, E.H.K. Stelzer, J.K.H. Horber, Microsc. Res. Tech. **44**, 378 (1999)
31. A. Rohrbach, E.H.K. Stelzer, J. Appl. Phys. **91**, 5474 (2002)
32. C. Deufel, M.D. Wang, Biophys. J. **90**, 657 (2006)
33. M.E.J. Friese, H. Rubinsztein-Dunlop, N.R. Heckenberg, E.W. Dearden, Appl. Opt. **35**, 7112 (1996)
34. M.E.J. Friese, A.G. Truscott, H. Rubinsztein-Dunlop, N.R. Heckenberg, Appl. Opt. **38**, 6597 (1999)
35. E.L. Florin, J.K.H. Horber, E.H.K. Stelzer, Appl. Phys. Lett. **69**, 446 (1996)
36. B.H. Lin, J. Yu, S.A. Rice, Phys. Rev. E **62**, 3909 (2000)
37. B.H. Lin, J. Yu, S.A. Rice, Colloids Surf. A Physicochem. Eng. Asp. **174**, 121 (2000)
38. P.J. Rodrigo, V.R. Daria, J. Glückstad, Opt. Lett. **29**, 2270 (2004)
39. J.H. Bao, Y.M. Li, L.R. Lou, Z. Wang, J. Opt. A Pure Appl. Opt. **7**, 76 (2005)
40. E. Fällman, O. Axner, Appl. Opt. **36**, 2107 (1997)
41. M. Goksör, J. Enger, D. Hanstorp, Appl. Opt. **43**, 4831 (2004)
42. J.H. Seinfeld, S.N. Pandis, *Atmospheric Chemistry and Physics: From Air Pollution to Climate Change* (Wiley, New York, 1998)
43. G. McFiggans et al., Atmos. Chem. Phys. Discuss. **5**, 8507 (2005)
44. J.R. Butler, J.B. Wills, L. Mitchem, D.R. Burnham, D. McGloin, J.P. Reid, Lab Chip **9**, 521 (2009)
45. L. Mitchem, J. Buajarern, A.D. Ward, J.P. Reid, J. Phys. Chem. B **110**, 13700 (2006)
46. E.R. Lyons, G.J. Sonek, Appl. Phys. Lett. **66**, 1584 (1995)
47. H.A. Kramers, Physica **7**, 284 (1940)
48. L.I. McCann, M. Dykman, B. Golding, Nature **402**, 785 (1999)
49. S.A. Tatarkova, A.E. Carruthers, K. Dholakia, Phys. Rev. Lett. **89**, 283901 (2002)
50. M.M. Burns, J.M. Fournier, J.A. Golovchenko, Science **249**, 749 (1990)
51. M.M. Burns, J.M. Fournier, J.A. Golovchenko, Phys. Rev. Lett. **63**, 1233 (1989)
52. D. McGloin, A.E. Carruthers, K. Dholakia, E.M. Wright, Phys. Rev. E **69**, 021403 (2004)
53. W. Singer, M. Frick, S. Bernet, M. Ritsch-Marte, J. Opt. Soc. Am. B Opt. Phys. **20**, 1568 (2003)
54. M. Guillon, O. Moine, B. Stout, Phys. Rev. Lett. **96**, 143902 (2006)
55. M. Guillon, B. Stout, Phys. Rev. A **77**, 023806 (2008)
56. M. Guillon, B. Stout, O. Moine, Phys. Rev. Lett. **100**, 199404 (2008)
57. S.Y. Liu, J.T. Yu, Phys. Rev. Lett. **100**, 199403 (2008)
58. M.P. MacDonald, L. Paterson, K. Volke-Sepulveda, J. Arlt, W. Sibbett, K. Dholakia, Science **296**, 1101 (2002)

59. P.R.T. Jess, V. Garces-Chavez, A.C. Riches, C.S. Herrington, K. Dholakia, J. Raman Spectrosc. **38**, 1082 (2007)
60. N.K. Metzger, E.M. Wright, W. Sibbett, K. Dholakia, Opt. Exp. **14**, 3677 (2006)
61. M. Dienerowitz, M. Mazilu, P.J. Reece, T.F. Krauss, K. Dholakia, Opt. Exp. **16**, 4991 (2008)
62. J. Rodriguez, D.L. Andrews, Opt. Lett. **33**, 2464 (2008)

Chapter 5
Spectroscopy of Optically-Tweezed Aerosol Droplets Containing Fluorescent Chromophores

The observation and characterisation of fluorescence from aerosol particles has been the subject of considerable research over recent decades. Fluorescence spectroscopy has previously been used in the characterisation of droplet composition, temperature and pH [1–5]. The potential for using fluorescence spectroscopy to analyse biological aerosol has recently been demonstrated, with unique fingerprints from different fluorophores, including amino acids, recorded in the ultra-violet and visible parts of the spectrum [6].

In the work described in this chapter, single aqueous droplets isolated using optical tweezers were loaded with absorbing molecular dyes. Numerous molecular dyes are commercially-available, offering a wide range of absorption and solvation properties. Following light absorption by the dyes used in this study, fluorescence competes with non-radiative collisional relaxation which leads to droplet heating. Both fluorescence and droplet heating are examined here using several dyes. These studies are the first detailed measurements of fluorescence from aerosol droplets isolated in optical tweezers [7]. It is anticipated that this may lead to the future use of fluorophores in the characterisation of droplet pH and temperature. These studies are an ideal model for benchmarking absorption techniques, with a view to later extending these techniques to the study of atmospherically-relevant systems such as water droplets containing black carbon [8]. Aerosols of this kind are of considerable interest, both because of their prevalence in polluted air and because absorption effects may be enhanced by the effective lens formed by the curved surface of the aqueous phase in which the soot is dispersed [9].

Electronic supplementary material The online version of this chapter (doi:10.1007/978-3-642-16348-7_5) contains supplementary material, which is available to authorized users.

K. J. Knox, *Light-Induced Processes in Optically-Tweezed Aerosol Droplets*, Springer Theses, DOI: 10.1007/978-3-642-16348-7_5,

5.1 Introduction

Resonance structure in the fluorescence emission from microspheres was first reported by Benner et al. in 1980 for dye-impregnated polystyrene beads moving freely in water [10]. The resonance structure was shown to be associated with the cavity modes of the fluorescing microspheres, which provide a mechanism for optical feedback, resulting in an enhancement in the fluorescence intensity at wavelengths commensurate with whispering gallery modes (WGMs). The first observation of such resonance structure in microdroplets in air was reported by Chang and co-workers in 1984 [11]. A droplet train experiment was used to demonstrate that an ethanol droplet doped with Rhodamine 6G yields a uniquely-structured fluorescence signature which depends on the droplet size. In fact, the first use of cavity-enhanced modes for the high precision determination of droplet size was performed using fluorescing microdroplets [12]. This work by Eversole et al. demonstrated that the fingerprint of WGMs in a fluorescence spectrum could be used to determine droplet size with nanometre accuracy, once refractive index dispersion and droplet temperature were accounted for.

Collecting fluorescence spectra from optically-tweezed particles was first attempted more recently. In 1996 two-photon excitation of fluorophores was demonstrated in condensed phase optical tweezers for beads in aqueous solution [13]. Subsequently, in 2006, Reiner et al. demonstrated the detection of fluorescence from single dye and red fluorescent protein molecules encapsulated in single aqueous droplets trapped within a liquid fluorocarbon medium [14], while cavity-enhanced fluorescence spectra have been recorded from optically-tweezed dye-impregnated polymer beads in aqueous solution [15]. In aerosol tweezers observations have been limited to spontaneous fluorescence spectra from acridine-dosed aqueous droplets exposed to 355 nm pulsed illumination [16].

Cavity-enhanced Raman spectroscopy (CERS) has proved extremely successful in determining the evolving droplet size, composition and mixing state of optically-tweezed aerosol droplets [17–19]. The work presented here describes an extension to the CERS approach for droplet characterisation, achieved by introducing absorbing molecularly-dispersed fluorescent dyes to aqueous droplets. The dyes used are Rhodamine B, Rhodamine 6G and Coumarin 1. Preliminary experiments have also been carried out which use quantum dots as the fluorescing species. The introduction of absorbing, fluorescent species has resulted in several outcomes, including:

- The observation of rapid droplet heating;
- The observation of resonance structure in droplet fluorescence emission spectra;
- The observation of a non-linear, four-wave mixing process in the microdroplets;
- The detection of fluorescence from only tens of quantum dots.

5.1.1 Relevant Theory

5.1.1.1 Fluorescence

Absorption of light energy by chromophores present in droplets results in electronic excitation of the dye molecules. The absorbed energy can be dissipated by fluorescence from the excited singlet state, phosphorescence from the excited triplet states of the dye molecules, or by the non-radiative quenching of excited electronic states which leads to droplet heating. The excited singlet state has a finite lifetime, typically 10^{-9} to 10^{-6} s [20], during which the molecule can vibrationally relax to the lowest vibrational state of the excited singlet state through molecular collisions. The molecule may also make a transition to a triplet excited state, termed intersystem crossing. As phosphorescence involves a transition between a triplet excited state and the singlet ground state it is spin-forbidden, and hence the lifetime of the excited triplet states is longer than that of the singlet, typically 10^{-4} to 10^{2} s [20]. While in excited singlet or triplet states, the dye molecule may undergo chemical reactions, often with oxygen or with other dye molecules. This leads to the removal of a fluorophore and a reduction in the fluorescence intensity, termed photobleaching. Depending on the stability of the products of the chemical reactions, such photobleaching may be temporary or permanent.

The processes described above are illustrated in Fig. 5.1. By careful dye selection it is possible to tune the absorption and subsequent fluorescence emission properties of a droplet.

The absorption and emission spectra of the dyes Rhodamine B, Rhodamine 6G and Coumarin 1 are shown in Fig. 5.2a–c, respectively.

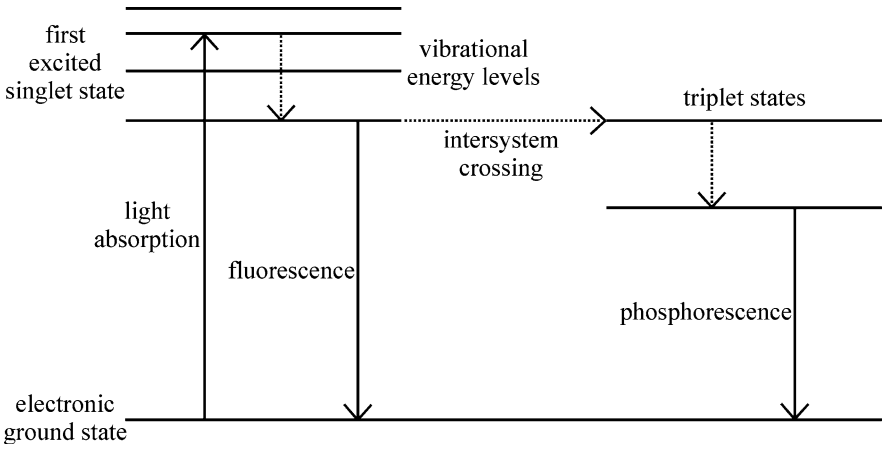

Fig. 5.1 Energy level diagram illustrating light energy absorption and dissipation processes for a fluorophore

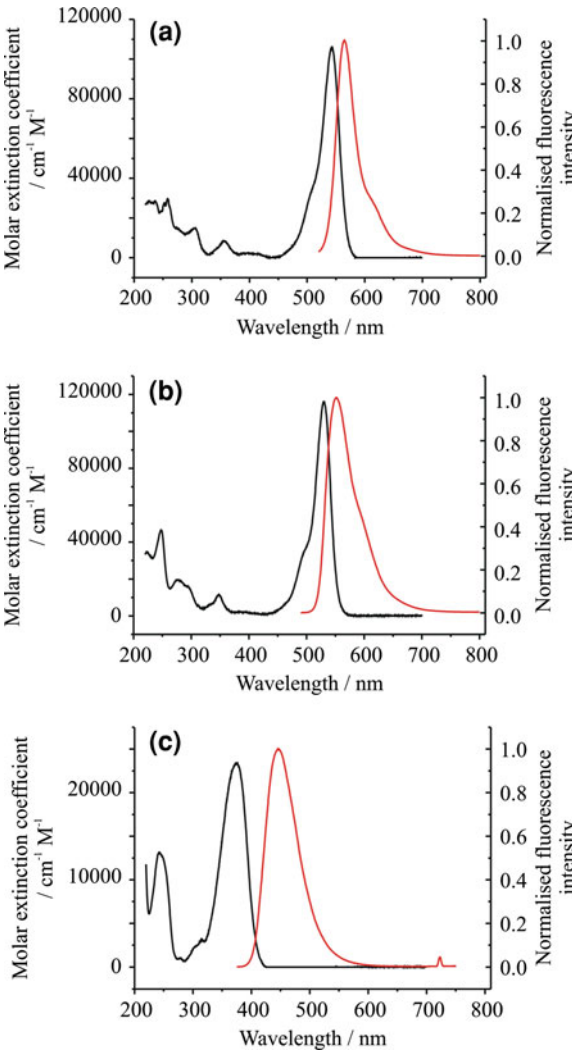

Fig. 5.2 Absorption and fluorescence emission spectra (in *black* and *red* respectively) for **a** Rhodamine B, **b** Rhodamine 6G and **c** Coumarin 1. Data taken from Refs. [21, 22], spectra recorded in ethanol

It can be seen that the Rhodamine dyes absorb strongly at the wavelength of 532 nm used in this work to tweeze aerosols, while Coumarin 1 displays negligible absorbance in this region. All three dyes are conjugated aromatic molecules; the Rhodamines readily dissolve in water, while Coumarin 1 is only sparingly soluble in water [23].

Quantum dots are semiconducting nanoparticles. Excitation involves promoting an electron from an occupied to an unoccupied state across the semiconductor band gap and fluorescence occurs when this electron relaxes back to an energy level below the band gap. The size of the band gap, and hence the wavelength of the fluorescence, is determined by the size of the quantum dot.

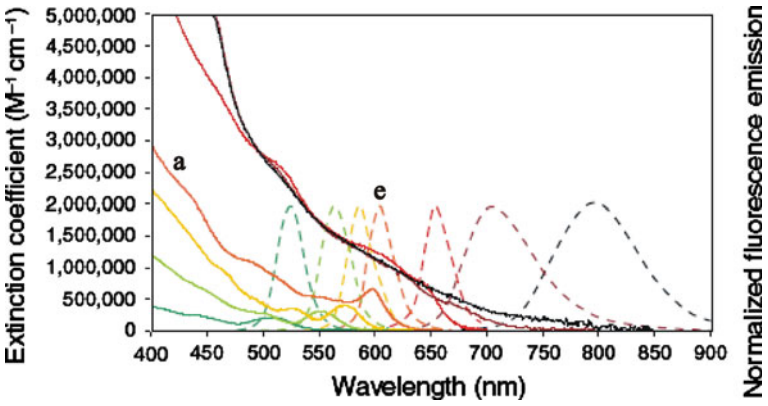

Fig. 5.3 Absorption and emission spectra for a range of quantum dots. The absorption and emission spectra relevant to the dots used in this study are marked with the letters a and e respectively. Figure reproduced from Ref. [24]

The quantum dots used in these studies consist of a semiconductor cadmium/selenium/tellurium core, a ZnS shell and a polyethylene glycol coating. Quantum dots offer some experimental advantages over molecular dyes. They display broad absorption, which means a wide range of excitation sources can be used, and they offer narrow emission spectra, the wavelength position of which is easily tuned through controlling the particle size, which in turn makes separation and collection of the fluorescence straightforward. Quantum dots also generally offer increased photostability compared with molecular dyes. Finally, the surface of the dots can be functionalised, offering control over the solvation properties of the dots. Absorption and emission spectra for a series of quantum dots are shown in Fig. 5.3 taken from literature provided by Invitrogen, the supplier of the dots used in the work presented later [24].

The dots used in these studies were selected to have an emission spectrum centred on 605 nm to allow convenient separation of the fluorescently-scattered light from the trapping and imaging illumination sources. The dots were functionalised with a hydrophobic coating.

5.1.1.2 Non-linear Scattering Processes

The high circulating light intensities which can be supported by microdroplets render them an ideal environment for observing non-linear light scattering processes [25]. The stimulated Raman scattering which is used for droplet sizing is a familiar example. Further non-linear optical effects which are only observed in bulk liquids under conditions of intense nanosecond pulsed laser illumination can be observed in the microdroplet environment for low intensity continuous-wave excitation [26]. This is a result of the high pump intensities which can build up in

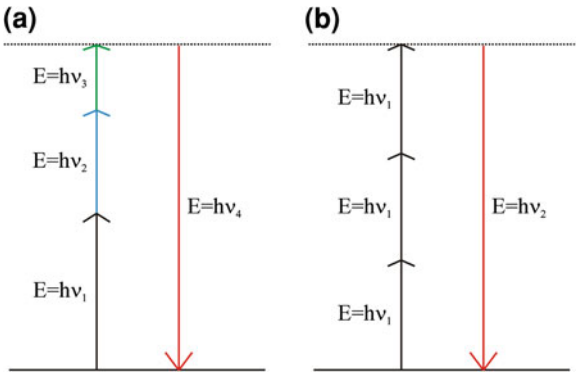

Fig. 5.4 Illustration of **a** third-order sum-frequency generation and **b** third-harmonic generation. Here E represents energy, h is Planck's constant and ν is the frequency

high quality factor cavity modes. Higher order Raman light scattering is an example of such a non-linear process. Raman-scattered light which circulates a droplet in a WGM can act as a pump source for higher order Raman scattering. Stimulated Raman scattering has previously been observed in microdroplets up to the fourteenth order [27, 28]. Another example is third-order sum-frequency generation. This process is illustrated in Fig. 5.4a, along with a special case of this process, third-harmonic generation, shown in part (b). The process involves the combination of three frequency components to produce a fourth. Third-harmonic generation has been observed in CCl_4 droplets, for which the pump laser and stimulated Raman frequencies generated light scattering at higher frequencies [29].

The occurrence of such parametric mixing processes depends on the induced non-linear polarisation of the medium, P^{NL}, by the applied optical field. Taking as an example sum-frequency generation as shown in Fig. 5.4a, the non-linear polarisation at the generated frequency v_4, $P^{NL}(v_4)$, is given by [30]:

$$P^{NL}(v_4) = \chi^{(3)} E(v_1) E(v_2) E(v_3) \tag{5.1}$$

where $\chi^{(3)}$ is the third-order non-linear susceptibility of the liquid medium and $E(v_i)$ is the magnitude of the droplet internal field at the frequency of the ith wave. Such processes are not typically observed in aqueous droplets as a result of the low $\chi^{(3)}$ of water (2.78×10^{-14} esu), which is a factor of $\sim$2–3 smaller than that of CCl_4 [31–33].

A further example of a higher order scattering process is parametric four-wave mixing, whereby two frequency components, v_1 and v_2, propagating in a nonlinear medium can combine to produce two further components, v_3 and v_4, as illustrated in Fig. 5.5 [26].

For all of these processes the energy of the absorbed and emitted photons must be conserved [30]. In the case of four-wave mixing the combination of frequencies must therefore satisfy the condition:

$$v_1 + v_2 = v_3 + v_4 \tag{5.2}$$

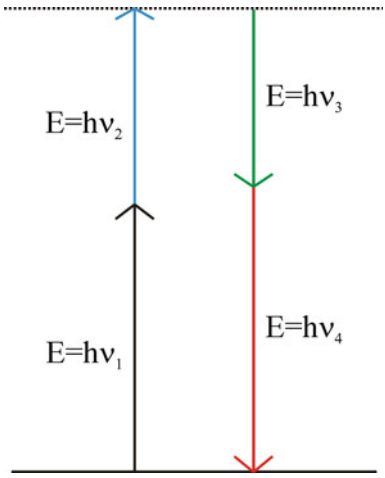

Fig. 5.5 Illustration of a four-wave mixing process. Here E represents energy, h is Planck's constant and ν is the frequency

The intensity of the mixing processes depends on the degree of spatial overlap of, and amount of phase matching between, the generating and generated waves [30]. These conditions are readily achieved if all of the frequency components are resonant with cavity modes of the droplet.

Four-wave mixing has previously been observed in CS_2 microdroplets in a droplet train experiment [26]. Two stimulated Raman-scattered frequency components, ν_1 and ν_2, were observed to generate two further scattered frequencies, ν_3 and ν_4, one to the red and one to the blue of the Raman band. While a continuous range of ν_3 and ν_4 satisfies condition 5.2, only sets of ν_3 and ν_4 for which these frequencies were resonant with cavity modes of the microdroplets were observed under the experimental conditions of low intensity illumination. This process has not previously been observed in aqueous droplets, again as a result of the low third-order susceptibility of water, which is $\sim$6 times lower than that of CS_2 [32].

5.2 Experimental Considerations

The fluorescently-scattered light from the droplets was recorded in the same way as the Raman-scattered light; it was collected using the trapping objective, imaged into a Jobin-Yvon Triax 550 spectrograph and the dispersed spectroscopic fingerprint recorded with a non-intensified liquid nitrogen-cooled CCD.

The solutions of the fluorescing species were prepared in deionised water using the following dyes: Coumarin 1 (Eastman), Rhodamine B (Acros Organics) and Rhodamine 6G (Lambda Physik). The Rhodamine dyes were typically used at μM concentrations, while Coumarin 1 was used at a concentration of $\sim$0.1 mM. The Coumarin 1 concentration range available was limited by its low solubility in aqueous solution [23]. NaCl was added at a concentration of 20 g L^{-1}.

Two different approaches were used to introduce the dye into the trapped droplets. In the case of Coumarin 1 the dye was dissolved in the solution to be trapped. Directly loading the trap from a nebulised stream containing the dye causes a large amount of dye to be deposited on the chamber coverslip. In the case of the Rhodamine dyes, which absorb strongly at the trapping wavelength, this results in a large background fluorescence signal which obscures the spectral signature of the droplet. The Rhodamine dyes were therefore introduced to trapped dye-free aqueous NaCl droplets via collisional bombardment with droplets from a nebulised solution of the dye. This process requires a lower flow of dye-doped aerosol to be introduced to the chamber than that required to load the trap, and as a consequence the large background signal arising from dye settling on the glass coverslip is reduced.

5.3 Results and Discussion

5.3.1 Rapid Droplet Heating

Following collisional bombardment with aqueous Rhodamine B-loaded droplets, trapped droplets have been observed to exhibit short flashes of fluorescence as the dye is incorporated into the droplet and subsequently photobleached on a timescale of seconds, as shown in Clip 13. This behaviour is consistent with the high absorption of Rhodamine B at the trapping beam wavelength, as shown in Fig. 5.2a. If larger amounts of dye are incorporated into the droplet considerable heating occurs as a consequence of absorption by the dye and the droplet can be observed to completely evaporate in less than a tenth of a second, as shown in Fig. 5.6. The first image represents time $t = 0$ s, immediately before the droplet was exposed to Rhodamine B. The second image was integrated over the next time window of 0.033 s, following inclusion of a RB-loaded droplet. The third image represents the next time window of 0.033 s, by which time the droplet has completely evaporated. Similar behaviour has also been observed for Rhodamine 6G.

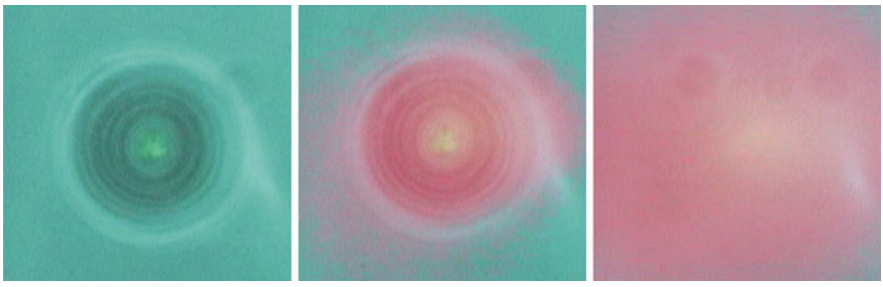

Fig. 5.6 In-plane droplet images showing rapid evaporation on inclusion of Rhodamine B

Table 5.1 Quantities used in the calculation of the power required to evaporate the droplet

Quantity	Value
Droplet volume prior to bombardment	6.6×10^{-16} m^3
Heat of vaporisation of water (298 K)	40.65 kJ mol^{-1} [34]
Time for complete evaporation of droplet	0.07 s
Laser power incident on droplet, P	35 mW
Quantum yield for fluorescence, Rhod. B, Φ_f	0.3 [35]
Molar absorption coefficient, Rhod. B (532 nm)	188740 cm^{-1} M^{-1} [22]
Rhodamine B concentration nebulised	8.7×10^{-6} M

The energy required for evaporation of the droplet of known initial volume can be calculated by considering the heat of vaporisation of water. It is assumed that the heat of vaporisation of the dilute NaCl solution of which the droplet consists is equal to that of pure water. This energy must be supplied to the droplet in 0.07 s, and the corresponding rate of heat deposition necessary to evaporate the droplet in this time has been calculated to be 2×10^{-2} mW over this time window.

The power delivered to the droplet as a result of dye absorption, P_a, is equal to the laser power incident on the droplet, P, scaled by the fractional proportion absorbed by the dye, F_a, and the proportion of that absorbed which results in non-radiative quenching. Hence P_a is given by:

$$P_a = P \cdot F_a(1 - \Phi_f) \tag{5.3}$$

where Φ_f is the quantum yield for fluorescence for Rhodamine B in aqueous solution. The laser beam waist is smaller than the droplet at the axial trapping position, and the entirety of the laser beam therefore passes through the droplet. F_a is determined from the Beer–Lambert law, using the dye absorption coefficient and taking the droplet diameter as the path length. It is assumed that no photobleaching of the dye occurs within the time it takes for complete evaporation. The quantities used in the calculation are detailed in Table 5.1.

The Rhodamine B concentration of the droplet which would be required for P_a to be equal to the necessary rate of heat generation of 2×10^{-2} mW has been calculated in this way to be $\sim 4 \times 10^{-6}$ M. This represents only a coarse estimate as the rate of heat loss from the droplet by conduction in the surrounding gas phase has not been considered. It is impossible to quantify how much dye was incorporated into the droplet, both because the droplet changes size too rapidly to determine the size immediately after dye incorporation, and because dye incorporation and the accompanying droplet evaporation occur simultaneously. It is however plausible that Rhodamine B could accumulate in the droplet to a concentration of approximately half of the initially nebulised concentration of 8.7×10^{-6} M by collisional incorporation, and hence rapid evaporation of a trapped droplet is consistent with these experimental conditions.

Laser-induced explosive evaporation has previously been demonstrated by exposing water droplets to pulsed laser radiation at a wavelength of 266 nm [36].

In this case it was absorption by the water molecules which was responsible for the rapid droplet evaporation.

5.3.2 *Observation of Cavity-Enhanced Fluorescence*

Cavity-enhanced fluorescence has been observed for the first time in optically-tweezed aerosol droplets. Resonance structure is observed in the fluorescence emission spectra of the dye as a result of the droplet acting as a low-loss optical cavity. Just as Raman-scattered light, which is resonant with the cavity modes of the droplet, may become amplified, so too may fluorescently-scattered light.

Figure 5.7 shows a typical cavity-enhanced fluorescence spectrum recorded for an aqueous droplet following incorporation of additional Rhodamine B droplets at a concentration of 8.7×10^{-6} M by collisional bombardment. The droplet does not completely evaporate, but instead remains trapped while the incorporated Rhodamine B fluoresces and subsequently photobleaches. This is consistent with a smaller concentration of dye accumulating in the droplet than would be necessary for complete droplet evaporation. The droplet spectrum before incorporation is shown in black. WGMs can be seen on the Raman OH band as expected. The rising baseline is a result of fluorescence from Rhodamine B present on the coverslip. The peak centred at $\sim$605 nm arises from Raman scattering by the immersion oil. The blue spectrum was recorded 1 s later, following dye

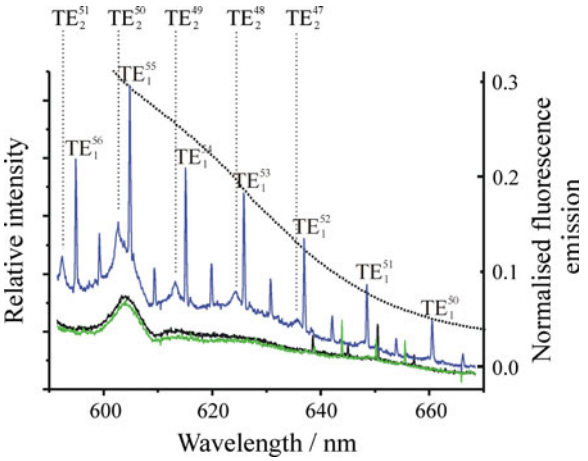

Fig. 5.7 Cavity-enhanced fluorescence from an aqueous droplet of radius 4.40 μm containing Rhodamine B. Droplet spectra before incorporation of the dye and for 1 and 2 s following dye incorporation are represented by *black*, *blue* and *green* lines, respectively. Mode assignments are provided for modes of transverse electric polarisation for the *blue* spectrum. A *curved dotted line* shows the normalised fluorescence emission from a bulk sample of Rhodamine B (data taken from Ref. [22])

incorporation. Cavity modes can be seen to extend beyond the Raman OH band, commensurate with the fluorescence emission band of Rhodamine B, and the spontaneous fluorescence band is considerably enhanced above the background. The dotted line shows the normalised fluorescence emission intensity of Rhodamine B. It can be seen that the intensity profile of the cavity-enhanced fluorescence spectrum follows the general intensity trend of the bulk fluorescence spectrum, for modes of the same polarisation and order.

The green spectrum was recorded after a further second, when it can be seen that the dye in the droplet has become completely photobleached. The dye in the aqueous solution present on the coverslip surface, however, has not been photobleached within this timescale. This may be the result of the 532 nm light intensity being lower at the level of the coverslip than that present in the droplet, as it is not tightly focussed there. This would result in fewer dye molecules being promoted to excited singlet or triplet states in which they can react with oxygen or other dye molecules and hence a slower rate of photobleaching. Other possible reasons for the reduced photobleaching rate in the solution present on the coverslip are a lower dye or dissolved oxygen concentration here than in the droplet, which would reduce the rate of irreversible reaction of excited state dye molecules. A thorough investigation of the photobleaching rates in optically-tweezed aerosol droplets represents a possible extension to this work. In principle a study of this nature could be used to investigate the partitioning of oxygen between the condensed and gas phases of an aerosol system.

Cavity-enhanced fluorescence has also been observed for Rhodamine 6G, as shown in Fig. 5.8. The spectrum shown in black was recorded immediately after dye loading from nebulisation of a solution of 2.2×10^{-6} M Rhodamine 6G, while those shown in blue and green were recorded 1 and 2 s later, respectively. The cavity resonances can be seen to be considerably broadened in the spectrum shown in black as a result of the droplet size changing rapidly while this spectral frame was acquired. The rapid photobleaching of the dye is evident from the decreased spontaneous fluorescence intensity and hence the stimulated peak intensities. The dotted line shows the normalised fluorescence emission intensity of the dye. It can

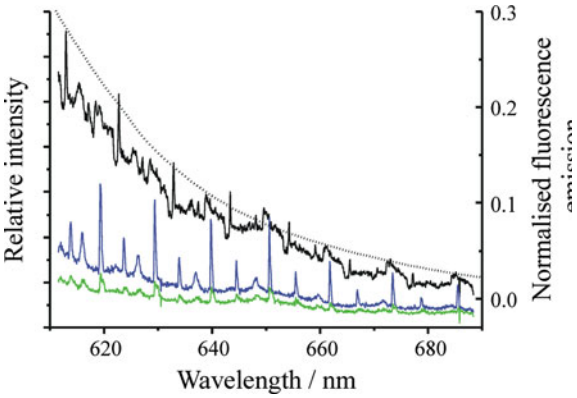

Fig. 5.8 Cavity-enhanced fluorescence spectra from an aqueous droplet containing Rhodamine 6G. The spectra were recorded at 1 s intervals; in order from earliest to latest: black, blue and green lines. A *dotted line* shows the normalised fluorescence emission from a bulk sample of Rhodamine 6G (data taken from Ref. [22])

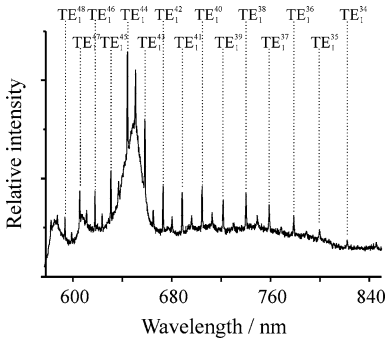

Fig. 5.9 Four-wave mixing spectrum from a droplet containing Coumarin 1. Droplet radius 3.73 μm, Coumarin 1 concentration 1.2×10^{-4} M. First order modes of transverse electric polarisation have been assigned

again be seen that the intensity profile of the cavity-enhanced fluorescence spectrum follows the intensity trend of the bulk fluorescence spectrum.

5.3.3 Observation of Four-Wave Mixing

Under certain circumstances droplets containing Coumarin 1 support cavity resonances at wavelengths which extend far beyond the Raman O–H band and outside of the dye fluorescence band. It should be remembered that Coumarin 1 does not absorb light at 532 nm, as shown in Fig. 5.2c above, and hence the spectroscopic effect of Coumarin 1 on droplets which are illuminated with only 532 nm light does not arise from direct excitation of the dye molecules followed by spontaneous fluorescence. A spectrum showing this effect is provided in Fig. 5.9. The spectrum is from a droplet which was trapped from a nebulised solution of Coumarin 1 at a concentration of 8.0×10^{-5} M and 20 g L^{-1} NaCl. The Coumarin 1 concentration of the droplet at the time when the spectrum was recorded had increased to 1.2×10^{-4} M as a result of the droplet losing water by evaporation. This is a composite spectrum; the spectrograph diffraction grating was moved to three different positions in order to sample the wide wavelength range. The relative humidity in the trapping chamber was stable throughout and hence the droplet did not change size significantly during the sequential measurement process, allowing the determination of such a composite spectrum.

The cavity resonances can be seen to extend to the blue and the red of the Raman O–H band, from ~580 to 840 nm. The optical components used prevented signal being collected below this wavelength range for this droplet. These observations are consistent with the droplets supporting a stimulated four-waving mixing process whereby two Raman O–H photons combine to produce two further scattered frequencies of light. This represents the first observation of a four-wave parametric mixing process in aqueous droplets under conditions of low intensity continuous wave illumination.

The combination of two Raman photons will result in the emission of a combination of ν_3 and ν_4 such that the condition $\nu_1 + \nu_2 = \nu_3 + \nu_4$ is satisfied.

Depending on the distribution of energy between v_3 and v_4 this will result in light being scattered to the blue and red of the Raman O–H band; for example, the absorption of two photons of wavelength 650 nm could result in the emission of a pair of photons of wavelengths 600 and 710 nm. The essential spatial overlap and phase matching for the mixing process require that v_1, v_2, v_3 and v_4 are all resonant with cavity modes of the droplet, as has been observed in previous studies of parametric mixing processes in microdroplets under conditions of continuous wave illumination [26, 29]. As a result cavity resonances are observed to the blue and red of the Raman O–H band, as can be seen in Fig. 5.9 above. As v_3 and v_4 become more separated in frequency their modes numbers will differ more significantly and hence the spatial overlap of the waves will diminish. This effect limits the wavelength range over which the additional peaks are observed and explains the decrease in intensity away from the OH band.

Four-wave mixing is not observed for aqueous droplets under standard trapping conditions in the absence of dye because of the low $\chi^{(3)}$ of water. Whereas studies of non-linear processes are often performed by using a solvent of high $\chi^{(3)}$, such as CS_2 or CCl_4, here $\chi^{(3)}$ is increased by resonance enhancement as a result of the presence of Coumarin 1 in the droplets. This effect arises because the combination of two Raman O–H photons coincides with the absorption band of Coumarin 1. For example, the combination of two photons of wavelength 650 nm corresponds to the absorption of a single photon with a wavelength of 325 nm, which lies within the absorption band of Coumarin 1, as shown in Fig. 5.2c. Resonance enhancement has previously been observed in microdroplets under conditions where the excitation frequency for Raman scattering coincides with the absorption band of the scattering species [37]. In this work aqueous droplets containing *p*-nitrosodiummethlyaniline were studied in a droplet train experiment. The Raman-scattering was observed to undergo resonance enhancement, resulting in a low detection limit for *p*-nitrosodiummethlyaniline of 10^{-7} M.

The energy available to be absorbed in the four-wave mixing process ranges from that corresponding to the absorption of two photons at the high wavelength edge of the Raman band at $\sim$670 nm to the absorption of two photons from the low wavelength edge at $\sim$630 nm, i.e. from 5.9×10^{-19} to 6.3×10^{-19} J. This range corresponds to the absorption of a single photon of wavelength 335–315 nm. The molar extinction coefficients of Coumarin 1 at these wavelengths are 3666 and 3078 cm^{-1} M^{-1}, respectively [21, 22].

A threshold condition for the four-wave mixing process has been observed. The onset of the four-wave mixing process has been observed to occur via an increase in the droplet Coumarin 1 concentration. Trapped droplets were observed to display initially the usual cavity-enhanced peaks on the water Raman O–H band, as shown in Fig. 5.10a.

Following partial droplet evaporation and increased concentration of the dye in response to a falling relative humidity in the trapping chamber, cavity resonances were observed across a broader spectral region, as shown in Fig. 5.10b. The resonance enhancement effect of Coumarin 1 will increase with concentration until cavity resonances associated with the four-wave mixing process are of a detectable

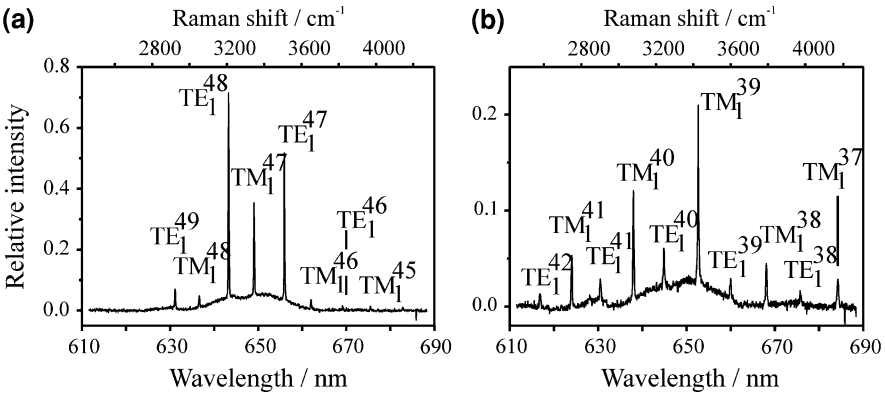

Fig. 5.10 **a** Cavity-enhanced Raman spectrum from a trapped droplet with a radius of 4.13 μm. **b** Spectrum including cavity resonances arising from the four-wave mixing process (droplet radius of 3.49 μm)

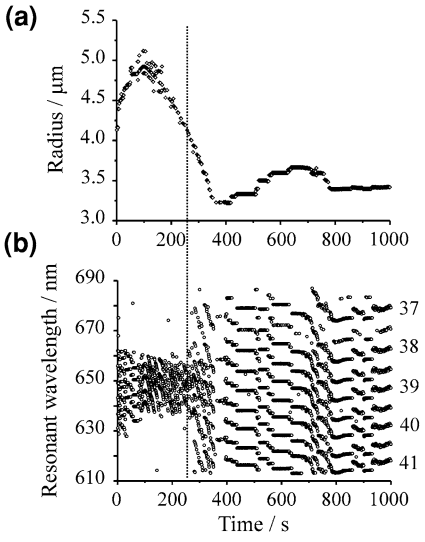

Fig. 5.11 The onset of four-wave mixing. **a** Variation of droplet radius with time. **b** Wavelengths of observable resonant modes in the droplet spectra. Mode numbers for first order resonances of TE polarisation for the final spectrum are shown on the right. A step increase in the number of resonant modes can be seen at around 250 s and is highlighted with a *dotted line*

intensity. It can be seen that in spectrum (b) the mode numbers of the supported resonances have decreased while the spacing between the modes has increased, when compared with spectrum (a), consistent with the droplet having evaporated to a smaller radius. The spectra in Fig. 5.10a, b correspond to the droplet with Coumarin 1 concentrations of 5.4×10^{-4} and 1.0×10^{-3} M, respectively.

Figure 5.11a shows the decrease in radius with time for the droplet from Fig. 5.10; the accompanying onset of four-wave mixing is shown in part (b), evident from the increase in the spectral range over which cavity resonances are observed. The long time variations in size can be attributed to fluctuations in relative humidity within the trapping chamber.

5.3.4 Consequences of Extended Resonant Structure

The occurrence of resonance structure over an extended spectral region as a result of the presence of an absorbing and fluorescing chromophore has a number of advantages for the characterisation of microdroplets. In the case of cavity-enhanced fluorescence, resonant structure extends across the fluorescence emission band, which for a typical dye can extend over several hundred nanometres. This is a much greater spectral range than in the case of typical Raman bands; for example, the O–H stretching band of water spans around 40 nm. However, as a result of photobleaching this structure is short-lived for molecular dyes, limiting its usefulness for droplet characterisation. The resonance structure arising from four-wave mixing in an aqueous Coumarin 1 droplet spans $\sim$300 nm. This process is not vulnerable to photobleaching, enhancing its usefulness. Two applications of extended resonance structure will now be outlined.

5.3.4.1 Sizing

As droplet size decreases the spacing between resonant modes in a progression increases [38, 39]. This places a lower limit on the size of droplet which can be accurately sized using CERS, as for smaller droplets fewer resonant modes will coincide with the range of spontaneous Raman scattering wavelength. Extending the bandwidth of the spontaneous light intensity available by addition of a fluorescent dye allows sizing of smaller droplets and in general increases the accuracy of sizing all droplets by providing more modes for comparison with Mie scattering theory. Figure 5.12 illustrates the advantage gained for sizing small particles. The three spectra, (a), (b) and (c) correspond to the same Coumarin 1-loaded droplet with radii of 4.97, 3.60 and 3.23 μm, respectively. The shaded region corresponds to the wavelength range coinciding with the Raman O–H band of water. For the droplet size corresponding to spectrum (a) the Coumarin 1 concentration is below that necessary for stimulated four-wave mixing to occur. As the droplet evaporates to smaller sizes the spacing between modes of the same polarisation increases, as indicated by the guide of fixed size. As a result the number of resonances which fall within the Raman O–H band reduces, and the accuracy of sizing the droplet spectra (b) and (c) would diminish if it were not for the extended resonant structure which occurs as a result of the presence of an absorbing chromophore, in this case Coumarin 1, in the droplet.

The choice of dye can additionally allow tuning of the emission range to suit different experimental configurations; such tuning is not possible in the case of Raman scattering without changing the excitation wavelength or the Raman scatterer.

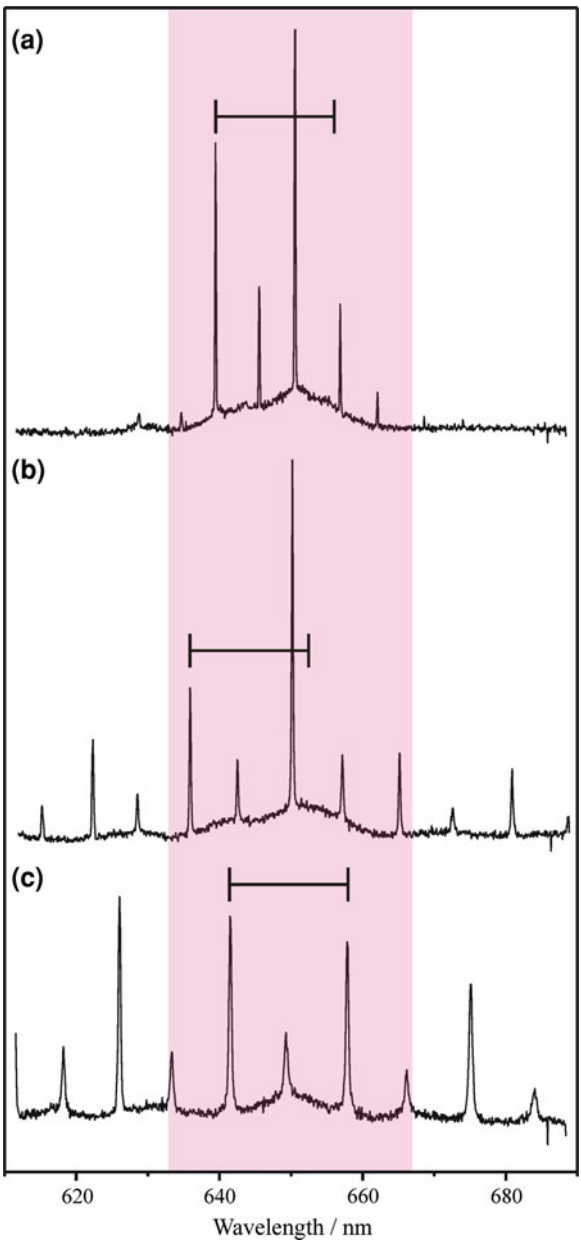

Fig. 5.12 Spectra from a single droplet of evolving size containing Coumarin 1. The shaded region corresponds to the wavelength range coinciding with the Raman O–H band. **a** Radius 4.97 μm, Coumarin 1 concentration 5.4×10^{-4} M, below the threshold for four-wave mixing. **b** Radius 3.58 μm, Coumarin 1 concentration 9.0×10^{-3} M, above the threshold for stimulated four-wave mixing. **c** Radius 3.20 μm, Coumarin 1 concentration 1.3×10^{-2} M

5.3.4.2 Quality Factors of Whispering Gallery Modes

Information may also be extracted from the shapes of the resonant modes. The quality factor of the droplet as an optical cavity may be determined at a given

wavelength from the width of a mode occurring at this wavelength. Using a dye to increase the spectral range over which the modes are observable allows the dependence of the quality factor on wavelength to be studied over a wider range, which can allow wavelength-resolved information about droplet absorption and scattering to be determined. Cavity resonances from fluorescing droplets have previously been used to obtain droplet absorption spectra for ethanol droplets containing Rhodamine 6G and bromocresol green or cresyl violet as the absorbing species [40]. In this work the intensities of the peaks in the fluorescence emission spectra, which depend on the cavity quality factor, were used to derive absorption information. Quality factors can also be used to characterise droplet deformation; the quality factor will decrease if the droplet becomes non-spherical [41].

The quality factor of a mode in an optical cavity is a measure of the losses occurring in the mode; the lower the losses the higher the quality factor. The quality factor, Q, is defined as [40]:

$$Q = \frac{\text{energy stored per cycle}}{\text{energy lost per cycle}} \tag{5.4}$$

Typical values of Q that have been reported include 10^8 for the first order TE modes of 15 μm diameter ethanol microdroplets [42], 10^4 for the first order TE modes of 40–60 μm diameter water droplets [43], and $\sim 10^3$ for the first order TE and TM modes of 4–5 μm radius fluorescent melamine beads [15].

Q can be expressed as a combination of an internal quality factor, Q_{int}, determined by losses within the droplet due to absorption and scattering, and an external quality factor, $Q_{\text{ext,}}$ determined by loss of light from the droplet due to imperfect reflection of the light in the mode at the droplet interface [44]:

$$\frac{1}{Q} = \frac{1}{Q_{\text{int}}} + \frac{1}{Q_{\text{ext}}} \tag{5.5}$$

The effect of external losses is evident in the dependence of Q on the cavity size and the mode number and order. Q increases with increasing droplet size and with increasing mode number, n_{mode} [40]. Q decreases with increasing mode order, l. Modes of higher order penetrate to greater distances from the droplet surface, impairing total internal reflection at the droplet interface and reducing Q_{ext} [12, 40]. As modes of transverse magnetic (TM) polarisation reside at greater depths than transverse electric (TE) modes, these are of lower Q for the same reason [12, 40].

The effect of internal losses on the cavity Q has been studied by Campillo and co-workers; the concentration of the broadband absorber nigrosine was varied in ethanol droplets containing Rhodamine 6G and the Q of the droplets determined [42]. The Q was seen to reduce by a factor of 10^4 as the nigrosine concentration was increased, associated with an increase in the internal absorption losses and a consequential reduction in Q_{int}. The solutions studied ranged from a nigrosine-free solution with an imaginary part of the refractive index, k, of $<1 \times 10^{-9}$ to one with a nigrosine concentration corresponding to $k = 7.8 \times 10^{-6}$.

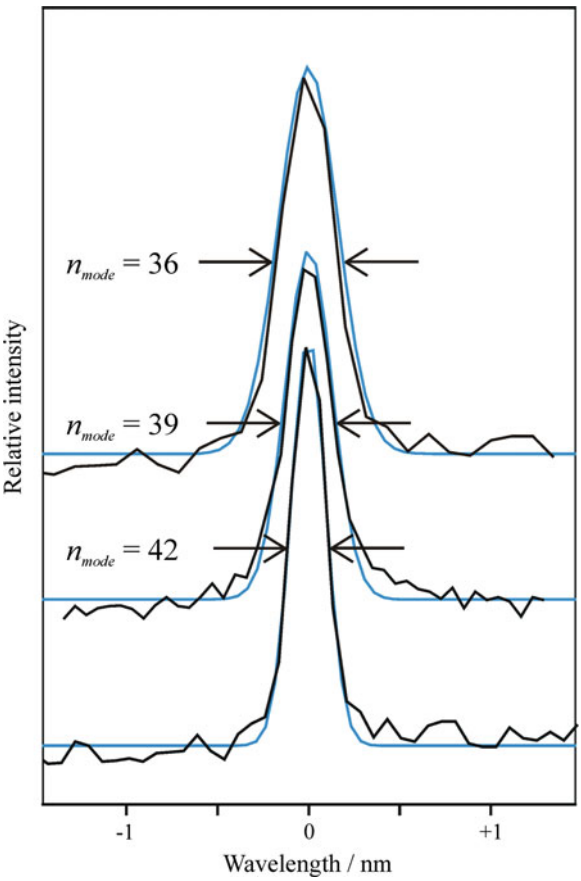

Fig. 5.13 Variation of FWHM of WGM resonance with n_{mode}. Modes of $n_{\text{mode}} = 36$, 39 and 42 are of Qs of 1260, 2184 and 2911 and for the droplet at radii of 3.22, 3.39 and 3.66 μm respectively. The experimentally-determined and the Gaussian-fitted lineshapes are shown in black and blue, respectively

Q can be determined for a cavity mode from a measurement in the frequency domain using [40, 45]:

$$Q = \frac{v}{\Delta v} \tag{5.6}$$

where v is the frequency of a cavity mode and Δv is the full-width at the half-maximum height of the resonance (FWHM); modes of lower Q thus appear broader when spectrally-resolved lineshapes are recorded. Figure 5.13 illustrates the decrease in FWHM with increasing n_{mode} and hence Q for three cavity resonances from the same droplet of evolving size. The experimentally-determined and the associated Gaussian-fitted lineshapes are shown in black and blue, respectively.

In this work the increased spectral range over which resonant modes are observable for aqueous droplets containing Coumarin 1 has been used to study the variation in Q across a single droplet spectrum and Q has also been studied across a series of these spectra. This represents the first systematic characterisation of cavity Qs for an optically-tweezed aerosol droplet.

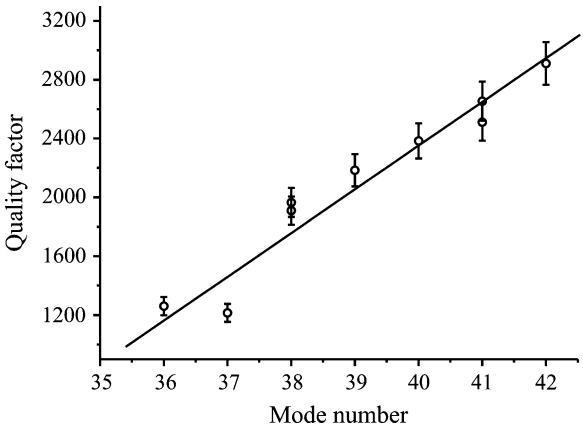

Fig. 5.14 Dependence of Q on n_{mode} for an evaporating droplet. The droplet radius varies from 3.22 to 3.66 μm

The dependence of Q on n_{mode} has been observed for a single droplet of evolving size. A series of spectra was recorded as the droplet evaporated in response to a falling relative humidity in the trapping chamber. One cavity resonance per spectrum was selected, the lineshape fitted to a Gaussian profile and the Q of the mode determined using Eq. 5.6. Resonances occurring at wavelengths within ±10 nm of 650 nm were selected in order to limit the effect of any wavelength dependence of Q_{int} as the result of absorption on Q. Although Coumarin 1 is not expected to absorb at these wavelengths, water has a low absorbance which varies with wavelength in this region.[1] The n_{mode} of the modes was determined by fitting the spectra and assigning the modes using the SCATA programme [46]. The Q has been observed to increase linearly with increasing n_{mode}, shown for first order modes of TE polarisation in Fig. 5.14. The effect is the result of an increase in Q_{ext}.

The Q of the first order droplet cavity modes has been found to vary between ~1000 and 3000 for droplets of radii around 3.5 μm. Q has also been determined for a relatively large dye-free droplet of radius ~8 μm to be ~5000. The values of Q determined for these droplets are lower than the Q of 10^4 previously determined for water droplets by Lin et al. [43]. Those droplets were, however, 20–30 μm in radius, considerably larger than the droplets used in this work. A comparison of these findings is provided in Fig. 5.15. It can be seen that the values of Q determined in the work presented here are consistent with the study of Lin et al., once the relative size of the droplets studied is taken into account [43].

Resonances such as those used in preparing the data shown in Fig. 5.14 are typically ~12 CCD pixels wide. The error associated with fitting the lineshapes to a Gaussian profile in order to determine their width is typically around ±5%, as illustrated by the error bars shown in Fig. 5.14. This is much greater than the error in determining the mode wavelength, which is ±0.08 nm for the

[1] See Fig. 3.2 in Chap. 3.

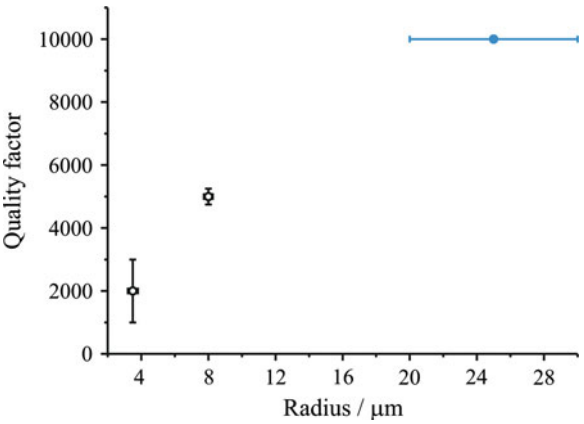

Fig. 5.15 Experimentally-determined values of Q from this study and those reported by Lin et al. [43], represented by *open black* and *closed blue circles*, respectively

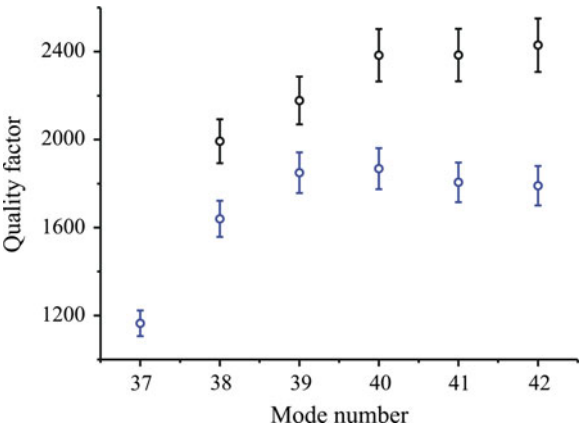

Fig. 5.16 Dependence of Q on n_{mode} across a single droplet CEF spectrum. Modes of TE and TM polarisation are shown in *black* and *blue*, respectively. Droplet radius 3.3 μm, Coumarin 1 concentration 8.9×10^{-4} M

600 groove mm^{-1} grating used. This error is further reduced by using the centre of the fitted Gaussian lineshape to be the resonant wavelength. The upper limit of Q which could be determined by this method would be ~ 8000, determined by the spectral resolution of the CCD chip. Modes of a higher Q than this would be narrower than a single CCD pixel and the lineshape would not be resolvable in the spectrum.

The variation of Q with n_{mode} has also been observed for a single droplet spectrum, as shown in Fig. 5.16. The Q is lower for modes of TM polarisation, as is expected. The modes span the wavelength range 612–686 nm, with higher n_{mode} corresponding to a lower mode wavelength. Re-absorption of the light scattered by the four-wave mixing process, resulting in a lowering of Q_{int}, may explain the observation that Q reaches a limiting value with increasing n_{mode}. However, the wavelength dependence of this effect is not consistent with the absorption behaviour of Coumarin 1, which is not expected to absorb light at these wavelengths. The effect is also inconsistent with absorption by the droplet water

content, as the absorbance of water decreases with decreasing wavelength in this spectral region. It is plausible that there is in fact a Coumarin 1 absorbance at these wavelengths, and that the Q of the droplet may be used to detect it, acting as a very sensitive spectrometer.

5.3.5 Quantum Dot Fluorescence

Preliminary imaging studies of fluorescing quantum dots encapsulated in optically-tweezed droplets have been carried out. Because of the increased photostability of quantum dots over molecular dyes, and the ability of the dot surface to be functionalised with hydrophilic or hydrophobic molecules, it is proposed that quantum dots could be used as fluorescent labels for distinct phases in multiphase aqueous/organic droplets, allowing the spatial resolution of droplet phase structure in a fluorescence image.

Decane droplets loaded with quantum dots with a hydrophobic coating and with an emission spectrum centred on 605 nm were optically trapped and their fluorescence images collected using both a simple and an electron-multiplied CCD camera [47]. Figure 5.17 shows the fluorescence image captured using the standard CCD camera from a trapped decane droplet loaded with quantum dots at a concentration of $\sim 2 \times 10^{-8}$ M, which corresponds to a droplet loading of ~ 400 quantum dots. Preliminary work using the electron-multiplied CCD camera has involved establishing an approximate limit of detection for the fluorescence, which is in the region of only tens of dots per droplet.

Future work will involve using the electron-multiplied CCD camera to study the kinetics of droplet phase separation following the coagulation of aqueous and organic droplets with high time resolution. This will include the layering of decane on water droplets [48]. It is also possible that confining small numbers of quantum

Fig. 5.17 A fluorescence image of a decane droplet loaded with quantum dots

dots in optically-tweezed aerosol droplets may represent a novel method for carrying out single-molecule fluorescence spectroscopy.

5.4 Summary

The addition of absorbing dyes to optically-tweezed droplets has enabled the observation of optical effects such as cavity-enhanced fluorescence and four-wave mixing for the first time. This is also the first observation of a parametric mixing process in a single aqueous microdroplet under conditions of continuous-wave illumination. The addition of absorbing dyes has also provided a demonstration of rapid droplet heating as a result of absorption. Detailed measurements of droplet absorption will be discussed in the next chapter.

References

1. R.J. Hopkins, J.P. Reid, J. Phys. Chem. A **109**, 7923 (2005)
2. R.J. Hopkins, C.R. Howle, J.P. Reid, Phys. Chem. Chem. Phys. **8**, 2879 (2006)
3. R.M. Sayer, R.D.B. Gatherer, J.P. Reid, Phys. Chem. Chem. Phys. **5**, 3740 (2003)
4. R.D.B. Gatherer, J.P. Reid, Chem. Phys. Lett. **357**, 153 (2002)
5. C. Maqua, V. Depredurand, G. Castanet, M. Wolff, F. Lemoine, Exp. Fluids **43**, 979 (2007)
6. R.K. Chang, Y.L. Pan, Faraday Discuss. **137**, 9 (2008)
7. K.J. Knox, R. Symes, J.P. Reid, Chem. Phys. Lett. **487**, 165 (2010)
8. T.C. Bond, R.W. Bergstrom, Aerosol Sci. Technol. **40**, 1 (2006)
9. K.A. Fuller, J. Opt. Soc. Am. A Opt. Image Sci. Vis. **12**, 893 (1995)
10. R.E. Benner, P.W. Barber, J.F. Owen, R.K. Chang, Phys. Rev. Lett. **44**, 475 (1980)
11. H.M. Tzeng, K.F. Wall, M.B. Long, R.K. Chang, Opt. Lett. **9**, 499 (1984)
12. J.D. Eversole, H.B. Lin, A.L. Huston, A.J. Campillo, P.T. Leung, S.Y. Liu, K. Young, J. Opt. Soc. Am. B Opt. Phys. **10**, 1955 (1993)
13. E.L. Florin, J.K.H. Horber, E.H.K. Stelzer, Appl. Phys. Lett. **69**, 446 (1996)
14. J.E. Reiner, A.M. Crawford, R.B. Kishore, L.S. Goldner, K. Helmerson, M.K. Gilson, Appl. Phys. Lett. **89**, 013904 (2006)
15. R. Symes, Ph.D. thesis: Characterising aerosols using linear and nonlinear optical spectroscopies, University of Birmingham, Birmingham, UK, 2005
16. J. Buajarern, Ph.D. thesis: Fundamental studies of inorganic and organic aqueous aerosols using optical tweezers, University of Bristol, Bristol, UK, 2007
17. J. Buajarern, L. Mitchem, J.P. Reid, J. Phys. Chem. A **111**, 9054 (2007)
18. J. Buajarern, L. Mitchem, J.P. Reid, J. Phys. Chem. A **111**, 11852 (2007)
19. J. Buajarern, L. Mitchem, J.P. Reid, J. Phys. Chem. A **111**, 13038 (2007)
20. R.A. Alberty, R.J. Sibley, *Physical Chemistry* (Wiley, New York, 1997)
21. G.A. Reynolds, K.H. Drexhage, Opt. Commun. **13**, 222 (1975)
22. H. Du, R.C.A. Fuh, J.Z. Li, L.A. Corkan, J.S. Lindsey, Photochem. Photobiol. **68**, 141 (1998)
23. V.P. Cheuv, O.D. Kameneva, V.M. Nikitchenko, M.M. Asimov, S.N. Kovalenko, J. Appl. Spectrosc. **57**, 717 (1993)
24. The future of fluorescence. Invitrogen (2008)
25. W.F. Hsieh, J.B. Zheng, R.K. Chang, Opt. Lett. **13**, 497 (1988)
26. H.B. Lin, A.J. Campillo, Phys. Rev. Lett. **73**, 2440 (1994)
27. J.B. Snow, S.X. Qian, R.K. Chang, Opt. Lett. **10**, 37 (1985)

28. J.Z. Zhang, D.H. Leach, R.K. Chang, Opt. Lett. **13**, 270 (1988)
29. W.P. Acker, D.H. Leach, R.K. Chang, Opt. Lett. **14**, 402 (1989)
30. D.H. Leach, W.P. Acker, R.K. Chang, Opt. Lett. **15**, 894 (1990)
31. V. Shcheslavskiy, G. Petrov, V.V. Yakovlev, Appl. Phys. Lett. **82**, 3982 (2003)
32. R. Barille, L. Canioni, L. Sarger, G. Rivoire, Phys. Rev. E **66**, 067602 (2002)
33. F. Kajzar, J. Messier, Phys. Rev. A **32**, 2352 (1985)
34. D.R. Lide (ed.), *The CRC Handbook of Chemistry and Physics*, 89th edn. (CRC Press/Taylor and Francis, Boca Raton, 2009)
35. M.J. Snare, F.E. Treloar, K.P. Ghiggino, P.J. Thistlethwaite, J. Photochem. **18**, 335 (1982)
36. J.H. Eickmans, W.F. Hsieh, R.K. Chang, Opt. Lett. **12**, 22 (1987)
37. K.H. Fung, D.G. Imre, I.N. Tang, J. Aerosol Sci. **25**, 479 (1994)
38. R. Symes, R.M. Sayer, J.P. Reid, Phys. Chem. Chem. Phys. **6**, 474 (2004)
39. L. Mitchem, J.P. Reid, Chem. Soc. Rev. **37**, 756 (2008)
40. J.D. Eversole, H.B. Lin, C.D. Merritt, A.J. Campillo, Appl. Spectrosc. **48**, 373 (1994)
41. G. Chen, R.K. Chang, S.C. Hill, P.W. Barber, Opt. Lett. **16**, 1269 (1991)
42. P. Chylek, H.B. Lin, J.D. Eversole, A.J. Campillo, Opt. Lett. **16**, 1723 (1991)
43. H.B. Lin, A.L. Huston, J.D. Eversole, B.L. Justus, A.J. Campillo, J. Opt. Soc. Am. B Opt. Phys. **3**, 250 (1986)
44. P.M. Aker, P.A. Moortgat, J.X. Zhang, J. Chem. Phys. **105**, 7268 (1996)
45. S.C. Hill, R.E. Benner, in *Optical Effects Associated with Small Particles*, vol. 3, ed. by P.W. Barber, R.K. Chang (World Scientific Publishing Co., Singapore, 1988)
46. J.P. Reid, *Size and Compositional Analysis of Aerosols* (2007)
47. Leach et al., Faraday Discuss. **137**, 403 (2008)
48. J. Buajarern, L. Mitchem, A.D. Ward, N.H. Nahler, D. McGloin, J.P. Reid, J. Chem. Phys. **125**, 114506 (2006)

Chapter 6
Ultra-Sensitive Absorption Spectroscopy of Optically-Tweezed Aerosol Droplets

The characterisation of light absorption by aerosol droplets is important for both the compositional analysis of particles and for determining the optical properties of aerosols, including the single-scattering co-albedo. Knowledge of the optical properties of aerosol particles in the atmosphere is crucial for understanding the effects of aerosol on radiative forcing, yet they remain poorly characterised.[1]

In the work presented in this chapter, a new experimental tool for probing the absorption properties of aerosol droplets on a single-particle basis will be demonstrated [1]. Optical tweezers are used to isolate individual water droplets and changes in the power of the trapping laser beam are used to induce changes in droplet absorption and hence in the droplet temperature. The accompanying change in the equilibrium size of the droplet can be used to derive the temperature change, which in turn can be used to determine the level of absorbance provided by the droplet. By simultaneously isolating two droplets using the dual trapping approach, comparative absorption measurements can be made. Despite the short optical pathlength for absorption that is available in the case of microdroplets, this has been shown to be a highly sensitive technique; temperature changes of a few milli-Kelvin are detectable for a micron-sized aqueous droplet. These temperature changes correspond to the measurement of absorbances of $<2 \times 10^{-7}$ over an optical pathlength of <10 μm or a sample volume of <1 pL.

As the new experimental strategy described is a single-particle technique it is also able to resolve the effect of particle composition on aerosol optical properties. It is anticipated that the technique will be applicable to the study of atmospherically-relevant systems such as aqueous droplets containing black or brown carbon. This will be valuable for enabling the currently large and complicated data sets associated with the optical properties of carbonaceous aerosol to be resolved on the basis of particle morphology, mixing state and the extent of chemical aging and

[1] See Chap. 1 for more details.

K. J. Knox, *Light-Induced Processes in Optically-Tweezed Aerosol Droplets*,
Springer Theses, DOI: 10.1007/978-3-642-16348-7_6,

transformation [2]. The optical properties of aqueous droplets containing organic and elemental carbon are of particular interest as it has been shown by experiment and theory that the absorption effects of the carbon could be enhanced as a result of lensing by the water [3]. Furthermore, this new method can be applied to the analysis of trace species contained in a microdroplet, with a lower limit of sensitivity that is determined only by the very weak absorption by the solvent and the minimum size change that is detectable spectroscopically. The advent of microfluidic and 'lab-on-a-chip' technologies makes it highly desirable to develop techniques for the measurement of optical absorption which require only small sample volumes [4–6].

6.1 Previous Studies

Optical absorption spectroscopy is a technique that is widely used for the detection of trace species and for the analysis of chemical composition [7, 8]. Making sensitive measurements of absorption for microdroplets is challenging because of the short optical pathlengths involved. Moreover, for techniques which measure total light extinction from particles it can be difficult to differentiate the losses resulting from absorption from those arising from light scattering, which often dominates over absorption [9].

The first measurement of a single particle absorption spectrum was reported in 1984 by Arnold et al. for a strongly absorbing aqueous ammonium sulphate droplet with an imaginary part of the refractive index of ~ 0.7 illuminated with light of wavelength ~ 9 μm [10]. A droplet was isolated using an electrodynamic balance (EDB) and cycles of heating and cooling induced via intermittent illumination with infrared light resulted in evaporation and growth of the droplet, respectively. The modulation of the wavelength shift of a cavity resonance in the Mie-scattered light arising from optical absorption and heating was used to monitor the resulting size change of the droplets. In this study, quantitative size information was not extracted; instead the magnitude of the wavelength shift was used to determine a relative absorption spectrum.

Three techniques for aerosol absorption studies were proposed by Lin and Campillo [9]. The first technique, phase fluctuation optical heterodyne spectroscopy, is based on a Mach–Zehnder interferometer. A flow of aerosol particles is exposed to a heating laser at a wavelength that is absorbed by the particles. A second laser beam, the 'reference', is divided using a beam splitter and directed along two paths. The reference beam travels directly towards a detector, while the 'signal' beam passes close to the aerosol particles before reaching the detector. The signal arising when the two beams are recombined at a detector depends on the difference in pathlength between the two beams. As a result of particle absorption, the buffer gas near to the aerosol flow will be elevated in temperature and have a lower refractive index than the buffer gas far from the particles or along the path followed by the reference beam. Thus, the heating of the bath gas will

affect the relative phase of the two beams when they are recombined. The absorbance of the aerosol particles can be derived by monitoring changes in the intensity of the signal when the two beams are recombined. Absorption by water vapour limits the sensitivity of this technique.

The second proposed method [9], photothermal modulation of Mie-scattered light, is very similar to the method of Arnold et al. described above. A variable wavelength laser operating in the infrared is used to heat and modulate the temperature, and hence size, of flows of ammonium sulphate and bisulphate droplets or of single droplets isolated using an EDB. The modulation of the wavelength of Mie resonances in the light scattered from a second laser is used to monitor the size change. In this study quantitative size information was again not extracted. For the flows of droplets, the size of the wavelength shift of a Mie resonance in the scattered light was assumed to be linearly proportional to the particle absorption, leading to relative absorption spectra being obtained. For the single isolated droplets no quantitative absorption data were reported. In a later publication this method was extended; a droplet that was isolated using an EDB was repeatedly exposed to laser heating and the evolving droplet size explicitly determined with high time resolution using Mie scattering theory [11]. The rate of heat and mass transfer during droplet growth events was modelled and used to determine the droplet temperature with and without laser heating. This approach predicted the temperature elevation of a droplet following illumination with the infrared laser, but no attempt was made to determine the absorption coefficient.

The final method proposed was photophoretic force spectroscopy [9]. An unevenly-heated particle will exhibit a temperature difference across its surface and colliding gas-phase molecules will leave with velocities which depend on the temperature of the surface at the position where they collide. As a result, the molecules will impart differing momentum to the particle and it will undergo light-induced motion. Relative single particle absorption spectra were obtained by this method. Depending on the relative temperatures of the front face and back face of the droplet, dependent on the magnitude of the absorption coefficient, positive or negative photophoretic effects can be observed in which the force exerted on the particle is either in the direction of laser beam propagation or in the backscattering direction.

In 1991 Davis and co-workers demonstrated that the absorbance of pure microdroplets can be measured by comparing the evaporation rates of electrostatically-levitated laser-heated droplets with those predicted theoretically [12]. The theoretical treatment of the mass transfer depends on the droplets being free from solutes and this method is therefore not applicable to aqueous droplets containing solutes. Davis and co-workers also demonstrated that as the force on an illuminated sphere arising from radiation pressure, termed the radiometric force, depends on the scattering and absorbing efficiencies of the sphere, measurements of this force can allow determination of the absorbance of a microdroplet. The radiometric force was calculated by considering the electrostatic force necessary to levitate the droplet with and without laser illumination. From knowledge of the scattering efficiency of the droplet, the absorption efficiency could be determined from the measured force.

Campillo et al. have used microdroplet resonant fluorescence emission lineshapes to study absorption by the broadband absorber nigrosine in a droplet train experiment [13].[2] The fluorescence intensity profile serves as a marker for absorption: when the resonant fluorescence wavelength overlaps with strong absorption by the nigrosine, the intensity of the resonant fluorescence is reduced.

The applications of microdroplet absorption behaviour for lab-on-a-chip techniques have been considered by Chiu et al. They have proposed laser-induced heating of optically-isolated aqueous droplets in a condensed phase organic medium as a means to control precisely the size of the droplets for the purpose of controlling nanoscale reactions for lab-on-a-chip technologies and for studying concentration-dependent phenomena such as protein crystallisation [14]. The last represents a bottleneck in the ongoing effort by the biochemistry community to characterise the three-dimensional structures of large numbers of proteins [15].

Recently Zare et al. have reported two highly-sensitive bulk liquid-phase absorption techniques. While typical UV–visible detection systems have a sensitivity limit of 1×10^{-5} absorbance units (AU) over a pathlength of ~ten millimetres, in 2005 they reported a method which used continuous-wave cavity ring-down spectroscopy (CRDS) capable of measuring absorbances of 2×10^{-7} over a sample pathlength of 300 μm [16]. In 2007 they reported a coaxial thermal lens detector capable of measuring absorbances of 3.5×10^{-8} over a sample pathlength of 200 μm [4].

The method described in this chapter represents the first application of optical tweezers to the study of absorption by single aerosol particles. It is the first method to use a combination of precise droplet sizing achieved via CERS and equilibrium Köhler theory to determine the droplet temperature change. Relying on measurements of the equilibrium droplet size, it represents the first method for measuring absolute microdroplet absorbances without the need to fit heat and mass transfer equations. As a result, precise knowledge of the droplet environment and of the time dependence of the droplet size changes is not necessary. The method presented here is the first demonstration of the use of optical absorption spectroscopy to measure weak absorption (imaginary part of the refractive index $\sim 2 \times 10^{-9}$, absorption coefficient $\sim 5 \times 10^{-4}$ cm^{-1}) in micron-sized, sub-picolitre volume droplets.

6.2 Light Extinction by Particles

The optical cross-section for the total light extinction by a particle, C_{ext}, can be expressed as the sum of the individual cross-sections for absorption and scattering [17]:

[2] See Sect. 5.3.4.2 for more details.

$$C_{ext} = C_{abs} + C_{sca} \tag{6.1}$$

where C_{abs} and C_{sca} are the scattering and absorption cross-sections, respectively. Any technique which seeks to probe particle absorbances must be able to discriminate between these two mechanisms of light extinction. Extinction of light by absorption involves the conversion of the light energy to a different form, for example via excitation of the internal vibrational modes of the molecules of a medium. As the excited molecules relax collisionally, the absorbed energy is ultimately converted to heat. Measuring changes in particle temperature is a convenient means by which to study absorption.

The extinction efficiency, Q, is defined as the ratio of the cross-section for light extinction to the geometrical cross-section of the particle, G_{xs}:

$$Q = \frac{C}{G_{xs}} \tag{6.2}$$

where $G_{xs} = 4\pi r^2$ for a spherical particle of radius r.

Q_{ext}, the total extinction efficiency, includes contributions from absorption and scattering and can be expressed as the sum of the individual efficiencies for absorption, Q_{abs}, and scattering, Q_{sca}, [17]:

$$Q_{ext} = Q_{abs} + Q_{sca} \tag{6.3}$$

The single scattering albedo, ω, and co-albedo, ω', are key quantities for climate modelling. They describe the fractional contribution of scattering and absorption to the total light extinction and are defined as [17]:

$$\omega = \frac{Q_{sca}}{Q_{ext}} \tag{6.4}$$

$$\omega' = \frac{Q_{abs}}{Q_{ext}} \tag{6.5}$$

Figure 6.1 shows the variation of Q_{ext} with particle size for a droplet with a composition of 20 g L^{-1} NaCl undergoing plane wave illumination with 532 nm wavelength light, calculated from Mie scattering theory using a programme based on the code of Barber and Hill [18]. The real part of the refractive index for this solution, m, is 1.3387 [19]. Water is assumed to be the only absorbing species in the droplet and at this wavelength the imaginary part of the refractive index, k, is 1.9×10^{-9} [20]. The sharp peaks in Q_{ext} are associated with cavity resonances; when the wavelength of the trapping laser is resonant with a cavity mode of the droplet, Q_{ext} is enhanced [21].

Figures 6.2a, and 6.3a show the separate contributions to Q_{ext} from Q_{sca} and Q_{abs}, respectively, for the same droplet, as its radius varies from 3 to 8 μm. Figures 6.2b and 6.3b show an expanded region of the plots. The smoothly varying part of each of the curves arises from non-resonant scattering or absorption, while the sharp features arise from resonant scattering or absorption at droplet size

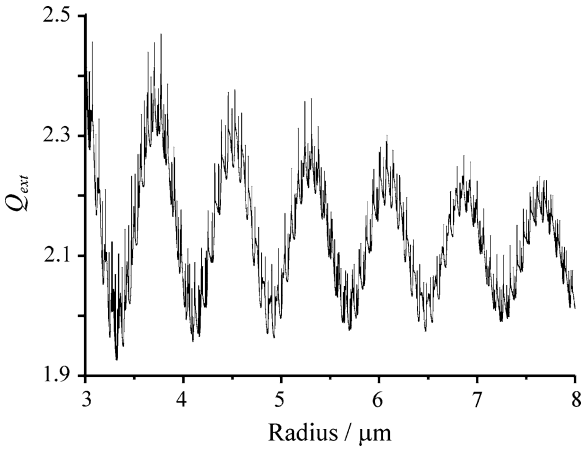

Fig. 6.1 Q_{ext} as a function of radius for a droplet with a composition of 20 g L^{-1} NaCl illuminated with 532 nm wavelength light

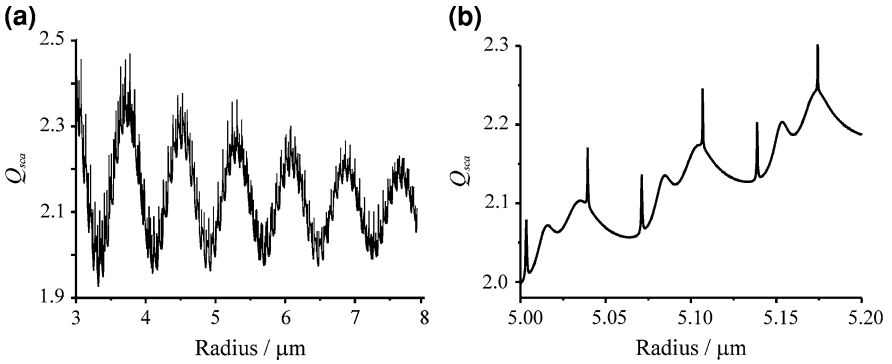

Fig. 6.2 Q_{sca} as a function of radius for a droplet with a composition of 20 g L^{-1} NaCl illuminated with 532 nm wavelength light

parameters commensurate with whispering gallery modes (WGMs). On resonance the absorption efficiency may increase by several orders of magnitude.

It can be seen that scattering dominates absorption for a weakly absorbing droplet such as this. Despite the dominance of scattering over absorption for weakly absorbing aqueous particles, the technique presented here is capable of quantifying the level of non-resonant absorption by such particles. The behaviour and benefits of resonant heating have yet to be fully addressed.

6.3 The Steady State Temperature of Optically-Tweezed Droplets

An optically-tweezed aerosol droplet constantly experiences an optical field and as a result the droplet temperature is elevated above that of the surrounding gas. If the laser power is maintained at a constant level a steady state is achieved with

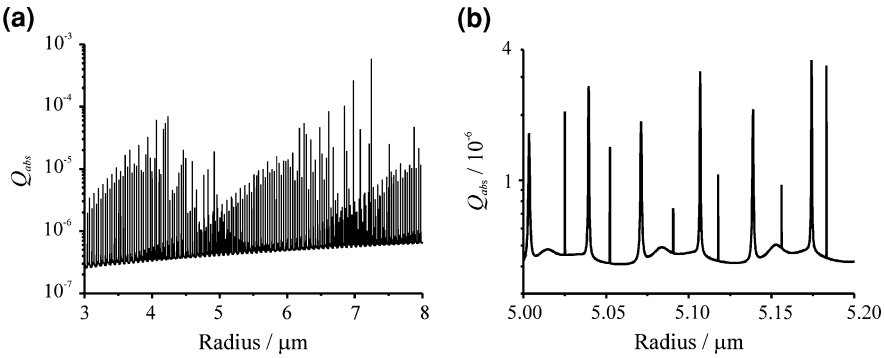

Fig. 6.3 Q_{abs} as a function of radius for a droplet with a composition of 20 g L^{-1} NaCl illuminated with 532 nm wavelength light

the heat conduction away from the droplet balancing the heat generated within the droplet by optical absorption. In this steady state the partial pressure of the water vapour at the droplet surface is equal to that of the surrounding gas and no net evaporation of, or condensation onto, the droplet occurs.

It has previously been reasoned by Reid and co-workers that the temperature elevation of an optically-tweezed aqueous droplet which is not resonant with the trapping laser beam is $\ll$1 K [22]. By comparing the energy absorbed by an illuminated spherical particle with heat conduction away from its surface, and neglecting evaporative cooling, the increase in droplet temperature, ΔT, as a result of light absorption can be approximated by [23]:

$$\Delta T = \frac{IQ_{abs}r}{4k_a} \tag{6.6}$$

where I is the irradiance (W m^{-2}), r is the particle radius (m) and k_a is the thermal conductivity of the surrounding medium (W m^{-1} K^{-1}).

As can be seen in Fig. 6.3, Q_{abs} varies significantly with droplet size, depending on whether the illuminating laser is resonant with the droplet cavity. When the wavelength of the trapping laser is resonant with a cavity mode of the droplet Q_{abs} will be significantly higher, by as much as three orders of magnitude. The effects of resonant absorption in microdroplets have been reported by Popp et al., who observed discrete jumps in the resonant wavelengths for a slowly-evaporating glycerol/water droplet, attributed to resonant absorption periodically raising the droplet temperature and causing a change in refractive index, and therefore the resonant wavelengths [24]. The effect of resonant absorption will be less significant in more volatile, purely-aqueous droplets as the onset of resonant absorption will cause partial evaporation of the droplet. This will change the droplet size and solute concentration and thus refractive index, and the input wavelength of the laser will therefore only remain resonant with the droplet for a very short period of time.

It must be noted that treatments which rely on a consideration of Q_{abs} assume plane wave illumination. So, while they are useful for establishing a qualitative understanding of microdroplet absorption, they are not strictly applicable to the droplets used in these measurements, which are illuminated with a tightly-focussed laser beam. It will be shown that a straightforward Beer-Lambert law analysis may instead be used to gain a quantitative description of the absorption of the trapping beam by optically-tweezed aerosol droplets.

The Beer-Lambert law describes the attenuation of light in a medium as a result of absorption [25]:

$$I = I_0 \exp(-\alpha_a l) \tag{6.7}$$

where I_0 and I are the incident and transmitted light intensities, respectively, α_a (cm^{-1}) is the absorption coefficient and l is the optical pathlength for absorption.

As introduced in Chap. 3, α_a is related to k by [18]:

$$k = \frac{\alpha_a \lambda}{4\pi} \tag{6.8}$$

Where λ is the wavelength of the illuminating light. α_a is related to C_{abs} as follows:

$$\alpha_a = C_{abs} N \tag{6.9}$$

where N is the number density of the absorbing species.

6.4 Experimental Determination of ΔT

In the measurements described here, changes in optical irradiance are used to induce droplet temperature changes. These temperature changes are accompanied by evaporation of water from the aqueous aerosol droplets or condensation of water onto the droplets. The changes in droplet size are monitored using CERS and Mie scattering theory and are used as a measure of the energy absorbed by the droplets.

A change in the trapping laser power induces a change in the droplet temperature through a change in the absorbed energy flux, leading to a change in the droplet water vapour pressure. If the laser power is increased the droplet temperature increases, causing the vapour pressure of water at the droplet surface to increase. A concentration gradient of water vapour in the gas phase is thus established, giving rise to diffusion of water vapour away from the droplet and a consequent decrease in droplet size. As the droplet size decreases the dissolved solute concentration increases, lowering the vapour pressure and counteracting the effect of the temperature elevation, in accordance with the solute effect [26].[3] As a result, the droplet

[3] As introduced in Sect. 2.1.2

will reach a new equilibrium size at the higher temperature, but remain in equilibrium with the surrounding partial pressure of water, which is determined by the ambient relative humidity (RH). Conversely, if the trapping power is reduced the droplet temperature decreases, leading to a net flux of water vapour to the droplet surface and an increase in droplet size. This results in a dilution of the droplet solutes and an increase in the vapour pressure of water at the droplet surface, until a new equilibrium size is established at the lower droplet temperature.

If two droplets are trapped simultaneously, the trapping power for one, referred to as the sample droplet, can be varied while that for the other, the control droplet, is maintained at a constant level. Figure 6.4 shows the evolution of the WGM wavelengths for such a measurement; open black circles show the recorded resonant wavelengths, while closed blue squares show the best fit simulated spectra from the droplet sizing process. Figure 6.4a shows the WGMs of the sample droplet following two trapping power changes. The trapping powers were determined using the dual objective technique as discussed in Chap. 3 [27]. At ~750 s the trapping power is increased from 19.4 ± 1.0 to 23.1 ± 1.0 mW, causing the

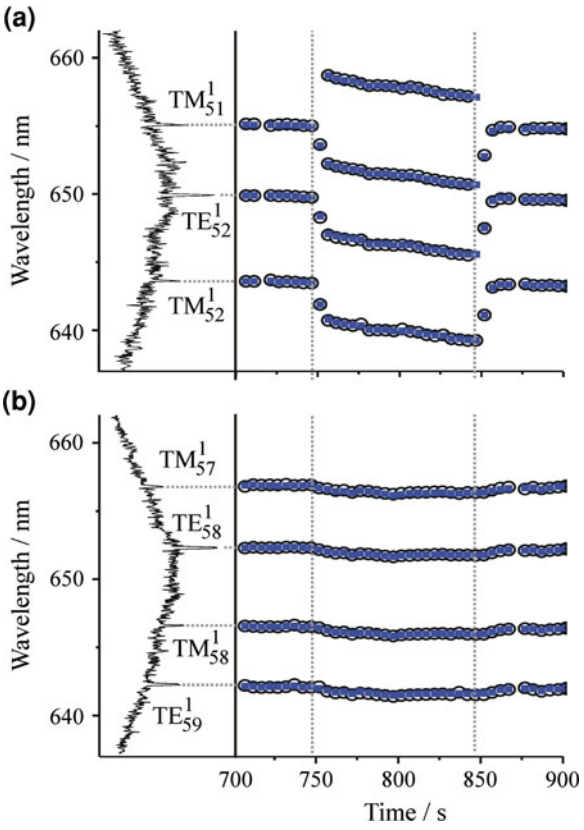

Fig. 6.4 **a** The evolving WGM wavelengths for the sample droplet between 700 and 900 s and the Raman fingerprint at 700 s. The *closed blue squares* and *open black circles* show the calculated and recorded wavelengths, respectively. **b** As (**a**), but for the control droplet

droplet to adopt a smaller equilibrium size; as a consequence the WGMs are observed to shift to shorter wavelengths, consistent with a reduction in droplet radius of $\sim$20 nm and a loss of $\sim 1.7 \times 10^{11}$ water molecules from the droplet. At $\sim$850 s the trapping power is decreased back to its original level and the droplet size increases back to almost the original level, lower in radius by $\sim$2 nm. The difference arises from a declining RH in the trapping chamber. The finite time over which the size changes occur arises from the time required to change the trapping power by adjusting the vertical position of the neutral density filter used to control the power. Figure 6.4b shows the evolution of the WGM wavelengths for the control droplet, for which the trapping power is held constant at 15 mW. This droplet also shows a decrease in radius of $\sim$2 nm, confirming that the RH of the chamber is declining with time. Although the droplets are separated by $\sim$30 μm in space, a small amount of cross-talk between the traps can be seen, with the control droplet showing a slight modulation in size corresponding to a decrease of $\sim$4 nm in radius.

The absorption measurement presented here is based on a consideration of the two competing factors which determine the droplet vapour pressure: solute concentration and temperature. From the measured droplet sizes before and after the change in droplet irradiance the apparent change in the vapour pressure of water at the droplet surface, $p_{w,d}$, which would arise from the solute effect can be determined. In fact no overall change to $p_{w,d}$ occurs once a stable size is re-established, provided that the RH has not changed, and the temperature of the droplet must therefore have changed. The droplet temperature change can be determined from the Clausius-Clapeyron relation as that which is necessary to counteract the solute effect on $p_{w,d.}$ This approach is shown schematically in Fig. 6.5 for the case of an increase in the trapping laser power for an aqueous NaCl droplet. The lower solid line represents the variation in wet particle radius with droplet vapour pressure, determined using the empirical relationship introduced in Chap. 2 as Eq. 2.9. The upper solid line is the result of applying a 1 mK

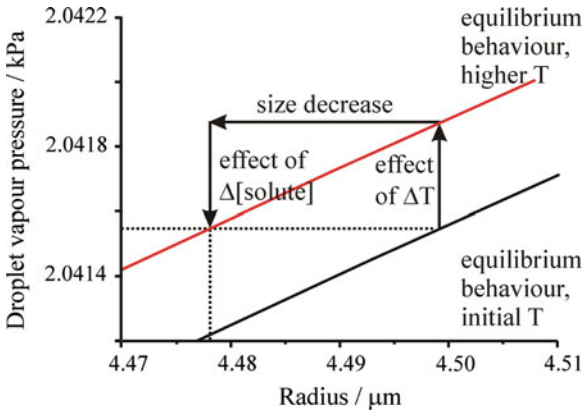

Fig. 6.5 Schematic illustration of the analytical approach used to determine the droplet temperature change associated with a given droplet size change

temperature increase to the droplet vapour pressures in accordance with the Clausius-Clapeyron relation. The droplet initially has a vapour pressure which is equal to that of the surroundings. However, as the laser power is increased the droplet radius reduces until the solute effect counters the effect of the temperature increase and a new equilibrium size is established, with the droplet vapour pressure maintained equal to that of the surrounding RH.

The sensitivity of this technique is limited by the smallest detectable droplet radius change of ~ 1 nm, which corresponds to the evaporation or condensation of $\sim 1 \times 10^{10}$ water molecules. This corresponds to the detection of a remarkably low temperature change of <0.2 mK for a droplet with a volume of <0.5 pL.

The methods used to quantify each of the two effects on $p_{w,d}$, the solute effect and the temperature effect, will now be discussed in more detail.

6.4.1 Vapour Pressure Change as a Result of Solute Concentration

To determine the magnitude of the solute effect on $p_{w,d}$, the variation of $p_{w,d}$ with wet particle radius, r_w, must be quantified. This can be determined from knowledge of the droplet solute loading and, hence, the dry particle radius, r_d, and from the empirical relationship relating the droplet growth factor (GF) and RH which was introduced in Sect. 2.1.2 [28, 29]:

$$GF = \left[1 + \left(a + bRH + cRH^2\right)\frac{RH}{1 - RH}\right]^{\frac{1}{3}} \tag{6.10}$$

where a, b and c are experimentally-determined constants which are specific to the solute present in the aqueous droplet. This expression can be rewritten in terms of the vapour pressure of water in the gas phase, p_w, and r_w and r_d, using the definitions of the GF and RH given in Chap. 2, Eqs. 2.1 and 2.10, respectively:

$$\frac{r_w}{r_d} = \left[1 + \left(a + b\left(\frac{p_w}{p^0}\right) + c\left(\frac{p_w}{p^0}\right)^2\right)\frac{\left(\frac{p_w}{p^0}\right)}{1 - \left(\frac{p_w}{p^0}\right)}\right]^{\frac{1}{3}} \tag{6.11}$$

where p^0 is the saturated vapour pressure of water at the droplet temperature. A constant droplet temperature of 18 °C, which is the ambient temperature of the laboratory, is assumed for the purposes of determining p^0; this corresponds to a value of p^0 of 2.0644 kPa [30].

Further, the expression can be written in terms of $p_{w,d}$, which is equal to p_w as the droplet is in equilibrium with the surrounding gas-phase partial pressure of water and is large in size allowing the Kelvin surface curvature effect to be neglected:

$$\frac{r_w}{r_d} = \left[1 + \left(a + b\left(\frac{p_{w,d}}{p^0}\right) + c\left(\frac{p_{w,d}}{p^0}\right)^2\right)\frac{\left(\frac{p_{w,d}}{p^0}\right)}{1 - \left(\frac{p_{w,d}}{p^0}\right)}\right]^{\frac{1}{3}} \tag{6.12}$$

The solute mass loading is determined from the composition of the nebulised solution and the size of the droplet when it is initially trapped, and r_d calculated from this using the density of the solute and assuming a spherical geometry. Hence, as r_w is known at all times from the CERS fingerprint of the droplet, so too is the apparent droplet $p_{w,d}$. The vapour pressure change, $\Delta p_{w,d}$, occurring as a result of the solute effect following a trapping power change can therefore be determined from:

$$\Delta p_{w,d} = p^f_{w,d} - p^i_{w,d} \tag{6.13}$$

where $p^f_{w,d}$ and $p^i_{w,d}$ are the apparent final and initial droplet vapour pressures determined from the final and initial droplet equilibrium sizes, respectively. For mixed composition droplets the Zdanovskii, Stokes and Robinson (ZSR) approximation is used to determine the droplet GF from the total wet particle radius, which assumes that each component takes up water independently [28].[4]

It must be restated that the $\Delta p_{w,d}$ determined in this way is only an 'apparent' change; it represents the change that would occur in isolation from a droplet temperature change. In fact the droplet will always be in equilibrium with the partial pressure of water vapour in the surrounding gas phase, which does not change significantly over the course of a trapping power change event. The apparent $\Delta p_{w,d}$ is countered by an equal and opposite change in vapour pressure as a result of the accompanying change in droplet temperature.

As the temperature changes induced are so small, neglecting the refractive index change of the droplet due to the temperature change introduces negligible error to the droplet sizing. The dependence of the wavelength on temperature of a first order resonant mode of transverse electric (TE) polarisation and a mode number of 58 for a 5 μm radius aqueous droplet of 20 g L^{-1} NaCl solute concentration is shown in Fig. 6.6. The dependence was determined by simulating droplet spectra at a range of temperatures using the SCATA programme, taking into account the variation of refractive index with temperature. It can be seen that even for a temperature change of 2 K, which is a factor of 10^3 greater than the temperature changes induced in this technique, the shift in the resonant mode is only $\sim$0.04 nm. This is very small compared to the typical wavelength shifts of $\sim$3 nm induced by the size variation induced by the temperature change.

Thermal expansion of the droplet can also be neglected. In the absence of evaporative loss from or condensation of water onto the droplet, the observed temperature changes of $\sim$2 mK would lead to a change in droplet volume of $\sim 2 \times 10^{-22}$ m^3 for a droplet with a radius of 5 μm, determined using the

[4] See Sect. 2.1.2 for more details.

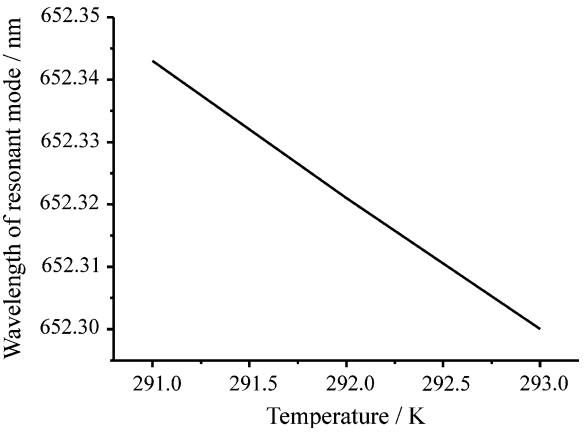

Fig. 6.6 Dependence of the wavelength of a resonant mode (TE polarisation, mode order 1, mode number 58) on temperature for a 5 μm radius droplet with an NaCl concentration of 20 g L^{-1}

thermal expansion coefficient of water at 293 K of 2.06×10^{-4} K^{-1} [30]. This would correspond to a change in droplet radius of $\sim 7 \times 10^{-4}$ nm, very much smaller than the radius changes of ~ 20 nm which result from mass transfer of water to or from the droplet.

6.4.2 Vapour Pressure Change as a Result of Temperature Elevation

The droplet temperature change causing an equal and opposite $\Delta p_{w,d}$ is determined using the Clausius-Clapeyron relation, which describes the variation of pressure with temperature [31]:

$$\ln\left(\frac{p_{w,d}^{f}}{p_{w,d}^{i}}\right) = \frac{\Delta H_{vap}}{R}\left(\frac{1}{T_i} - \frac{1}{T_f}\right) \tag{6.14}$$

where T_i and T_f represent the initial and final droplet temperatures, respectively, and ΔH_{vap} is the heat of vaporisation of water. T_i is assumed to be equal to the chamber temperature of 18 °C and $p_{w,d}^{f}$ and $p_{w,d}^{i}$ are determined using the approach detailed above, allowing T_f to be calculated. It is assumed that ΔH_{vap} does not vary with temperature over the temperature change that occurs during the power change event.

Although a constant chamber temperature that is equal to the ambient temperature of the laboratory of 18 °C is assumed, variations in the chamber temperature will occur because of the periodic cycling of the laboratory air-conditioning system. These temperature changes are, however, slow on the timescale of the droplet temperature changes examined here [32]. Further, the maximum temperature variation in the chamber is ±2 °C, which introduces a maximum error of ±2% to the calculation of the droplet temperature change according to Eq. 6.14.

6.5 Theoretical Determination of ΔT

In order to determine whether the experimentally-determined droplet temperature changes are reasonable, the temperature perturbation accompanying the change in laser power has also been modelled. The diameter of the droplets studied in this work is approximately one order of magnitude larger than the trapping beam waist at the laser focal point. Under these conditions, conventional plane-wave Mie-scattering calculations cannot be used to describe the particle light extinction and absorption efficiencies [33]. The non-uniform distribution of light intensity within the droplet would require a Mie-scattering approach to be extended to a generalised Lorenz-Mie framework [34]. However, as the entire laser beam intensity passes through the droplet, and as the droplet is of homogeneous refractive index, a straightforward Beer-Lambert law analysis of the absorbance can instead be used to predict the temperature change of a tweezed droplet.

The Beer-Lambert law describes the attenuation of light in a medium as a result of absorption, as introduced in Eq. 6.7 above.

The rate of heat generation by absorption, Q_{heat} (J s^{-1}), can be calculated from the Beer-Lambert law and the incident laser power, P (W or J s^{-1}):

$$Q_{heat} = (1 - \exp(-\alpha_a l)) \times P \tag{6.15}$$

where the bracketed quantity represents the fraction of incident energy absorbed, as calculated from the Beer-Lambert law. The pathlength for absorption, l, is equal to the droplet diameter, as illustrated in Fig. 6.7.

The rate of heat loss from the droplet must also be considered. For the small temperature changes considered here conduction is the dominant heat transfer mechanism. This can be demonstrated by considering the Grashof number, Gr, which is the ratio of buoyant to viscous forces for a sphere and is defined as [35]:

$$Gr = \frac{16 g \beta q_s r^4}{k_a v_a^2} \tag{6.16}$$

where g is the acceleration due to gravity, β is the inverse of the mean of the droplet surface temperature and the temperature of the surrounding gas medium, r is the droplet radius, k_a and v_a are the thermal conductivity and kinematic viscosity of the fluid surrounding the droplet, here air, respectively. k_a takes a value of 25.5×10^{-3} W m^{-1} K^{-1} at 291 K and v_a is 15.11×10^{-6} m^2 s^{-1} [30]. q_s is the local heat flux at the droplet surface, which is given by [12]:

$$q_s = -k_a \left(\frac{\partial T}{\partial R} \right)_s \tag{6.17}$$

where R is the radial coordinate.

When buoyant forces dominate the viscous forces, $Gr \gg 1$ and natural convection is significant. However, when $Gr \ll 1$ heat conduction is the dominant mechanism of heat transfer. For a droplet of 5 μm radius surrounded with air at 18 °C,

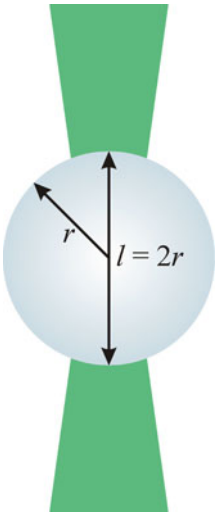

Fig. 6.7 Schematic illustration of illumination geometry of an optically-tweezed droplet

$Gr \sim 5 \times 10^{-26} q_s$. Exact calculation of q_s is not straightforward, but a generous estimate of the temperature gradient of 50 mK nm^{-1} at the droplet surface gives a value for Gr of $\sim 3 \times 10^{-18}$, from which it is clearly valid to assume conduction is the dominant heat transfer mechanism.

The rate of heat flow away from the droplet by conduction, Q_{cond} (J s^{-1}), can be calculated from the steady heat flux away from the droplet at the surface, q_s (J s^{-1} m^{-2}), and the surface area of the droplet:

$$Q_{cond} = q_s \times 4\pi r^2 \tag{6.18}$$

At steady state, the rate of heat conduction away from the droplet through the surrounding air must balance the rate of heat generation by absorption in the droplet, i.e. the sum of the rate of heat generation and conduction away from the droplet must equal zero, therefore:

$$Q_{heat} = Q_{cond} \tag{6.19}$$

and

$$(1 - \exp(-\alpha_a 2r)) \times P = k_a \left(\frac{\partial T}{\partial R}\right) \times 4\pi r^2 \tag{6.20}$$

The steady state temperature change of the droplet can thus be expressed as:

$$\Delta T = \frac{(1 - \exp(-\alpha_a 2r)) \times P}{k_a 4\pi r} \tag{6.21}$$

Equation 6.21 predicts the elevation of the temperature of an optically-tweezed droplet above the ambient chamber temperature. It predicts that the temperature of a water droplet of 5 μm radius illuminated with a typical trapping power of 35 mW of 532 nm light will be elevated above the ambient temperature by $\sim$10 mK. This is consistent with previous reasoning that the droplet temperature elevation is $\ll$1 K [22]. Equation 6.21 is used in this work to determine the droplet temperature change for a given change in trapping power, P, for comparison with the experimentally-determined temperature changes.

6.6 Results and Discussion

Figure 6.8 shows the evolving size of two droplets trapped simultaneously. The compositions of the droplets when initially trapped were 20 g L^{-1} NaCl and 50 g L^{-1} glutaric acid, represented by black and blue circles, respectively. Both droplets were illuminated with a constant trapping power of 22.8 mW. It can be seen that when the trapping power is held constant the sizes of the two droplets track each other as the droplets evaporate in response to a declining RH in the trapping chamber, in accordance with Köhler theory [26]. A step in the size of both droplets occurs at about 1630 s; the magnitude of the size change is different because of the difference in droplet radii. This behaviour has previously been examined in detail for NaCl and glutaric acid droplets by Hanford et al. [36].

If, however, the trapping power is changed, the droplet is observed to respond by growing or evaporating to a new equilibrium size. Figure 6.9 shows droplet size data for the same droplets featured in Fig. 6.4. The trapping power of a control droplet is maintained constant (blue line) while that of the other is varied (black line). The size of the control droplet decreases steadily in response to a slow change in the RH of the environment (blue circles), while that of the other droplet changes size abruptly as a result of a change in trapping power (black circles).

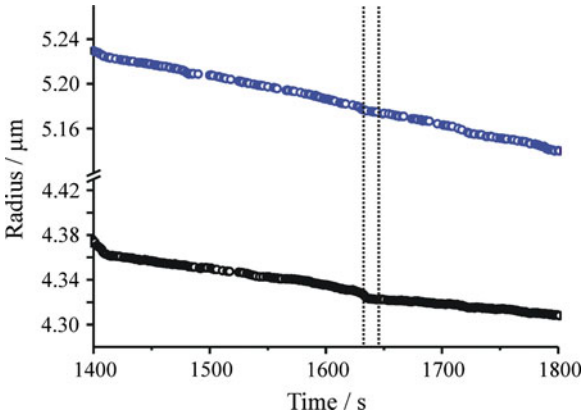

Fig. 6.8 Two simultaneously trapped droplets, of compositions when initially trapped of 20 g L^{-1} NaCl and 50 g L^{-1} glutaric acid, represented by *black* and *blue* circles, respectively

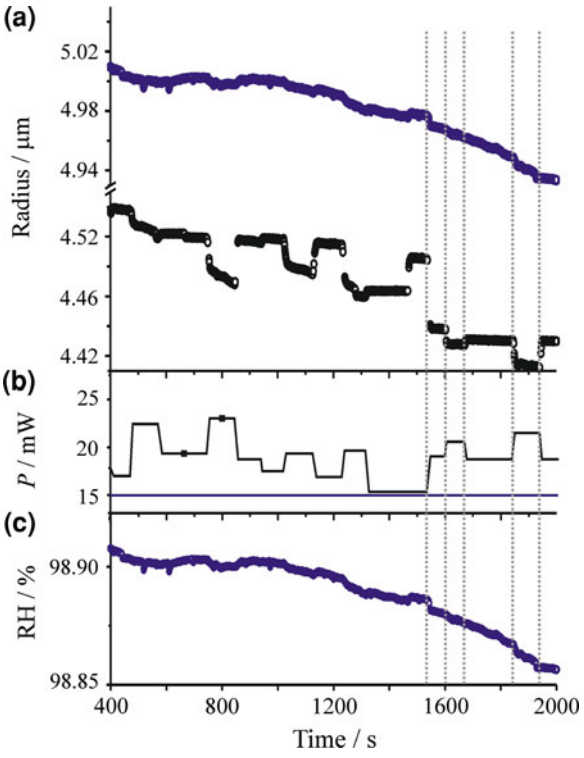

Fig. 6.9 **a** The evolving sizes of the control (*blue circles*) and sample (*black circles*) droplets with time. **b** The time dependence of the trap powers for each droplet. The *solid black* shows the power of the sample droplet trap, while the blue line shows that of the control droplet. **c** The ambient RH, as determined from the control droplet solute loading and wet particle size

The control droplet allows slow changes in the ambient RH to be monitored and means that the sharp changes occurring as a result of laser power changes can be attributed with confidence solely to changes in absorption.

From the size changes the temperature change of the sample droplet can be calculated using the GF approach described above. The observed droplet temperature changes as a function of the trapping power change are shown in Fig. 6.10, separated into changes associated with power increases and decreases. The data recorded when the power is reduced are more scattered than those associated with a power increase, a discrepancy which will be investigated in future work. A Beer-Lambert analysis has also been carried out, assuming that water is the only absorbing species in the droplets, with a value of α_a of 4.3×10^{-4} cm^{-1}. The results are illustrated in Fig. 6.10 by a dotted black line.

The experimental data are consistent with the droplet having a higher α_a than that of pure water. Values of $(1.03 \pm 0.17) \times 10^{-3}$ and $(1.51 \pm 0.16) \times 10^{-3}$ cm^{-1} can be estimated from the data for power decreases and increases, respectively, with an average salt concentration in these measurements of 0.36 M. The larger than expected value of α_a can be attributed to the presence of trace concentrations of absorbing impurities in the solute, here NaCl with a quoted purity of >99.5%.

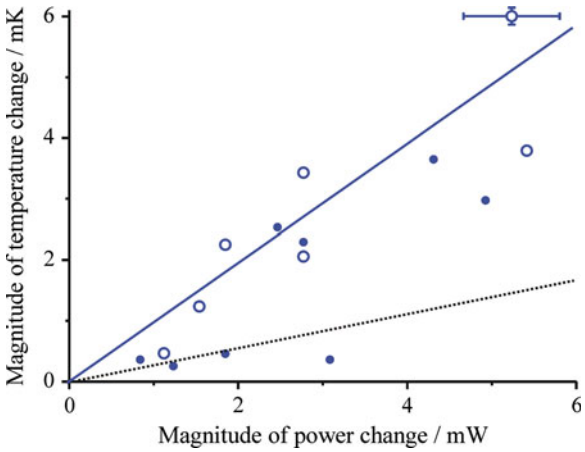

Fig. 6.10 Magnitude of the droplet temperature change observed following change in trap power for the experiment shown in Fig. 6.9 with an average solute concentration of 0.36 M. The *open blue circles* show temperature changes following increases in power, along with a line of best fit. The *closed blue circles* show measurements following a decrease in power. The *dotted black line* shows the calculated temperature response for a droplet in which water is the only absorbing species present. Representative error bars are shown for one measurement

A second experiment on a droplet with a higher NaCl concentration of 0.63 M was carried out and the results for power increases are compared with those for the more dilute droplet in Fig. 6.11. The α_a for the more concentrated droplet is estimated to be $(2.39 \pm 0.19) \times 10^{-3}$ cm^{-1}, confirming that the absorbance of the solution increases with salt concentration.

The measured values of α_a determined from the droplet size increases are shown in Fig. 6.12, along with the value for pure water. The values are consistent with an absorbing impurity present in the NaCl with a concentration of 1 μM and a molar absorption coefficient of $\sim$3000 M^{-1} cm^{-1}, although more data points would be necessary to confirm this.

The size changes used to determine the absorbance of these droplets were $\sim$20 nm in radius. Size changes as small as $\sim$2 nm in radius are, however, detectable spectroscopically using CERS. If the absorption due to the solvent and impurities was reduced through the selection of a solvent which is non-absorbing at the wavelength of interest or a change of illumination wavelength, an absorbance one order of magnitude smaller should therefore provide a resolvable size change. This would correspond to the measurement of an absorbance of $\sim 2 \times 10^{-7}$ over an optical pathlength of <10 μm. The limit of detection for this technique, referred to as the microdroplet growth factor (MDGF) approach, compares well with the recently reported values from Zare et al. using CRDS and coaxial thermal lensing, which were discussed earlier [37]. A summary of the limits of detection for various absorption techniques, arranged in ascending order of sample pathlength, is provided in Table 6.1 [1, 4, 16].

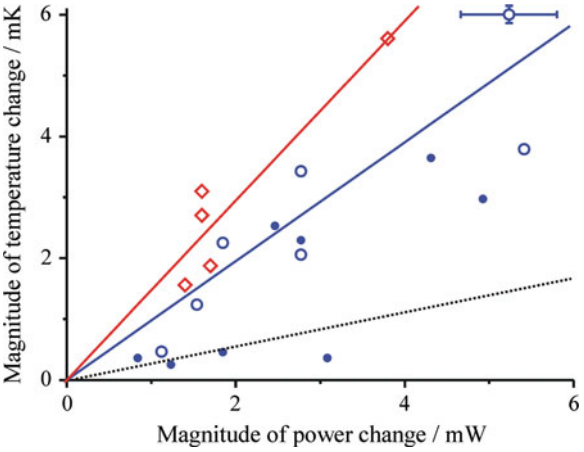

Fig. 6.11 Magnitude of the droplet temperature change observed following change in trap power for droplets with average solute concentrations of 0.36 and 0.63 M. The *open* and *closed blue circles* show temperature changes following increases and decreases in power, respectively, for the 0.36 M droplet. A line of best fit accompanies the *open blue circles*. The *open red squares* and line are for measurements on a droplet of solute concentration 0.63 M. The *dashed black line* shows the calculated temperature response for a droplet in which water is the only absorbing species present

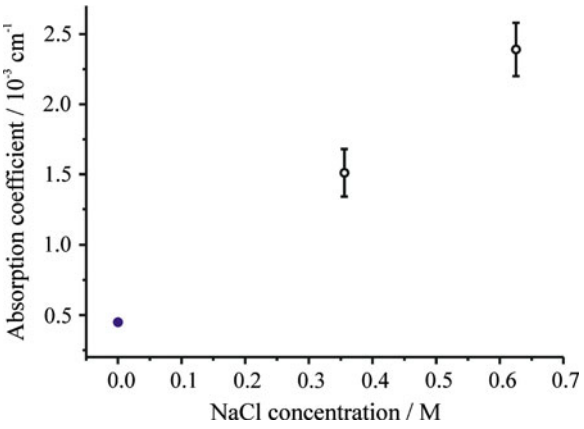

Fig. 6.12 Measured values of α_a and the value for pure water, represented by *open black* and *closed blue circles*, respectively

Recording such low absorbances would require the measurement of size changes of ~ 2 nm. Such measurements would be more susceptible to the effects of small changes in the droplet environment and would rely more significantly on the comparative aspect of the measurement, making use of direct comparisons of the sample and control droplet size changes.

Table 6.1 Summary of the limits of detection for various absorption techniques, arranged in ascending order of sample pathlength [1, 4, 16]

Technique	Sample pathlength/μm	Limit of detection for absorbance
MDGF	< 10	2×10^{-7}
Coaxial thermal lensing	200	3.5×10^{-8}
CRDS	300	2×10^{-7}
Typical UV–visible spectrometer	10,000	5×10^{-7}

6.6.1 Effect of Organics on Aerosol Absorption

The absorption behaviour of a droplet containing a mixture of NaCl and glutaric acid, a carboxylic acid found in tropospheric aerosol, has been studied using this method, demonstrating the applicability of the technique to the study the absorbance of aerosols composed of a mixture of compounds. The size response of the droplet to changes in the trapping power is shown in Fig. 6.13. The droplet contained NaCl at an average concentration of 0.16 M and glutaric acid at an average concentration of 0.26 M.

An analysis of the temperature changes of the droplet is shown in Fig. 6.14. A dotted line represents the predicted temperature changes which would occur if the absorbing impurity in the NaCl was the only absorber present in the droplet, using the absorption coefficient of the absorbing impurity present in the NaCl, which was determined previously.

It can be seen that the presence of the glutaric acid slightly increases the absorbance of the droplet. This may be the result of absorption by the glutaric acid or by an absorbing impurity present in this solute (Acros Organics, 99% pure). If the difference in absorbance can be attributed to the glutaric acid this would be consistent with an absorption coefficient of 9.4×10^{-4} cm^{-1} at 532 nm for this organic solute. Previous measurements made using UV–visible spectrometry [38] and aerosol CRDS [39] have, however, reported no absorbance in the visible by glutaric acid in solution at concentrations ~300 times higher than that used here

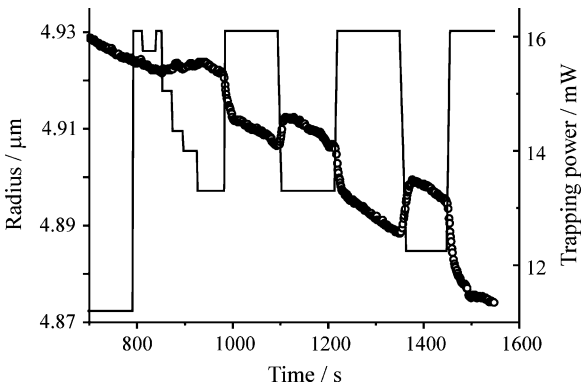

Fig. 6.13 The size response of an aqueous droplet containing NaCl at a concentration of 0.16 M and glutaric acid at a concentration of 0.26 M (represented by *open circles*) to changes in the trapping power (represented by a *solid line*)

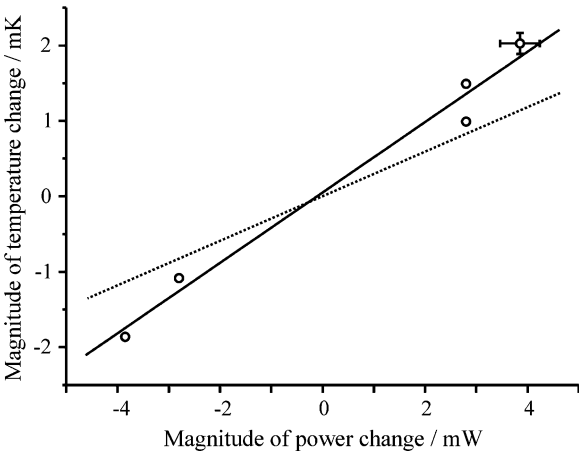

Fig. 6.14 Magnitude of the droplet temperature change observed following change in trapping power for an aqueous droplet containing NaCl at a concentration of 0.16 M and glutaric acid at a concentration of 0.26 M, represented by *open black circles*. A line of best fit accompanies the *open black circles*. The *dashed line* shows the calculated temperature response for a droplet in which the absorbing impurity in the NaCl is the only absorbing species present. Representative error bars are shown for one measurement

and by solid particles, respectively. It is therefore likely that this difference is attributable to an impurity in the glutaric acid, for example with an absorption coefficient of 3600 cm^{-1} M^{-1} at a concentration of 1 μM.

6.7 Further Development

The potential of this technique for studying atmospherically-relevant aerosol particles in order to reduce the uncertainty surrounding the aerosol direct effect on radiative forcing is yet to be explored. Some examples of the applications of the technique which will be investigated in the future are given below.

6.7.1 Use of Varying Illumination Wavelength

The technique described is highly suited to carrying out wavelength-dependent measurements, expected to enable the first measurement of a single-particle absorption spectrum. Such wavelength-dependent measurements can be carried out by introducing a secondary light source to a trapped droplet, independent of the trapping beam. This also offers the potential to investigate the effect of varying the illumination geometry by introducing the heating beam to the droplet along a path other than through the trapping microscope objective.

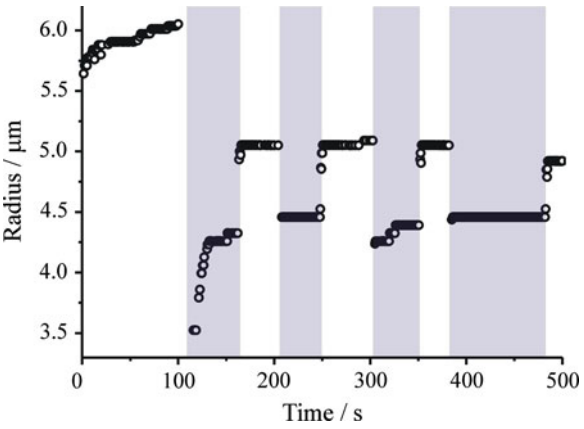

Fig. 6.15 Size change of an aqueous droplet dosed with Coumarin 1 upon illumination with a 408 nm light source. The *shaded regions* indicate illumination with 408 nm laser light

The effect of intermittent 408 nm illumination from a diode laser, in this case also focussed onto the droplet using the microscope objective, on the size of a droplet with a concentration of NaCl when first trapped of 20 g L^{-1}, is illustrated in Fig. 6.15; the shaded regions indicate illumination with 408 nm laser light. The droplet also contains Coumarin 1, the concentration of which when the droplet was first trapped was 6×10^{-4} M. The power of the 408 nm illumination experienced by the droplet was $\sim$0.3 mW and the 532 nm trapping power was 25 mW. The extra irradiance supplied by the 408 nm illumination is a factor of $\sim$3–20 lower than that associated with the changes in the power of the 532 nm trapping beam performed in the measurements described above. The sharp drop in radius, followed by a slower recovery to the new equilibrium size which occurs after $\sim$100 s, is yet to be fully rationalised but is thought to be associated with irreversible photobleaching of some of the Coumarin 1 dye.

As expected, increasing the irradiance experienced by the droplet causes its size to reduce and decreasing the irradiance results in a size increase. It can be seen that the changes in the droplet radius are much larger than those observed for a change in the 532 nm laser power, here $\sim$0.5 μm compared with $\sim$20 nm before. The size change observed corresponds to a temperature change of 120 mK, which is consistent with a droplet absorption coefficient of 0.65 cm^{-1}.

The absorption coefficient of water at 408 nm is slightly lower than that at 532 nm, so the additional heating can not be attributed to elevated absorption by the water content of the droplet. Using the absorption coefficient of Coumarin 1 at 408 nm, which is 2830 cm^{-1} M^{-1} [40], and the concentration of Coumarin 1 present in the droplet, this corresponds to a droplet absorption coefficient of $\sim$1.7 cm^{-1}. This is in reasonable agreement with the measured value for such a preliminary experiment.

The effect of resonant absorption may also have an effect under these conditions. The 408 nm diode laser has a relatively large bandwidth, as shown in Fig. 6.16, meaning that many WGMs fall within its spectral range.

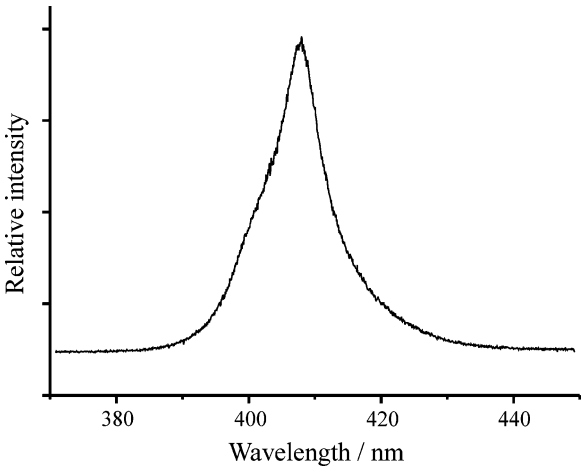

Fig. 6.16 408 nm diode laser emission profile

As a result of the large bandwidth, many wavelengths of the laser diode source may be simultaneously resonant with droplet WGMs. In contrast to the effect of 532 nm resonances, this means that the droplet can remain resonant with the 408 nm light even as the droplet size changes, giving rise to additional droplet heating. There is currently speculation about the importance of WGMs for the resonant heating of aerosol droplets in the atmosphere; it has been suggested that resonant absorption may represent a significant yet unaccounted-for energy sink in the atmosphere [41], while other studies have found the effect to be negligible [42]. The experimental technique described here has the potential to offer a considerable contribution to this debate.

It can be seen from Fig. 6.15 that the droplet size is often remarkably stable. This is a phenomenon related to the effect of resonant heating on the droplet vapour pressure, which complicates the interpretation of the behaviour of this droplet; it has only recently been rationalised and is discussed in detail in a report by Miles et al. [21].

6.7.2 Effect of Droplet Composition

As this is a single-particle technique it is able to resolve the effect of particle composition on aerosol optical properties. The example discussed in Sect. 6.7.1 above illustrates the usefulness of the technique for the study of more strongly absorbing droplets. In addition, the absorbance of aerosol droplets with a wide range of compositions can be studied using this technique; water-soluble organic species can be introduced to the droplet of interest via the initial nebulisation step, while insoluble organic species can be introduced via bombardment of a trapped aqueous droplet with a nebulised flow of droplets of an organic solvent containing the water-insoluble component. This will provide the basis for the study of a wide

range of atmospherically-relevant systems in the future, for example droplets containing black or brown carbon and mixed-phase particles.

6.7.3 Application to Kinetics of Mass Transfer

This absorption technique is based on inducing a small change to the droplet temperature and measuring the *magnitude* of the resulting mass transfer. This suggests an alternative application of this technique: by initiating the temperature change in a rapid and reproducible manner the *rate* of the mass transfer can be measured and used to determine the mass accommodation and evaporation coefficients of water at an aerosol surface. These are quantities of great atmospheric significance. This application of this absorption technique is the subject of Chap. 7.

6.8 Summary

The absorption properties of optically-tweezed aqueous aerosol droplets containing an inorganic and an organic solute have been studied with high sensitivity by varying the power of the 532 nm trapping beam. Changes in droplet size as a result of water uptake or evaporation following a change in the illuminating intensity can be used to quantify the associated particle temperature change and gain insights into the absorption behaviour of the droplet. This approach represents a highly promising technique for probing the absorption of weakly-absorbing particles, with the capability to detect temperature changes of a few milli-Kelvin, corresponding to absorbances of $\sim 2 \times 10^{-7}$ over an optical pathlength of < 10 μm. The dual-trapping approach outlined makes it possible to maintain one droplet at fixed illumination intensity while varying that of another. This allows the size changes of a droplet of interest which occur as a result of a change in trapping power to be distinguished from changes arising from varying environmental conditions. The technique is applicable to the study of droplets with a range of compositions and can be used to make wavelength-dependent measurements.

References

1. K.J. Knox, J.P. Reid, J. Phys. Chem. A **112**, 10439 (2008)
2. T.C. Bond, R.W. Bergstrom, Aerosol Sci. Technol. **40**, 1 (2006)
3. M. Gangl, M. Kocifaj, G. Videen, H. Horvath, Atmos. Environ. **42**, 2571 (2008)
4. F.P. Li, A.A. Kachanov, R.N. Zare, Anal. Chem. **79**, 5264 (2007)
5. M.A. Schwarz, P.C. Hauser, Lab. Chip **1**, 1 (2001)
6. J. Steigert, M. Grumann, T. Brenner, L. Riegger, J. Harter, R. Zengerle, J. Ducree, Lab. Chip **6**, 1040 (2006)

7. T. Yoshihara, M. Murai, Y. Tamaki, A. Furube, R. Katoh, Chem. Phys. Lett. **394**, 161 (2004)
8. J. Hodgkinson, M. Johnson, J.P. Dakin, Appl. Opt. **37**, 7320 (1998)
9. H.B. Lin, A.J. Campillo, Appl. Opt. **24**, 422 (1985)
10. S. Arnold, M. Neuman, A.B. Pluchino, Opt. Lett. **9**, 4 (1984)
11. C.B. Richardson, H.B. Lin, R. Mcgraw, I.N. Tang, Aerosol Sci. Technol. **5**, 103 (1986)
12. T.M. Allen, M.F. Buehler, E.J. Davis, J. Colloid Interf. Sci. **142**, 343 (1991)
13. P. Chylek, H.B. Lin, J.D. Eversole, A.J. Campillo, Opt. Lett. **16**, 1723 (1991)
14. G.D.M. Jeffries, J.S. Kuo, D.T. Chiu, J. Phys. Chem. B **111**, 2806 (2007)
15. A. Doerr, Nat. Methods **3**, 961 (2006)
16. K.L. Bechtel, R.N. Zare, A.A. Kachanov, S.S. Sanders, B.A. Paldus, Anal. Chem. **77**, 1177 (2005)
17. J.P. Reid, L. Mitchem, Annu. Rev. Phys. Chem. **57**, 245 (2006)
18. P.W. Barber, S.C. Hill, *Light Scattering by Particles: Computational Methods* (World Scientific Publishing Co. Inc., Singapore, 1990)
19. R.C. Millard, G. Seaver, Deep-Sea Res. Part A-Oceanographic Res. Pap. **37**, 1909 (1990)
20. D. Segelstein, M.S. thesis: The complex refractive index of water, University of Missouri, Kansas City, USA, 1981
21. R.E.H. Miles, M. Guillon, L. Mitchem, D. McGloin, J.P. Reid, Phys. Chem. Chem. Phys. **11**, 7312 (2009)
22. R.J. Hopkins, L. Mitchem, A.D. Ward, J.P. Reid, Phys. Chem. Chem. Phys. **6**, 4924 (2004)
23. C.H. Chan, Appl. Phys. Lett. **26**, 628 (1975)
24. J. Popp, M. Lankers, K. Schaschek, W. Kiefer, J.T. Hodges, Appl. Opt. **34**, 2380 (1995)
25. A. Beer, Ann. Phys. Chem. **26**, 78 (1852)
26. J.H. Seinfeld, S.N. Pandis, *Atmospheric Chemistry and Physics: From Air Pollution to Climate Change* (Wiley, New York, 1998)
27. N.B. Viana, M.S. Rocha, O.N. Mesquita, A. Mazolli, P.A.M. Neto, H.M. Nussenzveig, Phys. Rev. E **75**, 021914 (2007)
28. A.J. Prenni, P.J. De Mott, S.M. Kreidenweis, Atmos. Environ. **37**, 4243 (2003)
29. G.B. Ellison, A.F. Tuck, V. Vaida, J. Geophys. Res.-Atmospheres **104**, 11633 (1999)
30. D.R. Lide (ed.), *The CRC Handbook of Chemistry and Physics*, 89th edn. (CRC Press/Taylor and Francis, Boca Raton, 2009)
31. S.S. Godavarthy, R.L. Robinson, K.A.M. Gasem, Fluid Phase Equilib. **246**, 39 (2006)
32. J.R. Butler, L. Mitchem, K.L. Hanford, L. Treuel, J.P. Reid, Faraday Discuss. **137**, 351 (2008)
33. J. Lerme, G. Bachelier, P. Billaud, B. M. Broyer, E. Cottancin, S. Marhaba, M. Pellarin, J. Opt. Soc. Am. A Opt. Image Sci. Vis., **25**, 493 (2008)
34. G. Gouesbet, Part. Part. Syst. Charact. **11**, 22 (1994)
35. M.A. Antar, M.A.I. El-Shaarawi, Heat Mass Transf. **38**, 419 (2002)
36. E.K. Bigg, Atmos. Res. **20**, 82 (1986)
37. B. Kuswandi, J. Nuriman, J. Huskens, W. Verboom, Anal. Chem. Acta **601**, 141 (2007)
38. C.E.L. Myhre, C.J. Nielsen, Atmos. Chem. Phys. **4**, 1759 (2004)
39. A.A. Riziq, C. Erlick, E. Dinar, Y. Rudich, Atmos. Chem. Phys. **7**, 1523 (2007)
40. H. Du, R.C.A. Fuh, J.Z. Li, L.A. Corkan, J.S. Lindsey, Photochem. Photobiol. **68**, 141 (1998)
41. H.M. Nussenzveig, Appl. Opt. **42**, 1588 (2003)
42. C.S. Zender, J. Talamantes, J. Quant. Spectrosc. Radiat. Transf. **98**, 122 (2006)

Chapter 7
Kinetics of Aerosol Mass Transfer

It has been demonstrated that a small change in the power of the trapping laser beam can be used to induce a small change in droplet absorption. This gives rise to a small shift in the droplet temperature and hence in the equilibrium size at a given relative humidity. The change in equilibrium droplet size allows the absorption coefficient along the pathlength of the laser beam to be determined [1]. In the absorption studies it is the magnitude of the droplet size change necessary to re-establish equilibrium that is the important quantity to measure.

The following experiments examine the potential for extending this experimental technique to the study of the kinetics of mass transfer to and from an aerosol droplet. In this case it is the rate at which equilibrium is re-established that it is the important quantity to measure. In particular, a new technique for the determination of the mass accommodation coefficient, α, and the evaporation coefficient, γ_e, for water at an aqueous surface is demonstrated. These quantities are central to understanding the kinetics of aerosol mass transfer and although they have been the subject of many experimental studies they remain the subject of much debate [2, 3].[1] Mass transfer of water to and from aqueous droplets containing only inorganic solutes will be studied, as well as the effect of a dissolved organic compound on the rate of mass transfer.

7.1 Overview of the Technique

The technique used to study absorption employs changes in trapping power to initiate small perturbations in the temperature and size of an optically-tweezed droplet; no consideration is given to the rate of the droplet size changes. However, by

[1] See Sect. 2.2.2 for a detailed discussion.

K. J. Knox, *Light-Induced Processes in Optically-Tweezed Aerosol Droplets*,
Springer Theses, DOI: 10.1007/978-3-642-16348-7_7,

modifying the experimental approach it is possible to use these perturbations in droplet size to study the kinetics of aerosol mass transfer.

By initiating the droplet size change in a rapid and controllable way, the rate of the droplet size response can be monitored using CERS and used to derive α or γ_e. Essentially, the technique involves:

- Measuring the time-resolved droplet size evolution.
- Using the size evolution to determine a mass flux.
- Comparing the experimentally-determined mass flux with theoretical predictions in order to determine α or γ_e.

By reducing the pressure in the immediate environment of the droplet, the resistance to uptake resulting from gas-phase diffusion can be reduced, improving the sensitivity of the technique to the surface resistances characterised by α or γ_e.

The technique offers considerable flexibility because of the ability to change the droplet composition, for example by adding surface-active compounds. Further, it has been demonstrated that it is possible to perform a comparative measurement, whereby two droplets of different compositions are trapped and their mass transfer properties studied simultaneously. This appears to be the first simultaneous comparative measurement of the mass transfer processes at two different liquid surfaces.

The experimental approach used in this work is unique in its capability to study both evaporation and uptake under identical experimental conditions. There are further fundamental benefits compared with the existing methods for determining α or γ_e.[2]

Compared with ensemble studies the use of an isolated droplet allows the uptake or evaporation properties of the same, individual droplet to be studied and there will therefore be no averaging of the coefficients determined as a result of the presence of a distribution of droplet compositions in the sample. Further, the theoretical treatment of mass flux commonly applied to studies of aerosol mass transfer is strictly only applicable to isolated particles, as in the technique proposed here. During an uptake or evaporation event the water vapour pressure in the trapping chamber is perturbed negligibly, because of the large chamber volume compared with the volume of water involved in the size change of a single droplet, and the droplet environment is hence at steady state.

Compared with droplet train experiments, the use of a single isolated droplet, the evolving size of which is monitored using CERS, means that a more precise knowledge of droplet size and surface area is possible. Treatment of gas-phase diffusion is more robust for a stationary droplet as the Fuchs–Sutugin relation, even in a modified form, is not considered accurate enough to deal with mass transport to moving droplets [4]; this relation is applicable to the static droplets used in the technique employed here. Further, smaller droplets from a more atmospherically-interesting size regime are used in the proposed technique,

[2] The existing methods for determining α or γ_e were introduced in Sect. 2.2.6.

compared with the ~100 μm diameter droplets typically used in droplet train experiments. Cloud droplet sizes typically vary from a few microns to 50 μm in diameter [5], and results gained by this method are therefore more directly relevant to the growth of cloud condensation nuclei (CCN) in the atmosphere.

While some techniques measure a change in gas-phase composition to derive the mass transfer coefficients, in this technique uptake or evaporation is measured directly via the change in volume of an aerosol droplet and as a result background deposition or evaporation of water at the walls of the experimental chamber is not of concern.

Several studies are performed at saturation ratios which are higher than those that occur in the atmosphere. The experiments described here are carried out under conditions of less than 100% relative humidity, the regime in which many atmospheric aerosol particles will begin their approach to activation. Determining the balance between thermodynamic and kinetic control of droplet growth in this regime is important.

Techniques performed far from equilibrium, for example under conditions of rapid expansion, will suffer from considerable temperature and vapour pressure gradients which in turn will have an effect on mass transfer. As the temperature perturbations induced in the technique used in this work are small, on the order of only a few milli-Kelvin, heat and mass transfer can be decoupled, simplifying the analysis of the experimental data. As a result of the absorption studies the temperature changes initiated are well characterised. Further, the droplet vapour pressure is changed by only ~0.05% during an uptake or evaporation event.

7.2 Advantages of Working at Reduced Pressure

In order to measure the mass transfer coefficients precisely it is necessary to control the experimental conditions so that the resistance to uptake presented by gas-phase diffusion does not dominate that arising from surface resistances. Reducing the pressure at which measurements are made provides a means to reduce the resistance to uptake as a result of gas-phase diffusion.

The effect of the flow regime, characterised by the Knudsen number, *Kn*, can be seen from the simulations presented in Fig. 7.1. This figure shows the variation of the measured uptake coefficient, γ_{meas}, with pressure and hence *Kn*, for a droplet with a radius of 4 μm undergoing an increase in radius of 10 nm for three possible values of α. γ_{meas} is calculated using the resistance model, as described in Chap. 2, for each of the three values of α and with $1/\Gamma_{diff}$ calculated using the Fuchs–Sutugin relation. It can be seen that as *Kn* increases the value of γ_{meas} also increases as the rate of gas-phase diffusion increases and the free molecule regime is approached.[3] γ_{meas} tends to a limiting value of α as the pressure is reduced. These plots are equally applicable to evaporation, with α directly replaced with γ_e

[3] See Sect. 2.2.2 for a more detailed discussion.

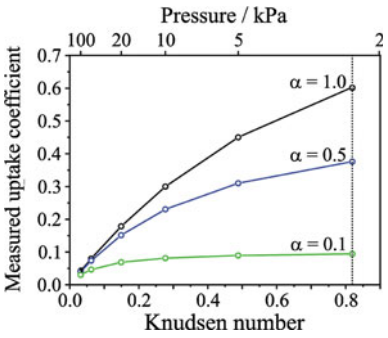

Fig. 7.1 The variation of γ_{meas} with Kn for a 4 μm radius droplet with three possible values of α at a temperature of 293 K. The dotted line corresponds to the vapour pressure of water at this temperature, representing the lower pressure limit attainable

and γ_{meas} replaced by the measured evaporation coefficient, $\gamma_{e,meas}$. The figure spans the continuum regime to the transition regime. The vertical dotted line corresponds to the vapour pressure of water at this temperature, representing the lower pressure limit attainable. Because of the relatively high vapour pressure of water, carrying out experiments on aqueous droplets in the free molecule regime requires the droplet size to be <2 μm. The limitations on trapping and determining the size of small droplets using optical tweezers and CERS make it impossible currently to perform experiments on droplets below this size limit. Hence experiments are restricted to the challenging transition regime, where gas-phase diffusion must be considered in the evaluation of α or γ_e.

Figure 7.1 illustrates the need to reduce the pressure in the experimental chamber. As the pressure is reduced the ability to discriminate between different values of α increases, which increases the sensitivity of the technique to the value of α. In the high Kn limit, γ_{meas} will tend to α, highlighting the desirability of performing these experiments in the free molecule regime.

Figure 7.1 also highlights an experimental challenge associated with determining α; γ_{meas}, and hence the rate of uptake measured, is less sensitive to the value of α as α approaches unity. Discriminating between, for example, $\alpha = 0.5$ and 1.0 is more difficult than between $\alpha = 0.1$ and 0.5. This places demands on the sensitivity of experimental techniques that seek to determine α via measurement of a rate of uptake, particularly if α is found to be high.

7.3 Modelling the Mass Transfer

To find α or γ_e from the measured droplet size evolution it is necessary to model the size response for comparison. A flux iteration approach is taken. For clarity the approach is described here for the case of an uptake event, but it is equally applicable to deriving α or γ_e, from the analysis of a droplet uptake or evaporation event, respectively.

As discussed in detail previously, reducing the trapping power leads to a decrease in droplet temperature [1]. As a result, the partial pressure of water at the

droplet surface is suddenly reduced below the partial pressure of water in the surrounding gas-phase, giving rise to a partial pressure gradient which results in a flux of water towards the droplet surface. Water condenses onto the droplet until dilution of the inorganic solute in the droplet results in an increase of the droplet vapour pressure back to the ambient level and the establishment of a new equilibrium droplet size at the new, slightly lower, temperature.

Determining the initial partial pressure gradient of water before any water vapour has condensed is an important step in modelling the mass transfer and relies on knowing the solute loading of the droplet with high accuracy. The initial partial pressure gradient is determined by considering the effect of the sudden change in droplet temperature on the droplet vapour pressure, $p_{w,d}$. As discussed in Sect. 6.4, the effect of the temperature change on the droplet vapour pressure is equal and opposite to the change in vapour pressure which would arise from the change in solute concentration that accompanies the droplet size change. This can be determined by considering the droplet size, r_w, before and after the power change event and the droplet dry particle radius, r_d. As discussed in Chap. 6, the empirical relationship relating the droplet growth factor and the relative humidity can be written as follows [6, 7]:

$$\frac{r_w}{r_d} = \left[1 + \left(a + b\left(\frac{p_{w,d}}{p^0}\right) + c\left(\frac{p_{w,d}}{p^0}\right)^2\right)\frac{\left(\frac{p_{w,d}}{p^0}\right)}{1 - \left(\frac{p_{w,d}}{p^0}\right)}\right]^{\frac{1}{3}} \tag{7.1}$$

where p^0 is the saturated vapour pressure of water at the droplet temperature. A constant droplet temperature of 18 °C, which is the ambient temperature of the laboratory, is assumed for the purposes of determining p^0; this corresponds to a value of p^0 of 2.0644 kPa [8]. Hence, as r_w is known at all times from the CERS fingerprint of the droplet, so too is the apparent droplet $p_{w,d}$. The vapour pressure change, $\Delta p_{w,d}$, which would occur as a result of the solute effect following a trapping power change can therefore be determined from:

$$\Delta p_{w,d} = p^f_{w,d} - p^i_{w,d} \tag{7.2}$$

where $p^f_{w,d}$ and $p^i_{w,d}$ are the apparent final and initial droplet vapour pressures determined from the final and initial droplet equilibrium sizes, respectively. This is equal to the droplet vapour pressure change arising from the droplet temperature change and gives rise to the partial pressure gradient of water and mass transfer to the droplet.

The partial pressure gradient of water can be expressed in terms of the molar concentration gradient, Δn_g, and the molar flux, J_{meas}, to the droplet is given by[4]:

$$J_{meas} = \gamma_{meas}\frac{\Delta n_g \bar{c}}{4} \tag{7.3}$$

[4] As introduced in Sect. 2.2.2.1.

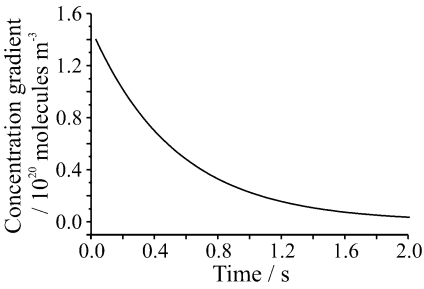

Fig. 7.2 Evolution of Δn_g of water in the gas phase surrounding a 4 μm radius 20 g L^{-1} NaCl droplet undergoing an uptake event with γ_{meas} = 0.031 which results in an increase in radius of 10 nm, occurring at a pressure of 100 kPa and a temperature of 293 K

The mean speed of molecules in a gas, $\bar{c}$ (m s^{-1}), is calculated using [9]:

$$\bar{c} = \sqrt{\frac{8k_BT}{\pi M_a}} \tag{7.4}$$

where M_a is the relative molecular mass of the adsorbing species (kg), k_B is the Boltzmann constant (J K^{-1}) and T is the temperature (K), and assuming a constant chamber temperature of 291 K.

The initial Δn_g is used to calculate the initial J_{meas} for a given value of γ_{meas}. Multiplying by the droplet surface area and a selected time interval, Δt, gives the number of moles of water deposited onto the droplet in this time:

$$J_{meas} \times 4\pi r^2 \times \Delta t = \gamma_{meas} \frac{\Delta n_g \bar{c}}{4} \times 4\pi r^2 \times \Delta t \tag{7.5}$$

The new droplet volume and hence r_w and thus Δn_g can therefore be found. The next time-step in the iteration may then be performed using the new Δn_g. As the iteration proceeds, Δn_g reduces stepwise as water condenses onto the droplet, until the partial pressure of water at the droplet surface is equal to the ambient partial pressure once again. Typically Δt is chosen to be several milliseconds.

Figure 7.2 shows the evolution of Δn_g of water in the gas phase surrounding a 4 μm radius droplet with a solute concentration of 20 g L^{-1} NaCl undergoing an uptake event with γ_{meas} = 0.031 which results in an increase in radius of 10 nm, occurring at a pressure of 100 kPa and a temperature of 293 K.

Simulated droplet size evolutions can be produced for given values of γ_{meas} by plotting the droplet radius at each time interval against time. The value of γ_{meas} for a droplet at a given pressure can be found by comparing the experimentally-determined droplet size evolution with such simulated droplet size evolutions. This is done by creating a calibration plot from a number of simulated size evolutions which relates the $^1/_e$ time of the size evolution to γ_{meas}. A representative calibration plot of this type is shown in Fig. 7.3 for a droplet with a radius of 4.3 μm undergoing a radius change of 4 nm at atmospheric pressure and a temperature of 291 K.

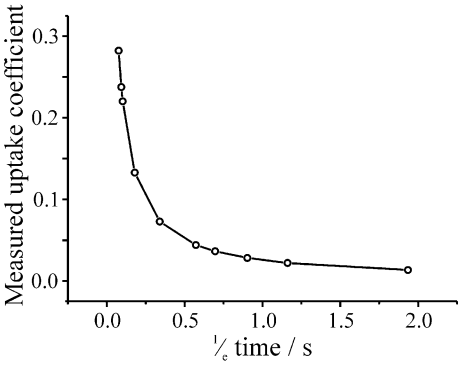

Fig. 7.3 Calibration plot of γ_{meas} against $^1/_e$ time for a droplet with a radius of 4.3 μm undergoing a radius change of 4 nm at atmospheric pressure and a temperature of 291 K

The value of γ_{meas} depends on α and Kn, as illustrated in Fig. 7.1. The value of γ_{meas} determined can therefore be used to determine the value of α by employing the resistance model for gas uptake [3, 10–12][5]:

$$\frac{1}{\gamma_{meas}} = \frac{1}{\Gamma_{diff}} + \frac{1}{\alpha} \tag{7.6}$$

and accounting for the resistance to uptake as a result of gas-phase diffusion, $1/\Gamma_{diff}$. $1/\Gamma_{diff}$ is calculated for the conditions relevant to the experimental run under consideration using the Fuchs–Sutugin relation [5, 10, 12]:

$$\frac{1}{\Gamma_{diff}} = \frac{0.75 + 0.283Kn}{Kn(1 + Kn)} \tag{7.7}$$

where Kn is the dimensionless Knudsen number, given by [3, 5]:

$$Kn = \frac{\lambda_{mfp}}{r} \tag{7.8}$$

where λ_{mfp} is the gas-phase molecular mean free path and r is taken to be the initial droplet radius prior to the laser power change. λ_{mfp} is calculated using [10]:

$$\lambda_{mfp} = \frac{3D_g}{\bar{c}} \tag{7.9}$$

where D_g is the diffusion constant of gas-phase water in the surrounding gas medium ($m^2\ s^{-1}$). In this case the surrounding medium is a mixture of air and water and D_g is calculated using a standard expression for diffusion in a mixture of gases [13]:

$$D_g = \frac{1}{\frac{1}{D_g(w-a)} + \frac{1}{D_g(w-w)}} \tag{7.10}$$

[5] See Sect. 2.2.1.1 for more details.

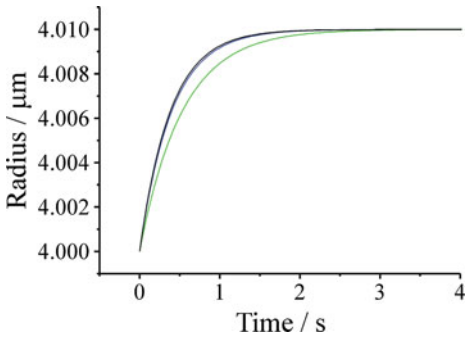

Fig. 7.4 Simulated droplet size change as a function of time for three values of α at 100 kPa and 293 K. The values of α are 1.0, 0.5 and 0.1 (*black*, *blue* and *green lines*, respectively)

where $D_g(w{-}a)$ and $D_g(w{-}w)$ are the diffusion constants for water in air and water in water respectively. $D_g(w{-}a)$ is calculated for each experimental run using [14]:

$$D_g(w-a) = \frac{1.9545 \times 10^{-7} T^{1.6658}}{p_a} \tag{7.11}$$

where p_a is the pressure of air in kPa, given by the measured chamber pressure less the saturated vapour pressure of water at the chamber temperature of 18 °C, 2.0644 kPa [8]. $D_g(w{-}w)$ at 293 K is given by [15]:

$$D_g(w-w) = \frac{1.5 \times 10^{-3}}{p_w} \tag{7.12}$$

where p_w is the pressure of water in kPa. $D_g(w{-}w)$ is calculated assuming a constant p_w of the saturated vapour pressure of water at the chamber temperature. The relative humidity throughout these experiments does not fall below 97% and this assumption therefore introduces an error of less than 3% to the value of $D_g(w{-}w)$. Hence $D_g(w{-}w)$ is assumed to be constant, with a value of 7.27×10^{-4} m^2 s^{-1}. Diffusion constants depend weakly on temperature, but failing to account for this introduces an error of less than 2% to the value of $D_g(w{-}w)$.

Figure 7.4 shows the simulated evolution of droplet size arising from the Δn_g plotted in Fig. 7.2 for the 4 μm radius droplet at a pressure of 100 kPa with three different values of α. This demonstrates the difficulty in distinguishing experimentally between values of α at atmospheric pressure, particularly for high values of α.

Figure 7.5 shows the simulated evolution of droplet size for the same 4 μm radius droplet at a pressure of 5 kPa. This shows the advantage gained by working at reduced pressure. These plots suggest the time resolution required in the spectroscopic determination of the evolving droplet size; if the initial rapid change in droplet size is to be characterised accurately then a spectral time resolution of less than 1 s is required.

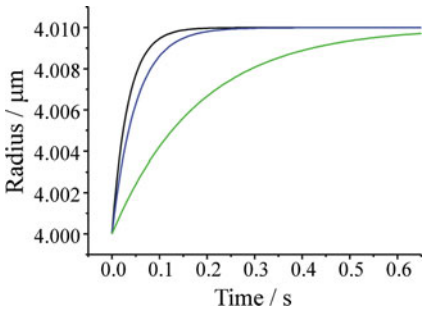

Fig. 7.5 Simulated droplet size change as a function of time for three values of α at 5 kPa and 293 K. The values of α are 1.0, 0.5 and 0.1 (*black*, *blue* and *green lines*, respectively)

7.4 Experimental Considerations

The experimental procedure for the kinetic measurements is as follows:

- Trap a droplet or pair of droplets and record the initial size(s) in order to establish the particle salt loading(s).
- Seal the chamber and allow the relative humidity to stabilise.
- Repeatedly change the laser power between two values separated by a few mW while the droplet is at atmospheric pressure and while recording the associated droplet size evolution(s).
- Reduce the chamber pressure and repeat the laser power change sequence.

Figure 7.6a shows the progression of whispering gallery mode (WGM) wavelengths recorded during a typical experimental run for an NaCl droplet at atmospheric pressure. The photodiode voltage is a measure of the relative laser power. The WGM wavelengths can be seen to respond to the sequence of laser power decreases and increases, shifting to longer wavelengths when the laser power decreases, corresponding to a size increase, and to shorter wavelengths when the laser power increases. The associated droplet size evolution is shown in Fig. 7.6b. It can be seen that during this experimental run the droplet size decreases steadily with time; this is the result of a falling relative humidity in the trapping chamber. The rate of the size change as a result of this relative humidity offset is always slow compared with the sharp changes in size which occur as a result of modulating the laser power. In this case a 5 nm size change occurs over 120 s as a result of relative humidity drift, compared with about the same size change in a few seconds for the power changes. Thus, the timescale for the size drift is much slower than the timescale of the kinetic measurement and can be neglected.

While the relative humidity offset means that as the run progresses the starting and ending droplet vapour pressures shift, this does not introduce a significant error into the model for the mass transfer as it is the change in vapour pressure that is most important. As the Köhler curve has a low gradient at the high relative humidities at which these experiments are performed, a small shift in the starting and ending relative humidities does not significantly affect the change in vapour pressure experienced by the droplet; from the start to the end of this run the

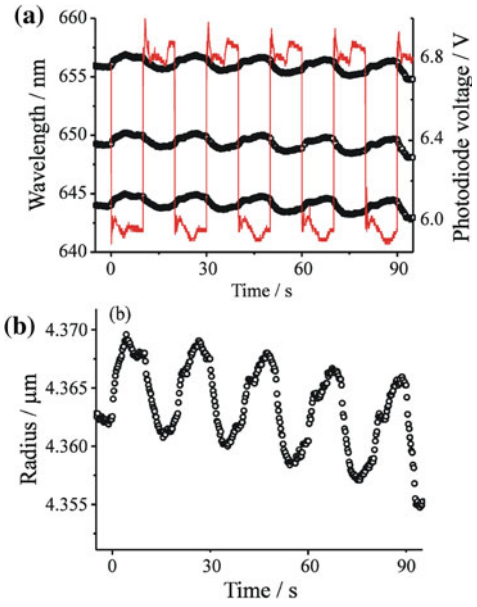

Fig. 7.6 **a** The evolution of WGM wavelengths during a sequence of trapping power decreases and increases, recorded with a spectral time resolution of 0.24 s. The photodiode voltage, representing the relative laser power, is shown in *red*. **b** The associated size evolution

magnitude of the vapour pressure change experienced by the droplet as the result of a power change event increases by less than 0.3% as a result of the decreasing relative humidity of the chamber.

The modifications to the absorption technique discussed in Chap. 6 which are necessary for the kinetic studies are:

- Initiation of the trapping power change in a rapid, controllable way.
- Control of the pressure in the droplet environment.
- Collection of droplet spectra with high time resolution.

These modifications will be discussed in more detail. The experimental set-up is shown schematically in Fig. 7.7.

7.4.1 Trapping Power Change

In the absorption measurements, a neutral density filter was used to control the laser power delivered to the optical trap. For the kinetic measurements it is necessary to change the trapping power more rapidly, so that the power changes on a timescale much shorter than the timescale of the droplet size evolution and the kinetics measurements. This was achieved by controlling the laser power output. Small trapping power changes of a few mW were used in order to minimise the perturbation of the droplet away from equilibrium conditions.

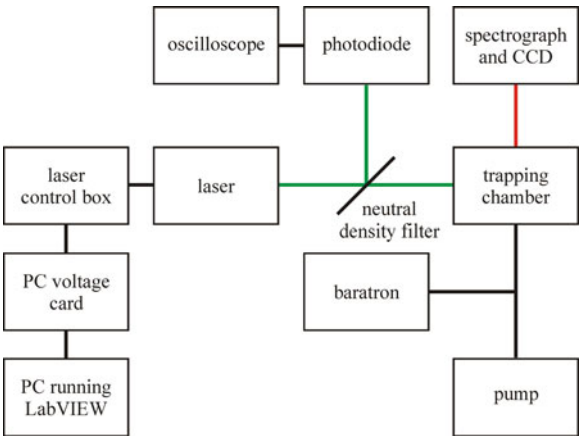

Fig. 7.7 Schematic of the experimental set-up used for the kinetic measurements

Two lasers were used for this work, a CW Ventus (Laser Quantum) laser with a maximum output of 500 mW and a 5 W Verdi (Coherent). Both lasers produce light with a wavelength of 532 nm. While controlling the laser power was more convenient using the Ventus laser, the high power output of the Verdi was necessary for performing the comparative dual trapping measurements.

For experiments carried out using the Ventus laser, the power was changed using the analogue input of the microprocessor-controlled power supply of the laser (MPC6000, Laser Quantum). The laser output depends on the voltage applied across this input and a PC voltage card was used to provide a voltage of 0–10 V. A LabVIEW programme [16] allowed automation of the laser power change and was used to provide a sequence of repeating power changes at a user-specified rate, typically one laser power change every 10–20 s.

For experiments carried out using the Verdi, which includes all of the comparative measurements, two laser power levels were pre-set using a function of the laser control box. It was necessary to switch between the pre-set levels manually.

The back-reflection from a neutral density filter placed in the trapping laser beam was directed onto a high-speed silicon photodiode (Thorlabs, DET110) with a rise/fall time of 20 ns. In combination with an oscilloscope (LeCroy Waverunner), the photodiode was used to maintain a time record of the relative laser power. Figure 7.8 shows examples of the change in power recorded using the photodiode for each of the lasers used. It can be seen that there is some instability in the laser power following the change in laser power. This is attributed to slow changes in the laser cavity temperature following a change in laser power. This presents a problem for measurements of mass transfer, as the size of the droplet will respond to these fluctuations in laser power, potentially complicating the analysis of the rate of the size change. The instability represents, however, only a small percentage of the total power change and occurs on a timescale of several seconds. The instability has an impact on measurements of slow size changes, for example those occurring at atmospheric pressure or with low mass transfer coefficients. For size changes which occur on a faster timescale, of around a second or less,

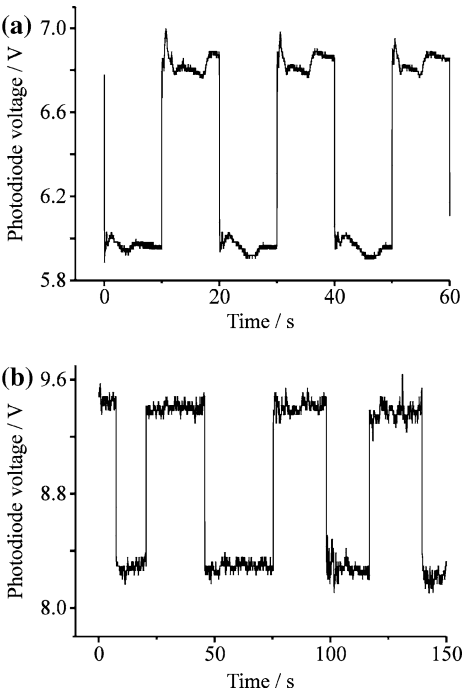

Fig. 7.8 Example photodiode voltage readings, representing records of the laser power from **a** the Ventus laser and **b** the Verdi laser

however, the instability does not present a significant problem and exponential size evolutions are observed, as predicted by the relevant theory. Figure 7.6 illustrates the problem of the laser power fluctuations for size changes occurring at atmospheric pressure. It can be seen that the size increases in particular are not smooth and that instead there is a discontinuity in the size evolution. Alternative means for changing the trapping power are under development.

7.4.2 Control of Pressure

In order to reduce the pressure a custom chamber was designed, as introduced in Chap. 3. A mechanical rotary vacuum pump (Edwards) was used to evacuate the chamber and a 0–1,000 Torr baratron (MKS Instruments) used to record the pressure, which was calibrated against two additional baratrons.

In order to carry out measurements at low pressure the chamber is evacuated until the required pressure is reached and then isolated from the pump. The pressure in the chamber increases by around 2 kPa during a typical experimental run lasting a few minutes, which is a result of the complications associated with achieving an airtight seal across a coverslip only $\sim$150 μm thick. The pressure immediately before and after each experimental run is recorded, and the average of these values taken to be the pressure for the entire run.

The liquid reservoir present in the chamber allows a vapour pressure of water to be maintained despite the chamber gas-phase being evacuated. Following evacuation the reservoir replenishes the chamber gas-phase with a vapour pressure of water, expected to occur over a few seconds. The reservoir consists of an aqueous salt solution of the same concentration as the solution nebulised to load the trap, for example 20 g L^{-1} NaCl. The corresponding relative humidity of the salt solution in the reservoir should be maintained in the chamber but in practice small changes in relative humidity are observed due to the imperfect sealing of the chamber. The composition of the reservoir is periodically monitored by measuring the refractive index of the solution, which is found to increase by <0.0001 over ~ 10 h, corresponding to an increase in salt concentration of <0.5 g L^{-1}, or an increase in relative humidity of $<0.03\%$. This indicates that the reservoir concentration does not change significantly as a result of the chamber evacuation and replenishment process.

7.4.3 Spectroscopy

A spectral time resolution of less than 1 s is needed to characterise the size evolutions measured in this work, which typically take place on a timescale of <1 s. The time resolution achievable is limited by the shutter speed of the spectrograph, a restriction which means that even if a time integration of, for example, 0.2 s is specified, spectra are actually acquired at a rate of around one every 0.24 s. The records of photodiode voltages collected are used to adjust the time-base of the collected sequences of spectra in order to take this into account. The fast response time of the photodiode means that a highly accurate time record of the droplet size evolution is obtained.

The strength of the Raman light scattered by the droplets also restricts the choice of spectral time resolution. The shorter the acquisition time used, the lower the number of photons which will be collected. Consequently there is a lower limit of time resolution for which a spectrum of sufficient signal to noise ratio to accurately size a droplet can be attained. This is particularly limiting in the case of small droplets. In some cases only one cavity resonance is resolved in the droplet spectra; for these it is often possible to determine the droplet size change by tracking the wavelength shift of a single resonance. In practice the minimum acquisition time achievable is approximately 0.2–0.4 s.

7.5 Preliminary Results and Discussion

The mass accommodation coefficients α and γ_e have been measured for aqueous droplets containing only inorganic salts and for droplets containing the surface-active compound stearic acid. The mass accommodation coefficients for water at

an aqueous surface have been measured both on single trapped droplets and during comparative measurements in which an aqueous droplet and a surfactant-loaded droplet are simultaneously trapped and studied. In both cases the droplets are subjected to a number of uptake and evaporation events at several pressures.

7.5.1 Studies of Aqueous Surfaces

Mass transfer of water at an aqueous surface was first investigated for a single trapped droplet. Wherever possible the droplets were sized directly using the SCATA programme. However, as a result of the short spectral acquisition times used, some of the collected spectra did not have a sufficient number of WGM resonances apparent above the spectral noise for direct sizing to be performed. In these cases all frames with a sufficient number of observable resonances were sized, and the remainder of the sizes determined from the wavelength of a particular WGM resonance, chosen to be one which was present in all spectra. The droplet radius can be determined from the wavelength of a resonance, as in the limit of small size changes the change in the resonant wavelength of a mode is directly proportional to the change in droplet radius, i.e. [17, 18]:

$$\frac{\Delta r}{r} = \frac{\Delta \lambda}{\lambda} \tag{7.13}$$

In order to make use of the multiple size evolutions recorded for each droplet and pressure, all of the size evolutions at a given pressure are represented relative to a common time and radius origin. The mean and standard deviation of the size change after each time interval may then be calculated in order to obtain a representative mean size evolution.

7.5.1.1 Atmospheric Pressure Measurements

Figure 7.9 shows the evolution of the size of a droplet with a radius of $\sim$4.36 μm, undergoing water uptake at atmospheric pressure, taken from the full size record for this droplet, shown in Fig. 7.6. The mean change in size at each spectral time interval is plotted for six uptake events for the same droplet. The effect of laser power fluctuations is clear from the increasing standard deviation in the mean size change with time. Simulated droplet evolutions are superimposed over the plot for four values of α. The simulated plots are created using the mean droplet start and end sizes to determine the appropriate starting vapour pressure gradient for the flux iteration. The uptake events are taken to end at the 'break' in the droplet size increase, which can be seen in Fig. 7.6 to occur after the droplet size has increased by about two-thirds of the total size change. This provides the best representation of the rate of uptake, as the smooth size change indicates that laser power

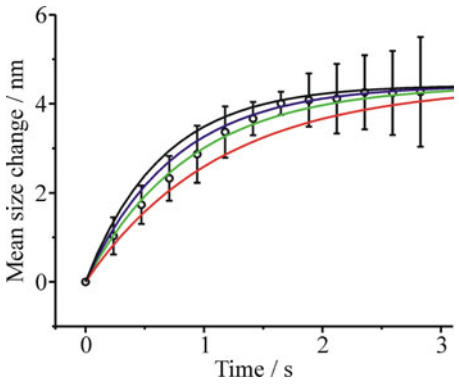

Fig. 7.9 The evolution of droplet size for uptake occurring at atmospheric pressure, represented by *open circles*. Simulated droplet size evolutions for α = 1.00, 0.20, 0.10 and 0.05 are represented by *black*, *blue*, *green* and *red lines*, respectively

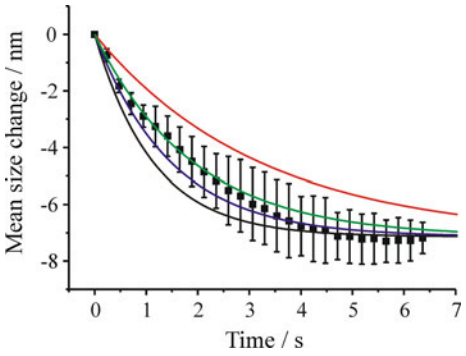

Fig. 7.10 The evolution of droplet size for evaporation occurring at atmospheric pressure. Simulated droplet size evolutions for γ_e = 1.00, 0.20, 0.10 and 0.05 are represented by *black*, *blue*, *green* and *red lines*, respectively

fluctuations have not affected the mass transfer up to this point. Provided that only the size change up until this break is used to determine the initial vapour pressure gradient, the modelling of the mass flux will not be affected.

The experimental data are consistent with $0.1 < \alpha < 0.2$, but it can be seen that even a simulated size evolution with a value of $\alpha = 1$ is a close match for the experimental data. This is indicative of the limited sensitivity of this measurement to the value of α when performed at atmospheric pressure.

Figure 7.10 shows the mean size change for six evaporation events for the same droplet, also occurring at atmospheric pressure. It can be seen that the evaporation does not follow exponential time dependence, contrary to the expected behaviour. This is a result of the problematic laser power fluctuations. The fitted model data are consistent with a value of $0.1 < \gamma_e < 0.2$, but because of the non-exponential form of the size evolution it is not possible to determine a reliable value of γ_e from these data.

Figure 7.11 shows the averaged uptake and evaporation plots overlaid. It can be seen that at early times uptake and evaporation proceed at the same rate within the error of the measurement, separating at later times as laser power fluctuations become important. The rates of uptake and evaporation are expected to be similar at atmospheric pressure even if α and γ_e are not equivalent, as a result of the

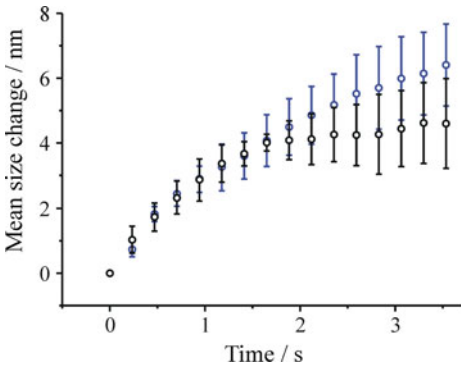

Fig. 7.11 Average uptake (*black circles*) and evaporation (*blue circles*) size evolutions for the same droplet, performed at atmospheric pressure

dominance of gas-phase diffusion, which will be the same for uptake and evaporation. The sensitivity of this measurement to the value of the surface resistances at atmospheric pressure is not sufficient to allow the conclusion that the values are the same.

7.5.1.2 Reduced Pressure Measurements

As expected, the rate of mass transfer increases and the timescale for re-equilibration decreases with decreasing pressure in the droplet environment as $1/\Gamma_{diff}$ decreases. Size evolutions for the same droplet, performed at atmospheric ($r = \sim 4.36$ μm) and two reduced pressures, 29 ± 1 kPa ($r = \sim 4.05$ μm) and 12 ± 1 kPa ($r = \sim 4.14$ μm), are shown in Figs. 7.12 and 7.13 for uptake and evaporation, respectively. The figures show the fractional progress in wavelength shift, which is proportional to the radius change for small size changes. The figures show only a single experimental size evolution; the error bars on these measurements represent the error in determining the resonant wavelength shift, which is determined by the resolution of the spectrograph. The values of $1/\Gamma_{diff}$ for each pressure are 26, 6.9 and 2.9 at atmospheric pressure, 29 and 12 kPa, respectively. Simulated size evolutions are shown for comparison as solid lines.

The size changes at reduced pressure occur at a much higher rate than those taking place at atmospheric pressure and the slow laser power fluctuations are therefore not as important. This can be seen in Figs. 7.12 and 7.13. The size evolutions occurring at 12 ± 1 kPa show smoother size evolutions than those occurring at the higher pressures, highlighting the importance of minimising the pressure at which measurements are made and also the need to develop an alternative means of changing the droplet temperature. As described previously, the sensitivity of the measurement to the value of the mass transfer coefficients is also increased as the pressure is decreased.

Figure 7.14 shows the lowest pressure uptake and evaporation events overlaid. It can be seen that the rates of uptake and evaporation, and thus α and γ_e, are the same to within the precision of these measurements.

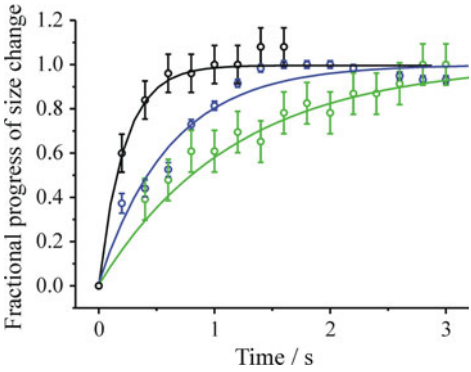

Fig. 7.12 The fractional progress in size change for three uptake events for the same NaCl droplet, each occurring at a different pressures; atmospheric (*green circles*), 29 ± 1 kPa (*blue circles*) and 12 ± 1 kPa (*black circles*). The values of α used to generate the overlaid simulated size evolutions for comparison are 0.08, 0.04 and 0.1 (atmospheric pressure, 29 kPa and 12 kPa respectively)

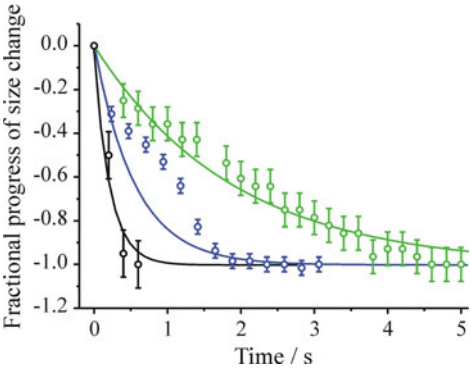

Fig. 7.13 The fractional progress in size change for three evaporation events for the same NaCl droplet, each occurring at a different pressures; atmospheric (*green circles*), 29 ± 1 kPa (*blue circles*) and 12 ± 1 kPa (*black circles*). The values of γ_e used to generate the overlaid simulated size evolutions for comparison are 0.02, 0.04 and 0.1 (atmospheric pressure, 29 kPa and 12 kPa respectively)

Figure 7.15 shows the averaged size evolution for three uptake events occurring at 12 ± 1 kPa for the droplet considered so far, along with a first order exponential fit to the data. Figure 7.16 shows a comparison of the averaged uptake occurring at atmospheric pressure and at 12 ± 1 kPa, also with first order exponential fits for the data. Again it is clear that reducing the pressure has the effect of increasing the rate of uptake as the rate of gas-phase diffusion increases.

Figure 7.17 shows a comparison of averaged uptake and evaporation events occurring at 12 ± 1 kPa. First order exponential fits to the data are also shown.

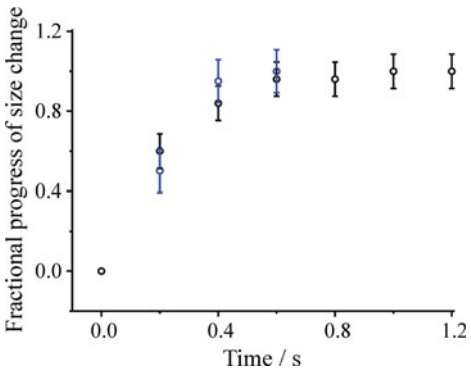

Fig. 7.14 Rates of uptake (*black circles*) and evaporation (*blue circles*) compared for the same droplet at a pressure of 12 ± 1 kPa

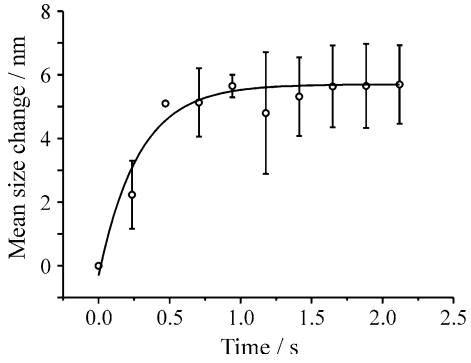

Fig. 7.15 Averaged size evolution for three uptake events occurring at 12 ± 1 kPa with a first order exponential fit to the data

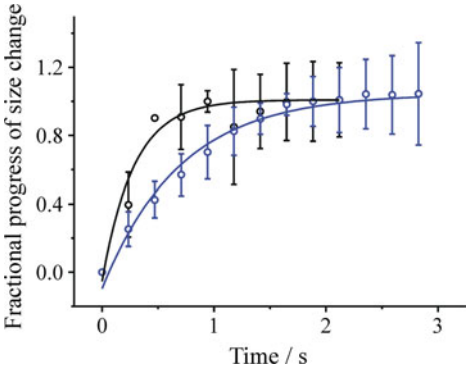

Fig. 7.16 Averaged size evolutions for uptake events occurring at atmospheric pressure (*blue circles*) and 12 ± 1 kPa (*black circles*), accompanied by first order exponential fits to the data

Two fits are shown for the evaporation data: the broken blue line represents a fit to all data points, while the solid blue line excludes the second data point, which is thought to be anomalous. It can again be seen that the rates are the same and hence that α and γ_e are the same within the precision of these measurements.

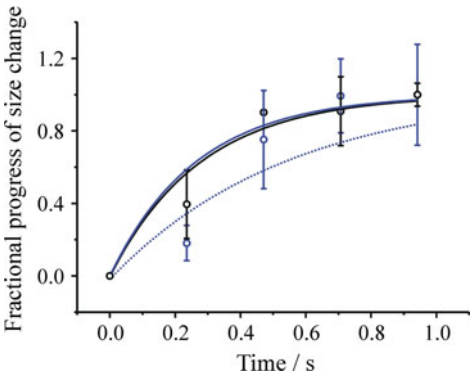

Fig. 7.17 Averaged size evolution for uptake (*black circles*) and evaporation (*blue circles*) events compared, occurring at 12 ± 1 kPa accompanied by first order exponential fits to the data. For the evaporation data the *broken blue line* represents a fit to all data points, while the *solid blue line* excludes the second data point, which is thought to be anomalous

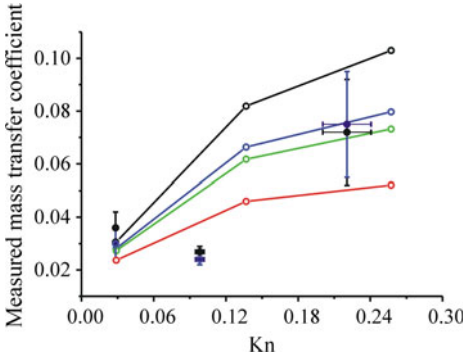

Fig. 7.18 The values of the mass transfer coefficients determined for uptake and evaporation, *closed black and blue circles*, respectively, compared with the theoretical pressure dependence of the mass transfer coefficients for a range of α or γ_e; 0.14 (*open black circles and line*), 0.1 (*open blue circles and line*), 0.09 (*open green circles and line*) and 0.06 (*open red circles and line*)

The $^1/_e$ times from the exponential fits to these averaged data points have been used to find γ_{meas} and $\gamma_{e,meas}$, referred to collectively as the measured mass transfer coefficients, from a calibration plot such as that presented in Fig. 7.3, and the findings compared with theoretical predictions. The values of the mass transfer coefficients determined are shown in Fig. 7.18, compared with the theoretical pressure dependence of mass transfer coefficients for a range of α or γ_e.

As expected, the high pressure measurements are adversely affected by laser power fluctuations and do not compare well with theory. The 12 ± 1 kPa measurement is, however, consistent with a value of α or $\gamma_e = 0.1 \pm 0.04$.

7.5.1.3 Conclusions

The single-trapping low pressure measurements show that the values of α and γ_e are both equal to 0.10 ± 0.04 at 291 K.

This is consistent with the values of α of 0.17 ± 0.03 at 280 K and 0.32 ± 0.04 at 258 K reported by the BC/ARI collaboration, if α is considered to vary linearly with temperature [11]. If linear temperature dependence is assumed this would predict a value of α of 0.10 at 291 K. Our results are also consistent with the recent electrodynamic balance study by Zientara et al. which gave a value for α of ~ 0.13 at 293.1 K [19], and the report by Cappa et al. that α and γ_e must be less than one [20]. Further, our results are consistent with CCN closure field studies which have found that $\alpha = 0.06$ [21].

The value found in this study is considerably lower than the value of $\alpha = 1$ reported in the UV/UH study [14, 22]. However, as previously discussed, the conditions under which those experiments were carried out were radically different from those used in our work, and comparisons are not likely to be meaningful.

7.5.2 *Comparative Studies of Aqueous and Surfactant-Rich Surfaces*

In the comparative measurements described here, the mass transfer properties of an aqueous NaCl droplet were compared with those of a droplet containing NaCl and the surface-active carboxylic acid stearic acid. Stearic acid was selected as a benchmark for this technique as it has previously been shown to have a significant effect on mass transfer at aqueous surfaces [23]. It also has an appreciable solubility in water, so it was not necessary to add an organic solvent to the aqueous droplets used. Stearic acid is present in organic films found on the surface of sea water, where it can have an affect on mass transfer between sea water and the air, and if transported into the atmosphere by sea spray, can affect mass transfer in aerosol particles [23].

In the measurement detailed here, one optical trap was loaded with a droplet containing stearic acid at a concentration of $\sim 3 \times 10^{-3}$ M and NaCl at a concentration of 20 g L^{-1} (referred to as the SA/NaCl droplet). A second trap was then loaded with a droplet containing only NaCl, at a concentration of 40 g L^{-1} (referred to as the NaCl droplet). The solute loading of the second droplet was determined from its size when first trapped. The solute loading of the first trapped droplet was found by using its initial trapped size and considering the size change when the second solution was nebulised into the experimental chamber. This size change is the combination of the relative humidity change and inclusions of the second solution into the first trapped droplet by coagulation. These effects are considered to be independent for the purposes of this calculation.[6] The effects of the small amount of stearic acid on the solution thermodynamics and wet particle size of the first droplet were neglected.

[6] As discussed in Sect. 3.4.

The critical micelle concentration (CMC) of stearic acid in water is 4×10^{-4} M [24] and as a result of micelle formation the concentration of stearic acid monomers in the droplet is difficult to predict. Because the CMC will vary with salt concentration as the droplet size changes, the concentration of stearic acid monomers in the droplet is also likely to vary. In the absence of micelle formation, the stearic acid loading of the droplet is consistent with the formation of a monolayer for droplets of less than $\sim$3.2 μm in radius. This is based on a molecule of stearic acid occupying an area of 0.26 nm^2 [23] and complete partitioning of the stearic acid to the droplet surface. The presence of NaCl in the droplet may lead to complexation of the stearate anion with Na^+, which may decrease the area occupied by the surfactant species as a result of charge shielding. Nonetheless, it is reasonable to assume for the purposes of the demonstration of this technique that a sufficiently large amount of stearic acid is present in the droplet to modify its surface properties. In the future more precise knowledge of the surface composition will need to be sought.

For the comparative measurement, in order to resolve the subtle difference between mass transfer rates at two surfaces of different compositions, the mass transfer coefficients were found by modelling and fitting each size evolution separately.

7.5.2.1 Atmospheric Pressure Measurements

Figure 7.19 shows the evolution of the WGM wavelengths for the two simultaneously-trapped droplets at atmospheric pressure, which shift as the droplet sizes vary with trapping power. Figure 7.20 shows the associated size evolutions. The photodiode voltage trace is shown in red; the SA/NaCl and NaCl droplets experienced laser power changes of $\sim$2.8 and 2.5 mW, respectively.

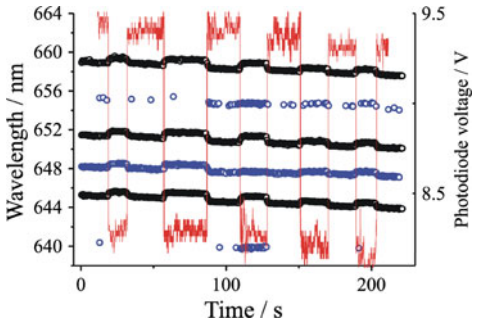

Fig. 7.19 The evolution of the WGM resonant wavelengths for the two simultaneously-trapped droplets at atmospheric pressure during a sequence of trapping power decreases and increases. The SA/NaCl and NaCl droplets are represented by *black* and *blue circles*, respectively. The photodiode voltage is represented by the *red line*

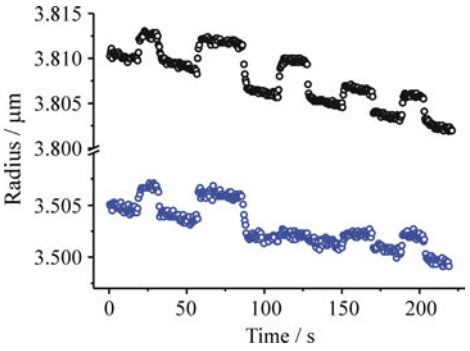

Fig. 7.20 The sizes of the two simultaneously-trapped droplets at atmospheric pressure during a sequence of trapping power decreases and increases. The SA/NaCl and NaCl droplets are represented by *black* and *blue circles*, respectively

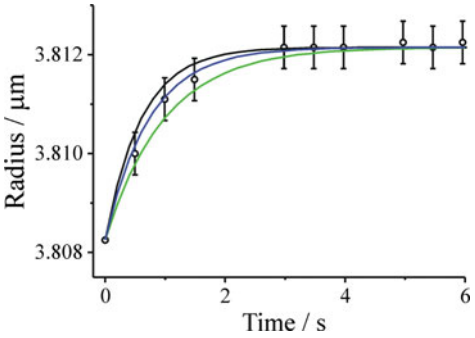

Fig. 7.21 Uptake event for the SA/NaCl droplet occurring at atmospheric pressure. Values of α of 0.05, 0.1 and 0.2 were used to create the overlaid simulated size evolutions, shown in *green*, *blue* and *black*, respectively

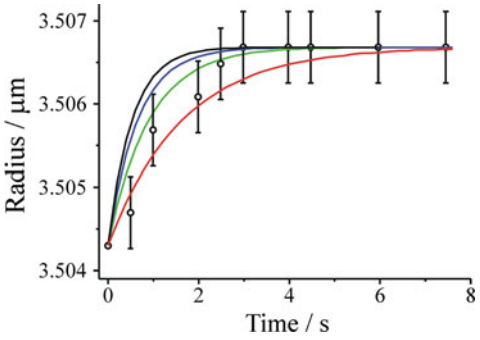

Fig. 7.22 Uptake event for the NaCl droplet occurring at atmospheric pressure. A value of α of 0.02 fits the experimental data, shown in *red*. Simulated size evolutions created using the values of α relevant to the simulated fits for the SA/NaCl droplet are overlaid for comparison: values of α of 0.05, 0.1 and 0.2 were used to create the overlaid simulated size evolutions shown in *green*, *blue* and *black*, respectively

Examples of single uptake events occurring at atmospheric pressure, along with simulated size evolutions used to determine α for the mass transfer, are shown in Figs. 7.21 and 7.22 for the SA/NaCl and NaCl droplets, respectively. The uptake

event for the SA/NaCl droplet is consistent with $0.05 < \alpha < 0.2$, while the uptake event for the NaCl droplet is consistent with a value for α of 0.02. Laser power fluctuations make the size evolution difficult to fit for the NaCl droplet; simulated size evolutions created using the values of α relevant to the simulated fits for the SA/NaCl droplet are overlaid for comparison. As expected, measurements taken at atmospheric pressure are not capable of resolving precisely the value of α because of the dominance of the resistance to mass transfer arising from gas-phase diffusion.

It can be seen in Fig. 7.20 that the magnitude of the droplet size change is sometimes not consistent between the two droplets; for example, at around 120 s the SA/NaCl droplet changes size more significantly than the NaCl droplet. This is likely to be associated with complications arising from resonant heating of the droplet, as discussed in Sect. 6.7.1.

7.5.2.2 Low Pressure Measurements

The size record of an experimental run carried out at a reduced pressure of 17 ± 1 kPa is shown in Fig. 7.23. Some unexpected fluctuations in the magnitude of the droplet size changes can again be seen, particularly for the SA/NaCl droplet, and are thought to arise from resonant heating; uptake or evaporation events occurring at similar times to these fluctuations are excluded from the analysis of the mass transfer coefficients. The size changes for the NaCl droplet can be seen to be smaller than those for the SA/NaCl droplet, which is thought to be a consequence of using a fibre to deliver the laser to the experimental set-up. Small movements of the fibre have been observed to change the polarisation of the laser output delivered, which affects the distribution of the trapping power between the two traps because the beam splitter used to divide the trapping beam displays a low level of polarisation-dependent behaviour. In this measurement the power change experienced by the NaCl droplet is now smaller than that experienced by the SA/NaCl droplet. This does not introduce an error into the determination of the mass transfer coefficients as it is accounted for when the vapour pressure gradient for the mass transfer is determined.

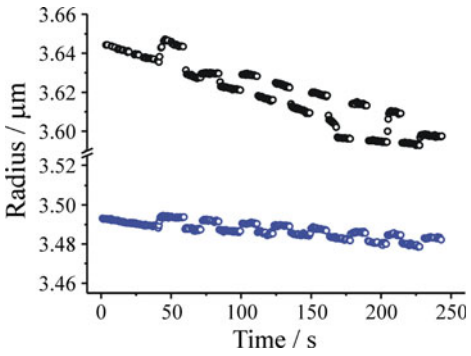

Fig. 7.23 The sizes of the two simultaneously-trapped droplets during a sequence of trapping power decreases and increases at a pressure of 17 ± 1 kPa. The SA/NaCl and NaCl droplets are represented by *black circles* and *blue circles*, respectively

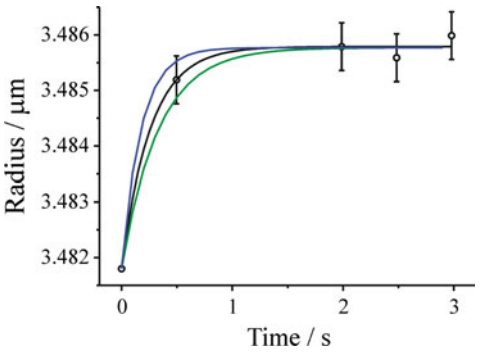

Fig. 7.24 Uptake event for the NaCl droplet occurring at a pressure of 17 ± 1 kPa, along with a first order exponential fit to the data (*black*). Simulated size evolutions with values of α of 1.4 and 0.07 are shown in *blue* and *green*, respectively

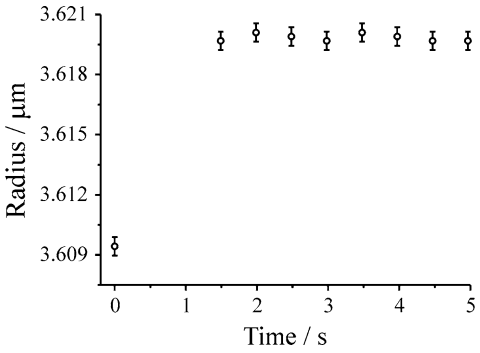

Fig. 7.25 Uptake event for the SA/NaCl droplet occurring at a pressure of 17 ± 1 kPa

An example of an uptake event taking place at 17 ± 1 kPa for the NaCl droplet is shown in Fig. 7.24, along with an exponential fit to the data (black). Simulated size evolutions with values of α of 1.4 and 0.07 are shown in blue and green, respectively. The use of a short spectral integration time of less than 1 s means that the spectral quality is somewhat reduced, and as a result it is not always possible to determine the droplet size while it is rapidly changing size during the first second of the size evolution. This was the only size evolution recorded for uptake for this droplet that provided information on the size at early times. The event is consistent with a value of $0.07 < \alpha < 1.4$, which is in turn consistent with the previous measurement of $\alpha = 0.10 \pm 0.04$ for water at an aqueous aerosol surface.

An example of a single uptake event occurring at this reduced pressure is shown in Fig. 7.25 for the SA/NaCl droplet. It is again not possible, because of reduced spectral quality, to determine the droplet size while it is rapidly changing during the first second of the size evolution.

Information about the size evolution at early times is essential for accurate determination of the mass transfer coefficients, and further data were therefore obtained for this droplet, at a pressure of 13 ± 1 kPa, for which improved spectral resolution was achieved. An example of an uptake event taking place at this pressure is shown in Fig. 7.26, along with an exponential fit to the data. A shaded feature illustrates the range of simulated size evolutions spanning $\alpha = 0.06$–0.14,

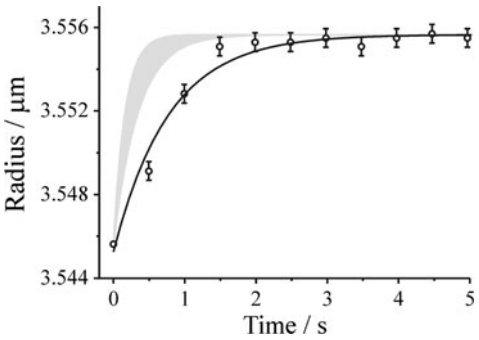

Fig. 7.26 Uptake event for the SA/NaCl droplet occurring at a pressure of 13 ± 1 kPa, along with a first order exponential fit to the data. The shaded feature illustrates the range of simulated size evolutions spanning $\alpha = 0.1 \pm 0.04$, as previously determined for water at a surfactant-free surface

consistent with $\alpha = 0.1 \pm 0.04$ as previously determined for water at a surfactant-free surface. It can be seen that the rate of uptake at a surfactant-rich surface is less than that observed to occur at a surfactant-free surface, consistent with a lower value of α at the former.

The mass transfer coefficients were determined for every size change event for which size information was available at early times by comparing exponential fits to the experimental data with simulated size evolutions. The mass transfer coefficients for the two droplets were determined as follows:

- SA/NaCl droplet: $\alpha = 0.03 \pm 0.01$ (mean of 3 size changes), $\gamma_e = 0.05 \pm 0.01$ (mean of 3 size changes).
- NaCl droplet: $0.07 < \alpha < 0.14$, $\gamma_e = 0.13 \pm 0.03$ (mean of 2 size changes).

7.5.2.3 Conclusions

While these findings represent only preliminary results, and will form the basis for further investigations, they suggest that surface-active organic compounds could have a significant effect on aerosol mass transfer, and that this effect may be resolvable using this experimental strategy.

The value of α determined for the aqueous NaCl droplet is consistent with that found from the detailed single-trapping measurement described above. The value of α determined for the aqueous SA/NaCl droplet is lower, as expected. In order to enhance the resistance to mass transfer it would be desirable to increase the surfactant mass loading of the droplet.

γ_e has been found to be higher than α for these measurements; this should be investigated in future work.

7.6 Factors Affecting the Measurements

There are several factors inherent to this technique which will affect the value of the mass transfer coefficients determined.

7.6.1 Surface Composition

In trying to determine a value for α or γ_e for the uptake of water on an aqueous surface it is important to consider if a pure water surface is indeed under study. This technique relies on the presence of a dissolved solute in the droplets. The solute effect forms the basis of the equilibrium droplet size changing as the laser power (and hence the droplet temperature) is changed. It is the shift between equilibrium sizes which provides the mass transfer to be studied.

While it is unlikely that the ions of the inorganic solute used, NaCl in these experiments, modify the surface properties significantly at the concentrations and relative humidities studied here [25, 26], it is possible that the salt used contains surface-active impurities. While the stated purity of the NaCl employed is $>99.5\%$, the large surface area to volume ratio of the droplets used means that any impurity which tends to partition to the surface could have a significant effect on mass transfer at the surface. Surface films tend to retard mass transfer of water and hence the mass transfer coefficients reported represent lower limits for water at a water surface. In the future these experiments should be performed on droplets with a wide range of salt concentrations, allowing extrapolation of the mass transfer coefficients for water at a pure water surface. Alternatively, further purification of the salt could be undertaken.

7.6.2 Temperature and Heat Transfer Considerations

Several assumptions relating to the temperature of the droplet and the associated heat transfer are made in the analysis:

- The heat and mass transfer can be decoupled; the mass transfer is assumed to take place under conditions of constant temperature.
- The droplet temperature is equal to the chamber temperature, which is assumed to be constant.
- The droplet temperature is uniform.
- The latent heat of condensing or evaporating water molecules can be neglected.

The errors associated with each of these assumptions are addressed in turn.

Decoupling of heat and mass transfer. Although it is a change in droplet temperature which gives rise to the vapour phase concentration gradient that leads to the mass flux recorded, the mass transfer is modelled as if it takes place at constant temperature. Decoupling the heat and mass transfer in this way is reasonable as the magnitude of the temperature change is small, on the order of a few mK, and because the heat transfer occurs on a much shorter timescale than the mass transfer. In the absence of convection, assuming that conduction is the only mechanism of heat dissipation, the time taken for the droplet to reach its new temperature, τ, is given by [27]:

$$\tau = \frac{r^2 \rho_d C_d}{3k_a} \tag{7.14}$$

where ρ_d and C_d are the density and specific heat of the droplet (998 kg m^{-3} and 4181.8 J kg^{-1} K^{-1} for water at 20 °C [8]), respectively. For a droplet of 4 μm radius τ = 8.8 ms, a much shorter timescale than for the mass transfer, which occurs on a timescale of seconds.

Droplet and chamber temperature. The droplet temperature is elevated compared to the chamber temperature by only $\sim$ 1 mK/mW of trapping power, i.e. by <35 mK [1], so it is reasonable to assume that the droplet temperature is equal to that of the chamber. While the laboratory is maintained at 18 °C by specialist air-conditioning units, the temperature inside the chamber is affected by heat from electrical instruments such as the CCD in the light-tight box in which the experiment is housed, and is expected to vary between 18 and 20 °C. Ideally the temperature in the chamber would be continuously monitored. This is difficult to achieve, however, owing to engineering constraints arising from the small size of the chamber, and represents a future development to the experimental design. Assuming a constant chamber temperature will not introduce significant error as the quantities involved in modelling the mass transfer, for example D_g, are only weakly dependent on temperature. Further, as it is a change in vapour pressure which is relevant for modelling the mass transfer, and Köhler curves are only weakly dependent on temperature, the effect of an uncertainty in the temperature of <2 K is limited.

Uniformity of droplet temperature. The trapping beam is of a smaller diameter than a trapped droplet, which can therefore be considered to have a central column illuminated with laser light, surrounded by non-illuminated fluid. As a result the droplet temperature will be non-uniform, with a higher temperature in the illuminated core than in the outer region. If large temperature gradients exist in the droplet these would have to be taken into account in modelling the droplet mass transfer. The thermal conductivity of water is much higher than that of air (0.6062 and 0.0262 W m^{-1} K^{-1} at 298 and 300 K, respectively [8]) and the rate of heat transfer within a liquid droplet is therefore fast compared with that in the air surrounding the droplet, with the result that the particle temperature will be approximately uniform.

A temperature non-uniformity that is more difficult to quantify arises from the laser hotspots present at the leading and back faces of the droplet along the laser axis, which result from focussing of the laser light by the droplet [28]. However, for weakly absorbing media, such as water at 532 nm, surface temperature gradients are expected to be negligibly small [28].

Latent heat of water. The flux of latent heat to the droplet will oppose the temperature change giving rise to the mass transfer for both uptake and evaporation, and so will retard the rate of mass transfer observed. For the example of a 4 μm droplet undergoing an increase in radius of 10 nm to 4.01 μm the amount of latent heat deposited in the droplet is 4.6 $\times$ 10^{-9} J (calculated using a latent heat of vaporisation of water of 2,270 kJ kg^{-1} [8]). In the absence of heat dissipation

mechanisms and assuming the specific heat of the droplet to be that of water, this would lead to an increase in the droplet temperature of ~ 4 mK, occurring over the course of the timescale of the mass transfer, which will be on the order of 2 s. It follows from the temperature equilibration times of ~ 10 ms calculated above that it can be assumed the rate of dissipation of the small amount of latent heat deposited in the droplet will be much higher than the rate of mass transfer and can thus be neglected in the analysis of the mass transfer.

7.7 Future Experimental Development

There are a number of possible developments which may be made to this technique to improve its accuracy and scope.

7.7.1 Means of Changing Droplet Size

Initiating the droplet size change in a more reproducible manner, free from the effects of laser power fluctuations, is a necessary improvement to this technique. The use of a secondary source of radiation, independent of the trapping beam, offers a solution. This second beam can be held at fixed power and the droplet alternately exposed or shielded from the beam using a mechanical shutter, for which a time response of <1 ms is possible, or deflected using an acousto-optic modulator. This will remove the problems of laser power fluctuations associated with abrupt changes in the laser power supply voltage.

Use of a second beam also offers an advantage in droplet illumination geometry. Initiating the droplet size change using a trapping power change will cause a change in the small temperature gradients which exist radially in the droplet and also across the droplet surface as a result of the laser hotspots. The second beam can be less tightly focussed, meaning that the droplet is effectively under conditions of plane wave illumination. If the power of this light source experienced by the droplet were modulated, the temperature change of the droplet would be spatially uniform.

7.7.2 Spectroscopy

It is highly desirable to establish a CCD trigger to synchronise the acquisition of droplet spectra to the power change. It would also be useful to increase the spectral time resolution of the measurements. To this end, efforts could be made to exclude background light from the experimental setup so that the spectrograph could be

operated with a permanently open shutter, removing the limitation of the mechanical shutter speed.

7.7.3 Increase Kn Using Smaller Droplets

Increasing the *Kn* at which the measurements are taken offers greater sensitivity in the determination of the mass transfer coefficients. This could be achieved by either reducing the pressure or the droplet size. The minimum pressure achievable is limited by the vapour pressure of water, while the limitations of trapping and sizing droplets using optical tweezers and CERS means that experiments on significantly smaller droplets are not currently possible. Different means of trapping and sizing aimed at investigating smaller droplets are under development.

7.7.4 Pressure Monitoring

Automating the recording of the pressure would allow the pressure at all times throughout each experimental run to be known, and would be an improvement on taking an average of the start and end pressures.

7.7.5 Reactive Studies

The mass accommodation coefficients of atmospherically-relevant species other than water on an aerosol particle are also of interest. In many cases reactive uptake occurs; important examples are HCl and $ClONO_2$ on aerosol particles [29]. These species have been shown to take part in heterogeneous reactions which catalyse their conversion to Cl and ClO respectively, which in turn catalyse ozone depletion in the stratosphere. Reactive uptake represents a possible future direction for the new technique which has been developed.

7.7.6 Simultaneously Probing Surface Composition

Combining the above procedure with a technique which directly probes the liquid/air interface would enable the surface composition and the rate of uptake or evaporation to be characterised simultaneously. Photoelectron spectroscopy has recently been used to probe the interfacial composition of aqueous methanol droplets in a droplet train experiment [30]. The technique is able to sample the composition of the interfacial region of the droplet with a depth resolution of

several Ångströms. The ability to simultaneously probe surface structure and mass accommodation or evaporation would provide a definitive resolution to the debate over the influence of organic layers on the uptake properties of aqueous droplets.

7.8 Summary

A new technique for the determination of mass transfer coefficients at an aerosol surface has been demonstrated. Using this technique, α and γ_e have been found to be equal to 0.10 ± 0.04 at 291 K.

As this work has determined a value of α of around 0.1, which is at the threshold below which cloud droplet activation is sensitive to the value of α, it will be important to carry out further measurements and to refine the technique in order to improve the accuracy of the results.

A rigorous characterisation of the effect of surface-active compounds on mass transfer at the surface of aerosol droplets should be possible using this technique, offering important benefits for climate prediction.

The capacity of the technique for making comparative measurements is yet to be fully-realised. Perhaps the most valuable application of this will be in carrying out comparative studies of the effect of chemical ageing on the mass transfer kinetics of droplets of different compositions. This could include studying how the mass transfer kinetics of oxidisable and non-oxidisable droplets vary with exposure to an atmospherically important oxidant such as ozone.

References

1. K.J. Knox, J.P. Reid, J. Phys. Chem. A **112**, 10439 (2008)
2. P. Davidovits et al., Geophys. Res. Lett. **31**, L22111 (2004)
3. P. Davidovits, C.E. Kolb, L.R. Williams, J.T. Jayne, D.R. Worsnop, Chem. Rev. **106**, 1323 (2006)
4. A. Morita, M. Sugiyama, H. Kameda, S. Koda, D.R. Hanson, J. Phys. Chem. B **108**, 9111 (2004)
5. J.H. Seinfeld, S.N. Pandis, *Atmospheric Chemistry and Physics: From Air Pollution to Climate Change* (Wiley, New York, 1998)
6. A.J. Prenni, P.J. De Mott, S.M. Kreidenweis, Atmos. Environ. **37**, 4243 (2003)
7. G.B. Ellison, A.F. Tuck, V. Vaida, J. Geophys. Res.-Atmos. **104**, 11633 (1999)
8. D.R. Lide (ed.), *The CRC Handbook of Chemistry and Physics*, 89th edn. (CRC Press/Taylor and Francis, Boca Raton, 2009)
9. P. Atkins, J. de Paula, *Physical Chemistry* (Oxford University Press, Oxford, 2002)
10. Q. Shi, Y.Q. Li, P. Davidovits, J.T. Jayne, D.R. Worsnop, M. Mozurkewich, C.E. Kolb, J. Phys. Chem. B **103**, 2417 (1999)
11. Y.Q. Li, P. Davidovits, Q. Shi, J.T. Jayne, C.E. Kolb, D.R. Worsnop, J. Phys. Chem. A **105**, 10627 (2001)
12. M. Sugiyama, S. Koda, A. Morita, Chem. Phys. Lett. **362**, 56 (2002)
13. A.S. Raspopin, T.V. Solomeina, J. Eng. Phys. Thermophys. **70**, 61 (1997)

14. P.M. Winkler, A. Vrtala, R. Rudolf, P.E. Wagner, I. Riipinen, T. Vesala, K.E.J. Lehtinen, Y. Viisanen, M. Kulmala, J. Geophys. Res.-Atmos. **111**, D19202 (2006)
15. M. Gershenzon, P. Davidovits, L.R. Williams, Q.A. Shi, J.T. Jayne, C.E. Kolb, D.R. Worsnop, J. Phys. Chem. A **108**, 1567 (2004)
16. J.A. Smith, LabVIEW programme, 2008
17. R. Symes, R.M. Sayer, J.P. Reid, Phys. Chem. Chem. Phys. **6**, 474 (2004)
18. R.M. Sayer, R.D.B. Gatherer, R.J.J. Gilham, J.P. Reid, Phys. Chem. Chem. Phys. **5**, 3732 (2003)
19. M. Zientara, D. Jakubezyk, K. Kolwas, M. Kolwas, J. Phys. Chem. A **112**, 5152 (2008)
20. C.D. Cappa, W.S. Drisdell, J.D. Smith, R.J. Saykally, R.C. Cohen, J. Phys. Chem. B **109**, 24391 (2005)
21. C. Fountoukis et al., J. Geophys. Res.-Atmos. **112**, D10S30 (2007)
22. P.M. Winkler, A. Vrtala, P.E. Wagner, M. Kulmala, K.E.J. Lehtinen, T. Vesala, Phys. Rev. Lett. **93**, 075701 (2004)
23. R. Tuckermann, S. Bauerecker, H.K. Cammenga, J. Colloid Interf. Sci. **310**, 559 (2007)
24. H.A. Capelle, L.G. Britcher, G.E. Morris, J. Colloid Interf. Sci. **268**, 293 (2003)
25. B. Winter, R. Weber, P.M. Schmidt, I.V. Hertel, M. Faubel, L. Vrbka, P. Jungwirth, J. Phys. Chem. B **108**, 14558 (2004)
26. R. Weber, B. Winter, P.M. Schmidt, W. Widdra, I.V. Hertel, M. Dittmar, M. Faubel, J. Phys. Chem. B **108**, 4729 (2004)
27. C.H. Chan, Appl. Phys. Lett. **26**, 628 (1975)
28. T.M. Allen, M.F. Buehler, E.J. Davis, J. Colloid Interf. Sci. **142**, 343 (1991)
29. D.R. Worsnop, Q. Shi, J.T. Jayne, C.E. Kolb, E. Swartz, P. Davidovits, J. Aerosol Sci. **32**, 877 (2001)
30. D.E. Starr, E.K. Wong, D.R. Worsnop, K.R. Wilson, H. Bluhm, Phys. Chem. Chem. Phys. **10**, 3093 (2008)

Chapter 8
Summary, Conclusions and Future Directions

The work presented in this thesis has sought to address two key deficiencies in the current understanding of aerosol effects on radiative forcing: those related to the aerosol direct effect and the aerosol indirect effect. The work has focussed on improving the understanding of the direct effect via the development of a technique for the quantification of aerosol optical absorption. An improvement of the understanding of the indirect effect was approached through the development of a technique for the quantification of the mass accommodation coefficient of water at aerosol surfaces. For both techniques it was necessary to be able to determine the role played by aerosol composition.

8.1 Summary of Findings

In order to address the uncertainties in the current understanding of the effects of aerosols on climate and to resolve the effect of composition, studies were carried out on a single-particle basis using optical tweezers to isolate individual particles. Because of the abundance and importance of water in the atmosphere, aqueous aerosol droplets were studied. Cavity-enhanced Raman spectroscopy was used to characterise the evolving size of the droplets in response to changes in their environment.

A study of the optical manipulation of droplets using aerosol optical tweezers was undertaken and the results presented in Chap. 4 [1]. While condensed phase optical manipulation has been extensively studied, this represents the first reported study of the trapping behaviour of optically-tweezed aerosol droplets. In particular, the factors affecting the equilibrium trapping position of an optically-tweezed aerosol droplet were investigated using a combination of imaging along two orthogonal axes and cavity-enhanced Raman spectroscopy. With an increase in trapping laser power, the trapped particle has been shown to reside in an equilibrium

K. J. Knox, *Light-Induced Processes in Optically-Tweezed Aerosol Droplets*,
Springer Theses, DOI: 10.1007/978-3-642-16348-7_8,

position displaced further above the laser focus. Similarly, smaller droplets were shown to reside further above the laser focus than large droplets. This observation led to the proposal of a novel method for measuring the size of optically-tweezed particles based on the power dependence of the trapping position. Several optical phenomena were also identified, including the first observation of optical binding in aerosol optical tweezers and of the bistability of the trapping position [2]. The observations made during these studies represent an essential prerequisite for the rigorous interpretation of measurements made using aerosol optical tweezers, in particular for studies of coagulation processes and particle interactions. These studies have provided experimental data for comparison with the first models of the optical forces operating in aerosol optical tweezers, which are currently under development by collaborators.

The study of the spectroscopy of optically-tweezed aerosol droplets containing absorbing fluorescent chromophores, presented in Chap. 5, represents the first detailed measurements of fluorescence from aerosol droplets isolated in optical tweezers [3]. The addition of absorbing dyes to optically-tweezed droplets has enabled the observation of optical effects such as cavity-enhanced fluorescence and parametric four-wave mixing for the first time. This is also the first observation of a parametric mixing process in a single aqueous microdroplet under conditions of continuous-wave illumination, observable as the result of resonant absorption. The extended resonant structure afforded by the presence of the chromophores has allowed a systematic study of the variation of the quality factor of trapped droplets as optical cavities with mode number, the first study of its kind for optically-tweezed microparticles. Preliminary experiments involving the introduction of quantum dots to optically-tweezed aerosol droplets have also been carried out for the first time [4]. It is anticipated that these studies will lead to the future use of fluorophores in the characterisation of droplet pH and temperature. They are also relevant to the analysis of biological aerosol. The studies are an ideal model for benchmarking absorption techniques; the rapid evaporation of an optically-tweezed droplet was observed, providing a qualitative representation of aerosol absorption.

In Chap. 6 a new technique for making quantitative measurements of aerosol absorption was described [5]. The technique is highly sensitive, capable of measuring absorbances as low as 2×10^{-7} over an optical pathlength <10 μm. This is the first demonstration of the use of optical absorption spectroscopy to measure weak absorption in micron-sized, sub-picolitre volume droplets. It is capable of measuring the absorbance of aerosol droplets with a range of compositions and is also adaptable to wavelength-resolved measurements. This work is summarised in more detail in the Conclusions section below.

A new technique for measuring the mass accommodation and evaporation coefficients of water at an aerosol surface was developed and is described in Chap. 7. It offers many advantages over existing methods, including the ability to make simultaneous comparative measurements. This work is summarised in more detail below.

8.2 Conclusions

The aims of this work, as given in Chap. 1, are restated below. The work set out to:

- develop a sensitive, quantitative technique for measuring aerosol optical absorption that may be used to study the absorption by both water-soluble and insoluble organic components.
- develop a technique for measuring the mass accommodation coefficient of water at the surface of an aqueous aerosol droplet that avoids the limitations of previous techniques.

The absorption technique developed to address the first aim offers quantitative information on the absorbance of a single aerosol droplet. As it is a single-particle technique it is able to resolve the effect of particle composition on aerosol optical properties. The absorbance of aerosol droplets with a wide range of compositions can be studied using this technique; water-soluble organic species can be introduced to the droplet of interest via the initial nebulisation step, while insoluble organic species can be introduced via bombardment of a trapped aqueous droplet with a nebulised flow of droplets of an organic solvent containing the water insoluble component.

It is anticipated that the technique will be applicable to the study of wide range of atmospherically-relevant systems such as aqueous droplets containing black carbon and mixed-phase aqueous/organic droplets. The technique is also highly suited to carrying out wavelength-dependent measurements, expected to enable the first measurement of a single-particle absorption spectrum. Measurements such as these will significantly reduce the uncertainty in the magnitude of the aerosol direct effect, which currently hampers modelling studies carried out to predict future climate change. Further, this new method can also be applied to the analysis of trace species contained in a microdroplet, limited only by the weak absorption of the solvent and the minimum size change that is detectable spectroscopically. This is expected to be of use for lab-on-a-chip technologies, which demand techniques for the measurement of optical absorption on very small sample volumes.

The technique developed for measuring the mass transfer coefficients of water at an aerosol surface has determined the mass accommodation and evaporation coefficients of water at an aqueous surface to be 0.10 ± 0.04 at 291 K. This is consistent with a number of recent laboratory and field studies. It has also been demonstrated that the technique is sensitive enough to resolve the effect of surface composition on the mass transfer coefficients. The mass accommodation and evaporation coefficients for a droplet containing the surfactant stearic acid have been measured to be 0.03 ± 0.01 and 0.05 ± 0.01, respectively.

The technique offers many advantages over previous techniques for determining the mass accommodation coefficient. For example, it is based on a direct measurement of mass flux; the use of stationary droplets is appropriate for the theoretical treatment used to model the mass transfer; the mass transfer is initiated

by only a slight perturbation of the droplet from stable equilibrium; the measurements are carried out at atmospherically-relevant relative humidities; the mass accommodation and evaporation coefficients can be measured under identical conditions for the same droplet; and comparative measurements can be made by isolating two droplets of different compositions. It is expected that extensive use will be made of this technique to resolve definitively the effect of a wide range of atmospheric compounds on the kinetics of aerosol mass transfer, improving the understanding of the aerosol indirect effect which represents one of the largest single uncertainties in modern atmospheric aerosol science.

8.3 Future Directions

Optical tweezers are sure to play a major role in future work carried out to develop the understanding of the optical, thermodynamic and kinetic properties of aerosols [6]. There are a number of areas of experimental development which will enhance the reach of optical tweezers as a tool with which to answer some of the most pressing questions in climate science. Some examples are discussed below.

8.3.1 Controlling the Gas-Phase Environment

To date, the gas-phase composition of the droplet environment has not been controlled precisely during optical tweezing experiments. While in the studies presented in this thesis no active control over the gas-phase composition was attempted, Reid et al. have previously increased the relative humidity of the gas-phase in the immediate droplet environment by introducing a flow of humidified nitrogen gas to the trapping chamber [7]. Work is currently underway to make possible the exertion of precise control on the relative humidity. This will involve pre-mixing dry and humidified nitrogen gas flows for introduction to the trapping chamber, allowing the droplet to be exposed to a wide range of relative humidities or indeed to cycles of increasing and decreasing relative humidity. This will enable the simulation of atmospheric processing of aerosol particles and, crucially, will enable studies of the optical, thermodynamic and kinetic properties of supersaturated aerosol droplets existing in the metastable state below the deliquescence relative humidity.

8.3.2 Studying Accumulation Mode Particles

The accumulation mode, which includes aerosol particles with diameters ranging from 0.1 to 1 μm, accounts for most of the total atmospheric surface area of

aerosol particles. Particles representative of this mode also have the longest atmospheric lifetimes. As a result, particles from this mode dominate atmospheric aerosol chemistry. There is therefore a need to study smaller particles than are currently investigated using aerosol optical tweezers or indeed any other single particle technique.

The trapping efficiency of optical tweezers falls off rapidly with decreasing particle size once the size approaches the laser spot width in the focal plane [8, 9]. The minimum size of particle which can be trapped in a stable state using optical tweezers with a 532 nm wavelength trapping beam is found to be ~ 1 μm in diameter [10]. Further, CERS using a 532 nm excitation beam is not appropriate for measuring the size of droplets of <2 μm in radius. Experimental development will therefore be required before studies on the accumulation mode can be carried out using optical tweezers. This may involve using trapping light of shorter wavelength in order to reduce the beam width in the focal plane, although enhanced absorption of the trapping light by aqueous droplets would have to be carefully considered. The size of smaller aerosol droplets could be determined using the resonant structure present in the elastic scattering of a broad band light source with a wavelength of <532 nm.

An alternative approach involves using a trapping beam with a non-Gaussian profile. The profile of a Bessel beam consists of a series of concentric rings of light intensity centred on a bright core which is pseudo-nondiffracting and which reconstructs after a distortion or obstruction. The nondiffracting nature of Bessel beams has resulted in their use for guiding aerosol droplets over distances of millimetres [11], while the reconstructing property has previously been applied in the simultaneous trapping of microparticles in multiple planes [12]. It has recently been demonstrated that a combination of a Bessel beam for particle isolation and elastic light scattering for particle characterisation can be used to perform single-particle studies on aerosol droplets of <1 μm radius [13]. This suggests a future direction for single-particle aerosol studies that would facilitate studying particles representative of the atmospherically-important accumulation mode.

8.3.3 Making Use of Optical Landscapes

The environments in which atmospheric aerosols exist are extremely complex. Holographic optical tweezing allows large arrays of individual aerosol droplets to be isolated [14, 15]. By controlling the architecture of the optical field it has recently been demonstrated that flows of aerosol droplets can be directed through the optical lattice of trapping positions, offering the potential to control precisely the trapping positions of aerosol particles with different compositions [16]. This suggests a mine of future possibilities, from studying the interactions of ensembles of aerosol particles with varying combinations of compositions to constructing complex droplet environments representative of the natural environment.

8.4 Final Remarks

The combination of the complementary studies presented in this thesis represents a significant advance to the technique of aerosol optical tweezing, and in particular to its application to studies of aerosol properties relevant for reducing the uncertainty in quantifying the aerosol direct and indirect effects on climate. Combining the techniques developed through this work with recent developments in the areas described above will produce a powerful tool for rationalising the effects of aerosols on the global climate system.

References

1. K.J. Knox, J.P. Reid, K.L. Hanford, A.J. Hudson, L. Mitchem, J. Opt. A-Pure Appl. Opt. (Special Issue: Opt. Manip.) **9**, 180 (2007)
2. K.J. Knox, D.R. Burnham, L.I. McCann, S.L. Murphy, D. McGloin, J.P. Reid, J. Opt. Soc. Am. B-Opt. Phys. **27**, 582 (2010)
3. K.J. Knox, R. Symes, J.P. Reid, Chem. Phys. Lett. **487**, 165 (2010)
4. J. Leach et al., Faraday Discuss. **137**, 403 (2008)
5. K.J. Knox, J.P. Reid, J. Phys. Chem. A **112**, 10439 (2008)
6. J.B. Wills, K.J. Knox, J.P. Reid, Chem. Phys. Lett. **481**, 153 (2009)
7. R.E.H. Miles, M. Guillon, L. Mitchem, D. McGloin, J.P. Reid, Phys. Chem. Chem. Phys. **11**, 7312 (2009)
8. K. Svoboda, S.M. Block, Annu. Rev. Biophys. Biomol. Struct. **23**, 247 (1994)
9. W.H. Wright, G.J. Sonek, M.W. Berns, Appl. Phys. Lett. **63**, 715 (1993)
10. L. Mitchem, J.P. Reid, Chem. Soc. Rev. **37**, 756 (2008)
11. M.D. Summers, J.P. Reid, D. McGloin, Opt. Express **14**, 6373 (2006)
12. V. Garces-Chavez, D. McGloin, H. Melville, W. Sibbett, K. Dholakia, Nature **419**, 145 (2002)
13. H. Meresman, J.B. Wills, M. Summers, D. McGloin, J.P. Reid, Phys. Chem. Chem. Phys. **11**, 11333 (2009)
14. D.R. Burnham, D. McGloin, Opt. Express **14**, 4175 (2006)
15. J.R. Butler, J.B. Wills, L. Mitchem, D.R. Burnham, D. McGloin, J.P. Reid, Lab. Chip **9**, 521 (2009)
16. J.B. Wills, J.R. Butler, J. Palmer, J.P. Reid, Phys. Chem. Chem. Phys. **11**, 8015 (2009)

Appendices

Appendix I: SCATA programme [1]

1 Example SCATA input file

Parameter	Comments
&FLREAD	**Block containing information on spectral data files**
ROOT = “ru1_”	Root of spectral file names
STRTFRME = 21	First spectral frame for analysis
ENDFRME = 37	Final spectral frame for analysis
STEP = 1	Step size between frames for analysis
EXTEN = “.txt”	Extension of spectral frame name
COL = 3	Number of columns in spectral file
HEADER = 0	Number of lines of header in spectral file
/	
&FILES	Block controlling the files that are written/read
PKSRCHF = “pkdp1.dat”	Output of peak search
ASSIGNF = “assg1.dat”	Output file detailing peak assignments
SIZEF = “size1.dat”	Output of full sizing process
RRANGEF = “rrge1.dat”	Output of coarse sizing process
CHMF = “comp1.dat”	Output file detailing droplet composition
/	
&SIZECALC	**Block containing information on sizing calculation**
CALCTYP = 3	Calculation type (for example peak search, coarse or full sizing)
NDROP = 1	Number of droplets in data set
MINRES = 3	Minimum number of resonances in spectrum for analysis to proceed
ERRTHSH = 2	Error threshold for reported size to be accepted
LMAX = 2	Highest mode order of resonance expected to be present in spectra
RLOW = 3.6E-6	Minimum droplet radius for fitting
RHIGH = 4.8E-6	Maximum droplet radius for fitting

(continued)

(continued)

Parameter	Comments
SHLLSTP = 5e-9	Relating to sizing of inhomogeneous droplets
NOSHLL = 1	Relating to sizing of inhomogeneous droplets
SHLLMIN = 10.e-9	Relating to sizing of inhomogeneous droplets
/	
&COMP	**Block containing information relating to tracking the droplet composition and for calculating refractive index**
REFFLAG = 6	Defines refractive index treatment applied
REFIN = 1.333	Refractive index to be used for sizing at constant refractive index (not used in these studies)
REFSCALE = 1.72E-4	Gradient of concentration dependence of refractive index
REFSHELL = 1.433	Relating to sizing of inhomogeneous droplets
CONC = 50.	Concentration of solution nebulised
RHCALC = 1	Specifies method used to estimate relative humidity (RH) from the droplet composition and size
NINT = 2	Relating to peak integration (not used in these studies)
RI1 = 1.333	Further variables used to control alternative refractive index
RI2 = −4225	treatments (not used in these studies)
RI3 = 8.997e-7	
RI4 = 1.666e-8	
RI5 = 0.	
RI6 = 0.	
RI7 = 0.	
/	
&PEAKFIND	**Block containing information for peak searching**
TOLSTD = 0.8	Defines the tolerance on gradient searching
INTTOL = 1.08	
COSMIC = 70000.	Intensity threshold above which a peak is assumed to arise from a cosmic ray and is disregarded
WMIN = 636	Minimum wavelength of spectrum
WMAX = 670	Maximum wavelength of spectrum
WINDOW = 20	Integration window in which to calculate a background integral on top of which to look for a peak
WIDTH = 5	Integration window in which to calculate a peak integral to look for a peak on top of the background integral
/	

2 Example SCATA output file from full sizing calculation

Frame number	Size/m	Error in fitting of resonant wavelengths/m	Number of modes used in calculation	RH calculated from droplet composition and size
21	4.303E-06	9.31E-12	4	0.989036
22	4.303E-06	9.31E-12	4	0.989036
23	4.303E-06	9.31E-12	4	0.989036
24	4.303E-06	1.31E-11	4	0.989036
30	4.370E-06	1.56E-11	4	0.98953
33	4.436E-06	1.20E-11	3	0.989994
34	4.436E-06	1.20E-11	3	0.989994
35	4.436E-06	2.33E-12	3	0.989994
36	4.436E-06	1.20E-11	3	0.989994
37	4.436E-06	1.20E-11	3	0.989994

Appendix II: Source and Purity of Chemicals

Chemical	Source	Purity/%
Coumarin 1	Sigma-Aldrich	99
Decane	Sigma-Aldrich	>99
Glutaric acid	Acros Organics	99
Quantum dots	Molecular Probes Inc.	Not provided
Rhodamine 6G	Lambda Physik	Not provided
Rhodamine B	Acros Organics	>99
Sodium chloride	Fisher Scientific	>99.5
Stearic acid	Fluka	>99.5

Appendix III: MathCad Code of Optical Forces Model [2]

	Comments
theta0 = 41.47*pi/180;	half angle of the cone of incident light theta0 = asin(N1*N2)
a = 4.5E-6;	particle radius
na = 1.00;	medium refractive index
nw = 1.338311;	layer refractive index
ng = 1.51;	coverslip refractive index
np = 1.338311;	particle refractive index
k = ng*2*pi/532E-9;	wavenumber in the coverslip
power = 10E-3;	power in Watts
roe = 1000;	density of water
X = k*a*(na/ng);	adjustment for wavenumber in the surrounding medium (i.e. air)
m = np/na;	ratio of particle and medium refractive indices
N1 = nw/ng;	water to coverslip refractive index ratio
N2 = na/nw;	air to water refractive index ratio
cmax = round(X + 4*X^(1/3) + 2);	sum over the angular momentum up to this value
Ntheta = 1000;	number of elements in array of 'theta'
thetag = theta0*[1:Ntheta]/Ntheta;	creates an array of numbers (angles) in 'Ntheta' steps from 0 to theta0
thetaw = asin(sin(thetag)/N1);	corresponding angles in the aqueous layer
thetaa = asin(sin(thetaw)/N2);	corresponding angles in air
N = (N1*N2);	refractive index ratio between air and coverslip
A = 0.91;	fraction of available beam power that fills on the objective aperture fraction(gamma,theta0,N); 0.3729
gamma = (sqrt((log(1-A))/(-2)))/(sin(theta0));	relates to the Gaussian nature of the beam entering the objective 0.8;
dh = (10*N1)*1E-6;	aqueous layer thickness
BIGX = 20E-6;	displacement of objective when raising focus above coverslip/aqueous layer
L2 = ((BIGX*N1)-dh)*N2;	actual height of paraxial focus above aqueous layer due to objective displacement
%Spherical aberration transmission	
T12 = (2*cos(thetag))./(cos(thetag) + N1*cos(thetaw));	transmission through glass water interface
T23 = (2*cos(thetaw))./(cos(thetaw) + N2*cos(thetaa));	transmission through water air interface
%vector describing z position of sphere	
res = 401;	resolution of the axial direction. i.e. how many points are calculated on the force curve
no_radii = 4;	number of sphere radii out from the focus (z = 0) the force is calculated for

(continued)

(continued)

	Comments
z = ([1:res]-(((res-1)/2) + 1))/((res-1)/2)*no_radii*a;	calculates an array in microns describing the axial sphere position
%solid angle and Abbe sine condition	
sc = sin(thetag).*sqrt(cos(thetag));	arising from the integral representation of focussed beams
%gaussian beam	
g = exp(-(gamma^2)*(sin(thetag).^2));	arising from the integral representation of focussed beams
%Mie scattering	
for c = 1:1:cmax + 1	
[ac(c),bc(c)] = Me(c,X,m);	call to function Me(c,X,m) to calculate Mie coefficients a_[268] and b_[268]
end	
%rotation matrix	
dc(1,:) = (cos(thetaa/2)).^2;	calculates the matrix elements of finite rotations
dc(2,:) = ((2*cos(thetaa)) - 1).*((cos(thetaa/2)).^2);	calculates the matrix elements of finite rotations
for v = 3:cmax + 1	
dc(v,:) = ((v*((2*v)-1))/((v.^2)-1))*(((cos(thetaa)-(1/(v*(v-1)))).*dc(v-1,:))-(((((v-1).^2)-1)/((v-1)*((2*v)-1)))*dc(v-2,:)));	calculates the matrix elements of finite rotations
end	
%calculates the G_[268] values for every axial position (do the integration over the z vector kind of)	
for y = 1:res	
psi = k*((-((dh/N1) + (L2/(N1*N2)))*cos(thetag)) + (N1*N2*(L2)*cos(thetaa)) + (dh*N1*cos(thetaw)) + (z(y)*N1*N2*cos(thetaa)));	aberration function for two interfaces
cc2 = exp(i*psi);	
grand = sc.*g.*cc2.*T12.*T23;	
G(:,y) = (theta0/Ntheta)*dc*grand.';	
Gprime(:,y) = (theta0/Ntheta)*dc*(grand.*cos(thetaa)).';	
end	
ac1 = zeros(1,cmax + 1);	new array for the a_{j + 1) values
bc1 = zeros(1,cmax + 1);	new array for the b_{j + 1) values
for s = 1:1:cmax	
ac1(s) = ac(s + 1);	creating the a_{j + 1) values
bc1(s) = bc(s + 1);	creating the b_{j + 1) values
end	

(continued)

(continued)

	Comments
G1 = zeros(cmax + 1,res);	new array for the G_{j + 1) values
for t = 1:1:cmax	
G1(t,:) = G(t + 1,:);	creating the G_{j + 1) values
end	
for f = 1:cmax + 1	
coeff1(f) = (2*f) + 1;	coefficients for Q_[62] and Q_[23]
coeff2(f) = (f*(f + 2))/(f + 1);	coefficients for Q_[62] and Q_[23]
coeff3(f) = ((2*f) + 1)/(f*(f + 1));	coefficients for Q_[62] and Q_[23]
end	
Qez = (coeff1.*(ac + bc))*(G.*Gprime.");	
Qsz = (coeff2.*((ac.*ac1.") + (bc.*bc1."))*(G.*G1.")) + ((coeff3.*ac.*bc.")*(G.*G."));	
total = real(Qez);	
Qe = ((4*gamma.^2)/(A*N1*N2))*total;	
total2 = real(Qsz);	
Qs = ((-8*gamma.^2)/(A*N1*N2))*total2;	
d = z/a;	
ABB(:,1) = d;	
ABB(:,2) = ((Qe + Qs).');	final Q results (optical force efficiency)
FABB(:,1) = ABB(:,1);	
FABB(:,2) = (((ABB(:,2)*na*power)/3E8)-((4/3)*pi*(a^3)*roe*9.81))*1E12;	final force results taking into account gravity

References

1. J.P. Reid, *Size and Compositional Analysis of Aerosols* (2007)
2. D.R. Burnham, Ph.D. thesis: Microscopic Applications of Holographic Beam Shaping and Studies of Optically Trapped Aerosol, University of St. Andrews, St. Andrews, 2009